Electroluminescent devices based on polymeric thin films

Young, Jung Gun

Electroluminescent Devices based on Polymeric Thin Films

By

Jung Gun Young

A thesis submitted in partial fulfilment
of the requirements for the degree of PhD

School of Engineering
University of Durham
2001

DECLARATION

I hereby declare that the work carried out in this thesis has not been previously submitted for any degree and is not currently being submitted in candidature for any other degree.

Signed.....
Candidate

The work in this thesis was carried out by the candidate

Signed.....
Director of Studies

Signed.....
Candidate

Acknowledgement

There are a number of people I would like to thank for their help and advice. Particularly I cannot express enough my thanks to my supervisor, Professor Mike Petty for his enthusiasm, advice and consideration concerning my research and subsistence in Durham away from my beloved family over 3 years.

When I look back on the last 3 years, it seems to me that time has flown like an arrow through happy, dull and angry moments. During this time I left two things: one was friendship with my lovely friends and the other thing was this little 'thesis'. I cannot ever forget the life in Durham.

I have always pondered what the Ph. D. degree could bring to me and what I should do to deserve it. As for this profound question, Dr. C. Pearson, Dr. C.S. Wang and my best friend, N.B. Pomeroy, have given me helpful directions by showing how to research and think differently in their own way. I really thank them from my heart. Special thanks to Professor M.R. Bryce and Dr. C.S. Wang for the supply of materials and also to Yu Hyun Gyu for the kind supply of ITO glasses. I admit that without their help I would not be here at the moment.

I would like to thank all the people who helped me to build good memories in Durham: specially to Choi Yoon Jeong, In Nam Sik, Lee Yong Gyu, my church members and all the colleagues in our group.

Finally I sincerely thank my parents who always think about my health, stand by me and sacrifice themselves for me.

12th. May. 2001

Abstract

This thesis is concerned with the preparation of organic light-emitting diodes (LEDs) by using different thin film technologies: the Langmuir-Blodgett (LB) technique; spin-coating and thermal evaporation.

The π-conjugated polymer, poly(2-methoxy-5-(5'-ethylhexyloxy)-*p*-phenylenevinylene) (MEH-PPV), was used as the emissive layer and was deposited onto patterned indium-tin oxide (ITO) glass using the LB technique or spin-coating. Y-type LB films of MEH-PPV were deposited at a surface pressure of 17 mN m^{-1} with a transfer ratio of 0.95 ± 0.03. Many efforts were made to improve the LB film device performance parameters, such as external quantum efficiency and operating lifetime, by inserting an electron transporting or insulating layer between the emissive layer and top cathode. Annealing the LB films was found to result in an improved operating lifetime.

LEDs based on spun films possessed higher external quantum efficiencies than devices made from LB films. The more ordered LB films had a higher probability of intra- and intermolecular interactions and formed more excimer states within the structure. This led to a lower quantum efficiency compared to devices incorporating spun films. The operating lifetime of the LEDs was highly dependent on the morphology of the film surface. A smoother film surface is required for a longer device operating lifetime.

A new electron transporting material, 2,5-bis[2-(4-*tert*-butylphenyl)-1,3,4-oxadiazol-5-yl]pyridine (PDPyDP), was deposited on top of the MEH-PPV spun film. Despite a high external quantum efficiency of 0.7 %, this device suffered from dark regions in the electroluminescence output resulting in degradation of the device. The dark area formation was attributed to delamination of the aluminium electrode from the PDPyDP layer, which was lessened by: (a) annealing the degraded devices; (b) evaporating a thicker aluminium layer at a high rate and (c) inserting a buffer layer (Alq_3) between the PDPyDP and the Al top electrode.

CONTENTS

Chapter 1 **Introduction** **1**

Chapter 2 **A Review of Organic Electroluminescent Devices** **5**

2.1 Introduction 5

2.2 History 5

2.2.1 Inorganic LEDs 6

2.2.2 Organic LEDs 7

2.3 Organic LED Structure 10

2.4 Charge Transporting and Emitting Materials 12

2.4.1 Hole Transporting Materials 13

2.4.2 Electron Transporting Materials 14

2.4.3 Emissive Materials 15

2.5 Electrodes 17

2.6 Device Stability 19

2.7 Multi-Colour Fabrication 20

2.8 Future Directions 23

2.9 Summary 24

References 25

Chapter 3 **Optical and Electronic Properties of LEDs based on Conjugated Polymers** **29**

3.1 Introduction 29

3.2 Conjugated Polymers 29

3.3 Peierls Distortion 32

3.3.1 Polarons 33

3.3.2 Solitons 35

3.4 Photoluminescence 37

3.5 Modelling of I-V Characteristics of Organic LEDs 40

3.5.1 Metal-Semiconductor Contact 41

3.5.2 Fowler-Nordheim Tunnelling 45

3.5.3 Space Charge Limited Current 46

3.6 Electron-Hole Recombination and Exciton Formation 49
3.7 Excimer Formation 52
3.8 Radiative and Nonradiative Decay of Singlet States 53
3.9 Quantum Efficiency and Energy Efficiency 54
3.10 Summary 56
References 57

Chapter 4 Experimental Techniques 60
4.1 Introduction 60
4.2 Film Deposition 61
4.2.1 Langmuir-Blodgett Technique 61
Materials suited to the LB Technique 61
Surface Pressure versus Area Isotherm 62
Multilayer LB films 63
Deposition modes 64
Surface Pressure Measurement 66
Experimental Details 67
4.2.2 Thermal Evaporation 70
Experimental Details 71
4.2.3 Spin-Coating 73
Experimental Details 73
4.3 Optical Characterisation 74
4.3.1 Optical Microscopy 74
4.3.2 UV-Vis. Absorption Spectroscopy 74
4.3.3 Photoluminescence Spectroscopy 75
4.3.4 Scanning Electron Microscopy 76
4.3.5 Electron Probe Microanalysis 76
4.3.6 Electroluminescence Spectroscopy 77
4.3.7 Atomic Force Microscopy 78
4.4 Device Fabrication 79
4.4.1 ITO Patterning 79
4.4.2 Deposition of the Organic Layer 79
4.4.3 Metal Evaporation 80
4.5 LED Characteristics 81

4.6 A.c. Impedance Spectroscopy 82
4.7 Low Temperature Conductivity 83
4.8 Surface Profilometer 84
4.9 Summary 85
References 86

Chapter 5 **MEH-PPV Devices Prepared Using the Langmuir-Blodgett Technique 88**
5.1 Introduction 88
5.2 LB Film Deposition and Characterisation 88
5.2.1 Material 88
5.2.2 Surface Pressure versus Area Isotherm and LB Deposition 90
5.2.3 LB Film Characterisation 93
UV-Vis. Absorption Spectroscopy 93
Film Thickness Measurement 94
5.3 Current-Voltage Characteristics 95
5.3.1 Schottky Barrier 96
5.3.2 Space Charge Limited Current 98
5.3.3 Fowler-Nordheim Tunnelling 102
5.4 EL Characteristics 104
5.4.1 Light Output 104
5.4.2 Ca Top Electrode 107
5.4.3 PL and EL Spectra 109
5.5 Summary 110
References 111

Chapter 6 **Improvements in MEH-PPV LB Film Device Performance** 114
6.1 Introduction 114
6.2 Incorporation of Insulating LB layers 114
6.2.1 Background 114
6.2.2 Device Structures 115
6.2.3 Device Characteristics 116
ITO/AA/MEH-PPV/Al Devices 116

ITO/MEH-PPV/AA/Al Devices 118
6.2.4 Energy Band Model 121
6.3 Incorporation of an Electron Transporting Layer 124
6.3.1 Background 124
6.3.2 LB Deposition of PHPY 124
6.3.3 Dual-Layer device Characteristics 126
6.3.4 Alternate-Layer Device 129
6.3.5 Optimisation of Film Thickness 131
6.4 Thermal Annealing Effects 133
6.4.1 Background 133
6.4.2 Device Fabrication 134
6.4.3 Device Performance 135
6.4.4 Optical Characterisation 137
6.4.5 Operating Lifetime 139
6.4.6 Improvement of Operating Lifetime 146
6.5 Summary 147
References 148

Chapter 7 Devices based on MEH-PPV Spin-Coated Films 150
7.1 Introduction 150
7.2 Comparison of Spun and LB Films 150
7.2.1 Spin-Coating of MEH-PPV 151
7.2.2 Comparison of Optical Properties 151
7.2.3 Comparison of Device Characteristics 155
7.2.4 Device Operating Lifetime 157
7.3 Dual-Layer Devices 159
7.3.1 Background 159
7.3.2 Device Structure 160
7.3.3 Device Characteristics 161
7.3.4 Dark Area Formation in the EL Image 164
7.4 Rubrene Doping of MEH-PPV 165
7.4.1 Background 165
7.4.2 Device Characteristics 165
7.4.3 Device Operating Lifetime 169

7.5 Use of Interfacial Layers 170
7.5.1 Background 170
7.5.2 Device Structures 171
7.5.3 Device Performance 172
7.5.4 Dark Area Formation (Storage Lifetime) 175
7.5.5 Operating Lifetime 177
7.6 Annealing Experiments 179
7.6.1 Experimental Details 179
7.6.2 Comparison of Dark Area Growth for Devices Stored in Air or in Vacuum 180
7.6.3 Effect of Annealing on I-V Characteristics 181
7.6.4 Effect of Annealing on PL, UV-Vis. Absorption Spectra 183
7.6.5 Effect of Annealing on Dark Areas in EL Image 185
7.6.6 AFM Studies 187
7.6.7 Storage and Operating Lifetime Tests 189
7.7 Al Evaporation 191
7.8 Summary 195
References 196

Chapter 8 **Conclusions and Suggestions for Further Work** **198**
8.1 Conclusions 198
8.2 Suggestions for Further Work 203
8.2.1 Prevention of Reflection at the Glass-Air Interface 204
8.2.2 Elimination of Total Reflection within the Glass 207
8.2.3 Increase of the Critical Angle, θ_c 208
References 209

Publications **210**

Chapter 1.

Introduction

Organic electroluminescence was reported in 1963 by Pope et al. [1] at about the same time as the first commercial GaAsP light emitting diodes (LEDs) were introduced. Subsequently, progress in LEDs was primarily in the inorganic area before Tang and VanSlyke [2] significantly improved the performance of organic LEDs in 1987, using a multilayer structure.

Organic LEDs have an advantage over their inorganic counterparts in that they have a significant potential for large area flat panels with a full colour range and low cost. Flexible (plastic) display products can also be made [3]. There has been much academic and commercial interest in improving device characteristics such as the external quantum efficiency, brightness and device lifetime. External quantum efficiencies of over 8 % [4] and colours covering the entire visible range [5] have now been obtained. However, there remains a problem of device durability (operating lifetime), which is caused by the oxidation, chemical degradation and mismatch of the top metal electrode with the organic layer.

Electroluminescence (EL) based on π-conjugated polymers was first discovered by Burroughes et al. in 1990 in Cambridge [6]. Interest in these polymers has grown significantly due to the ease of producing LEDs using polymer solutions, and the strong luminescence yield from several conjugated polymer systems [6, 7]. It is now possible to produce light from polymer LEDs across the entire visible range [8].

The thin organic layers required for organic LEDs are usually deposited by the spin-coating method or thermal evaporation. The Langmuir-Blodgett [9] (LB) technique and layer-by-layer self-assembly [10] offer alternative methods for building up ultra-thin organic films of nanometre dimensions. The LB technique provides a means to deposit uniform coatings of organic materials over a large area and for the preparation of highly ordered organic systems with molecular architectures and thicknesses that are controllable at the molecular level.

Poly(2-methoxy-5-2'-ethylhexyloxy)-*p*-phenylenevinylene), MEH-PPV, is an attractive material for LED fabrication and is used as both the emitting and hole transporting layer. In this research, several strategies have been applied to organic LEDs using MEH-PPV films to increase the external quantum efficiency and the device lifetime.

Chapter 2 begins with a review of electroluminescence and its progress to date. Organic materials based on small molecules and conjugated polymers are introduced. The theory of electroluminescence and the modelling of current-voltage (I-V) characteristics in organic LEDs are introduced in Chapter 3. Three methods are commonly used to prepare organic thin films: LB film deposition, thermal evaporation and spin-coating. Experimental details of the film deposition techniques mentioned above and film characterisation by using several optical spectroscopies are described in Chapter 4. The fabrication of organic LEDs and the measurement equipment for the electrical characteristics are also detailed.

Chapter 5 is the first chapter of results and is concerned with the properties of MEH-PPV LB films and the I-V characterisation of simple light emitting devices based on MEH-PPV LB film. The I-V curves are fitted to several models to describe

the conduction mechanism within an MEH-PPV single-layer device. Supplementary experiments, such as a.c. impedance spectroscopy and low temperature d.c. electrical measurements, are also described to identify the dominant mechanism. Methods to improve the performance of LEDs based on MEH-PPV LB films are reported in Chapter 6. These include insertion of thin arachidic acid LB layers and an electron-transporting polymer, poly(6-hexylpyridine-2,5-diyl) (PHPY), between the MEH-PPV layer and the aluminium (Al) top electrode, and annealing of the MEH-PPV LB films prior to the Al evaporation.

Comparisons are made between the single-layer MEH-PPV devices based on LB films and spun films in Chapter 7. The remainder of Chapter 7 is concerned with dual-layer devices incorporating a novel electron transporting layer, 2,5-bis[2-(4-*tert*-butylphenyl)-1,3,4-oxadiazol-5-yl]pyridine (PDPyDP), on the MEH-PPV spun films. Several strategies are adopted in this chapter to increase the stability of this dual-layer device. Finally, conclusions from the whole thesis, including suggestions for the further work, are provided in Chapter 8.

Every journey begins with one step. There will always be explorers who strike out upon their own paths. Afterwards others can then follow these and go further, in their own endeavours, to perhaps greater riches and rewards. It is my wish that my small contribution will play some part in the future explorations of organic LEDs.

References

1. M. Pope, H.P. Kallmann and P. Magnante, *J. Chem. Phys.*, **38**, 1963, 2042.

2. C.W. Tang and S.A. VanSlyke, *J. Appl. Phys.*, **65**, 1989, 3610.

3. P. Yam, *Sci. Am.*, **273 (1)**, 1995, 75.

4. M.A. Baldo, S. Lamansky, P.E. Burrows, M.E. Thompson and S.R. Forrest, *Appl. Phys. Lett.*, **75**, 1999, 4.

5. C.C. Wu, J.C. Sturm, R.A. Register, J. Tian, E.P. Dana and M.E. Thompson, *IEEE. Trans. Electron Devices*, **44**, 1997, 1269.

6. J.H. Burroughes, D.D.C. Bradley, A.R. Brown, R.H. Marks, K. MacKay, R.H. Friend, P.L. Burn and A.H. Holmes, *Nat.*, **347**, 1990, 539.

7. B. Hu, Z. Yang and F.E. Karasz, *J. Appl. Phys.*, **76**, 1994, 2419.

8. M. Berggren, M. Granstrom, O. Inganas and M. Andersson, *Adv. Mater.*, **7**, 1995, 900.

9. M. Ahlskog, J. Paloheimo, H. Stubb, P. Dyreklev, M. Fahlman, O. Ingannas and M.R. Andersson, *J. Appl. Phys.*, **76**, 1994, 893.

10. M. Onoda, A. Chuma, H. Nakayama, T. Yamaue, K. Tada and K. Yoshino, *J. Phys. D. Appl. Phys.*, **30**, 1996, 2364.

Chapter 2.

A Review of Organic Electroluminescent Devices

2.1 Introduction

Electroluminescence, the process of light emission from a material following injection of electrical charge carriers, has been the subject of both academic and commercial interest for many decades. This chapter begins with the history of light emitting devices followed by their principles of operation. Organic materials for hole transporting, electron transporting and emissive layers are introduced in Section 2.4. Important device performance parameters, such as stability, quantum efficiency and multi-colour tuning, are described in the following section. Finally, the future of organic LEDs in the flat panel display market is discussed.

2.2 History

Inorganic electroluminescent materials have been known for many years, and LEDs based on these materials have been commercially available since the early 1960s. EL from molecular organic materials was discovered about the same time, but it was only in the mid-1980s that devices using fluorescent organic dyes with brightnesses and operating voltages suitable for commercial applications were developed by Tang and VanSlyke [1] and Adachi and Tsutsui et al. [2].

2.2.1 Inorganic LEDs

Light emitting diodes using *p-n* junctions of inorganic semiconductors have dominated this field for thirty years or so. However, efficient blue emission has recently been achieved. Inorganic semiconductors are difficult to form over extended areas, making the process uneconomic for large displays.

Although blue and green LEDs have been made from materials such as silicon carbide and gallium phosphide, they are not efficient because of their indirect energy band gaps. This means that the electrons and holes have different momenta and can only recombine by scattering from lattice vibrations. The most intense research has focused on II-VI materials, such as zinc selenide, and III-V nitrides, such as gallium nitride, as these materials have direct band gaps and emit light at blue and green wavelengths. The difficulty in fabricating inorganic LEDs is that these compounds should have a similar lattice constant to the substrate. If not, any mismatch creates strain in the layers, which is generally released as dislocations.

In 1991, Michael Haase and colleagues at 3M demonstrated the first pulsed operation of green laser diodes based on II-VI materials. The short lifetime of these devices (preventing their commercialisation) is thought to be due to crystal defects. Comparatively few defects in II-VI compounds can cause others to propagate, disrupting the weak bonding in the material and causing the device to fail. In the case of III-V nitrides (despite the fact that gallium nitride has a direct band gap suitable for blue light emission) there is no lattice-matched substrate for the growth of gallium nitride.

So far, only one ternary compound, indium gallium nitride, has been used as the active layer of blue and green light emitting devices. The addition of indium to

gallium nitride is vital for achieving strong light emission. The band gap of the material can be varied between 2.0 and 3.4 eV by altering the indium content. This corresponds to emission wavelengths between 620 and 365 nm.

2.2.2 Organic LEDs

Organic electroluminescence was first observed from single crystals of anthracene by Pope et al. in 1963 [3]. These workers observed a bright blue emission from 10-20 μm thick crystals at voltages above 400 V. In 1982, Vincett et al. [4] evaporated films of anthracene which were an order of magnitude thinner than the single crystals used by Pope. Roberts et al. [5] deposited anthracene derivatives with short alkyl chain by using the LB technique. Thus high fields could be generated across these devices at a much lower voltage and the efficiency was improved considerably. Unfortunately the lifetime of these structures was very short.

In 1987, a breakthrough in device performance was made by Tang et al.[1]. These workers separated the functions of charge transport and emission by introducing a charge-transporting layer. Their dual-layer device, based on tris (8-hydroxyquinoline) aluminium (Alq_3) emitted 1000 cd m^{-2} with an external quantum yield of 1 %. This concept was extended to three layers by using an emitter layer sandwiched between electron and hole transporting layers [2]. However, the stability of the devices was poor. A further improvement was made by Tang's group at Kodak [6]. An addition of a small percentage of an emissive organic dye (DCM) into a host matrix (Alq_3) was found to alter the emission colour, and to improve the efficiency and lifetime of the devices [6].

Research on polymer electroluminescence was first reported by Partridge of the National Physical Laboratory in the UK, in 1983 [7]. Partridge built an LED based on poly(N-vinyl carbazole), PVK, that emitted blue light. However, the low luminance of the device meant that this work did not attract much attention. This situation changed in 1990 when Friend and colleagues at Cambridge University reported light emission from a π-conjugated polymer called poly(*p*-phenylenevinylene) or PPV [8]. Polymers offer several advantages over their small molecule counterparts in that they are mechanically more robust, and less prone to recrystallisation. Very recently, Cambridge Display Technology (CDT) reported green emission from a polyfluorene based polymer with a luminous efficiency of over 20 lm W^{-1} [9].

Devices combining polymers and small molecules also offer good performance. One such example is a polymer doped with a dye that emits red, blue or green light. Kido and colleagues have built single layer devices using dye dispersed PVK, which emitted white light with a maximum luminance of over 4000 cd m^{-2} [10]. Figure 2.1 summarises the remarkable improvements in device performance in organic and inorganic devices since the 1960s.

Organic devices have improved rapidly since their introduction. Such LEDs have an advantage over their inorganic counterparts, in that they have a significant potential for the development of large area flat panels with a full colour range (blue to red) at low cost [11-13]. Flexible (plastic) display products [14] can also be made since the organic thin films are deposited without the lattice-matching requirements that limit most inorganic semiconductors to a narrow range of substrates.

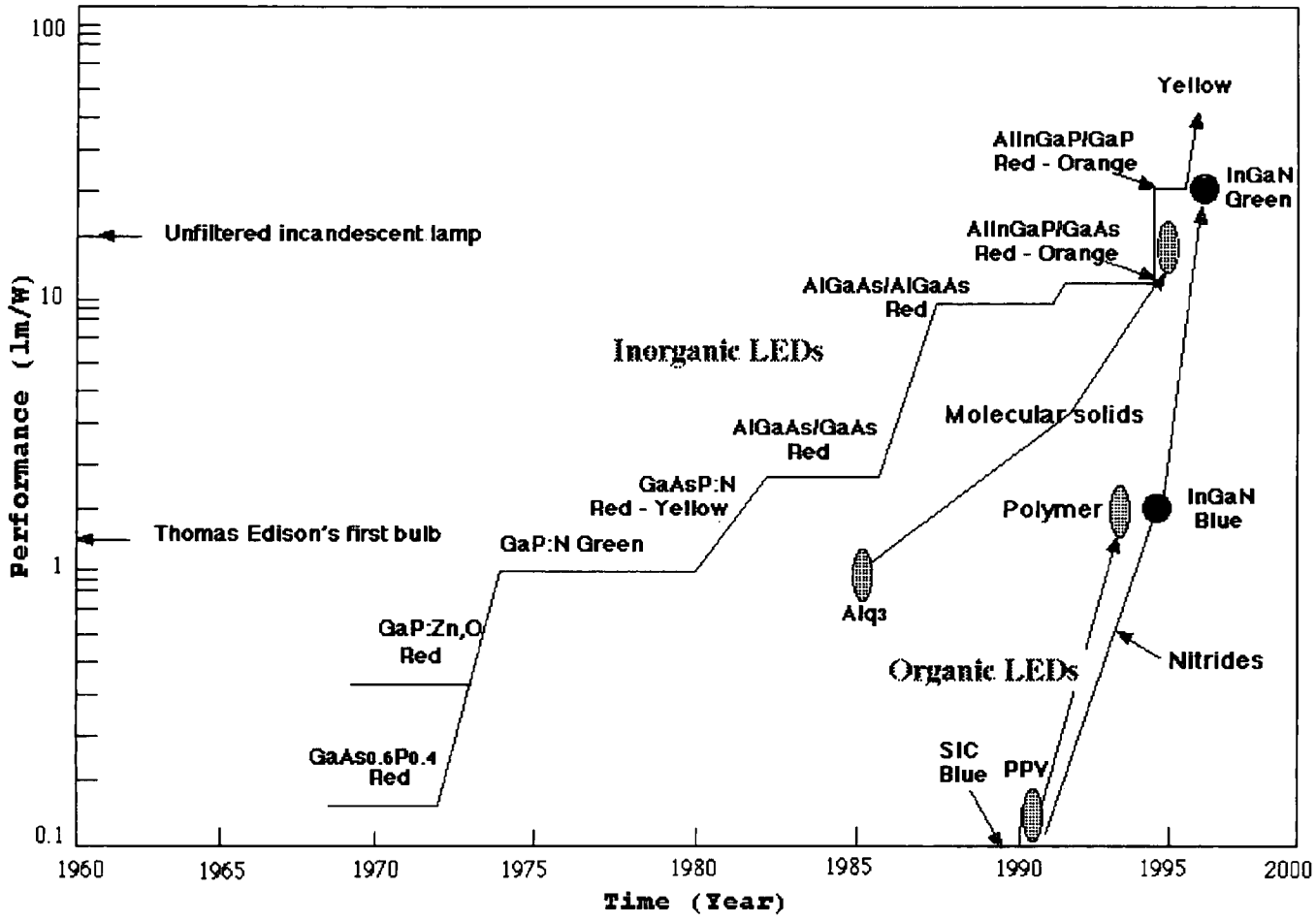

Figure 2.1 Progress in LED efficiencies since the early 1960s [10].

For multi-colour fabrication, conventional photolithographic techniques are not available due to the solubility of organic materials in various chemicals. Efforts to date to integrate different colour organic LEDs on the same substrate have exploited patterning by using a shadow mask for small molecules [15] and ink-jet printing in the case of the polymers [16]. A further problem with organic LEDs is that morphological changes in the organic materials due to the joule heating during device operation is detrimental to both the device performance and lifetime.

2.3 Organic LED Structure

The structure of all organic LEDs is straightforward: one or more organic films are sandwiched between two electrodes, one of which should be transparent to allow the EL emission to leave the device. A schematic energy-level diagram is shown in figure 2.2. In this case, indium tin oxide is the transparent anode and calcium is the cathode.

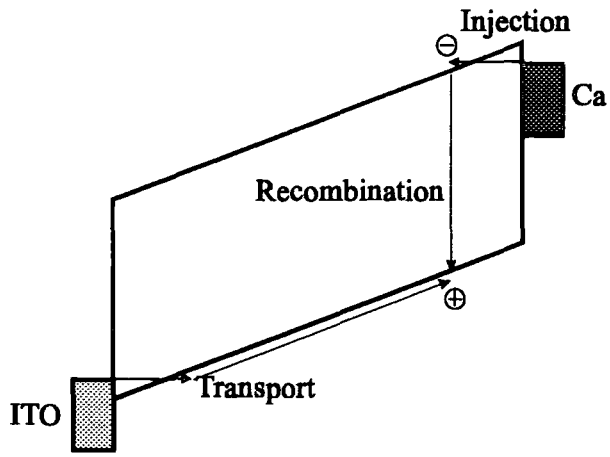

Figure 2.2 Schematic band diagram of organic LED under forward bias.

The principle of organic electroluminescent devices is quite similar to that of inorganic light emitting diodes. Important processes are (I) charge injection, (II)

charge transport within the charge transporting layer, (III) exciton formation in the emitter region of the device via Coulombic interaction and (IV) finally radiative decay of the excitons.

Electrons and holes can be injected over energy barriers from negative and positive electrodes, respectively, under appropriate voltages. These interfacial barriers are due to the band offsets between the semiconducting organic layer and the metal electrode: the energy level difference between the work function of the ITO anode and the highest occupied molecular orbital (HOMO) for holes; and the energy level difference between the work function of calcium and the lowest unoccupied molecular orbital (LUMO) for electrons. Electrons and holes are attracted to one another within the organic film and form either singlet or triplet excitons. Among these, the singlet excitons may decay radiatively, giving out light which is observed through the transparent electrode. Under reverse bias, there is a small leakage current and no emission.

To increase the device efficiency, it is necessary that the number of electrons be balanced with that of holes providing a high probability of carrier recombination. To achieve the balance requires that the injected positive and negative charge carriers have similar mobilities. Time-of-flight measurements have shown that very low negative carrier mobilities are seen in many organic solids due in part to the strong trapping capability of oxygen in such materials [6]. The greater self-absorption of EL occurs when emission, on average, takes place deeper within the film, i.e. closer to the negative electrode, which also acts like a quenching site [17]. Hence, for efficient LEDs it is necessary to have the recombination zone away from the metal electrode. Figure 2.3 shows a device incorporating an electron transporting layer. In this

example, 2-(4-biphenylyl)-5-(4-*tert*-butylphenyl)1,3,4-oxadiazole (PBD) dispersed in a poly(methyl-methacrylate) (PBD:PMMA) layer was deposited as an electron transporting layer on top of PPV emissive layer. The PBD:PMMA layer transports electrons away from the negative electrode, and also inhibits the transport of hole leakage currents, causing the build up of a hole space charge at the interface between PPV and PBD:PMMA. This increases the field across the PBD:PMMA layer and provides enhanced electron injection. Using this electron-conducting, hole-blocking layer the external quantum efficiency of the device increased from 0.1 % to 0.8 % [18].

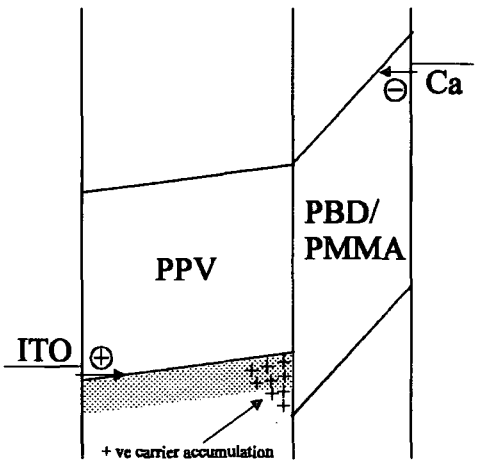

Figure 2.3 Schematic energy level structure for ITO/PPV/PBD:PMMA/Ca multilayer heterostructure device [18].

2.4 Charge Transporting and Emitting Materials

Charge transporting materials must have a high mobility for either electrons or holes and possess suitable energy band offsets with appropriate electrodes. These materials must also establish good electrical contacts with the electrodes without any chemical reaction which may reduce the device performance and lifetime. The organic

materials for both types of layers are required to have good thermal stability and be capable of forming high quality thin films. The emissive materials should possess the necessary delocalised electronic structures to yield a strong fluorescence at a desired wavelength.

2.4.1 Hole Transporting Materials

Useful hole transporting materials (HTMs) require a high glass transition temperature (T_g) because the operating lifetime of the organic LEDs is closely related to the thermal stability of the organic materials. They should also form a low energy barrier for hole injection from the anode into the emissive layer and an ability to block electron injection from the emissive layer to the HTM layer. Several HTMs are shown in Figure 2.4.

Most common HTMs are the arylamines, for example, 4,4'-tris(3-methylphenylphenylamino)biphenyl (TPD) [2], *N,N'*-di(naphthalene-1-yl)-*N,N'*-(3-methylphenyl)1,1'-biphenyl-4,4'-diamine, (NPB) [19], and 4,4',4''-tris(3-methylphenylphenylamino)triphenylamine (*m*-MTDATA) [20]. The hole mobility of TPD is about 10^{-3} cm^2 V^{-1} s^{-1} at 1 MV cm^{-1} [21]. Although TPD is the most commonly used compound for a HTM, recrystallisation of TPD is a serious problem during device operation [22,23]. Various groups have modified the structure of TPD (T_g, 63 °C) to increase T_g. This reduces recrystallisation and increases the thermal stability of the EL device [24]. Further compounds which have higher T_g values are starburst amines [25]. In particular, *m*-MTDATA forms a stable amorphous film with a higher T_g of 75 °C and has 0.4 eV smaller hole injection barrier from the ITO electrode than TPD [26].

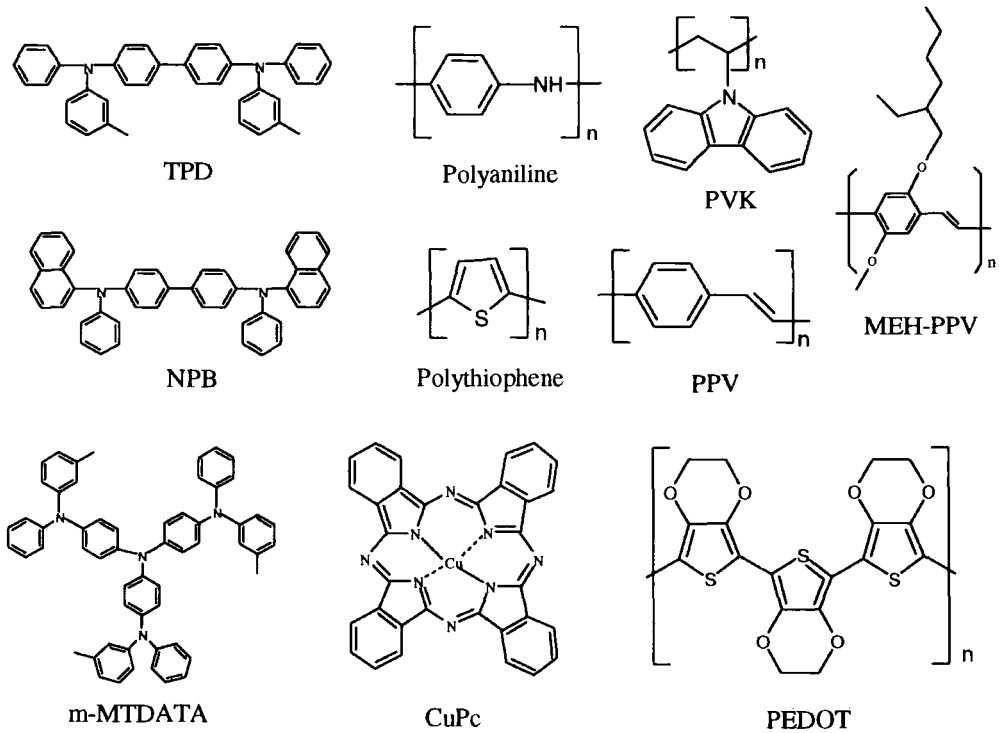

Figure 2.4 A selection of typical organic hole-transporting materials.

2.4.2 Electron Transporting Materials

The criteria for good electron transporting materials (ETMs) are the ability to block holes, transport electrons and the provision of a small barrier to electron injection from the metal cathode. A frequently used material is tris (8-hydroxyquinoline) aluminium (Alq_3), which has a broad green emission, peaking at 530 nm. One of the best attributes of Alq_3 is its propensity to form high quality thin films by thermal evaporation and its relatively high T_g (175 °C). The electron mobility of Alq_3 was estimated to be around 10^{-5} cm^2 V^{-1} s^{-1} [21], which is a factor of 100 smaller than the hole mobility of TPD.

Other good candidates are compounds containing oxadiazole groups, which are electron deficient. These block holes and transport electrons very efficiently. One

of such oxadiazole derivatives is PBD [27]. However, this material has a relatively low melting temperature of 168 °C. A new material, 1,3-bis[2-(4-*tert*-butylphenyl)-1,3,4-oxadiazole-5-yl]benzene (OXD-7) [28], has been developed, which has a much higher melting point of (> 240 °C) and consequently is much more stable. By replacing the oxygen in 1,3,4-oxadiazoles (OXD) with nitrogen, the derivative, 1,2,4-triazole (TAZ), was obtained. TAZ has been shown to have a higher electron transporting capability than that of OXD [29]. Cyano substituted PPV derivatives (CN-PPV) increase the polymer electron affinity by some 0.9 eV over PPV [30]. A selection of electron transporting materials is shown in Figure 2.5.

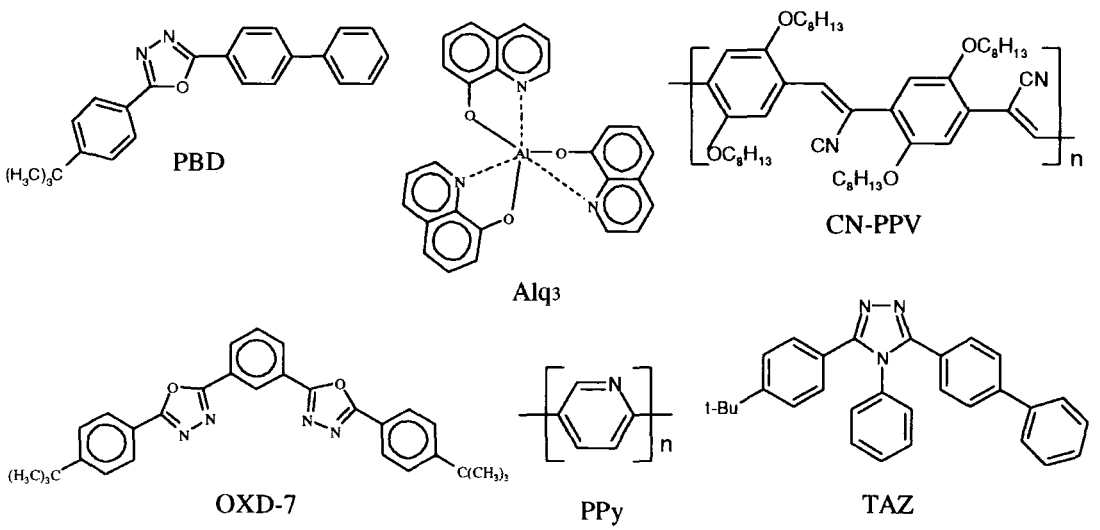

Figure 2.5 A selection of electron transporting materials.

2.4.3 Emissive Materials

Most organic fluorescent dyes tend to suffer from various degrees of 'concentration quenching' which causes the emission bands to broaden. This is particularly true in the solid state. By doping or dispersing organic fluorescent dyes (guest) in a host matrix (emitter), self-quenching can be minimised and emission from

the guest molecule can be obtained by energy transfer. The Kodak [31] group has demonstrated that most organic fluorescent dyes (so long as they could be evaporated and were energetically compatible) are useful as dopants.

Some of the desired criteria for dopants for full colour EL displays are: (I) a high fluorescence quantum yield, (II) overlap between the emission of the host emitter and the absorption of the dopant to allow efficient energy transfer, (III) emission peak at the blue, green and red region of the visible spectrum and (IV) narrow emission bandwidth to maintain chromatic purity. Figure 2.6 shows a selection of materials for the emissive layer and dopant in organic LEDs. Materials are positioned on the figure to indicate their approximate emission wavelengths.

The emission colour can be changed by modifying the molecular structure [33] or by doping a small percentage of a highly emissive material into one of the transporting layers. Tang and colleagues [1,6] found that adding a small percentage of DCM to an Alq_3 layer shifted the emission from green to orange-red. Polymer LEDs can have a variety of available emission colours simply by changing the side-chains [34] and/or copolymerisation which controls the degree of conversion to the conjugated form [35]. These lead to a change in the π-π^* electronic energy gap which determines the colour of emission. Dialkoxy-PPV derivatives are particulary attractive due to their solubility in common organic solvents. Of this group, MEH-PPV is the most commonly used material. It is employed in the emitting and/or hole transporting layers of LEDs.

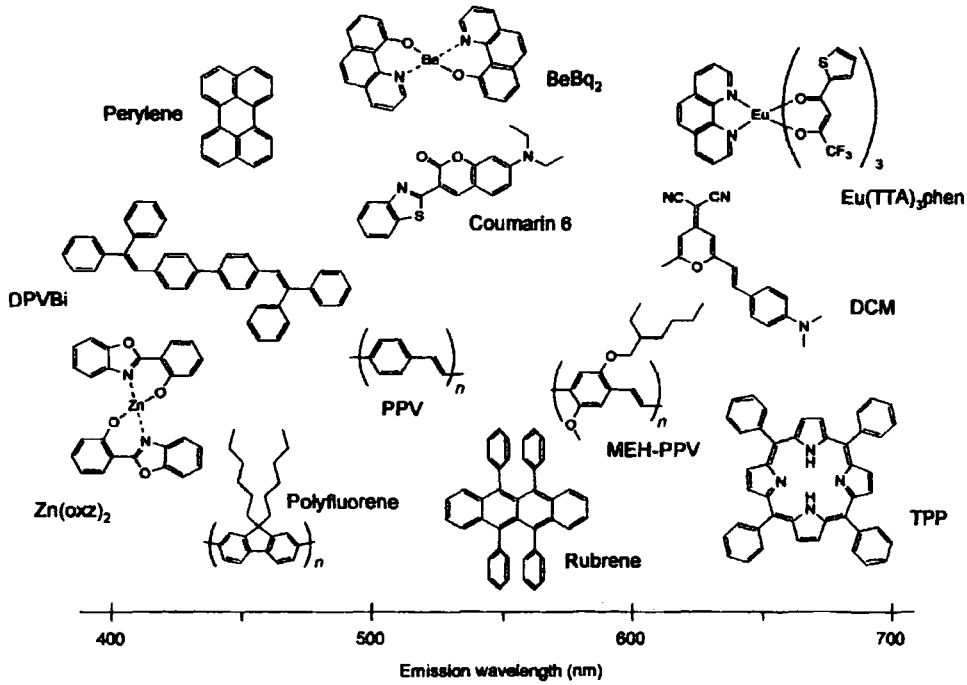

Figure 2.6 A selection of common emissive materials and dopants in organic LEDs [32].

2.5 Electrodes

To ensure the balanced injection, it is necessary to equalise the barriers that arise at the two polymer/electrode interfaces. Moreover, to ensure that injection is readily achieved at a low drive voltage, a small injection barrier is required. The use of a transparent ITO electrode as the hole injection electrode allows the EL emission to readily leave the device. The combination of electrode materials for both electron and hole injection are listed in Table 1.

Scott et al. [36] showed that the ITO anode acted as a source of oxygen, which caused an oxidation of MEH-PPV, resulting in a loss of conjugation length. The surface of ITO is also notoriously uneven, causing the formation of electrical shorts which shorten the device lifetime. Therefore, it is advantageous to use a very thin buffer layer between the ITO and the hole transporting layer to improve hole

injection. Suitable compounds are copper phthalocyanine (CuPc) [37] or a conductive polymer, e.g. polyaniline (PaNi) [38] or poly(3,4-ethylenedioxythiophene) (PEDOT) [39], as shown in Figure 2.4. This increases the adhesion of the subsequent organic layers and improves the device lifetime. Oxygen plasma treatment of the ITO glass can also be used to reduce the turn-on voltage and increase the external quantum efficiency [40].

Hole injection (high work function)	Electron injection (low work function)
Indium-tin oxide	Al
Al:Al_2O_3	Mg:Ag
Au	Ca
Pt	In
p-type Si etc.	*n*-type Si etc.

Table 1. Electrode materials for organic LEDs [18].

A range of cathode electrode materials has been used [41]. For ITO/PPV/Al devices (injection barrier to electrons: 1.6 eV), the external quantum efficiency is about 2×10^{-3} %. Replacing Al with Ca (injection barrier to electrons: 0.3 eV) results in an enhancement in efficiency to 0.1 %. Changing to gold, which has a higher work function (injection barrier to electrons: 2.7 eV), leads to an external quantum efficiency of only 5×10^{-6} %. Although Ca and Mg electrodes are good candidates for the cathode, these are too reactive in air to apply for use in 'real' devices. To some extent, this problem can be alleviated by using coevaporated or layered metals [6,42] such as Mg:Ag or Li:Al where the composite has a low work function but relatively low reactivity.

2.6 Device Stability

The degradation of organic LEDs during operation occurs in three ways: (I) decay of luminance, (II) a voltage increase across the LED in constant current mode and (III) the growth of nonemissive regions (dark areas). To date, the following causes have been proposed for these effects: (I) morphological instability or crystallisation of amorphous organic film [43]; (II) delamination of the organic layer from the adjacent electrode [44,45]; (III) the formation of a high energy barrier at the ITO anode [24] and (IV) interdiffusion between the organic layers [46].

As already noted, the high glass transition temperature, T_g, of the hole transporting layer dominates the heat resistance of the device. The design of appropriate starburst amines [25] and oligomer amines [47] are good approaches to obtain material with high T_g.

Interfacial effects between the organic layer and the electrode are both material- and process-dependent. Organic buffer layers such as CuPc and PaNi can be inserted between ITO and the hole transporting layer to increase the hole injection and device lifetime. Recently, the deposition of a thin LiF layer prior to the Al electrode was also reported to improve the electron injection and device lifetime [48].

Doping is an important aspect of organic LED fabrication in terms of efficiency, colour-tuning and device lifetime. By choosing a proper dopant, the energy barrier at the organic/organic interface is lowered, leading to longer device lifetime. It has been reported that the lifetime of Alq_3-based organic EL devices was greatly improved by doping the emitting layer with organic dyes such as rubrene and perylene [49,50].

In Figure 2.7, selected lifetime data are reviewed as a function of initial luminance, with symbols for several research groups. The square area indicates practical display requirements: a lifetime of more than 10,000 hours with an initial luminance higher than 100 cd m^{-2}. Green, yellow, blue and red emitting devices are now within this practical application area.

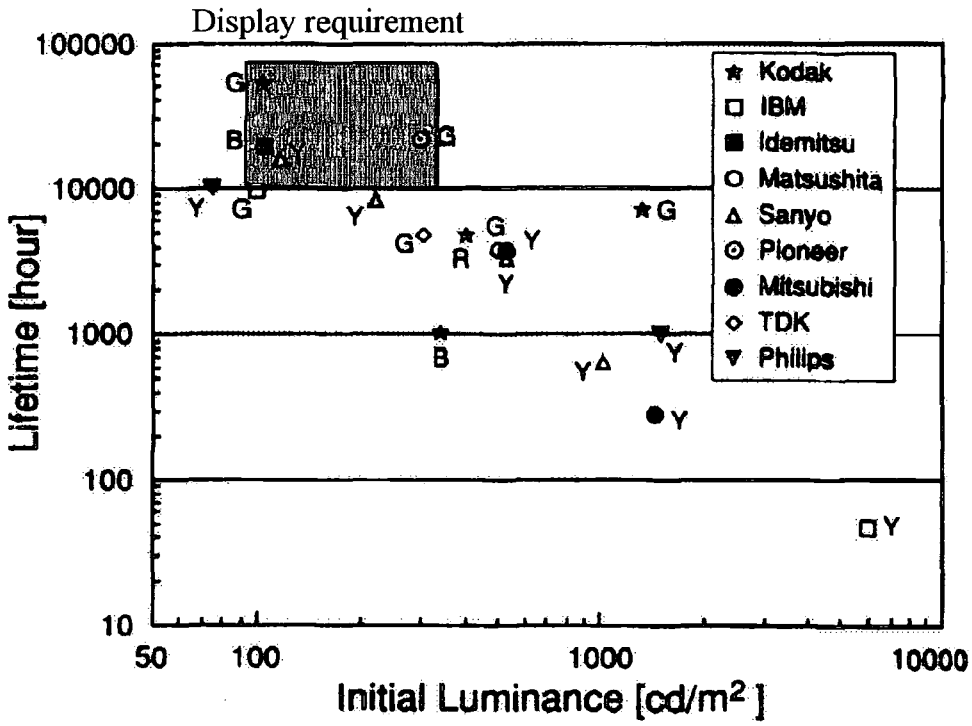

Figure 2.7. Review of the lifetime data plotted as a function of the initial luminance for various LEDs. Each symbol indicates the research group and is denoted by the emission colour: R(red), G(green), B(blue) and Y(yellow) [43].

2.7 Multi-Colour Fabrication

A wide range of materials, which efficiently produce EL throughout the visible spectrum, has now been reported (Figure 2.6). The colour of light emission can readily be controlled by altering the materials which make up the device. However,

this can often lead to a decrease in efficiency and broad lines which are not appropriate for a full colour display.

An alternative method of colour tuning involves doping small amounts of fluorescent dyes into the device structure. The doping technique has been used to fabricate organic LEDs whose colours span the entire visible spectrum with good efficiencies and device lifetime [48,50]. Another benefit of dye doping is that dye-doped devices often give significantly narrower EL spectra than non-doped devices. In order to create saturated colours it is important for the individual red, green and blue EL spectra to be as narrow as possible. If the EL spectra are broad, substantially unsaturated or washed out colours will result.

Various different ways of making full colour displays have been proposed and summarised in Figure 2.8.

(I) Separating RGB emitting sub-pixels on the same substrate using etching [51].

(II) Incorporating organic white emitters with pixelated RGB colour filters [52].

(III) Integrating organic blue emitters with pixelated RG down materials [53].

(IV) Adjusting the emission of a single type of broadband organic emitter by integrating with pixelated microcavities [54].

(V) Stacking the RGB emitters on top of one another [55].

The above methods all have potential drawbacks. Colour filters and down converters have inherent energy inefficiencies. Microcavities have a direction dependent resonance frequency which causes angular colour and brightness variations. Stacked structures require transparent metal contacts and possess the problem of loss of the emitted light by absorption in the semi-transparent electrodes. Structure (I) involves the patterning of films and microprocessing.

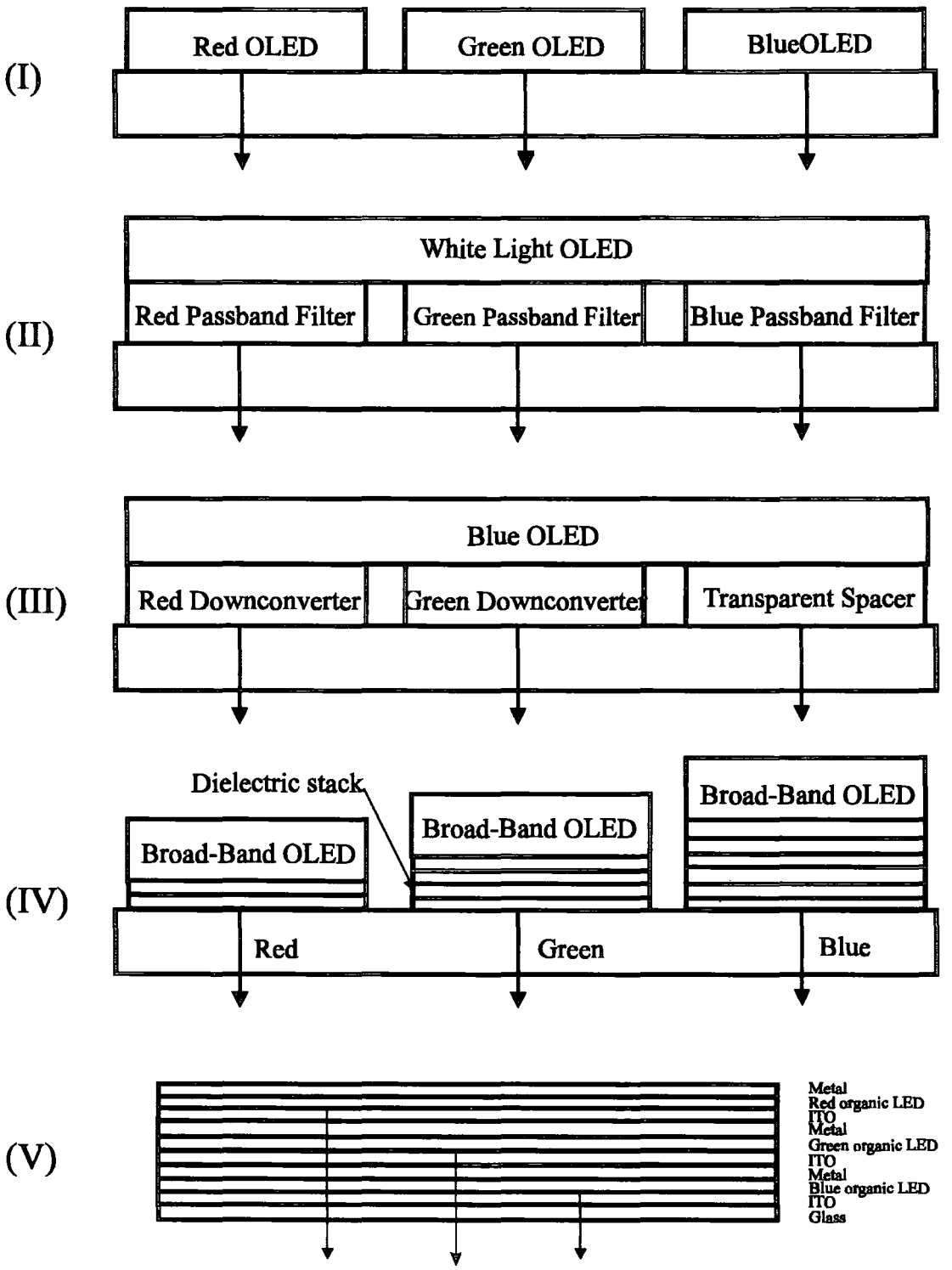

Figure 2.8 Schematic representations of the various methods used for achieving a full-colour display [55].

This inevitably requires the use of solvents, acid and water in conventional lithographic technique, resulting in the degradation or even the failure of devices.

Each of the techniques described above has unique strengths and weaknesses. The optimum device structure for commercial full colour displays will also be heavily influenced by the ease with which it can be mass-produced.

2.8 Future Directions

Organic LEDs have ideal characteristics for many display applications. The attractions of organic LED technology is based on the following features: low operating voltage, simple methods of device fabrication, full colour range, no viewing angle dependence and high brightness at low drive voltages/current densities.

The first commercial organic light emitting display with high resolution was introduced using small molecules by Pioneer, in a car stereo, in 1997 [56]. This monochrome display had a high external quantum efficiency of more than 4 % and device lifetime of more than 10,000 hours for continuous operation. The first active-matrix red-green-blue (RGB) display was demonstrated by TDK in 1995. One advantage of the active-matrix driving scheme is that each pixel can be operated at low current density levels, leading to high luminous efficiencies.

Organic displays on the market so far are based on light emission from small molecules rather than from polymers because polymer displays generally offer lower efficiencies and shorter device lifetime. UNIAX has recently demonstrated a two-inch diagonal passive-matrix high resolution display with PPV. Meanwhile CDT and Seiko Epson have developed a two-inch active matrix polymer display with PPV and polyfluorene materials by inkjet printing [57]. Small molecules can be patterned

through a fine metal shadow mask. In contrast, most polymers are deposited by the spin-coating technique which makes it difficult to create different colour lines in the device. One approach is being tried to use inkjet printing with three cartridges possessing polymer solutions for the red, green and blue colours [16].

Products which are currently being developed are small emissive displays (e.g. for mobile telephones) and backlights for liquid-crystal displays (LCDs). The final target of organic LEDs is the replacement of the LCDs market for flat panel displays. LCDs are the dominant flat panel display technology today and will remain so for many years in spite of the complex processing procedure required to make an LCD display panel (e.g. thin film transistor (TFT) processing, colour filter (CF) processing, liquid crystal (LC) processing, assembly and packaging). Furthermore, only 10 % of the light generated by the backlight can be emitted to the outside world. Looking beyond the LCD era, organic LEDs offer much in terms of potential performance, easy fabrication and low cost.

According to Stanford Resources, 48.7 million flat panel displays were sold in 1995 and this figure will increase by an average of 12 % annually accounting for $20.8 billion in sales in 2002 [58]. Although significant work remains to realise a full colour emissive display and high device stability, the advantages of organic LEDs in weight, power consumption and cost provide a compelling economic incentive.

2.9 Summary

Organic LEDs have very attractive features that are likely to give them a prominent place in the flat panel display market in the future. The development of both manufacturing process technology and new materials increases the potential of

organic LEDs to be applicable to various display areas in the future. To date, the luminance is comparable with the typical luminance levels from a cathode-ray tube (~300 cd m^{-2}) or a fluorescent lamp (~8000 cd m^{-2}) with high external quantum efficiency. However, organic LEDs still have some problems in terms of device stability and screen resolution which must be improved for full commercialisation.

References

1. C.W. Tang and S.A. VanSlyke, *Appl. Phys. Lett.*, **51**, 1987, 913.
2. C. Adachi, S. Tokito, T. Tsutsui and S. Saito, *Jpn. J. Appl. Phys*, **28**, 1988, L296.
3. M. Pope, H.P. Kallmann and P. Magnante, *J. Chem. Phys.*, **38**, 1963, 2042.
4. P.S. Vincett, W.A. Barlow, R.H. Hann and G.G. Roberts, *Thin Sol. Fi.*, **94**, 1982, 171.
5. G.G. Roberts, T.M. McGinnity, W.A. Barlow and P.S. Vincett, *Thin Sol. Fi.*, **68**, 1980, 223.
6. C.W. Tang, S.A. VanSlyke and C.H. Chen, *J. Appl. Phys.*, **65**, 1989, 3610.
7. R.H. Partridge, *Polymer*, **24**, 1983, 733.
8. J.H. Burroughes, D.D.C. Bradley, A.R. Brown, R.H. Marks, K. MacKay, R.H. Friend, P.L. Burn and A.H. Holmes, *Nat.*, **347**, 1990, 539.
9. I.S. Millard, *Synth. Met.*, **111-112**, 2000, 119.
10. J. Kido, *Photonic and Optoelectronic Polymers*, **612**, 1997, 381.
11. J.R. Sheats, H. Antoniadis, M. Hueschen, W. Leonard, J. Miller, R. Noom, D. Roitman and A. Stocking, *SCI*, **273**, 1996, 884.
12. L.J. Rothberg and A.J. Lovinger, *J. Mater. Res.*, **11**, 1996, 3174.
13. P. Yam, *Sci. Am.*, **273 (1)**, 1995, 75.
14. G. Gu, Z. Shen, P.E. Burrows and S.R. Forrest, *Adv. Mater.*, **9**, 1997, 725.

15. C.W. Tang and J.E. Littman, *U.S. Patent*, no. 5,294,869, 1994.

16. T.R. Hebner, C.C. Wu, D. Marcy, M.H. Lu and J.C. Sturm, *Appl. Phys. Lett.*, **72**, 1998, 519.

17. V. Choong, Y. Park, Y. Goo, T. Wehrmeister, K. Mullen, B.R. Hsieh and C.W. Tang, *Appl. Phys. Lett.*, **69**, 1998, 1492.

18. D.D.C. Bradley, *Synth. Met.*, **54**, 1993, 401.

19. H. Vestweber and W. Riess, *Synth. Met.*, **91**, 1997, 181.

20. Y. Shirota, Y. Kuwabara, H. Inada, T. Wakimoto, H. Nakada, Y. Yonemoto, S. Kawami and K. Imai, *Appl. Phys. Lett.*, **65**, 1994, 807.

21. C. Hosokawa, H. Tokailin, H. Higashi and T. Kusumoto, *Appl. Phys. Lett.*, **60**, 1992, 1220.

22. E.M. Han, L.M. Do, N. Yamamoto and M. Fujihira, *Thin Sol. Fi.*, **273**, 1996, 202.

23. S. Goncalves-Conto, M. Carrard, L. Si-Ahmed and L. Zuppiroli, *Adv. Mater.*, **11**, 1999, 112.

24. S. Tokito, H. Tanaka, K. Noda, A. Okada and Y. Taga, *Appl. Phys. Lett.*, **70**, 1997, 1929.

25. C. Giebeler, H. Antoniadis, D.D.C. Bradley and Y. Shirota, *Appl. Phys. Lett.*, **72**, 1998, 2448.

26. T. Sano, Y. Hamada and K. Shibata, *IEEE. J. Sel. Top. Quantum Electron.*, **4**, 1998, 34.

27. C. Hosokawa, N. Kawasaki, S. Sakamoto and T. Kusumoto, *Appl. Phys. Lett.*, **61**, 1992, 2503.

28. Y. Hamada, C. Adachi, T. Tsutsui and S. Saito, *Jpn. J. Appl. Phys.*, **31**, 1992, 1812.

29. J. Kido, C. Ohtaki, K. Hongawa, K. Okuyama and K. Nagai, *Jpn. J. Appl. Phys.*, **32**, 1993, L917.

30. M.S. Weaver, D.G. Lidzey, T.A. Fisher, M.A. Pate, D. O'Brien, A. Bleyer, A. Tajbakhsh, D.D.C. Bradley, M.S. Skolnick and G. Hill, *Thin Sol. Fi.*, **273**, 1996, 39.

31. C.W. Tang, C.H. Chen and R. Goswami, *U.S. Patent*, no. 4,769,292, 1988.

32. T.H. Richardson, *Functional Organic and Polymeric Materials*, **Chichester**, Wiley, 1971, 365.

33. J. Kido and J. Endo, *Chem. Lett.*, **7**, 1997, 593.

34. O. Inganas, M. Berggren, M.R. Andersson, G. Gustafsson, T. Hjertberg, O. Wennerstrom, P. Dyreklev and M. Granstrom, *Synth. Met.*, **71**, 1995, 2121.

35. P.L. Burn, A.B. Holmes, A. Kraft, D.D.C. Bradley, A.R. Brown, R.H. Friend and R.W. Gymer, *Nat.*, **356**, 1992, 47.

36. J.C. Scott, J.H. Kaufman, P.J. Brock, R. DiPietro, J. Salem and J.A. Goitia, *J. Appl. Phys.*, **79**, 1996, 2745.

37. S.A. Vanslyke, P.S. Bryan and C.W. Tang, *Int. Workshop Inorganic and Organic Electroluminescence Proc.*, **Berlin**, 1996, 195.

38. S. Karg, J.C. Scott, J.R. Salem and M. Angelopoulos, *Synth. Met.*, **80**, 1996, 111.

39. Y. Cao, G. Yu, C. Zhang, R. Menon and A.J. Heeger, *Synth. Met.*, **87**, 1997, 171.

40. J.S. Kim, M. Granstom, R.H. Friend, N. Johansson, W.R. Salaneck, R. Daik, W.J. Feast and F. Cacialli, *J. Appl. Phys.*, **84**, 1998, 6859.

41. P.L. Burn, A.B. Holmes, A. Kraft, D.D.C. Bradley, A.R. Brown and R.H. Friend, *MRS Proc.*, **Boston**, 1991, USA.

42. J. Kido, K. Nagai and Y. Okamoto, *IEEE. Trans. Electron Devices*, **40**, 1993, 1342.

43. Y. Sato, S. Ichinosawa and H. Kanai, *IEEE. J. Sel. Top. Quantum Electron.*, **4**, 1998, 40.

44. J. McElvain, H. Antoniadis, M.R. Hueschen, J.N. Miller, D.M. Roitman, J.R. Sheats and R.L. Moon, *J. Appl. Phys.*, **80**, 1996, 6002.

45. W. Bijnens, I.D. Wolf, J. Manca, J. D'Haen, T.D. Wu, M. D'Olieslaeger, E. Beyne, R. Kiebooms, D. Vanderzande, J. Gelan, W.D. Ceuninck, L.D. Schepper and L.M. Stals, *Synth. Met.*, **96**, 1998, 87.

46. M. Fujihira, L.M. Do, A. Koike and E.M. Han, *Appl. Phys. Lett.*, **68**, 1996, 1787.

47. W. Riess, H. Reil, P.F. Seidler and H. Vestweber, *Synth. Met.*, **99**, 1999, 213.

48. Y. Sato, S. Ichinosawa and H. Kanai, *Int. Workshop Inorganic and Organic Electroluminescence Proc.*, **Berlin**, 1996, 255.

49. Y. Sato, S. Ichinosawa and H. Kanai, *Int. Workshop Inorganic and Organic Electroluminescence Proc.*, **Berlin**, 1996, 385.

50. C.W. Tang, *Dig. SID Int. Symp.*, **San Diego**, 1996, 181.

51. C.C. Wu, J.C. Sturm and R.A. Register, *Appl. Phys. Lett.*, **69**, 1996, 3117.

52. J. Kido, M. Kimura and K. Nagai, *SCI*, **267**, 1995, 1332.

53. A. Niko, S. Tasch, F. Meghdadi, C. Brandstatter and G. Leising, *J. Appl. Phys.*, **82**, 1997, 4177.

54. A. Dodabalapur, L.J. Rothberg and T.M. Miller, *Electron. Lett.*, **30**, 1994, 1000.

55. P.E. Burrows, G. Gu, V. Bulovic, Z. Shen, S.R. Forrest and M.E. Thompson, *IEEE. Trans. Electron Devices*, **44**, 1997, 1188.

56. J. Kido, *Physics World*, 12 (3), 1999, 27.

57. H. Kobayashi, S. Kanbe, S. Seki, M. Kimura, S. Miyashita, J.H. Burroughes and R.H. Friend, *Synth. Met.*, **111-112**, 2000, 125.

58. D.E. Mentley, *http://www.stanfordresources.com.*

Chapter 3.

Optical and Electronic Properties of LEDs based on Conjugated Polymers

3.1 Introduction

Light emitting devices incorporating conjugated polymer have become the subject of intense research since the first report of electroluminescence in poly(*p*-phenylenevinylene) (PPV) [1]. This chapter begins with an introduction to conjugated polymers and their properties including a description of energy levels, optical transitions and photoexcitations. The operation of LEDs is determined by three processes: charge injection; charge transport and charge recombination. The main theoretical models describing I-V characteristics of LEDs are outlined. A brief explanation of electron-hole recombination, including radiative and nonradiative decay, is then provided.

3.2 Conjugated Polymers

Since 1977 a new class of conducting materials has been studied in some detail: electrically conducting polymers. The prototype of these new substances is polyacetylene. It was discovered that, upon treatment with bromine, the polymer (which is a good insulator in its pristine form) converts into a quasi-metal [2]. Today many polymers with similar properties are known. Figure 3.1 shows the chemical structure of the most important compounds.

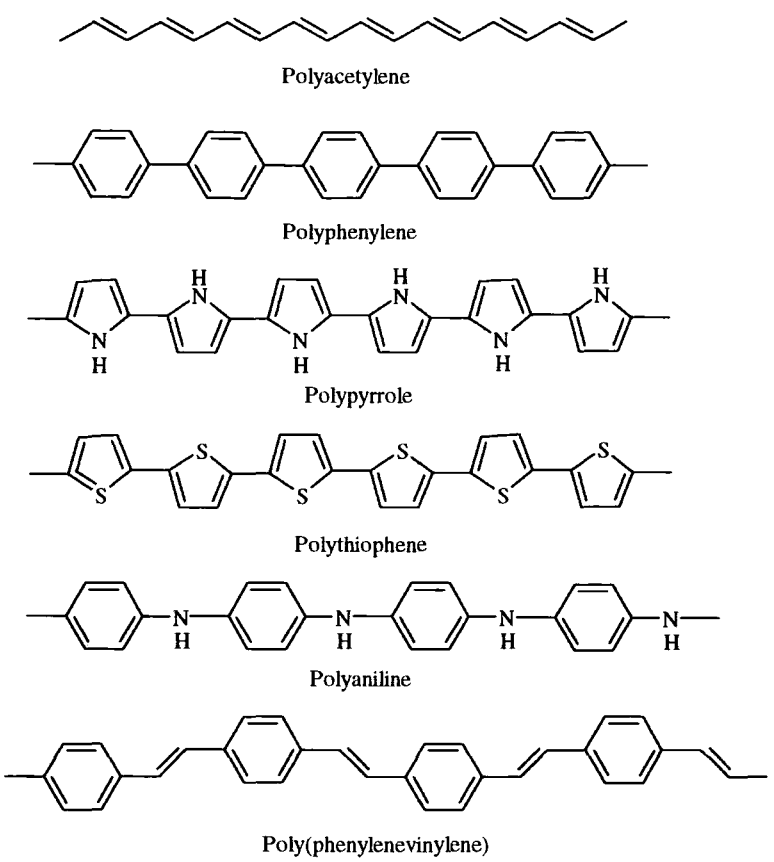

Figure 3.1 Chemical structure of several conjugated polymers.

The main characteristic of all of these polymers is the presence of a so-called conjugated quasi one-dimensional chain, where the chemical bonding between the atoms in the mainly carbon "backbone" of the polymer chain alternates between single and double bonds. The electrons in a σ-bond are strongly localised and form a strong chemical bond. In contrast, the electrons in the π-bonds are not localised and form much weaker bonds. As a result, the electrons in a cloud that extends along the entire length of the conjugated chain are free to move along the molecule as shown in Figure 3.2.

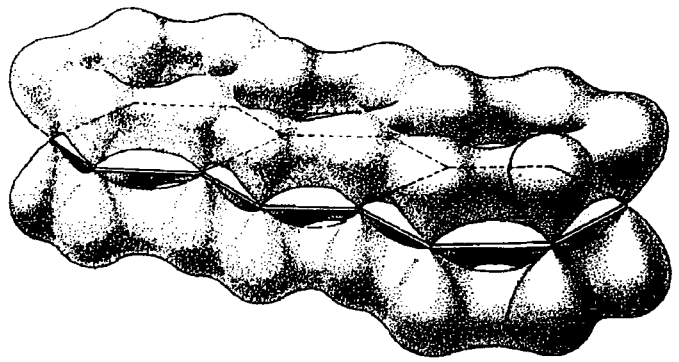

Figure 3.2 The bonding in ethylene consists of one sp^2-sp^2 σ bond and one p_z-p_z π bond.

On exposure of these conjugated polymers to suitable electron acceptors (oxidising agents) or electron donors (reducing agents), a transformation from an insulator to a conductor takes place. It is this dramatic transition from an electrically insulating state to an electrically conductive state that has stimulated the worldwide interest in these materials.

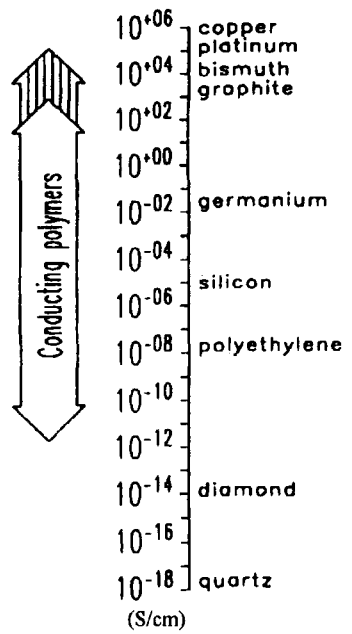

Figure 3.3 Conductivities of synthetic metals compared to those of conventional materials.

In Figure 3.3 the conductivity of doped polymers is compared to that of conventional materials. The conductivity can be changed by more than 14 orders of magnitude by doping. One of the highest values of conductivity is 10^5 S cm^{-1} for iodine-doped polyacetylene [3].

Charge transport in polymer semiconductors does not occur in the same way as in inorganic semiconductors. When electrons or holes are injected at the electrode, the polymer chain is physically distorted (Peierls distortion) unlike the ions in an inorganic semiconductor which have fixed positions. So, the charge carrier couples with the distortion to form a mobile polaron – an entity that incorporates both the charge carrier and the accompanying local chain distortion.

3.3 Peierls Transition

The electronic properties of doped conjugated polymers are strongly influenced by the coupled motions of π-electrons with lattice vibrations (phonon modes). Lattice instabilities of this type were initially proposed by Peierls [4].

Structural relaxations of the lattice surrounding the charged defect sites are possible due to the strong electron-phonon coupling that exists in quasi-one dimensional systems. Such distortions would not be expected in rigid 3-D structures. The specific types of charged defects formed on the polymer backbone during doping depend on the structure of the polymer chain. Essentially two main types of conjugated polymer backbone can be identified: those with degenerate ground state structures and those with nondegenerate ground state structures. An infinite chain of trans-polyacetylene having two equivalent structures with the same energy (Figure 3.4) is known as a polymer with a degenerate ground state structure. In contrast

poly(*p*-phenylenevinylene) (PPV) has two alternative bond structures, bensenoid and quinoid, which do not have equivalent energies. This kind of polymer is known as a polymer with a nondegenerate ground state structure.

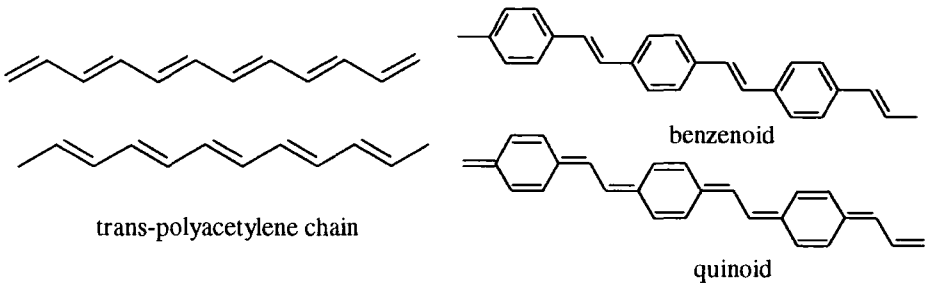

Figure 3.4 Bond alternations of trans-polyacetylene chain and PPV.

3.3.1 Polarons

In non-degenerate ground state polymers such as polypyrrole, the doping process removes electrons from the π-system of the backbone creating a free radical (unpaired electron with spin 1/2) and spinless positive charge (cation), as shown in Figure 3.5. The radical and cation are coupled to each other via a local bond rearrangement forming a sequence of quinoid-like rings. The quinoid-like lattice distortion is of higher energy than the remaining part of the benzenoid-like bonding configuration. Thus separation of these defects along the chain and the concomitant creation of the additional high energy quinoid-like structure costs a considerable amount of energy. This limits the number of quinoid-like rings that can link these two bound species together. In the case of polypyrrole, the lattice distortion is believed to extend over about four pyrrole rings. This combination of a charged site coupled to a free radical via a local lattice distortion is called a polaron. Polaron formation creates

new localised electronic states in the forbidden energy gap, with the lower energy states being occupied by single unpaired electrons (a polaron has spin).

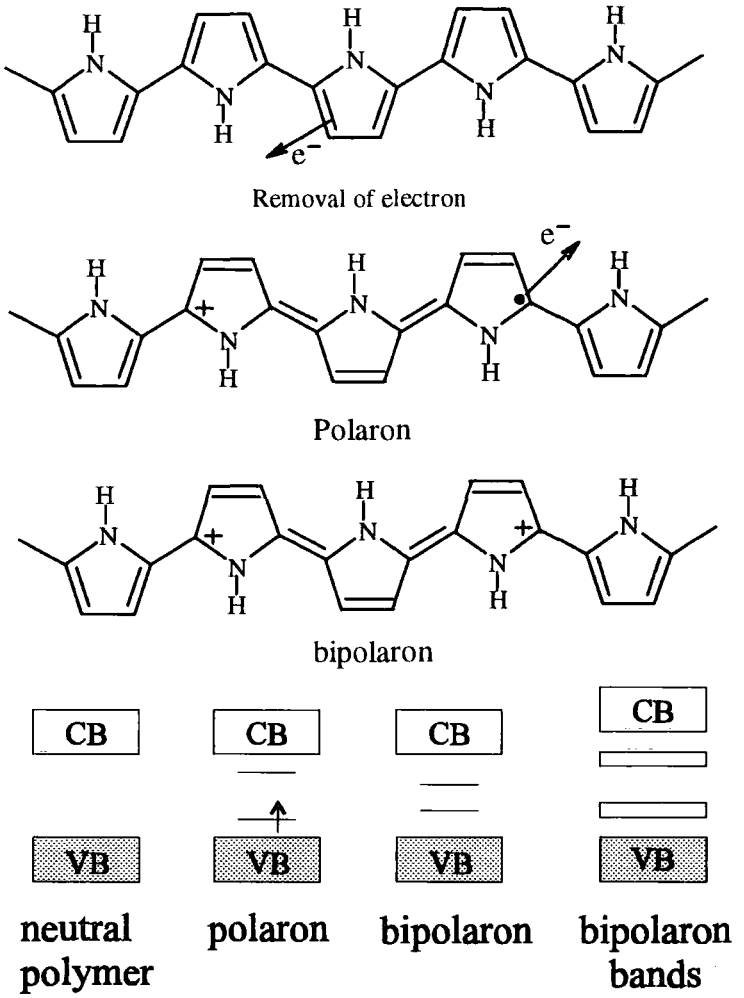

Figure 3.5 Oxidation of polypyrrole and the creation of polaron and bipolaron states.

On further oxidation, an electron can be removed from either the polaron or the remaining neutral portion of the chain. In the former case, the free radical of the polaron is removed and a dication is created. This is comprised of two positive charges coupled through the lattice distortion. This new spinless defect is called a bipolaron. On the other hand, removal of an additional electron from a neutral portion of the chain would create another polaron along the chain. The former process is thermodynamically more favourable than the latter. Bound states create defect levels

symmetrically located above the valence band and below the conduction band. The new empty bipolaron states are also located symmetrically within the band gap, about 0.75 eV away from the band edges in the case of polypyrrole. Continued doping of the polymer creates additional localised bipolaron states which can overlap to form continuous bipolaron bands (in Figure 3.5).

3.3.2 Solitons

In the case of conjugated polymers with degenerate ground state structures, such as polyacetylene, the initial oxidation creates polarons symmetrically located within the gap as shown in Figure 3.6. Further oxidation of the polymer creates polymeric dications. Since the ground state structure of polyacetylene is two-fold degenerate, the charged cations are not bound to each other by a higher energy bonding configuration and can freely separate along the chain.

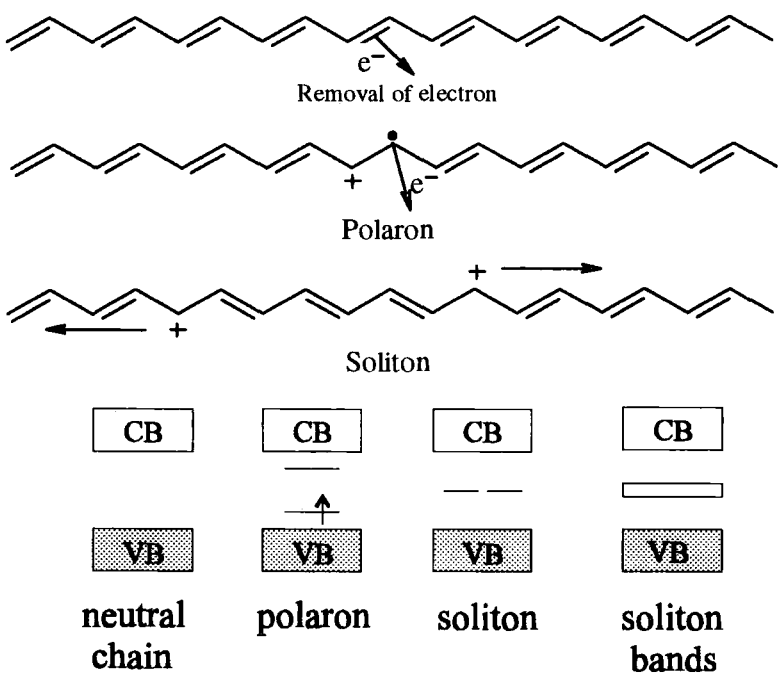

Figure 3.6 Oxidation of polyacetylene and the creation of polaron and soliton state.

On either side of this defect, there is a reversed orientation of the conjugated system with identical energy: such defects are called solitons. Solitons are believed to delocalise over about 12 C-H units. Soliton formation results in the creation of new localised electronic states that appear at the middle of the energy gap as indicated in Figure 3.6. At high enough doping levels, the charged solitons interact with each other to form a soliton band.

Experimental evidence supports the existence of solitons, polarons and bipolarons, in the form of optical spectra. Figure 3.7 shows optical spectra of a thin film of poly(3-octyl thiophene) in its neutral and oxidised state [5]. Before doping, a strong interband transition which is centred around 500 nm is evident. After doping to a state of high conductivity, the interband transition decreases and two new absorption bands resulting from transitions of electrons from the valence band to the two newly created bipolaron states are clearly observed.

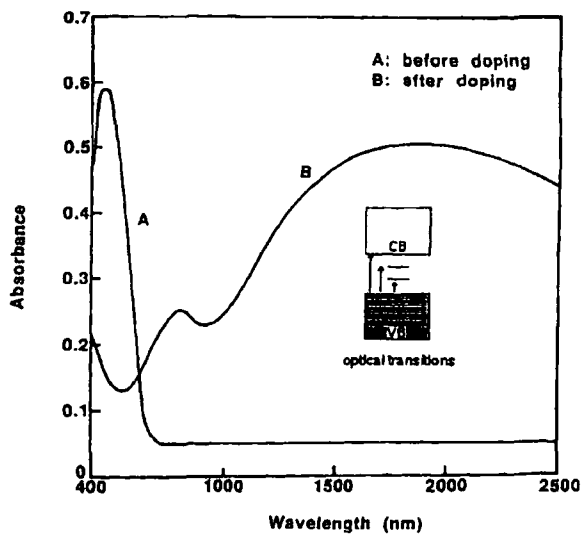

Figure 3.7 Optical spectra of a thin film of poly(3-octyl thiophene) (a) before doping, (b) after doping with $NOPF_6$. Inset shows the optical transitions of a bipolaron [5].

3.4 Photoluminescence

Luminescence is the spontaneous emission of optical radiation (infrared, visible, or ultraviolet light) by matter: organic, inorganic molecules; polymers; organic or inorganic crystals; and amorphous substances. The causes of the excitation are various. If the exciting cause is a photon, the process is called photoluminescence; if it is an electron it is called electroluminescence. Chemiluminescence is luminescence resulting from a chemical reaction; bioluminescence is the luminescence produced by a living organism.

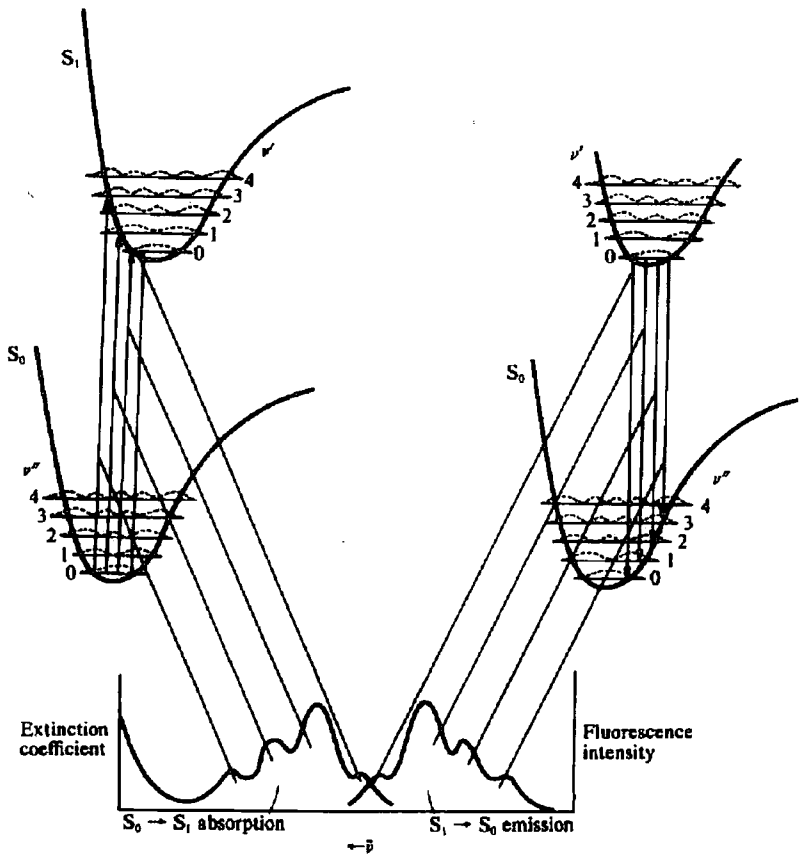

Figure 3.8 Schematic diagram of the mirror image relationship of absorption and luminescence [6].

Photoluminescence (PL) is the radiative decay of an excitation caused by absorption of a photon. The process of absorption of a photon involves the interaction of the electric and magnetic fields of the light wave with static and dynamic electrical components of the molecules. The electronic transitions are strongly coupled to vibrational modes, which leads to vibronic structure in the absorption and emission profiles. A photoluminescence spectrum, in the simplest case, is a very similar (but not identical) mirror image of the absorption spectrum, as shown in Figure 3.8.

Absorption occurs from the populated $v''= 0$ vibrational level of the electronic ground state, S_0, to the various vibrational levels of the excited state. After excitation of the molecule to an upper vibronic state, the nuclear coordinates are not in their equilibrium configuration for the new electronic state, and hence radiationless relaxation between the vibrational states occurs to $v'= 0$ level of the excited state S_1. Since electronic transitions take place on a much faster time scale (~ 10^{-15} s) than the nuclear motions (~ 10^{-13} s), most electronic transitions are completed before the nucleus can alter its configuration. Thus the electronic transitions are represented by vertical, or so-called Franck-Condon transitions, as shown in Figure 3.8.

Radiative transitions can occur from the lowest vibrational level of the excited state to the various vibrational levels of the ground state. The vibrational relaxation that occurs, however, produces a red shift of the emission spectrum compared to the absorption spectrum. Even the 0-0 transitions do not completely overlap and there is a shift between the 0-0 absorption and luminescence peaks. This energy difference is called the Stokes' shift. Thus absorption spectroscopy can provide information about the vibrational states of the excited state and luminescence spectroscopy can provide information about the vibrational states of the ground state.

Absorption and photoluminescence in polymeric systems is more complicated than the situation in simple molecules. In a polymer material, the excited electron forms a bound state with the hole in the valence band. This entity is called an exciton. Excitons in conjugated polymers have a typical lifetime in the range of 70-250 ps at room temperature [7, 8] and are believed to be mobile along the disordered polymer chain. This disordered chain will produce a distribution of the extent of exciton delocalisation, resulting in a number of chain segments with various conjugation lengths. Shorter conjugation lengths produce a larger band gap while longer conjugation lengths produce a smaller band gap. The lowering of the band gap with increasing conjugation length arises due to the linear combination (overlap) of neighbouring π orbitals, producing a decreasing π-π^* energy difference.

During absorption, light with sufficient energy will excite all conjugation lengths, resulting in a broadening of the absorption spectrum. Absorption produces mobile excitons on the polymer chains, which can then migrate to a chain segment with a longer conjugation length and decay radiatively, producing more vibronic and narrow emission spectra at a lower energy, red-shifting the photoluminescence and contributing to a seemingly larger Stokes' shift. For example, Bradley [9] reported the Stokes' shift in PPV (in Figure 3.9) and proposed that the electronic excited states responsible for emission were associated with excitons. The absorption spectrum has a less pronounced and broad structure and the mirror image, which is observed in organic material, cannot be seen.

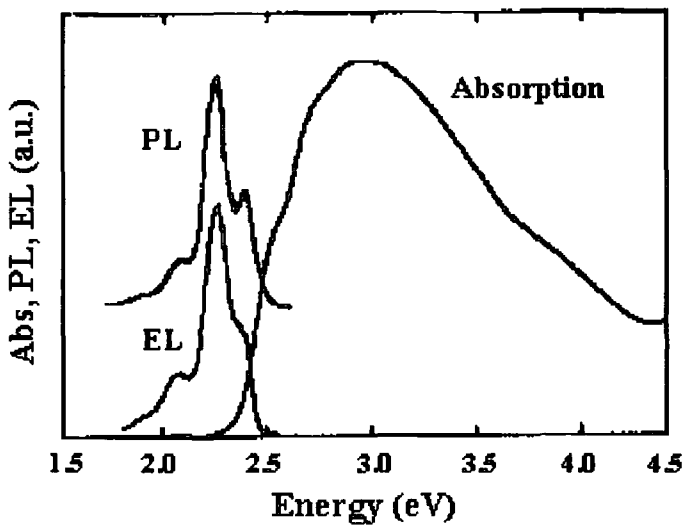

Figure 3.9 PPV absorption and emission spectra [9].

3.5 Modelling of I-V Characteristics of Organic LEDs

The theoretical modelling of organic LEDs operation is a growing but complicated field of study. Both injection dominated and bulk dominated mechanisms have been proposed as the rate limiting process in the current-voltage behaviour of polymer and small molecule organic LEDs. Proposed injection dominated mechanisms are tunnelling [10, 11] and thermionic emission [12]. Proposed bulk dominated mechanisms are Ohmic conduction [13], space charge limited (SCL) current conduction [10, 13, 14] and space charge limited conduction with an exponential trap distribution [15].

The charge-carrier injection and transport processes within polymer LEDs are much more complex than in inorganic crystalline devices, due to the lack of a three-dimensional crystal lattice, local structural disorder, different inter- and intramolecular interactions, the existence of amorphous and crystalline regions and chemical impurities. This situation is complicated by the interface between the polymers and the

electrodes. Polaron formation as well as structural relaxation also further complicate the situation.

The modifications to models outlined above have produced improved agreement with the experimental data for organic systems. For example, thermionic emission at lower voltages and tunnelling emission at higher voltages has been used to explain the I-V characteristics of ITO/poly(*p*-phenylene)-ladder-copolymer/metal device [16]. Karg et al. [17] showed ITO/PPV/Al or Ca devices in which the I-V characteristics displayed Schottky behaviour at low current density but were characteristic of SCL currents at high current density. Also, the tunnelling model incorporating SCL current conduction provided a good fit for Al/*p*-PPV/Al devices [18].

3.5.1 Metal-Semiconductor Contact

When a metal and another solid are brought into intimate contact, their Fermi levels must be the same at the interface to achieve thermodynamic equilibrium. Since the work function of the metal and the Fermi energy of the solid material are not necessarily the same, this requires a transfer of charge between the metal and the solid. The theory of contacts between doped semiconductors and metals was developed by Mott [19] and Schottky [20]. Figure 3.10 shows the band diagram of a metal/*p*-type semiconductor/metal structure with an Ohmic and a rectifying contact. The bands bend at the interface depending on the relative positions of the Fermi levels with respect to the vacuum potential. This band bending results in the accumulation or depletion of holes at the interface, and a potential barrier (Schottky barrier) is formed at the depleted junction.

The contact type can usually be predicted by considering the work function differences between the metal and the polymer. Conducting polymers are typically *p*-type semiconductors forming rectifying contacts with metals of lower work functions. The term W in Figure 3.10 represents the distance over which the bands are bent. This is referred to as the depletion width. The barrier to hole injection formed at this interface is known as a Schottky barrier.

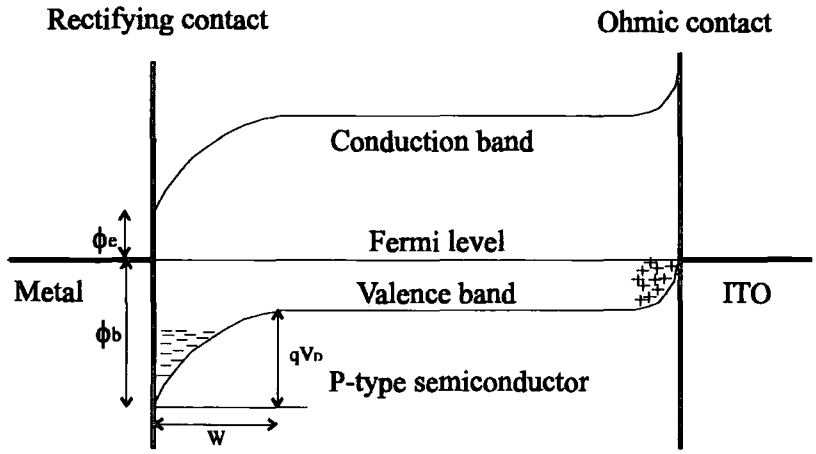

Figure 3.10 Schottky barrier formation in *p*-type semiconductor.

When the current transport is dominated by the depletion layer, asymmetric current-voltage (I-V) curves are observed. The I-V characteristics of a Schottky diode is described by the Shockley equation [21]

$$J = J_s[\exp(\frac{qV}{nkT}) - 1] \qquad (3.1)$$

where J_S is the reverse saturation current, k Boltzmann's constant and n the ideality factor, which describes deviations from the ideal thermionic emission model. The saturation current density J_S is given by

$$J_s = A^* T^2 \exp(-\frac{q\phi_b}{kT}) \qquad (3.2)$$

where A^* is the Richardson constant (vacuum value: 120 A cm^{-2} K^{-2}) and ϕ_b is Schottky barrier height. Equation (3.1) shows that the I-V characteristics are independent of the thickness of the polymer layer. Karg et al. [17] showed that the I-V characteristics of two PPV LEDs (200 and 800 nm) behaved almost identically.

The theoretical Schottky barrier height to holes is calculated with the following equation

$$\phi_h = E_g - \phi_e = E_g - (\phi_m - \chi) \qquad (3.3)$$

hence, the barrier height to electron injection is

$$\phi_e = E_g - \phi_h \qquad (3.4)$$

where E_g is the energy band gap of semi-conducting material, ϕ_e the injection barrier to electrons, ϕ_m the work function of metal and χ the electron affinity of material.

An electric field applied across a Schottky contact effectively lowers the barrier potential energy through an image force effect and modifies thermionic emission over the depletion region. The voltage and temperature dependence of the current is [22]

$$J = A^* T^2 \exp\left[-\frac{q}{kT}(\phi_b - \sqrt{qV / 4\pi L\varepsilon\varepsilon_0})\right] \qquad (3.5)$$

where ε is the relative permittivity, ε_o the permittivity of free space and L sample thickness. A relationship of J proportional to $V^{1/2}$ is observed for thermionic emission.

Scherbel et al. [23] showed the existence of a Schottky barrier in ITO/PPV/Al LEDs by a.c. impedance spectroscopy.

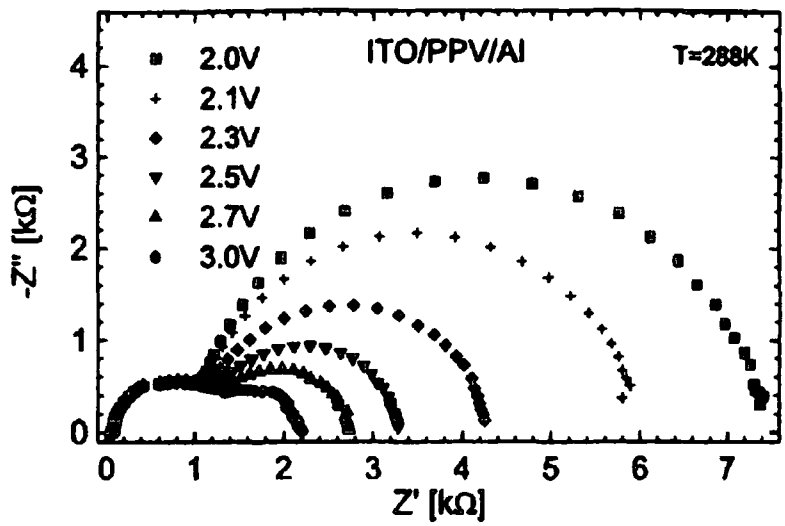

Figure 3.11 Cole-Cole plot of the impedance of an ITO/PPV/Al sample at room temperature for various forward bias voltages.

The real and imaginary parts of the impedance Re(Z) and Im(Z) were recorded at frequencies from 100 Hz to 10 MHz at a range of different applied biases, Figure 3.11 (Cole-Cole plot). Two semicircles can be interpreted in terms of two parallel RC circuits in series. The right-hand semicircle strongly depends on bias voltage and diminishes with increasing forward bias. The change in impedance with bias voltage is dominated by the change in the depletion width. However, the response of the bulk region (left-hand semicircle) is nearly unaffected by bias voltage. The junction capacitance C_j is given by the following equation [21]

$$C_J = A\sqrt{\frac{q\varepsilon_0\varepsilon N_A}{2(V_D - V)}} \qquad (3.6)$$

where N_A is the ionised acceptor concentration, V_D the diffusion voltage. Equation 3.6 predicts a linear dependence of $1/C^2$ on the reverse bias ($V < V_D$). The width of the depletion region is given by

$$w = \sqrt{\frac{2\varepsilon\varepsilon_0(V_D - V)}{qN_A}}. \tag{3.7}$$

3.5.2 Fowler-Nordheim Tunnelling

At sufficiently low temperatures, or for large barriers at high fields, emission due to quantum mechanical tunnelling through the barrier, known as field emission, can become important [24]. The rate of tunnelling through a triangular barrier is given at low temperatures by [25]

$$J \approx F^2 \exp(-k/F) \tag{3.8}$$

where

$$k = \frac{4\sqrt{2qm^*}}{3h}\phi_b^{3/2} \tag{3.9}$$

and m^* is the relative effective mass and h is Planck's constant. Tunnelling currents are frequently analysed using a Fowler-Nordheim plot, where $\ln(J/F^2)$ is plotted against 1/F to give a straight line. The gradient of this can be used to extract the barrier height. Parker [11] showed that the I-V characteristics of ITO/MEH-PPV/Al LED depended, not on the voltage, but instead on the electric field strength. This clearly points to a tunnelling model for carrier injection in which one, or both, of the carriers is field emitted through a barrier at the electrode/polymer interface. Here,

holes and electrons are able to tunnel into the polymer when the applied electric field tilts the rigid bands of polymer sufficiently, as shown in Figure 3.12.

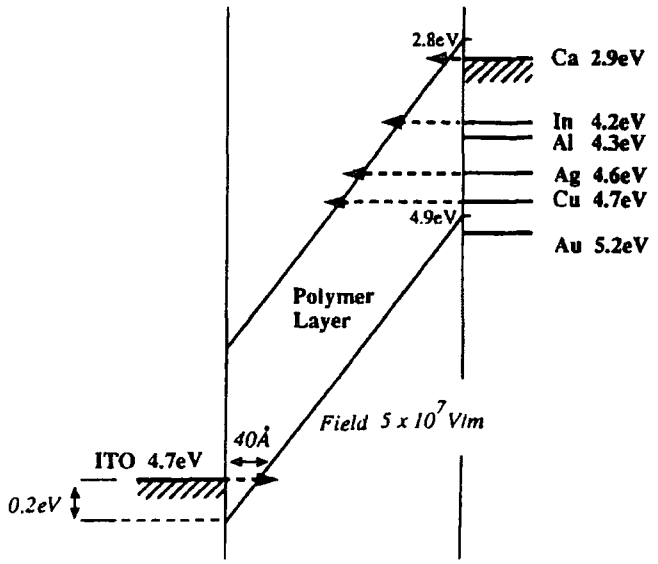

Figure 3.12 F-N model for the MEH-PPV device, indicating position of the Fermi level for various electrode materials [11].

Equation (3.8) cannot account for the temperature dependence and thickness dependence observed in some I-V characteristics. Theoretically, all the measured data with different thickness and at different temperatures should lie on top of each other and the theoretically derived straight line. At high electric fields, the Fowler-Nordheim tunnelling model can provide a fit to the experimental results. Deviations from linearity at lower field strength are likely to be due to a thermionic emission contribution to the current [11].

3.5.3 Space Charge Limited Current

If the applied field is large enough and the metal makes an Ohmic contact to the semiconducting material, single-carriers are injected into the bulk of the

semiconductor. The carrier concentration near the contact increases due to the flow of current. A consequence of the carrier injection is the formation of a space charge cloud of charge carriers in the vicinity of the contacts. Mutual repulsion between the individual carriers limits the charge injection and the resulting current is said to be space charge limited (SCL).

At low voltages, where the equilibrium charge density, n_o, is larger than the injected charge density, the Ohmic current

$$J_{\Omega} = qn_0\mu\frac{V}{d} \tag{3.10}$$

is predominant over the SCL current.

For a trap-free material, neglecting diffusion currents, and when the equilibrium charge density is negligible in comparison to the injected charge density, the space charge limited current is given by Child's law [26]

$$J_{SCL} = \frac{9}{8}\varepsilon_0\varepsilon\mu\frac{V^2}{d^3} \tag{3.11}$$

Space charge limited current theory with a trap distribution proposes that the space charge, which limits conduction, is stored in the traps. The number of free charge carriers under given conditions then depends on the position of the quasi-Fermi level [6]. At higher voltages, the filling of traps below the quasi-Fermi level results in the current being governed by both the density and energy distribution of the traps. This current is said to be trap charge limited (TCL). The introduction of this trap distribution can result in a higher power dependence of current on voltage expressed by

$$J \propto d\left(\frac{V}{d^2}\right)^{m+1} \tag{3.12}$$

where, m is defined by

$$m = E_t / kT \tag{3.13}$$

and E_t is the characteristic energy of the trap distribution. This parameter is directly related to the depth of the trap distribution from the energy level within the band gap. For example, a smaller value indicates a distribution of traps (for holes or electrons) closer to the LUMO or HOMO energy level when m > 1. In the case of a trap free insulator, m is equal to 1.

If the injected charge density is high enough so that the quasi-Fermi energy moves above the trapping level, then the traps become completely filled. In this case, known as the trap-filled limit (TFL), the density of charge in traps becomes negligible compared to the injected charge, and the current reverts to the trap-free value. If the traps are sufficiently deep, as the voltage is increased the current can change directly from the Ohmic regime to the TFL regime, as shown in Figure 3.13.

In three-dimensionally bonded inorganic semiconductors, room temperature mobilities are high, typically 10^2 to 10^4 cm^2 V^{-1} s^{-1}. However, for conjugated polymers, hole mobilities have been found to be within the range 10^{-4} to 10^{-6} cm^2 V^{-1} s^{-1}. This low mobility is attributed to larger hopping distances, increased disorder, and also to the effect of traps. Electron mobilities have proved to be at least two orders of magnitude lower than hole mobilities [26]. Since mobilities in conjugated polymers are very low, space charge effects are likely to be important in determining the electrical characteristics of polymer devices. Campbell et al. [28] showed a good

agreement of the recorded I-V characteristics of ITO/PPV/Al LED devices with different thickness and at different temperature with a space charge limited current model incorporating an exponential distribution of traps. It is possible that the Ohmic behaviour is not observed due to the high current densities in polymer LEDs, even at low bias [28].

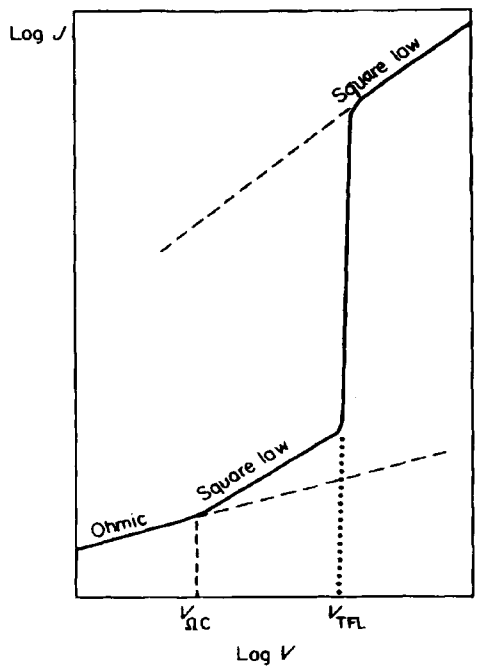

Figure 3.13 Typical current-voltage characteristic for a one-carrier space charge limited current controlled by a single set of trapping centres.

3.6 Electron-Hole Recombination and Exciton Formation

In conjugated polymers with non-degenerate ground states, injected charge from the electrode is transported in the form of negative or positive polarons, in the case of electrons and holes, respectively. Polarons tend to be more mobile than bipolarons, and hence can dominate the transport. The polarons migrate under the effect of the applied field and can meet up with an oppositely charged polaron to form polaron excitons.

An exciton is regarded as a free electron and hole pair which is coupled together through Coulomb capture to form a single system with specific energy levels. This exciton migrates throughout the crystal or conjugated polymer and forms the lowest excited molecular state and then decays radiatively as shown in Figure 3.14.

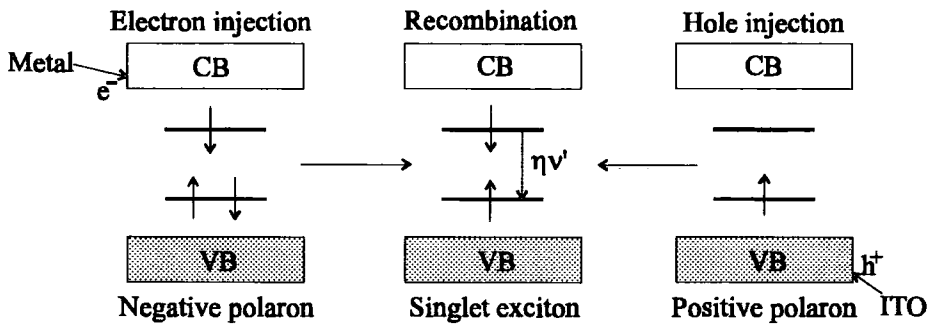

Figure 3.14 Scheme of electroluminescence processes.

The injection of charges with random spin signs will statistically produce both singlet and triplet excitons. 75 % of the excited molecules formed in electron-hole recombination are in the triplet state, while 25 % are in a singlet state. A triplet state has a lower total energy relative to the corresponding singlet state because the two unpaired electrons in the triplet state are prevented from being too close to each other, reducing the electrostatic repulsion between them. The singlet and triplet states are

$$\text{Singlet} = \frac{1}{\sqrt{2}}[(\uparrow\downarrow) - (\uparrow\downarrow)]$$

$$\text{Triplet} = (\uparrow\uparrow)$$

$$\frac{1}{\sqrt{2}}[(\uparrow\downarrow) + (\uparrow\downarrow)]$$

$$(\downarrow\downarrow)\ [29]. \qquad (3.14)$$

Only the singlets are coupled by dipole allowed transitions to the ground state and this is the origin of the 25 % limit on EL efficiency compared with PL efficiency. Considering the confinement of light inside the device by refraction at the interfaces [30], the theoretical external quantum efficiency is expected to range between 2 % and 7 % [9].

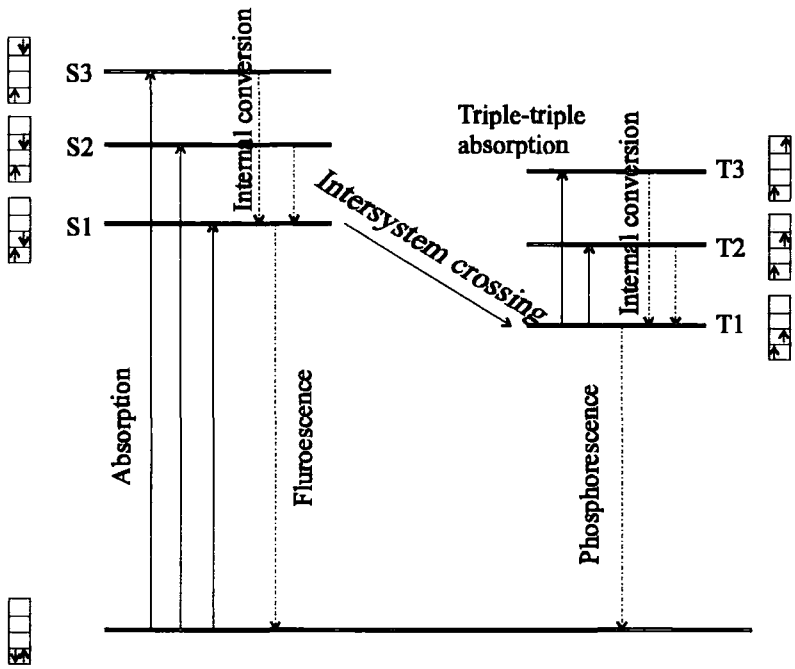

Figure 3.15 Jablonsky diagram representing the important photophysical processes [31].

The emission from fluorescence and phosphorescence occurs due to radiative decay from singlet and triplet excited states, respectively (Figure 3.15). For fluorescence, emission occurs with no net change in spin angular momentum, while for phosphorescence, emission is accompanied by a change in spin angular momentum. Radiative decay of triplets is much slower than that of singlets due to the singlet generation via triplet-triplet collisions [32]. This is the source of the delayed fluorescence in, e.g., anthracene and related organic materials [33, 34]. In some

definitions a persistence of more than 10 nanoseconds (10^{-8} s) is treated as phosphorescence.

The comparison of the PL and EL spectra can also show their non-similarities. The distinct difference between PL and EL spectra results from the difference in charge distribution within the structure. In the case of PL, the luminescence originates from the bulk of film whereas in the case of EL, the injected positive and negative charges move under the electric field and recombine in the recombination zone with a specific electronic energy level.

3.7 Excimer Formation

Excimers refer to dimers that exist only in the excited state while the ground state of the pair dissociates. One common way in which excimers (E_1^*) are formed by interaction of an excited state of a molecule, S_1^*, with the same species in the ground state, S_0

$$S_1^* + S_0 \rightarrow E_1^* \tag{3.15}$$

The formation of the excimer is well known in aromatic molecules and particularly in π-conjugated polymers in which the stiff backbone with relatively planar geometries and strong intermolecular interactions lead to cofacial chain packing in the solid state. The excimer state has lower energy than the exciton state confined to one chain and suppresses intrachain excitons. Therefore, the emission of the excimer

$$E_1^* \rightarrow S_0 + S_0 + h\nu_E \tag{3.16}$$

is red shifted, broad and featureless.

Miyashita et al. [35] observed that the most intensive excimer emission from the LB multilayer when compared to that from the spun film and the solution. In the LB multilayer structure of π-conjugated polymers, the excimer state can be formed by energy transfer between the conjugated polymer backbones both within the same layer and between the adjacent layer, as shown in figure 3.16.

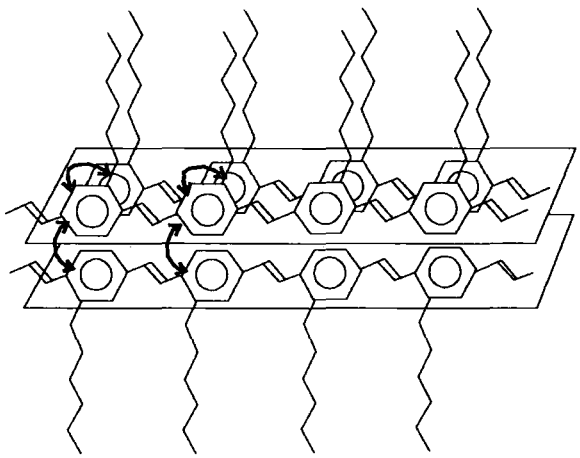

Figure 3.16 Schematic illustration of energy transfer between the conjugated polymer chains in LB film structure.

3.8 Radiative and Nonradiative Decay of Singlet States

The same singlet states that give rise to PL are responsible for the EL emission. Hence, the information from PL studies provides insights into the potential of organic materials for EL applications. High PL efficiency is a necessary, but not sufficient condition for efficient EL. The reasons for this are that there are numerous competing non-radiative decay channels: (I) multiple phonon emission both to the ground state and to low lying states by successive emission of phonons [36]; (II) intersystem crossing, i.e. some of the singlets initially formed may convert into triplets [37]; (III) singlet-singlet collisional annihilation and (IV) migration of excitons to, and

subsequent decay at quenching sites. Quenching sites involved may be bipolarons with deep intra-gap levels [9], excimers and exciplexes formed by intermolecular contacts of two identical or two dissimilar molecular units [38], chemical defects such as C=O groups [39] and contaminants associated with the synthesis or subsequent processing.

The recombination of the singlet excitons in conjugated polymers is influenced by some or all of these quenching mechanisms, depending on the material and experimental parameters such as temperature, excitation energy, and disorder in the solid state.

3.9 Quantum Efficiency and Energy Efficiency

The definition of external quantum efficiency, η_ϕ(ext), is the ratio of the number of photons emitted from the device to the number of electrons which flow through the device

$$\eta_\phi = \frac{(P/h\nu)}{(I/e)} \tag{3.17}$$

where P is the power emitted at a drive current and the photon energy is hν.

It is also sometimes of interest to consider the internal quantum efficiency, η_ϕ, of a device. This relates to the number of photons produced at the junction rather than those emitted from the device, and thus ignores the photons that are absorbed after emission. The external and internal quantum efficiency are connected by the factor η_{ext}, which is approximately evaluated by using the refractive index of emissive medium n [40]

$$\eta_{ext} = 1/(2n^2) \tag{3.18}$$

Figure 3.17 shows the elementary processes, beginning from the recombination of holes and electrons and ending by the light leaving the device. The external quantum efficiency is expressed as

$$\eta_\phi(ext) = \eta_\phi \eta_{ext} \tag{3.19}$$

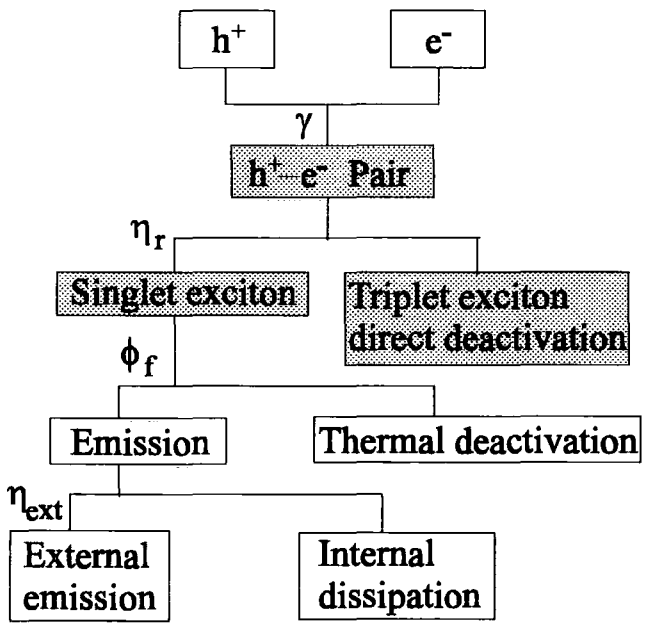

Figure 3.17 Schematic representation of the elementary processes for charge recombination, production of singlet excitons, emission and external emission.

The internal quantum EL efficiency, η_ϕ, is given by using capture quantum efficiency γ, efficiency of production of singlet excitons η_r and quantum efficiency of fluorescence ϕ_f

$$\eta_\phi = \gamma \eta_r \phi_f \tag{3.20}$$

A fraction of total injected charges can meet with the opposite charges to form excitons. This fraction is represented by the capture quantum efficiency, γ. Only a quarter of excitons can be exited as spin singlet state, η_r. Triplet excitons decay non-radiatively limiting the efficiency of operation. The excited singlet excitons can migrate to a lower energy chain segment and emit light. However, migration to quenching sites and other non-radiative decays lower the quantum efficiency of fluorescence ϕ_f.

In a practical system, however, power efficiency is important and must be taken into account. The power efficiency and external quantum efficiency are related according to

$$\eta_p = \eta_\phi(ext)(h\nu / eV) \qquad (3.21)$$

where hν and V denote the photon energy of emitted light and applied voltage, respectively. Another indicator for the device efficiency is luminous efficiency η_L, which is the total luminous flux per unit input power (lm W^{-1}).

3.10 Summary

Conjugated polymers possess π-electrons which are not localised and extend along the entire length of the conjugated chain, inducing semiconducting properties. After doping of, and charge injection to, conjugated polymers, structural relaxations of the polymer backbone surrounding the charged defect, called polarons or solitons, are formed and are important in the performance of polymer LEDs.

Although the charge-carrier injection and transport processes within organic LEDs are much more complex than inorganic crystalline devices, Schottky, Fowler-Nordheim and SCL current models can provide insight into the barrier heights and charge mobilities within the organic layer, and hence into the device operation. To date, the application of such models to the complex situations in organic LEDs has not been fully successful in describing the I-V characteristics at different temperatures and for different thickness regimes.

Only the singlet states of excitons can decay with the emission of light, which limits the EL efficiency to 25 %. Considering the non-radiative decay and the total reflection within the device, the external quantum efficiency of organic LEDs is expected to be in the range between 2 % to 7 %.

References

1. J.H. Burroughes, D.D.C. Bradley, A.R. Brown, R.H. Marks, K. MacKay, R.H. Friend, P.L. Burn and A.H. Holmes, *Nat.*, **347**, 1990, 539.

2. C.K. Chiang, C.R.F. Fincher, Y.W. Park, A.J. Heeger, H. Shirakawa, E.J. Louis, S.C. Gau and A.G. MacDiarmid, *Phys. Rev. Lett.*, **39**, 1977, 1098.

3. H. Naarmann and N. Theophilou, *Synth. Met.*, **22**, 1987, 1.

4. R. Peierls, *Quntum Theory of Solids*, Oxford University Press, **Oxford**, 1955.

5. T.A. Skotheim, *Handbook of Conducting Polymers*, **1&2**, Marcel Dekker Press, **New York**, 1986.

6. M. Pope and C.E. Swenberg, *Electronic Processes in Organic Crystals*, Clarendon Press, **Oxford**, 1982.

7. I.D.W. Samuel, B. Crystall, G. Rumbles, P.L. Burn, A.B. Holmes and R.H. Friend, *Chem. Phys. Lett.*, **213**, 1993, 472.

8. U. Lemmer, R.F. Mahrt, Y. Wada, A. Greiner, H. Bassler and E.O. Gobel, *Appl. Phys. Lett.*, **62**, 1993, 2827.

9. D.D.C. Bradley, *Synth. Met.*, **54**, 1993, 401.

10. R.N. Marks, D.D.C. Bradley, R.W. Jackson, P.L. Burn and A.B. Holmes, *Synth. Met.*, **55**, 1993, 4128.

11. I.D. Parker, *J. Appl. Phys.*, **75**, 1994, 1656.

12. J. Gmeiner, S. Karg, M. Meier, W. Riess, P. Strohriegle and M. Schwoerer, *Acta. Polym.*, **44**, 1993, 201.

13. P.W.M. Blom, M.J.M. de Jong and J.J.M. Vleggar, *Appl. Phys. Lett.*, **68**, 1996, 3308.

14. P.W.M. Blom, M.J.M. de Jong and M.G. van Munster, *Phys. Rev. B.*, **55**, 1997, R656.

15. P.E. Burrows, Z. Shen, V. Bulovic, D.M. McCarty, S.R. Forrest, J.A. Cronin and M.E. Thompson, *J. Appl. Phys.*, **79**, 1996, 7991.

16. J. Gruner, P.J. Hamer, R.H. Friend, H.J. Huber, U. Scherf and A.B. Holmes, *Adv. Mater.*, **6**, 1994, 748.

17. S. Karg, M. Meier and W. Riess, *J. Appl. Phys.*, **82**, 1997, 1951.

18. M. Koehler, J.R. de Lima, M.G.E. da Luz and I.A. Hummelgen, *Synth. Met.*, **173**, 1999, 29.

19. N.F. Mott, *Proc. Cambr. Phil. Soc.*, **34**, 1938, 568.

20. W. Schottky, *Naturwiss*, **26**, 1938, 843.

21. E.H. Rhoderick and R.H. Williams, *Metal-semiconductor Contacts*, Clarendon Press, **Oxford**, 1988.

22. S.M Sze, *Physics of Semiconductor Devices*, Wiley Press, **New York**, 1981.

23. J. Scherbel, P.H. Nguyen, G. Paasch, W. Brutting and M. Schwoerer, *J. Appl. Phys.*, **83**, 1998, 5045.

24. W. Hwang and K.C. Kao, *Electrical Transport in Solids*, Pergamon Press, **Oxford**, 1981.

25. L.S. Roman, I.A. Hummelgen, F.C. Nart, L.O. Peres, and E.L. de Sa, *J. Chem. Phys.*, **105**, 1996, 10614.

26. M.A. Lampert and P. Mark, *Current Injection in Solids*, Acadmic Press, **New York**, 1970.

27. J. Obrzut, M.J. Obrzut and F.E. Karasz, *Synth. Met.*, **29**, 1989, E103.

28. A.J. Campbell, D.D.C. Bradley and D.G. Lidzey, *J. Appl. Phys.*, **82**, 1997, 6326.

29. M.N. Kobrak, and E.R. Bittner, *J. Chem. Phys.*, **112**, 2000, 5399.
30. G. Gu, D.Z. Garbuzov, P.E. Burrows, S. Venkatesh and S. R. Forrest, *Opt. Lett.*, **22**, 1997, 396.

31. P.W. Atkins, *Molecular Quantum Mechanics,* Oxford University Press, **Oxford**, 1983.

32. L.S. Swanson, J. Shinar, A.R. Brown, D.D.C. Bradley, R.H. Friend, P.L. Burn, A. Kraft and A.B. Holmes, *Phys. Rev. B*, **46**, 1992, 15072.

33. T. Azumi and S.P. McGlynn, *J. Chem. Phys.*, **39**, 1963, 1186.

34. C.E. Swenberg, *J. Chem. Phys.*, **51**, 1969, 1753.

35. T. Miyashita, M. Matsuda, M.V. Auweraer and F.C. Schryver, *Macromolecules*, **27**, 1994, 513.

36. P.L. Danielsen and R.C. Ball, *J. Physique*, **46**, 1985, 1611.

37. C.E. Swenberg and N.E. Geacintov, *Organic Molecular Photophysics*, Wiley Press, **New York**, 1973.

38. S.A. Jenekhe and J.A. Osaheni, *SCI*, **265**, 1994, 765.

39. M. Yan, L.J. Rothberg, F. Papadimitrakopoulos, M.E. Galvin and T.M. Miller, *Phys. Rev. Lett.*, **73**, 1994, 744.

40. N.C. Greenham, R.H. Friend and D.D.C. Bradley, *Adv. Mater.*, **6**, 1994, 491.

Chapter 4.

Experimental Techniques

4.1 Introduction

Technological applications of new materials often require them to be in the form of thin films. The term 'thin film' is generally used to describe layers with thicknesses ranging from 1 nm to 10 μm. Many thin-film processing techniques have already been developed for the fabrication of electronics and optoelectronic components. Particular types of organic compound are necessary for certain processes. For example, polymer materials are usually deposited by spin-coating, whereas low molecular weight compounds can be sublimed using thermal evaporation. Materials which have an amphiphilic nature can be deposited, layer by layer, using the Langmuir-Blodgett technique. Film thickness uniformity is essential for device commercialisation. Other important factors are the cost of the thin-film process, the time taken for coating and the availability of continuous coating.

This chapter starts with an overview of the three processing methods mentioned above and provides experimental details for these techniques. The optical characterisation of the films is explained in Section 4.3. The fabrication of organic LEDs is detailed in Section 4.4 and the measurement equipment for the electrical and optical characteristics is described in Section 4.5. The rest of this chapter is concerned with the description of a.c. impedance spectroscopy, low temperature conductivity and surface profiling.

4.2 Film Deposition

4.2.1 Langmuir-Blodgett Technique

Materials Suited to the LB Technique

The LB technique requires amphiphilic molecules to be 'trapped' at the interface between two phases (liquid-gas). For this to occur, the 'amphiphilic balance', i.e. the balance between the hydrophilic and hydrophobic constituents within the same molecule, must be correct for the two phases concerned.

In the case of the air/water interface, materials such as long chain fatty acids and alcohols can be used as film forming materials. The hydrocarbon part -CH_2- of the molecule is responsible for the material's repulsion from water while the polar -COOH or -OH group has sufficient affinity for water to anchor the molecule in the aqueous subphase (Figure 4.1).

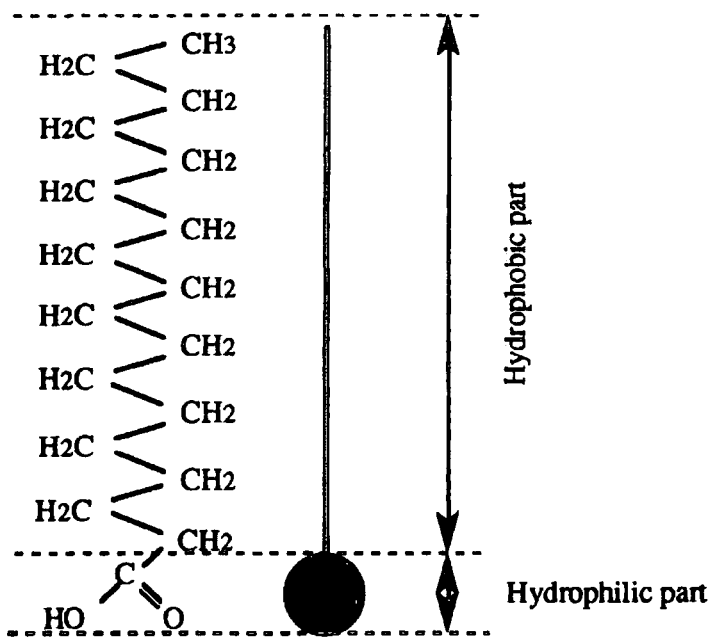

Figure 4.1 Representation of the amphiphilic molecule of stearic acid.

Surface Pressure versus Area Isotherm

The most important indicator of the monolayer properties of a long chain fatty acid is provided by a plot of surface pressure (π) as a function of the area of water surface available to each molecule (A). The measurement is undertaken at a constant temperature and the result is known as a π-A isotherm [1]. It is important to study such isotherms before the LB dipping characteristics are investigated. For example, information can be obtained on the molecular packing and the stability of the compressed layer.

A general surface π-A isotherm for a long chain fatty acid is shown in Figure 4.2. On examination, a number of distinct regions are apparent. At very large surface areas, the surfactant molecules are so far apart that there are negligible interactions between them and their density is so low that their effect on the subphase surface is very small. The film therefore behaves as an 2-dimensional ideal gas. As the surface area is reduced, the hydrocarbon chains will begin to interact. The 'liquid' state that is formed is generally called the 'expanded monolayer phase.' The hydrocarbon chains of the molecules in such a film are in a random, rather than a regular, orientation with their polar groups in contact with the subphase.

On further compression there is an abrupt increase of slope. This phase change represents a transition from the liquid phase to an ordered solid-like arrangement or 'condensed phase.' Here, the molecules are relatively well oriented and closely packed. The zero-pressure molecular area (A_o), obtained by extrapolating the slope of the 'solid-phase' to zero pressure - the point at which this line crosses the X axis - is the hypothetical area occupied by one molecule in the condensed phase at zero pressure.

Eventually, the collapse pressure, π_c, is reached at which the film loses its monomolecular form. The forces exerted on it become too strong for confinement of the molecules in the two-dimensional solid phase and molecules are ejected out of the monolayer plane.

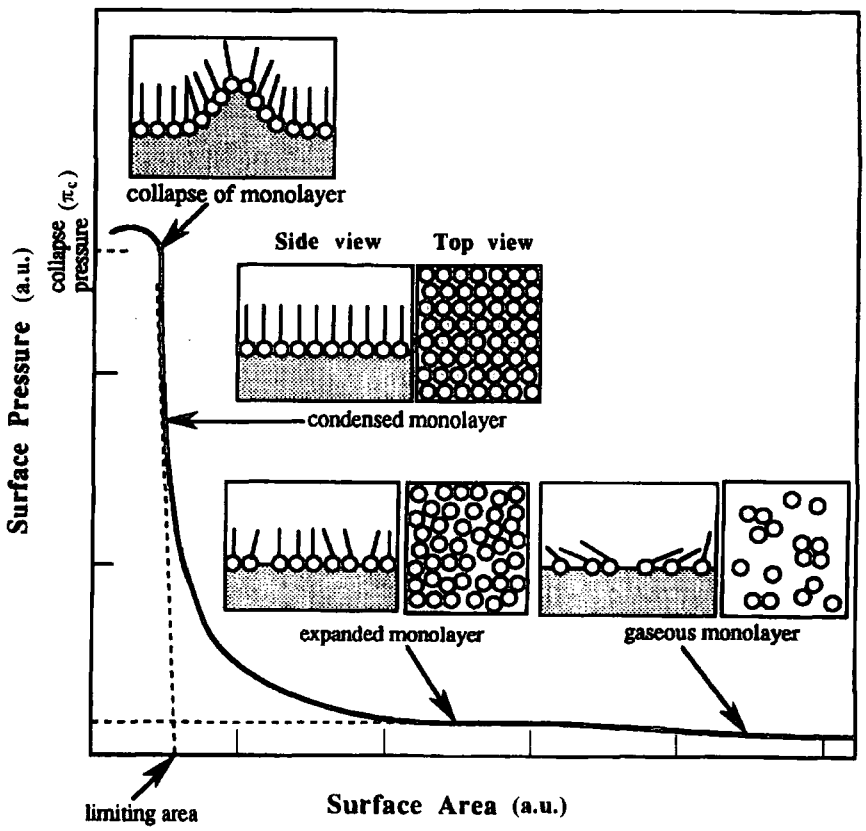

Figure 4.2 π-A isotherm of long chain fatty acid.

Multilayer LB Films

Langmuir-Blodgett films consist of monomolecular layers stacked sequentially onto a solid substrate. A suitably treated substrate is lowered into the water, breaking through the floating Langmuir film. This film attaches itself to the substrate, coating it in a monomolecular layer. Once the first layer has been deposited, further layers will

be transferred on each subsequent dipping cycle. Multilayers can therefore be deposited, as shown in Figure 4.3.

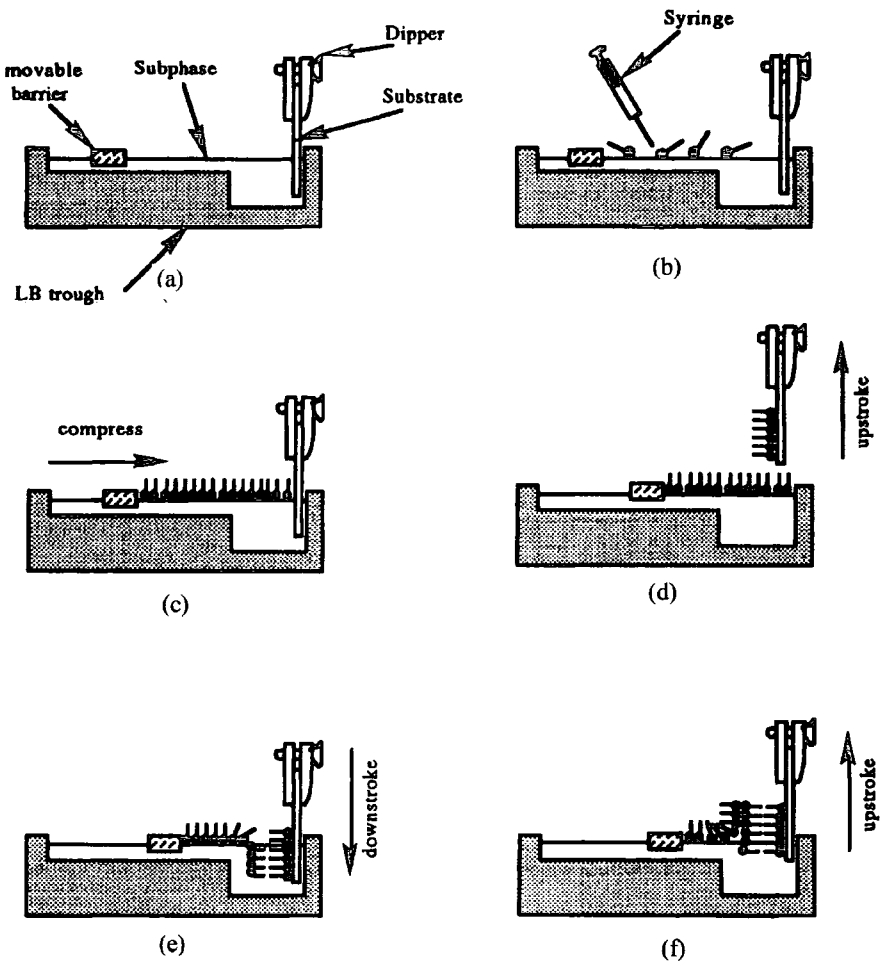

Figure 4.3 Deposition of multilayers by the LB technique.

Deposition Modes

The molecular orientation in the multilayer film depends on the monolayer material used. A schematic diagram illustrating the commonest form of LB film deposition is shown in Figure 4.4. If the substrate is hydrophilic, the first monolayer is transferred as the substrate is raised through the subphase. The substrate may therefore be placed in the subphase before the material is spread, or may be lowered

into the subphase through the compressed monolayer on the first downward stroke with no film transfer. Subsequently, a monolayer is deposited on each traversal of the substrate. The monolayers stack in a head-to-head and tail-to-tail configuration of the molecules: this deposition mode is referred to as Y type. Although Y-type layers are the most easily produced multilayer arrangement, situations in which a monolayer deposits only as the substrate is being inserted into the subphase (X-type) or only as the substrate is being removed (Z-type) have been reported.

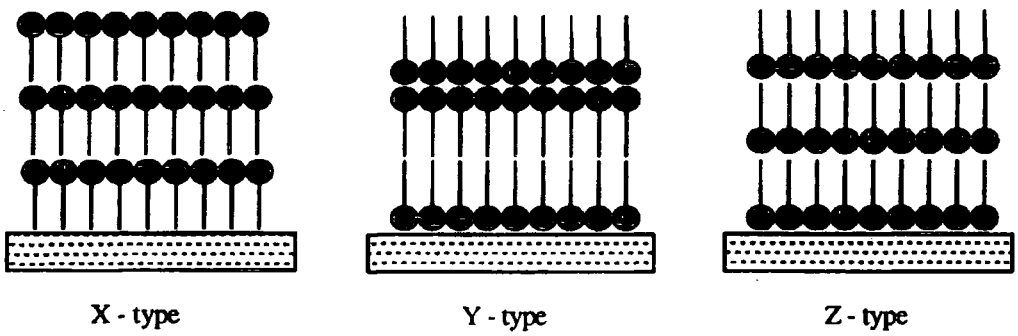

Figure 4.4 Structures of X, Y and Z type mulitlayers.

Film deposition may usefully be characterised by transfer ratio, τ, given by Langmuir et al. [2]

$$\tau = \frac{A_L}{A_{LB}} \times 100 \qquad (4.1)$$

where A_L is the reduction in the area occupied by the monolayer on the water surface and A_{LB} is the area of the solid substrate. Transfer ratios significantly outside the range 0.95 to 1.05 suggest poor film homogeneity.

Surface Pressure Measurement

The presence of a monomolecular film on a liquid surface will affect the surface tension. In monolayer experiments it is normal to refer to a measurement of surface pressure. This pressure π is equal to the reduction of the pure liquid surface tension by the film, i.e.

$$\pi = \gamma_0 - \gamma \qquad (4.2)$$

where γ_0 is the surface tension of the pure liquid and γ is the surface tension of the film covering the surface. Values of π of the order of mN m^{-1} are generally encountered in monolayer studies on a water surface. The most common method for monitoring the surface pressure is the Wilhelmy plate. An absolute measurement of π is made by suspending a plate from a sensitive balance in the monolayer. Figure 4.5 shows the experimental arrangement. The forces acting on the plate are due to gravity and surface tension downwards and buoyancy, due to displaced water, upwards.

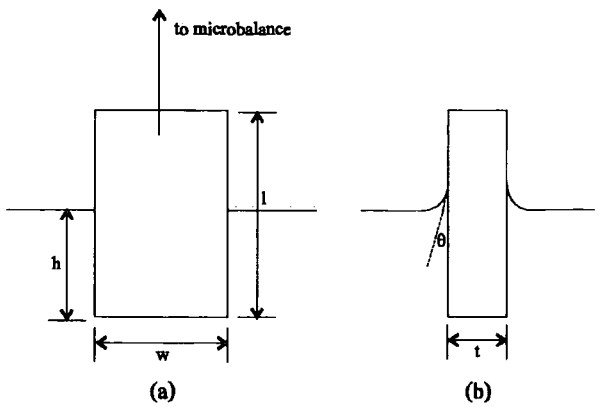

Figure 4.5 A Wilhelmy plate: (a) front view, (b) side view.

For a rectangular plate of dimensions l, w and t and of material of density ρ_w immersed to a depth h in a liquid of density ρ_L, the net downward force F is given by

$$F = \rho_w glwt + 2\gamma(t + w)\cos\theta - \rho_L gtwh \qquad (4.3)$$

where θ is the contact angle on the solid plate and g is the gravitational constant. For a completely wetted plate (i.e. θ = 0), and if the thickness (t) of the sensor is very much smaller than the width (w), the change in force due to a change in surface tension is given by

$$\Delta\gamma = \frac{\Delta F}{2w} \qquad (4.4)$$

Experimental Details

The deposition of LB films was undertaken using troughs designed and built in Durham and housed in a class 10,000 microelectronics clean room. The trough used in this work is shown in Figure 4.6. The barrier, which was made from glass fibre coated with polytetrafluoroethylene (PTFE), was supported by six PTFE rollers. Two of these rollers were fixed and the other four attached to movable metal arms driven by a variable speed d.c. motor.

The subphase was ultra-pure water which was very carefully purified by pre-filtering, reverse osmosis, carbon filtration, two stages of de-ionisation, UV sterilisation and 0.2 μm particulate filtration. Water quality was monitored using an Anatel Total Organic Carbon (TOC) analyser which indicated a resistivity of > 17.5 MΩ cm and TOC content of < 5 ppb.

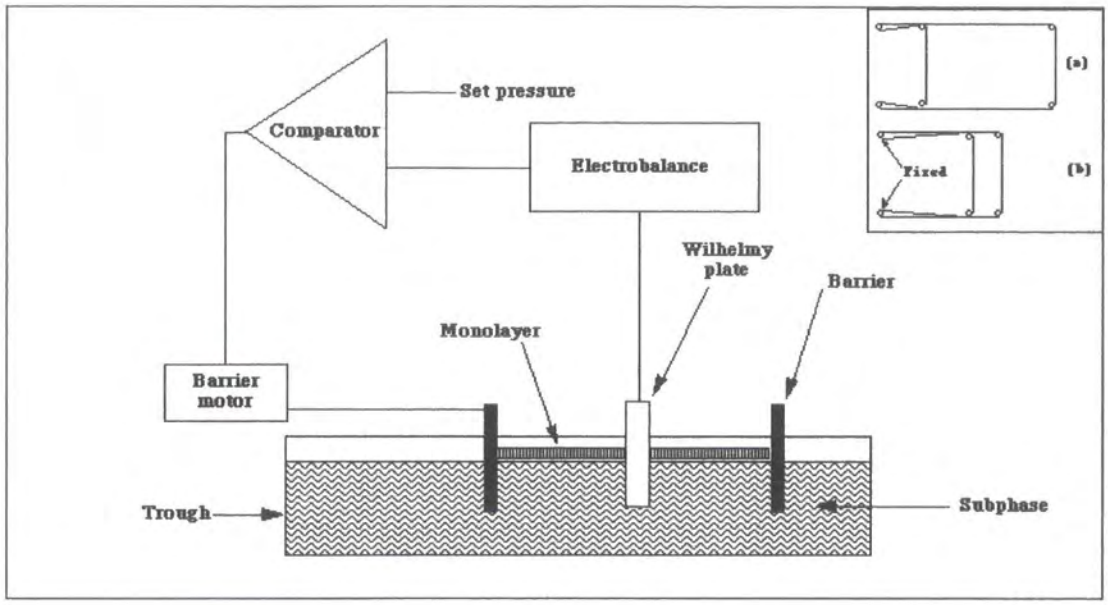

(a)

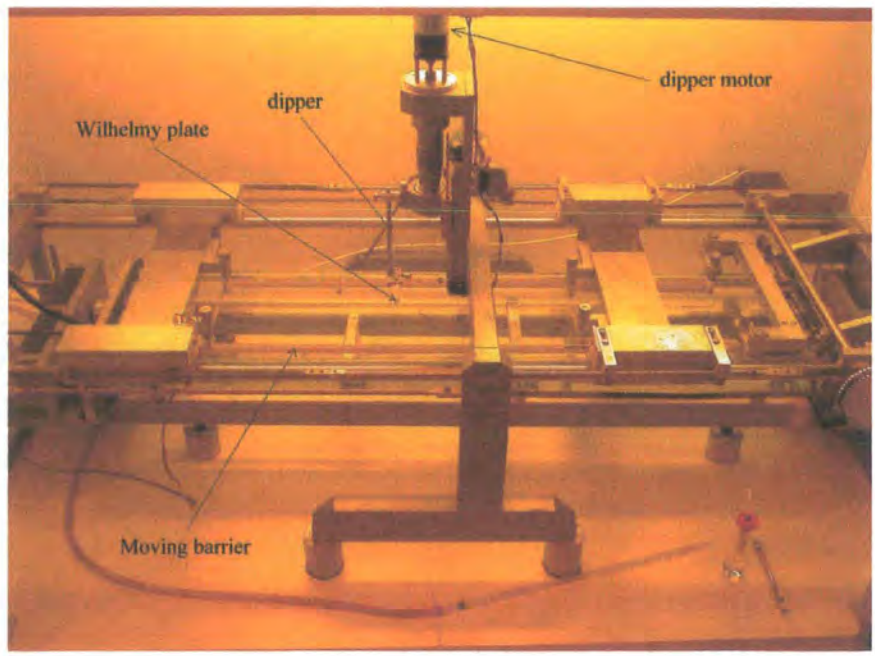

(b)

Figure 6. (a) Schematic diagram of the feedback system used to allow the control of monolayer surface pressure. (b) A photograph of the Langmuir trough used in this research.

The surface pressure was monitored by means of a Wilhelmy plate, which consisted of a piece of chromatography paper (3 cm long and 1 cm wide). This was partially immersed in the subphase and linked to microbalance by a thread. Changes in the force on the plate due to variations in surface tension were transmitted to the balance and converted to an electrical signal. This was used, via a feedback loop, to adjust the area enclosed by the barrier and hence control the surface pressure during film deposition. A desired surface pressure could be selected on the control box, the electronics would then close the barriers to achieve the set pressure and the feedback system would maintain it.

The trough was cleaned with Analar grade propan-2-ol and rinsed with ultra-pure water. The water surface was judged to be clean when the barriers could be compressed and the surface pressure changed by less than 0.5 mN m^{-1}. The substrate was clamped into a suitable holder which was mounted onto the dipping head. The speed of the dipping was adjusted by means of the potentiometers on the control electronics.

The surface pressure was zeroed and the solution of material (dissolved in chloroform) was dispensed, using a micro-syringe, by dropping it onto the water surface. The chloroform was allowed to evaporate for a few minutes and then the film could be compressed to the set point pressure. The trough area and surface pressure against time were recorded using a Y-t chart recorder. The π-A isotherm was recorded with an X-Y recorder. Isotherms were measured at a compression rate of 3.8 cm^2 sec^{-1}. The plot obtained was examined and used to select a suitable pressure for film deposition, usually on the steepest part of the isotherm. Films were

transferred from a pure water subphase at a temperature of 18 ± 2 °C and pH of 5.8 ± 0.2. The dipping pressure and speed were dependent on the materials used.

The substrates were selected depending on the specific application. Quartz was used for UV-Vis. absorption spectroscopy and the PL spectroscopy. To fabricate an EL device, ITO glass was used as the bottom electrode.

4.2.2 Thermal Evaporation

This method has been used extensively to deposit films of inorganic materials, such as metals and their corresponding alloys. However, the technique is now being used for the formation of layers of low-molecular weight organic compounds. The rate of evaporation G from a surface at temperature T is given by the Langmuir expression [3], as follows

$$G = p(\frac{M}{2\pi RT})^{1/2} \qquad (4.5)$$

where p is the vapour pressure of the material at temperature T, M is the molecular weight and R is the gas constant. In the vapour phase, the molecules travel at high velocities making frequent collisions with others in the vacuum system. The average distance a molecule will travel before colliding with another is called the mean-free path, λ. For a straight line path between the evaporating material (source) and the substrate, it is necessary to use low pressures ($< 10^{-6}$ mbar), where the mean free path of the gas atoms is much greater, leading to straight line propagation of evaporant. This makes it possible to reproduce finely defined patterns by the introduction of a

shadow mask between the source and substrate. The low pressure also prevents contamination of the source material by oxidation and other impurities.

The deposition of thin films by thermal evaporation consists of several distinguishable steps: (I) creation of vapour phase species; (II) material transport from the source to the substrate in the vapour phase; and (III) condensation and film growth on the substrate. The microstructure of an evaporated thin film depends on the evaporation rate, substrate temperature and the chemical and physical nature of the substrate surface. The physical nature of evaporated films can be changed by post-deposition heat treatment (annealing). This is usually associated with a change in the crystallinity of the film.

Experimental Details

In all vacuum deposition techniques, it is essential that the gaseous species travel in a straight line from the source to the substrate. The mean free path without any collision with other particles depends on the vacuum state. For pressures down to 10^{-5} mbar, λ is so large that molecules effectively collide only with the target substrate. The thermal evaporator is composed of two parts: the pumping system which determines the ultimate pressure and the vacuum chamber in which evaporation takes place, as shown in figure 4.7.

A high vacuum (10^{-3} ~ 10^{-6} mbar) can be achieved by two stages of pumping. For roughing the chamber down to ~10^{-2} mbar, an Edwards 2M8 rotary pump was used. Following this, an Edwards E04K diffusion pump with Duravak Silicone 74 oil was used, allowing the pump to reach an ultimate pressure of ~10^{-6} mbar.

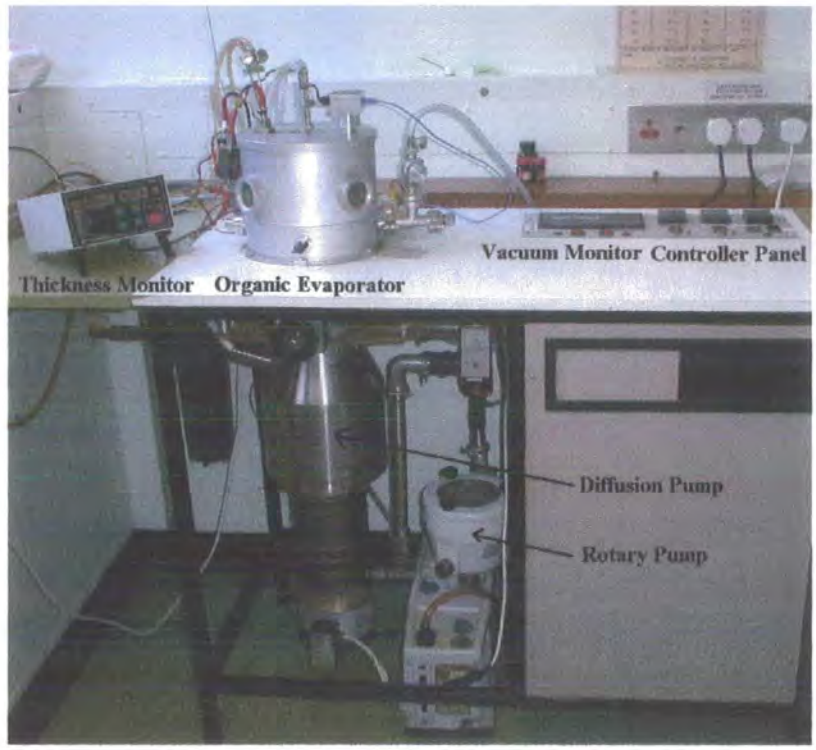

Figure 4.7 A photograph of thermal organic evaporator.

The vacuum chamber is the most of important part of a vacuum system in which molecules were evaporated onto target substrate. Resistive heating was used to provide the vapour. Several evaporation sources are commercially available to suit the needs of a particular material. These include filaments, boats and crucibles of different shapes, sizes and materials. For this work, organic materials were placed inside a glass crucible which was surrounded by a filament heat source. To monitor the temperature of the powder in the crucible during the evaporation, a thermocouple was inserted into the cavity of crucible. The thermocouple was connected to a CAL 9900 temperature controller to maintain uniform evaporation temperature. The film thickness and the evaporation rate were monitored by an Edwards film thickness monitor (FTM7).

4.2.3 Spin-Coating

Spin-coating is exploited extensively by the microelectronics industry for depositing layers of photoresist, generally polyimides, onto silicon wafers [4]. A quantity of a polymer solution is first placed on the semiconductor wafer, which is then rotated at a fixed speed of several thousand rpm (or the solution can be applied while the substrate is slowly rotating). The resist solution flows radially outwards, thus reducing the fluid layer thickness. Evaporation of the solvent results in a film of uniform thickness. A simple theory predicts the following relationship between the thickness of the spun film, d, the viscosity coefficient of the solution, η, its density, ρ, the angular velocity of the spinning, ω, and the spinning time, t [4]

$$d = \left(\frac{\eta}{4\pi\rho\omega^2}\right)^{1/2} t^{-1/2} \qquad (4.6)$$

This equation works reasonably well for practical concentrations of spinning solution. However, very dilute solutions often lead to pinholes in the final film and to a disordered film. A more ordered film may be achieved by a post-deposition treatment, such as thermal annealing or using an electric field normal to the film plane [5].

Experimental Details

The thickness of the spun film is dependent on the viscosity coefficient of the solution, the angular velocity of the spinning and the spinning time. In this project, the solution was dropped on top of the ITO patterned glass or quartz before spinning. MEH-PPV solution (6.6 mg ml^{-1}) in a solvent of 50 % chloroform and 50 % *p*-xylene

was judged to have the appropriate viscosity. At first, a low spin speed (800~1000 rpm) was used to spread the solution evenly on the substrate for 3 seconds and afterwards, the film thickness was reduced to the required thickness for 30 seconds with a high spin speed (2600-2800 rpm). The high spin speed was adjusted by calibrating the film thicknesses against the speed. During the spinning, the substrate was fixed to the substrate holder which had holes connected to a rotary pump vacuum system. The thickness and roughness of film was measured physically with a stylus profilometer.

4.3 Optical Characterisation

4.3.1 Optical Microscopy

The film morphology was first assessed using a Vickers optical microscope. This was used in reflection mode without polarisation. Objective lenses with magnification factors of 10, 20, 40 and 100 times were available. Optical micrographs were recorded using a 35 mm camera. The degradation of the organic LEDs, which were subjected to a constant current stress experiment, was also studied using this equipment. Photographs of the electroluminescence images of the LEDs were recorded using the camera in a dark room. The EL light projected through the ITO glass to the camera with an exposure time of two minutes.

4.3.2 UV-Vis. Absorption Spectroscopy

The optical absorption spectra of multilayer LB films or spun films deposited onto quartz were measured in the range of 200 - 800 nm in 1 nm steps with a scan

speed of 240 nm min^{-1} using a Perkin-Elmer Lambda 19 ultraviolet/visible/near-infrared spectrophotometer. The baseline was first established by using two identical quartz plates. One of these was then used as a reference while the other was replaced by the sample. The intensity of light passing through an absorbing material is reduced according to the Beer-Lambert equation [6]

$$I = I_0 \exp(-\alpha l) \tag{4.6}$$

where I is the measured intensity after passing through the material, I_0 is the initial intensity, α is the absorption coefficient and l is the path length. Equation 4.6 is often written as

$$A = -\log_{10}(\frac{I}{I_0}) \tag{4.7}$$

where A is the absorbance of the sample and is given by $A = (\log_{10}e)\alpha l = 0.43\alpha l$.

For an LB film, the absorbance is linearly dependent on the number of layers. Hence, by measuring the absorbance at a fixed wavelength, the reproducibility of the film deposition process could be ascertained.

4.3.3 Photoluminescence Spectroscopy

Fluorescence spectra were obtained using a Perkin Elmer LS-50B Luminescence spectrometer. The light source was a Xenon flash tube, which produced an intense, short duration pulse of radiation with a width at half the maximum intensity of less than 10 μs. The exciting light, at a specific wavelength, was focused onto the sample and light emitted from it was focused onto the entrance slit

of the emission monochrometor, and measured with a photomultiplier tube (PMT), Hanamatsu R928 model. When operating in the fluorescence mode, the signal was integrated over 80 μs to collect all the light emitted from the sample, for each wavelength studied.

The ranges of the excitation and the emission monochrometer were 200 - 800 nm and 200 - 900 nm, respectively. The excitation slits, 2.5 - 15 nm, and the emission slits, 2.5 - 20 nm, could be varied. Widening the slits produced more incident light but reduced the spectral resolution of the instrument. The scanning speed could be selected from 10 - 1500 nm min^{-1}. All the films were deposited on quartz plates which were fixed to a sample holder specially designed for the plate type samples.

4.3.4 Scanning Electron Microscopy

Scanning electron microscopy was undertaken using a Cambridge Instruments Stereoscan 600 system. The electron beam accelerating voltage was variable and could be set at 1.5, 7, 15, or 25 kV. The system offered a wide range of magnification, from 20 to 100,000. Highly insulating samples become electrically charged under the electron beam and produced unstable images. Such samples were therefore coated with a 1 nm thick layer of gold, produced by glow discharge using a Polaron Instrument SEM coating unit, to obtain a conductive surface.

4.3.5 Electron Probe Microanalysis

Material characterisation was undertaken using an electron microprobe (EMP) to excite X-rays characteristic of the elements present in the sample under

investigation [7]. This makes use of the electron beam, focusing lenses and deflection coils of the scanning electron microscope, with the addition of an X-ray detector. Such an energy-dispersive spectrometer (EDS) is useful for rapid sample analysis and has the ability to analyse all energies simultaneously. The detector can be positioned very close to the sample resulting in high detection efficiency. A Link Systems 860 Series 2 EDS fitted to the Cambridge Instruments Stereoscan 600 SEM was used. X-rays emitted from the sample passed through a thin window onto a liquid nitrogen cooled reverse biased Si(Li) detector. The charge pulses (generated by X-rays absorbed by the detector) were converted to voltage pulses which were then amplified and passed to a multi-channel analyser (MCA), where the data were displayed as a histogram of intensity versus electron voltage. The software of the analyser allowed for the peak identification or quantification of the components in the sample.

4.3.6 Electroluminescence Spectroscopy

Electroluminescence spectra were measured while the LED was held at a constant voltage or current by using a Ocean Optics USB 2000 miniature fibre optic spectrometer, which is responsive from 200 nm to 1100 nm. This is composed of 2048-element linear CCD (charge-coupled device) array detector. A CCD is an array comprised of many thousands of microscopically small light sensitive elements. One or more of these are considered to represent a single point of light, or pixel. Light falling on a CCD causes a minute electrical charge, proportional to the brightness of the light, to be held within each element. The light emitted from the source was collected using an optical fibre and then focused onto a movable diffraction grating,

which spectrally split the collected light. The spectrum could then be measured by a CCD array.

4.3.7 Atomic Force Microscopy

The film topography was observed with a Topometrix Explorer Scanning Probe atomic force microscope (AFM) using a Si_3N_4 cantilever in contact mode, and a scan area of 5×5 μm. Figure 4.8 shows the contact AFM mode.

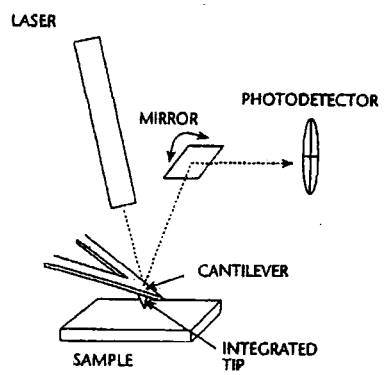

Figure 4.8 Atomic force microscope system (contact mode).

The probe tip (which is mounted to the end of the cantilever) scans across the sample surface, coming into direct physical contact with the sample. As the probe tip scans, varying topographic features cause deflection of the tip and cantilever. A light beam from a small laser is bounced off the cantilever and reflected on to a photodetector. The amount of deflection of the cantilever or the force it applies to the sample can then be calculated from the difference in light intensity on the photodetector.

Hooke's Law gives the relationship between the cantilever's motion, d, and the force required to generate the motion, F

$$F = -kd \tag{4.8}$$

Movement of less than one angstrom can be measured.

4.4 Device Fabrication

4.4.1 ITO Patterning

For organic LEDs, ITO is almost exclusively used as the semitransparent electrode, due to its high surface conductivity and high optical transmission. The ITO used in the research was from the Samsung Co., with a sheet resistivity of 32 $\Omega\,\square^{-1}$. This was patterned into stripes (2 mm width) with a photoresist pen and, after drying, the exposed ITO was etched using zinc powder mixed with 50 % diluted hydrochloric acid. The photoresist was removed using acetone and the patterned ITO glass was rinsed using deionised water. After patterning, the resistance between stripes was checked to make sure that ITO electrodes were isolated from each other. The substrates were then cleaned by sonication in deionised water, acetone and propan-2-ol for 30 minutes each and finally dried with a nitrogen gun. This cleaning procedure was crucial to obtain high quality films free from pin-holes.

4.4.2 Deposition of the Organic Layer

Organic LEDs were fabricated by depositing films onto ITO patterned glass substrates. The organic films were prepared by the LB technique, spin-coating and thermal evaporation. Multilayer deposition using different techniques, such as a spin-coated film onto an LB films or a thermally evaporated film onto a spin-coated film,

was also used. When spinning onto an organic film, a careful choice of solvent was necessary so as not to dissolve the underlying layer.

4.4.3 Metal Evaporation

The device structure was completed by vacuum evaporation of metal stripes (1 mm width) onto the film at a pressure of around 10^{-6} mbar through a shadow mask. Electrodes with thickness of around 150 nm were evaporated onto the organic layer and the film thickness was monitored by a quartz crystal sensor during evaporation. An evaporated aluminium electrode was used as the cathode in most devices. Electrodes with a low work function, such as calcium and magnesium, were partially protected from the effects of oxidation by the subsequent evaporation of an aluminium capping layer. Before evaporating the cathode electrode, all LB films were placed for 12 hours in a high vacuum of 10^{-6} mbar to remove any moisture. The active area of LEDs was 2 mm^2, defined by the overlap of the ITO stripe and cathode electrode. Organic LEDs were stored in a vacuum chamber (~ 10^{-1} mbar) to minimise device degradation [8,9]. The final device structure is shown in Figure 4.9.

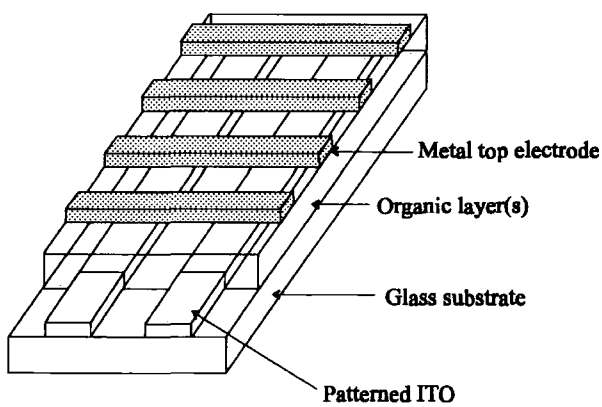

Figure 4.9 The structure of an organic LED device.

4. 5 LED Characteristics

A diagram of the equipment used for the investigation of the LED characteristics is shown in figure 4.10.

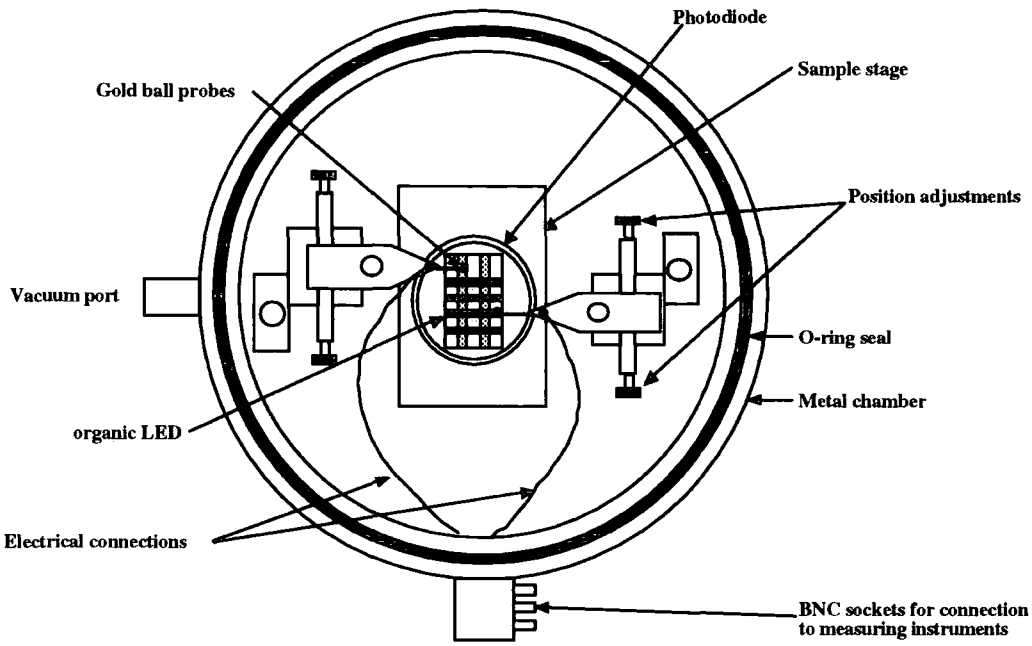

Figure 4.10 Sample chamber for electrical and light output measurements.

The current and light output from the LEDs were measured simultaneously under vacuum (~10^{-1} mbar) in an electrically screened chamber. Biases were supplied by a Keithley 2400 source using a linear staircase step of 0.5 V with a 1.5 s delay between measurements. The LEDs were mounted over a large area silicon photodiode (standard RS photodiode, 100 mm^2). The photocurrents generated were recorded using a Keithley 485 digital picoammeter. Operation was controlled by a computer and the device current and photocurrent from the photodiode at all voltages were recorded. For the external quantum efficiency measurements, the light power was calculated with conversion factor of 0.32 amp $watt^{-1}$ at 590 nm, corresponding to the electroluminescence peak of MEH-PPV [10]. Not all the light from the LED (e.g.

wave guided light) was collected by the photodiode and hence the external quantum efficiencies quoted in this research are lower limits.

The current versus voltage characteristics were found to be strongly dependent on the bias scan history of device [11]. For example, an irreproducible and spiky behaviour was recorded during the first scan. All curves shown in this thesis (unless otherwise mentioned) are scans taken after reproducible characteristics had been obtained.

4.6 A.c. Impedance Spectroscopy

A.c impedance spectroscopy is a powerful tool to study relaxation in organic and inorganic materials, both in solution and in the solid state. This allows the investigation of the capacitance versus voltage for polymer LEDs [12], the interface characteristics of the polymer/Al junction [13], i.e. depletion regions, and the corresponding doping or trap concentrations. The complex a.c. impedance, Z, is expressed as

$$Z = Z' - jZ'' \qquad (4.9)$$

where Z′ is the real part and Z″ is the imaginary part of the impedance.

Impedance spectroscopy measurements were performed with a Hewlett Packard 4192 Impedance Analyser. Impedance spectra were taken by measuring the capacitance and conductance of the devices under various applied d.c. biases with the frequency of the a.c. modulation voltage (70 mV r.m.s.) taking 51 points, logarithmically spaced in the frequency range from 5 Hz to 13 MHz. The real and imaginary parts of the impedance were then plotted in the complex plane (Cole-Cole

plot). The device could then be modelled by an equivalent circuit consisting of several 'layers' connected in series, each layer consisting of a resistance in parallel with a capacitance.

4.7 Low Temperature Conductivity

To investigate temperature induced variations in the I-V characteristics of samples, an Oxford Instruments DN704 liguid nitrogen exchange gas cryostat was used (Figure 4.11).

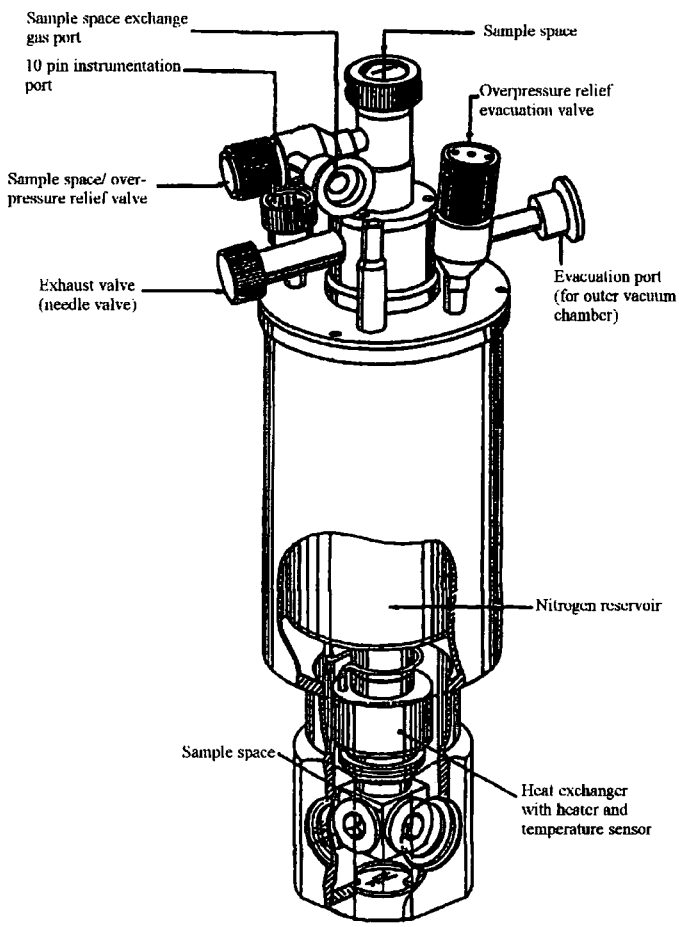

Figure 4.11 Schematic diagram of the liquid nitrogen cryostat.

A liquid nitrogen (boiling point = 77 K) reservoir was surrounded by an evacuated chamber, forming the upper part of the sample chamber. The sample was cooled by allowing a flow of liquid nitrogen from the reservoir to the copper heat exchanger. Nitrogen gas leaving the heat exchange block could exit from the cryostat through an exhaust valve in the top plate. A vacuum system consisting of a rotary vane backing pump and an oil vapour diffusion pump was used to evacuate the chamber. A small device (2 mm × 1mm) was held in position on the sample holder and electrical contacts to the electrodes were carefully made using silver paint. After insertion of the sample, the tube was evacuated and flushed out with helium gas to ensure removal of any water vapour before closing off.

A heating coil and temperature sensor connected to an Oxford Instruments DCT-2 precision temperature controller allowed control of the temperature (77 ~ 300 ± 2 K). Temperature variation was achieved by balancing the heat input against the cooling power available, which could be regulated by opening and closing the exhaust valve. After allowing the temperature to stabilise, biases were applied by a Keithley 2400 source using a linear step of 0.5 V with a 1 s delay between measurements.

4.8 Surface Profilometer

The stylus profilometer is a mechanical instrument which has been used to measure film thickness. In this technique, a stylus is moved slowly across the surface of the sample under test. The upward force on the stylus varies with the height of the surface and therefore a graph of the pressure, measured electronically, against stylus position provides a profile of the surface which can be calibrated to give height measurement. For the measurement of the organic film thickness, a step is first

created by carefully wiping away a portion of film using a suitable solvent. To prevent the stylus from penetrating the film surface, a layer of aluminium of 150 nm thick was deposited over the step. The stylus profilometer used was a Tencor Instruments Alpha-step 200. A stylus force of 8 mg was used together with 40 μm sec^{-1} scanning speed.

The value of surface roughness (R_a) is useful to qualify the uniformity of film. The arithmetic average surface roughness is determined using the graphical-centreline method. Figure 4.12 shows the principle of measurement of surface roughness.

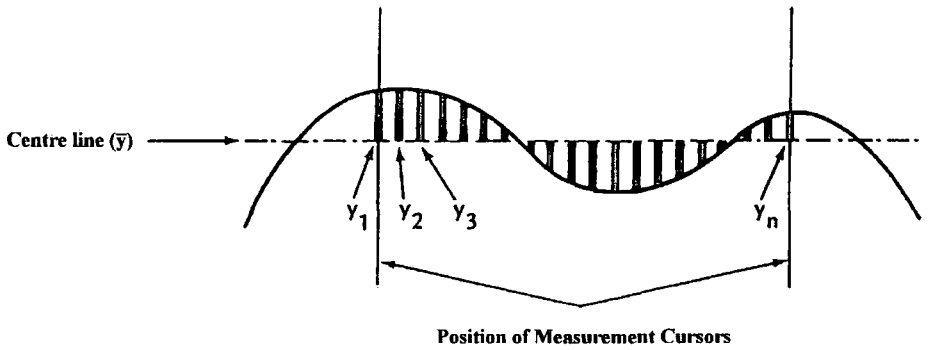

Figure 4.11 Measurement of film roughness.

$$R_a = \frac{|y_1| + |y_2| + |y_3| + \cdots\cdots + |y_n|}{n} \qquad (4.10)$$

Where, y_1, y_2,····, y_n are the deviations from the centreline and n is the number of points between the measurement cursors.

4.9 Summary

Three different methods for the preparation of organic thin films have been discussed: the LB technique, thermal evaporation and spinning. Optical

characterisation of the films using UV-Vis. spectroscopy, microscopy, scanning electron microscopy and energy dispersive spectroscopy have been described. The measurement of photoluminescence and electroluminescence were also explained. The fabrication of organic LEDs was detailed and the equipment for the measurement of current-voltage and light output was described. The thickness and roughness of film were determined by the surface profilometer and atomic force microscopy. Finally, the technique of a.c. impedance spectroscopy and low temperature conductivity were outlined.

References

1. A. Pockels, *Nat.*, **48**, 1893, 152.

2. I. Langmuir, V.K. Schaefer and H. Sobotka, *J. Am. Chem. Soc.*, **59**, 1937, 1751.

3. L.I. Maissel and R. Glang, *Handbook of Thin Film Technology*, McGraw-Hill Press, **New York**, 1970.

4. I. Brodie and J.J. Muray, *The Physics of Micro/Nano-Fabrication*, Plenum Press, **New York**, 1992.

5. M. Petty, J. Tsibouklis, M.C. Petty and W.J. Feast, *Ferroelectronics*, **150**, 1993, 267.

6. M.C. Petty, *Langmuir-Blodgett Films: An Introduction*, Cambridge University Press, **Cambridge**, 1996, 216.

7. D.K. Schroder, *Semiconductor Material and Device Characterisation*, John Wiley and Sons Inc., 1990.

8. L.M. Do, E.M. Han, Y. Niidome, M. Fujihira, T. Kanno, S. Yoshida, A. Maeda and A.J. Ikushima, *J. Appl. Phys.*, **76**, 1994, 5118.

9. J.C. Scott, J.H. Kaufman, P.J. Brock, R. Dipeitro, J. Salem and J.A. Goitia, *J. Appl. Phys.*, **79**, 1996, 2745.

10. G.Y. Jung, C. Pearson, M. Kilitziraki, L.E. Horsburgh, A.P. Monkman, I.D.W. Samuel and M.C. Petty, *J. Mater. Chem.*, **10**, 2000, 163.

11. F. Garten, J. Vrijmoeth, A.R. Schlatmann, R.E. Gill, T.M. Klapwijk and G. Hadziioannou, *Synth. Met.*, **76**, 1996, 85.

12. I.H. Campbell, D.L. Smith and J.P. Ferraris, *Appl. Phys. Lett.*, **66**, 1995, 3030.

13. M. Esteghamatian and G. Xu, *Synth. Met.*, **75**, 1995, 149.

Chapter 5.

MEH-PPV Devices Prepared Using the Langmuir-Blodgett Technique

5.1 Introduction

The thin organic layers needed for LED devices can usually be produced by the spin coating for polymers and by thermal evaporation for dyes and low molecular weight materials. The Langmuir-Blodgett technique [1,2] and layer-by-layer self-assembly [3] have also been used to provide multilayer LED structures with accurately defined thicknesses.

In this chapter, the LB film deposition conditions and characteristics of poly(2-methoxy-5-(2'-ethylhexyloxy)-*p*-phenylenevinylene) (MEH-PPV) are discussed. LED devices have been made using these films and their current versus voltage characteristics are described. The experimental data are fitted using Schottky barrier, Fowler-Nordheim and space charge limited (SCL) current models. A.c. impedance results and low temperature d.c. electrical characteristics are presented. The effect of replacing the Al top electrode with a Ca electrode is also studied.

5.2 LB film Deposition and Characterisation

5.2.1 Material

MEH-PPV is a particularly attractive material for LED fabrication due to its solubility in common organic solvents. This material can be used as both the emitting

layer and the hole transporting layer in light emitting devices. MEH-PPV was obtained from Aventis (formerly Hoechst) and its structure is shown in Figure 5.1. The molecular weight is of the order of 30,000. This polymer contains an alternating system of single and double bonds. Due to this, π-electrons are delocalised along the polymer backbone. Each repeat unit consists of phenylene and vinylene moieties. The geometry and the molecular length were obtained when the repeat unit had the lowest molecular energy by using the Hyper MM+ programme.

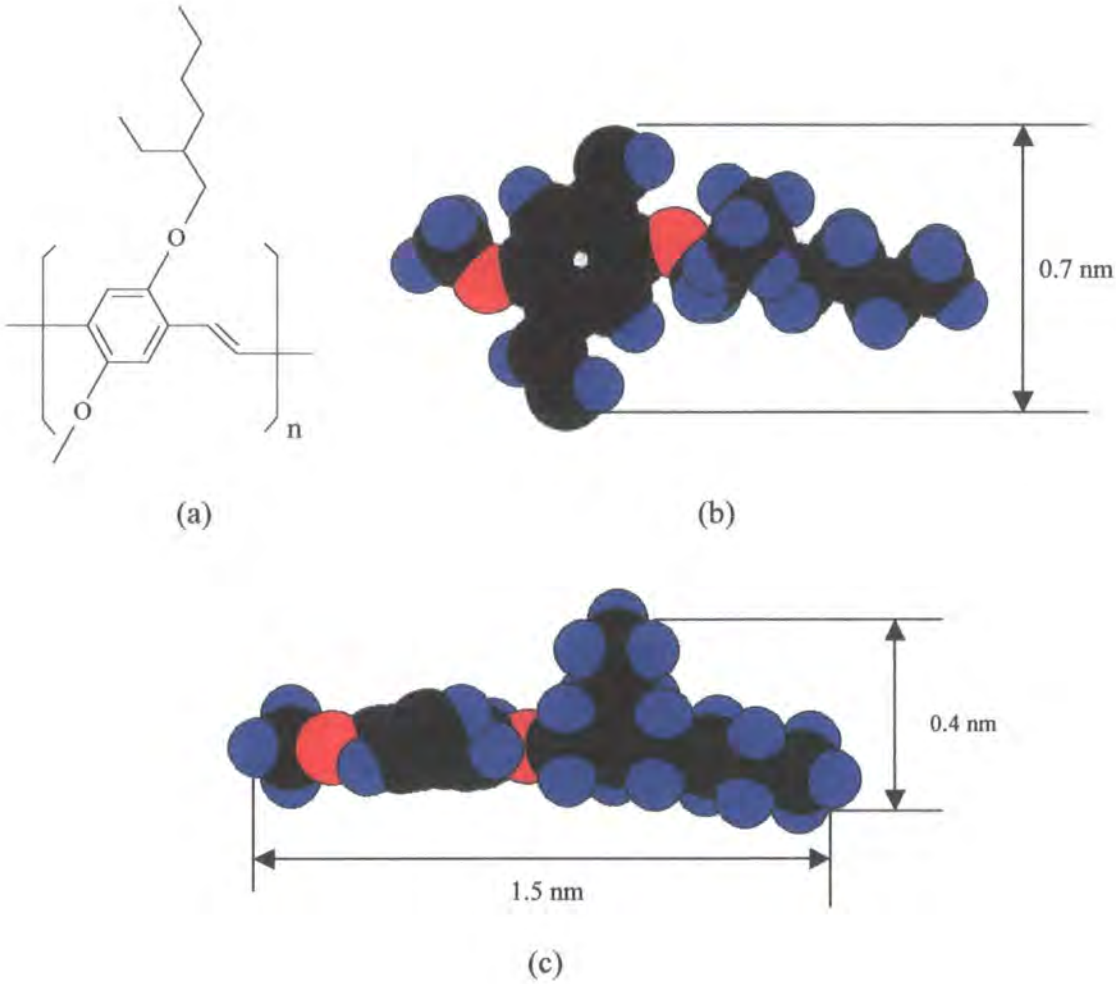

Figure 5.1 (a) Molecular structure of MEH-PPV, (b) top view and (c) side view. The geometry was optimised using HyperMM+.

5.2.2 Surface Pressure versus Area Isotherm and LB Deposition

MEH-PPV was dissolved in chloroform to a concentration of 0.35 mg ml^{-1} and sonicated for 1 hour for better dissolution of the high molecular weight components. 250 µl of this solution was distributed onto a pure water subphase using a microsyringe. The formation of reddish islands was visible on the subphase during spreading of the MEH-PPV solution. After allowing 15 minutes for evaporation of the chloroform, the layer was compressed at a speed of 1.9×10^{-3} nm^2 $molecule^{-1}$ sec^{-1}. The resulting surface pressure (π) versus area (A) isotherm measured at 18 °C and a pH of 5.2-5.6 has some interesting features, as shown in Figure 5.2.

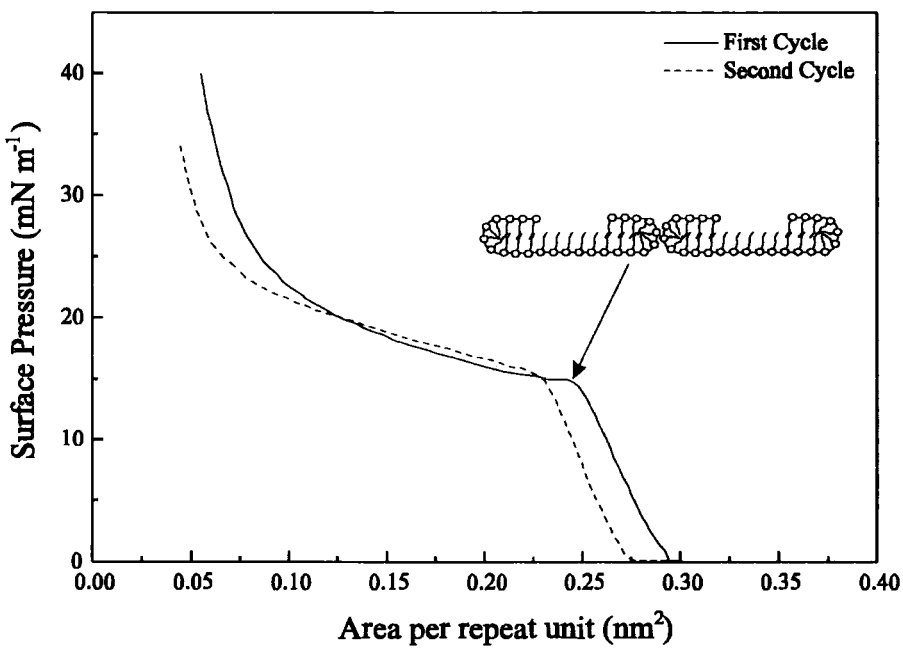

Figure 5.2 π-A isotherm of MEH-PPV with a compression speed of 1.9×10^{-3} nm^2 $molecule^{-1}$ sec^{-1}.

A 'condensed' region is evident below 16 mN m^{-1}. Further compression reveals a 'collapse' of the layer, where the surface pressure rises slowly. Upon opening the barrier, more reddish islands were evident floating on the water surface. On the second compression of the layer, the π-A curve was shifted to a smaller

molecular area. This behaviour could be explained by the irreversible aggregation of polymer chains or a slight solubility in the water subphase. Further compression curves were nearly the same as the second one (the time to complete a full isotherm measurement was ~ 2 mins).

The above features are common in the isotherms of polymeric compounds. Aramata et al. [3] compared the π-A isotherms of a porphyrin monomer and polymer and reported irreversible behaviour in the polymer layer due to the aggregation of the polymer chains, in contrast to the monomer layer. In general, polymeric materials have a greater structural variation on the subphase surface than simple molecules due to the flexibility of their backbone chains.

The area per repeat unit extrapolated to zero surface pressure (first compression) is about 0.28 nm^2 which coincides with the area of the smallest face of the molecule in Figure 5.1 (treating the molecule as a rectangular box, 0.7 nm × 0.4 nm × 1.5 nm). The smaller area per repeat unit obtained from the second compression and subsequent compressions indicated that the monolayer probably collapsed to form a multilayer on the water surface.

The monolayer area subjected to constant surface pressure of 15 mN m^{-1} (before collapse) over a long period (several hours) decreased. This instability of the monolayer is possibly caused by the short side chain length. Materials with short alkyl side group were reported to have an inadequate hydrophobic/hydrophilic balance and dissolve into the subphase [4].

LB film deposition was undertaken onto solid substrates at two constant surface pressures: 15 mN m^{-1} (before the transition) and 17 mN m^{-1} (after the transition). At 15 mN m^{-1}, no deposition onto ITO glass was recorded whilst at 17

mN m^{-1}, an orange coloured film could be built-up at a dipping speed of 3 mm min^{-1}. The area per the repeat unit was 0.2 nm^2 at this surface pressure. This is smaller than the calculated value (0.28 nm^2) from molecular modelling, suggesting that the floating film is more than one monolayer in thickness.

The area of the floating layers at a surface pressure of 17 mN m^{-1} also decreased gradually with time. If the layer was left for a long time before dipping, e.g. 2 hours, the polymer film became so rigid that any attempt to immerse a substrate simply led to the formation of a hole in the layer. For this reason, deposition was started after allowing stabilisation of the floating layer for around 15 minutes. For the first few cycles, the deposition mode was Z-type but then changed to Y-type with a transfer ratio of 0.95 ± 0.03. A dipping record at 17 mN m^{-1} is shown in Figure 5.3. At surface pressures higher than 17 mN m^{-1}, the polymer layer became too rigid to deposit.

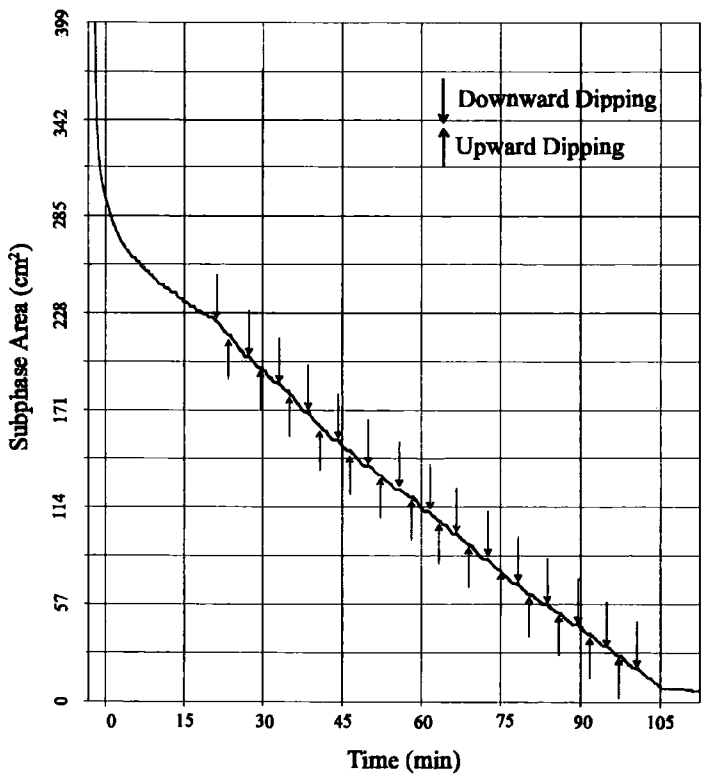

Figure 5.3 Surface area versus time chart during the LB deposition of MEH-PPV.

5.2.3 LB film Characterisation

UV-Vis. Absorption spectroscopy

Figure 5.4 shows the UV-Vis. absorption spectra of MEH-PPV LB films of different thicknesses deposited onto quartz. The spectra have main peaks at 360 nm, 400 nm and 500 nm. This spectral shape is somewhat different to that of MEH-PPV spun films which have a broad absorption band at 500 nm and a small peak at 360 nm [5]. The absorption spectrum of the MEH-PPV spun film is dependent on the concentration of the polymer solution and the choice of solvent. These factors affect the degree of interchain interaction and aggregation [5]. The absorption peak at 500 nm is attributed to the π-π^* electronic transition [6]. A plot of the absorption intensity at 500 nm versus the number of LB layers is inset in Figure 5.4. The approximately linear dependence suggests reproducible LB deposition.

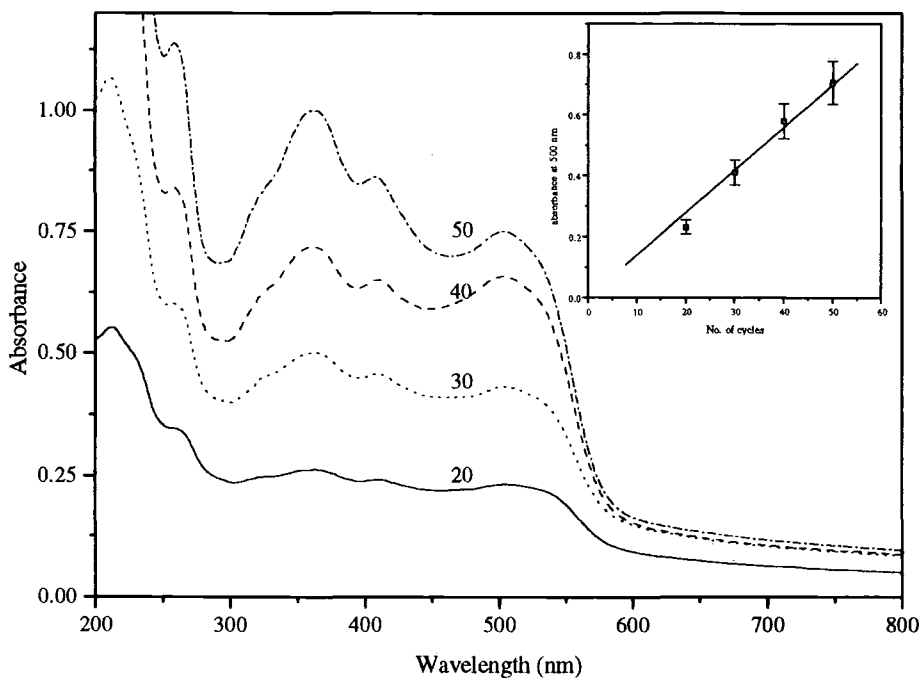

Figure 5.4 UV-Vis. spectra of MEH-PPV LB films (20, 30, 40, 50 cycles). The linear dependence of the absorption at 500 nm on the number of dipping cycles is shown inset.

Film Thickness Measurement

LB films with different thicknesses (40, 55, 70, 80 cycles) were deposited and the film thicknesses were measured using a stylus profilometer. A plot of thickness versus the number of LB layers is shown in Figure 5.5. The data points lie on a straight line, again confirming the reproducible nature of monolayer transfer onto the substrate. The average thickness of one LB layer of MEH-PPV is 2.3 ± 0.2 nm, which is greater than the longest dimension of the molecule, Figure 5.1. This result suggests that more than one layer was deposited onto the substrate during each dipping stroke.

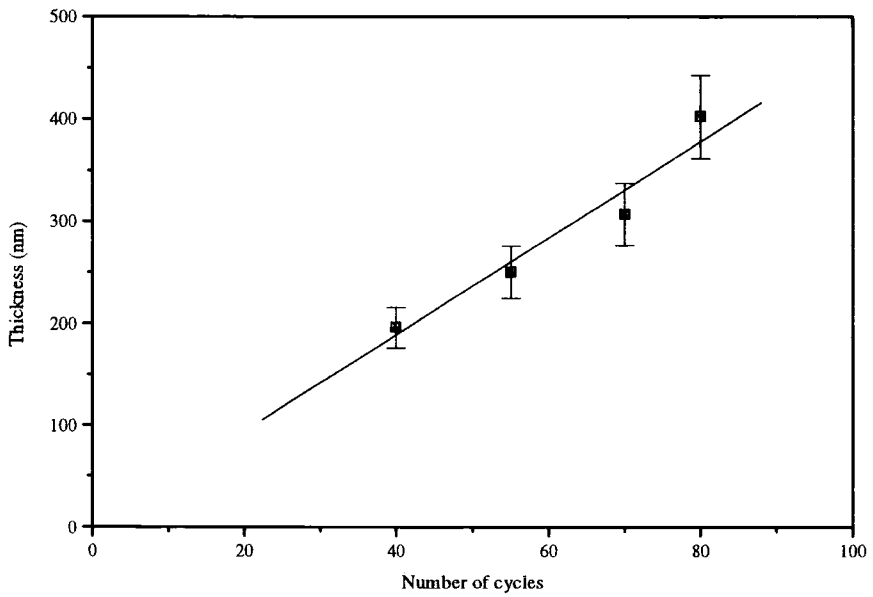

Figure 5.5 The thickness of MEH-PPV LB films with different numbers of layers.

The error in the film thickness (evaluated for ~ 10 measurements from different samples with the same number of deposition cycles) increases with increasing number of dipping cycles. The origin of this variation may be ascribed to the uneven packing of the collapsed layer as shown in Figure 5.2. The floating layer is not a perfect bilayer configuration (some parts remain as a monolayer). This can be judged by the area per repeat unit of the mulilayer which is not exactly one half of that

deduced from the 'condensed' phase. Films deposited from this floating layer would result in an uneven LB film thickness.

5.3. Current-Voltage Characteristics

MEH-PPV LB films with different thickness (40, 55 and 70 cycles) were deposited onto ITO glass and a metal top electrode (Al) was then evaporated on to the polymer film. The film thicknesses were 196 nm, 259 nm and 308 nm for 40, 50 and 70 LB cycles, respectively. In forward bias, the ITO electrode was the anode. The current (I) against voltage (V) characteristics of these devices are shown in Figure 5.6.

For a constant forward voltage, the device currents decrease as the LB film thickness is increased, indicating bulk controlled current flow through the devices. Reducing the film thickness also lowers the device operating voltage. In the following section, the I-V data shown in Figure 5.6 are fitted with several physical models to elucidate the conduction mechanisms in the LEDs.

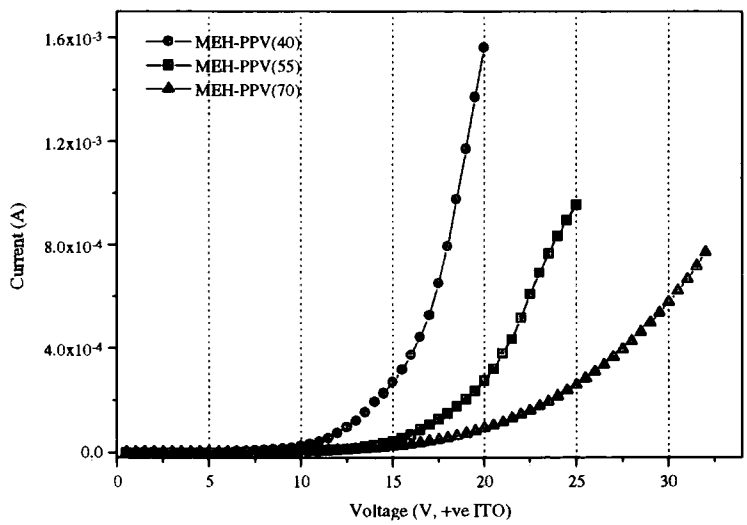

Figure 5.6 Thickness dependence of the I-V characteristics for ITO/MEH-PPV (40, 55, 70 cycles)/Al devices.

5.3.1 Schottky Barrier

The current (log) versus voltage (linear) plot for Schottky analysis is shown in Figure 5.7. Typical I-V characteristics of devices with a Schottky barrier at the interface with an electrode show an exponential current rise (Shockley formula, Equation 3.1) of 5-6 orders of magnitude within 1 V (normally between 1 and 2 V). However, the currents between 1 and 2 V of our devices only increase by approximately one order of magnitude. Also, the Shockley formula shows that the I-V characteristics are independent of the thickness of the polymer layer. Karg et al. [7] demonstrated that the I-V characteristics of PPV devices with different thickness (200 and 800 nm) were identical and independent of the film thickness. In contrast, the currents in our devices are dependent on film thickness, as shown in Figure 5.6.

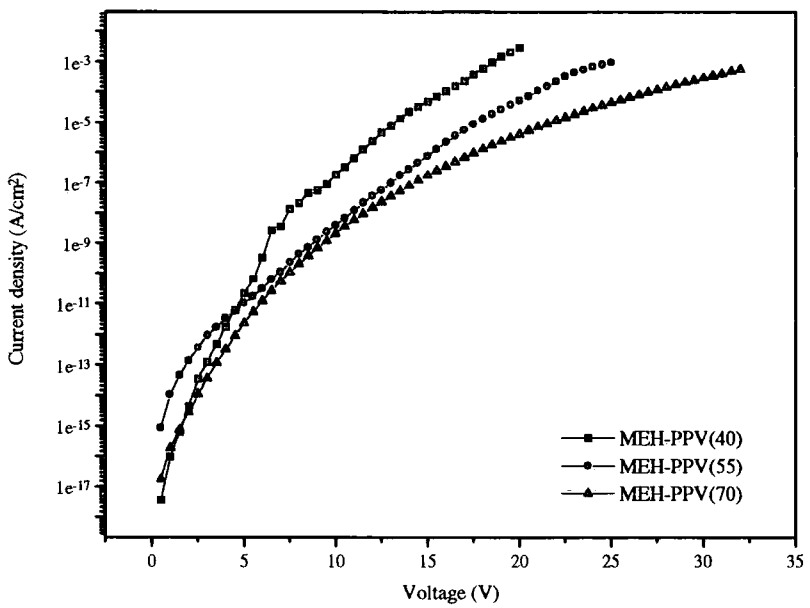

Figure 5.7 Current (log) versus voltage (linear) plot for ITO/MEH-PPV(40, 55, 70 cycles)/Al devices

The Cole-Cole plots obtained from a.c. impedance spectroscopy experiments can provide an insight into the electrical equivalent circuit of a device. Figure 5.8

shows the forward bias impedance (Z) results in the form of Cole-Cole plots (Im (Z) versus Re (Z)). In the graph, the frequency increases from right to left (5 Hz to 13 MHz) around the semicircles.

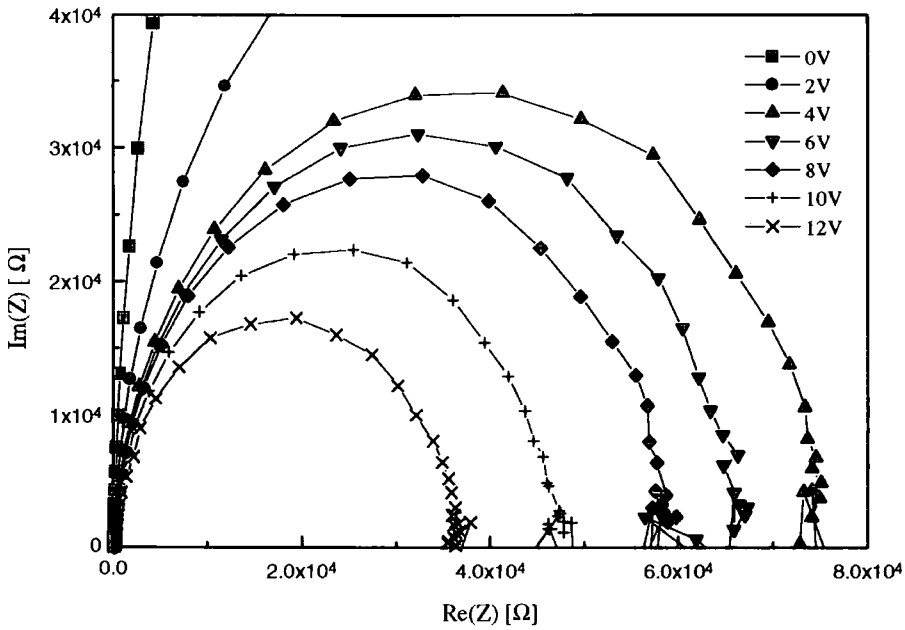

Figure 5.8 Cole-Cole plots for an ITO/MEH-PPV(55 cycles)/Al sample at various forward bias voltages.

The data exhibit a series of semicircles, the diameters of which correspond to resistances. The resistance decreases with increasing forward bias. Close inspection (not evident from the scale of the figure) reveals that the high frequency intercept of the semicircle with the abscissa is about 100 Ω for all values of the applied forward voltage. This is the result of a small series resistance R_s associated with the ITO contact and lead resistances.

This Cole-Cole plot is similar to those reported for other single layer LEDs based on spun MEH-PPV [8], PPV [9,10] and poly(6-hexyl-2,5-pyridinediyl) [11]. Our LEDs can be modelled by an equivalent circuit consisting of a parallel resistance

and capacitance combination (R_1, C_1) in series with a resistance R_s as shown in Figure 5.9.

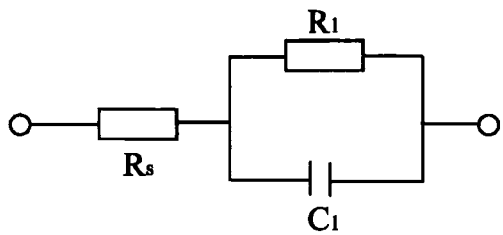

Figure 5.9 Equivalent circuit of ITO/MEH-PPV(LB)/Al device.

Karg et al. [12] and Sherbel et al. [13] reported two semicircles with 'thick' PPV devices which could be modelled by two parallel resistor-capacitor networks connected in series: one resulting from the Schottky barrier and the other from the nondepleted bulk polymer. The impedance of the depletion region rapidly decreased with increasing forward bias. However, the response of the bulk region was almost unaffected by bias. This showed that most of the electric fields were consumed within the depletion region governing the I-V characteristics of the devices.

However, the single semicircle of our device, which diameter decreases with applied bias, suggests that a depletion layer is absent and that the applied voltage is dropped across the bulk.

5.3.2 Space Charge Limited Current

Figure 5.10 shows the I-V characteristics, on a log-log scale, for the MEH-PPV devices whose electrical characteristics have previously been shown in Figure 5.6.

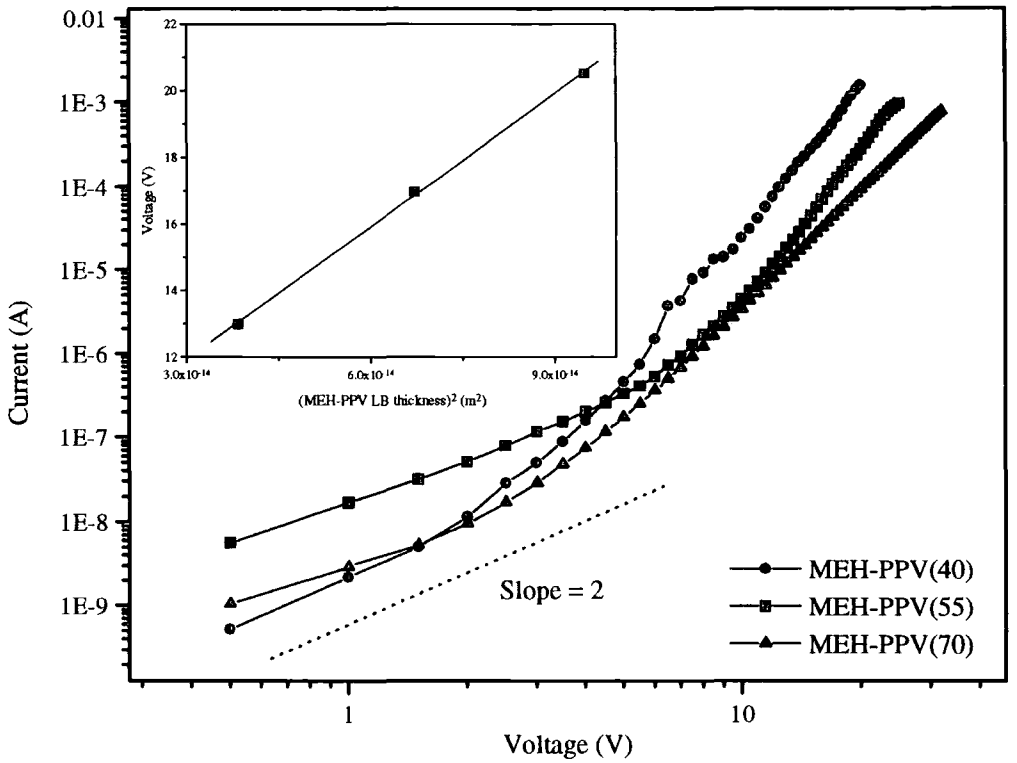

Figure 5.10 Log-log graph showing the current against voltage characteristics for ITO/MEH-PPV(40,55,70 cycles)/Al devices. The inset shows the dependence of voltage on the square of the layer thickness at 1 mA.

Two regions can be seen in the figure: a low applied bias region with a small slope (prior to the onset of EL) and a high applied bias region with a larger slope (here, significant EL was measured). These are typical characteristics in organic LED devices [14]. The slope changes from 1.8~2.6 in the low applied voltage regime (SCL current, Equation 3.11) to 4.6~5.7 in the high applied voltage regime (TCL current, Equation 3.12). The different regions in the I-V characteristics may be explained in terms of either a change in the field dependence of the mobility [15] and/or the movement of the Fermi level through different trap distributions in the polymer energy gap [16]. Stallinga et al. [17] and Campbell et al. [18] showed the existence of traps near the HOMO energy level in a spun MEH-PPV device. For the TCL model,

$J_{TCL} \propto \frac{V^{m+1}}{d^{2m+1}}$, to be valid in high voltage region, the voltage should be roughly proportional to the square of the film thickness at a constant current. The inset in Figure 5.10 shows the linear dependence of voltage on the square of film thickness at a current of 1 mA within the TCL regime.

The I-V characteristics of an ITO/MEH-PPV(55)/Al device were recorded over the temperature range from 80 K to 290 K and the data, in the form of a log-log plot, are shown in Figure 5.11. The results also show two distinct regions. The slopes of the curves at different temperatures are shown in Table 2.

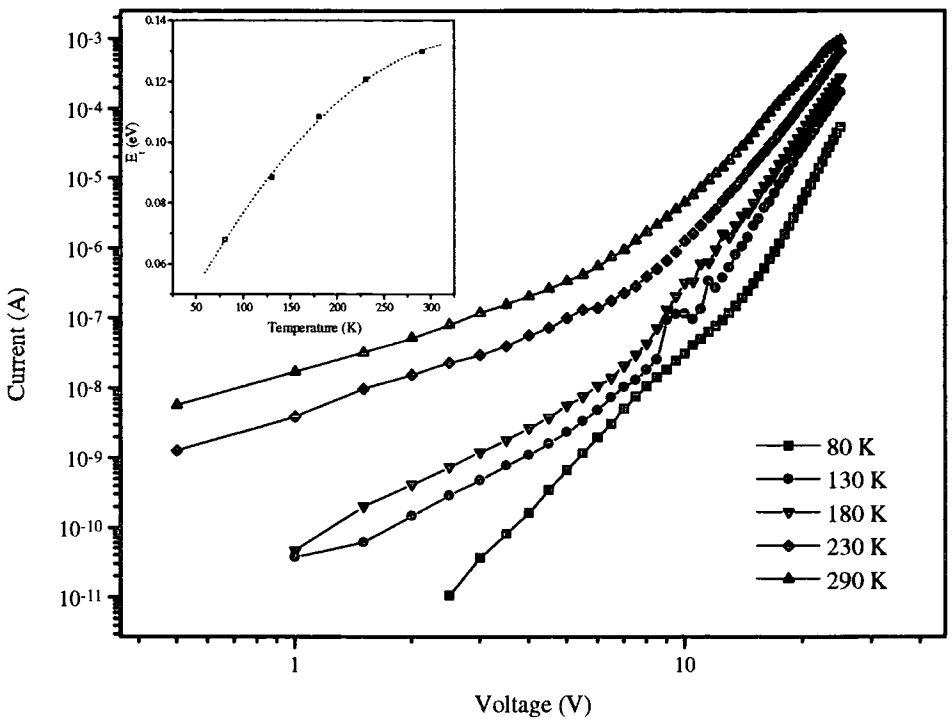

Figure 5.11 Variation of the I-V characteristics with temperature for an ITO/MEH-PPV(55 cycles)/Al sample. Inset: Variation of the trap distribution characteristic energy E_t.

In the low voltage region, the slope increases from 1.8 to 5.7 on cooling from 290 K to 80 K and in the high voltage region, from 6.2 to 10.7 within the same

temperature range. In the low voltage region where no light emission can be measured, the increase of I with V is relatively small. However, the current in the high voltage region increases much more rapidly with applied bias. As the devices are cooled, the rate of change of I with V increases, whilst the current flow for a given voltage decreases over the whole bias range. For example, the current at 3 V decreases by nearly four orders of magnitude. However, the difference becomes small at high voltage such that there is one order of magnitude difference in current at 25 V.

Temperature (K)	Slope (m + 1)	
	Low Voltage	High Voltage (E_t (eV))
80	5.7	10.7 (0.06)
130	3.4	8.9 (0.08)
180	2.9	8.0 (0.11)
230	1.9	7.1 (0.12)
290	1.8	6.2 (0.13)

Table 2. Slopes of curves in Figure 5.11 in the low and high voltage region. The variable, m, is the power law exponent in Equation 3.12 and E_t is the characteristic energy of the trap distribution.

Within the TCL current region, the value of E_t, the characteristic energy of trap distribution, is related to temperature and the power law exponent, m, by the equation, $m = \frac{E_t}{kT}$ (Equation 3.13). The inset in Figure 5.11 shows the variation of E_t (within the TCL regime) with temperature. The calculated value of E_t increases and becomes saturated with increasing temperature, 0.06 eV at 80 K and 0.13 eV at 290 K. As the parameter E_t is directly related to the energy location of the trap distribution in the forbidden energy gap, the lower value (i.e at 80 K) indicates traps distributed closer to the HOMO level of the MEH-PPV.

5.3.3 Fowler-Nordheim Tunnelling

Fits to the Fowler-Nordheim (F-N) model for the I-V characteristics of Figure 5.6 are shown in Figure 5.12. For high electric field, all three curves lie on top of each other. The I-V characteristics are controlled by majority carriers, which are determined by the smaller of the two triangular tunnelling barriers at the electrodes. In ITO/MEH-PPV/Al devices, the barrier to holes (0.2 eV) is much smaller than that to electrons (1.5 eV) [22].

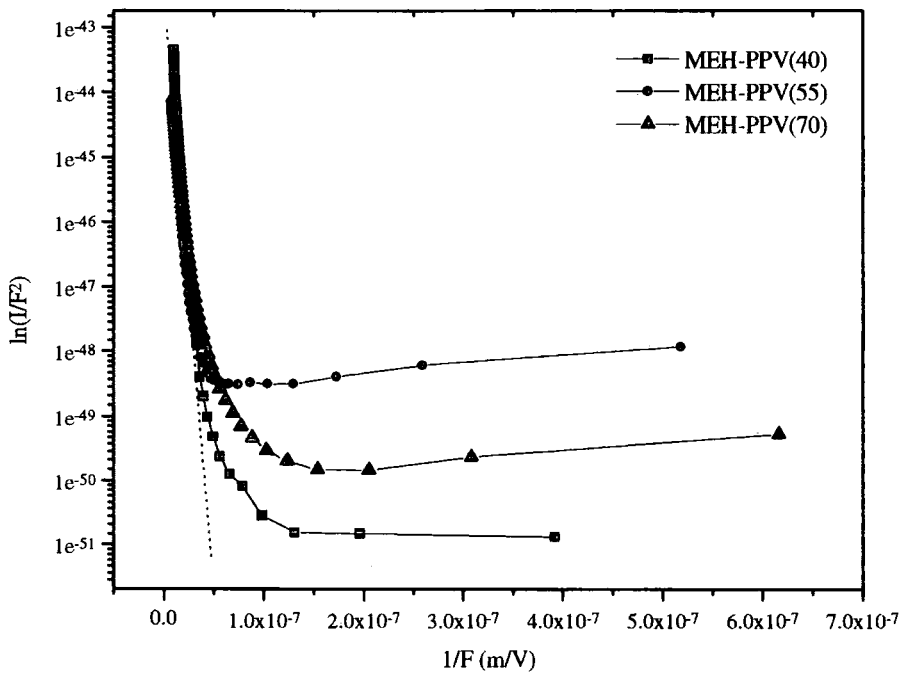

Figure 5.12 F-N plot for MEH-PPV devices with F-N fitting line.

The high field data give a barrier for holes at the ITO/MEH-PPV interface by using Equation 3.9, slope $k = \frac{4\sqrt{2qm^*}}{3h}\phi_b^{3/2}$, with a free electron mass (m^*), 9.1×10^{-31} kg: 0.4 eV, 0.33 eV and 0.25 eV for the devices with 40, 55 and 70 LB layers, respectively. The tunnelling barrier height decreases with increasing film thickness. This barrier height is comparable with other devices based on spin-coated MEH-PPV

with various cathode electrodes, i.e. 0.2~0.3 eV [22], and 0.34 eV [23]. The theoretical value of the hole barrier is likely to change between samples depending on the Fermi level of the ITO which can vary significantly depending on preparation procedure [24,25] and the HOMO level of the MEH-PPV (4.9 eV [22], 5.3 eV [15,26]).

The F-N model (Equation 3.8) cannot account for the temperature dependence and the thickness dependence of the current. The experimental data should coincide regardless of film thickness and temperature. Figure 5.12 shows that F-N plots for devices with different thicknesses coincide at high fields but deviate from the fitting line at low fields. The deviation from linearity at lower fields has been explained in terms of a thermionic emission contribution to the device current [27].

F-N plots of the I-V characteristics of the ITO/MEH-PPV(55)/Al device at different temperatures are shown in Figure 5.13 and the variation of the calculated F-N barrier with temperature insets. It is found that the barrier height varies with temperature, changing from 0.39 eV at 290 K to 0.47 eV at 80 K. The apparent increase of the barrier height at low temperature indicates that tunnelling is not actually the current limiting process. Lupton and Samuel [28] reported that the deviation of barrier height with temperature is due to thermionic emission, especially within the temperature region where the variation is strong, here 180 – 300 K.

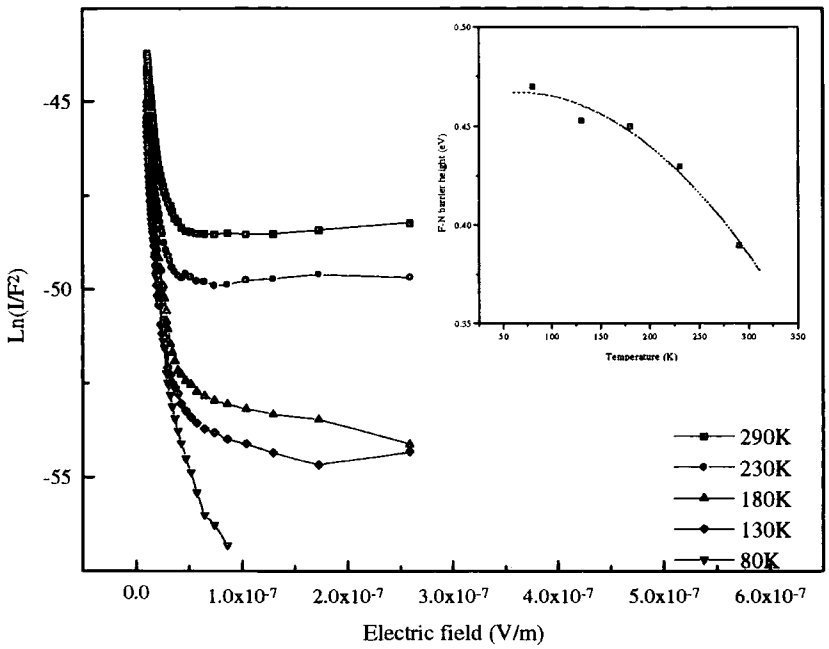

Figure 5.13 F-N plots for an ITO/MEH-PPV(55 cycles)/Al device at various temperatures. Inset shows the variation of the F-N barrier height with temperature.

In conclusion, the space charge limited current model with a trap distribution seems to provide the best description of the conduction mechanism of the devices based on MEH-PPV LB films over various thickness and temperature ranges.

5.4 EL Characteristics

5.4.1 Light Output

The current and light output versus voltage curves for an ITO/MEH-PPV (50 cycles, 210 nm)/Al device are shown in Figure 5.14 for both forward (+ve ITO) and reverse bias. The inset shows the same data on a log (current, light output)-linear (voltage) scale.

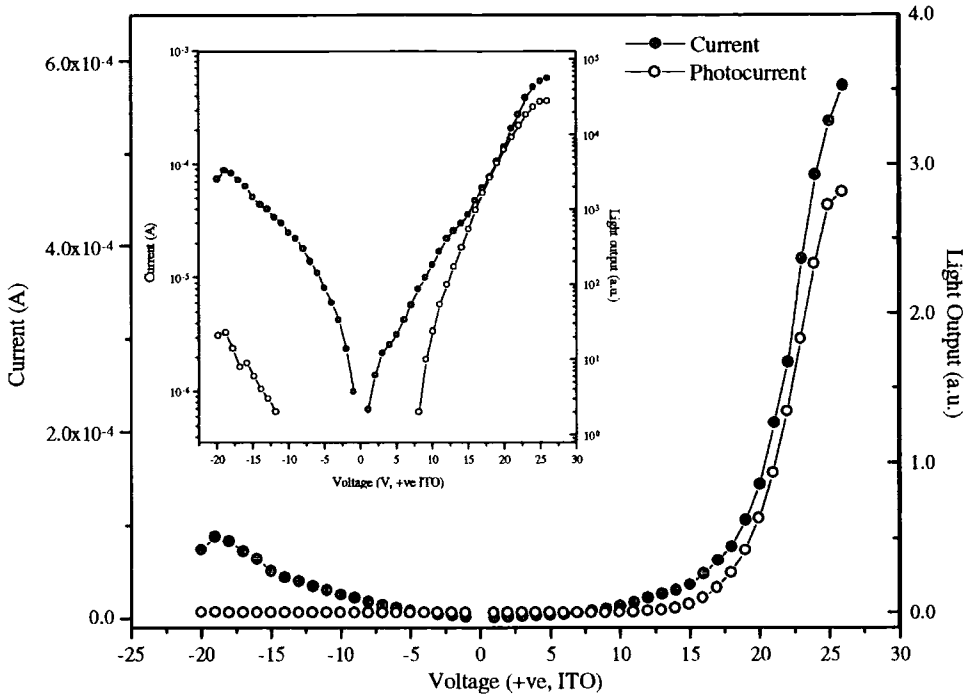

Figure 5.14 Current and light output versus voltage characteristics for an ITO/MEH-PPV(50 cycles)/Al device. The inset shows the logarithm (current, light output) versus linear (Voltage) characteristics.

Below 20 V, the devices display practically no rectifying behaviour. Above 20 V, the current increases dramatically under forward bias whilst it becomes saturated and decreases at higher voltages under reverse bias.

When a forward bias was applied to these devices, orange light emitted from the device could be seen in a dark room. The light output occurred above the turn-on voltage (8 V) under forward bias. However, a very faint emission was also seen at high voltages under reverse bias. The turn-on voltage (onset of light output) is related to the injection of electrons at the polymer/Al electrode interface. The turn-on voltage under forward bias is 4 V lower than that in reverse bias. This phenomenon confirms that in forward bias the electron injection from the Al to the polymer LUMO level is much easier than from the ITO to the polymer LUMO level under reverse bias. This can be explained by the energy diagram in Figure 5.15 which shows that the energy

barrier for electron injection is 1.5 eV under forward bias and 1.9 eV under reverse bias.

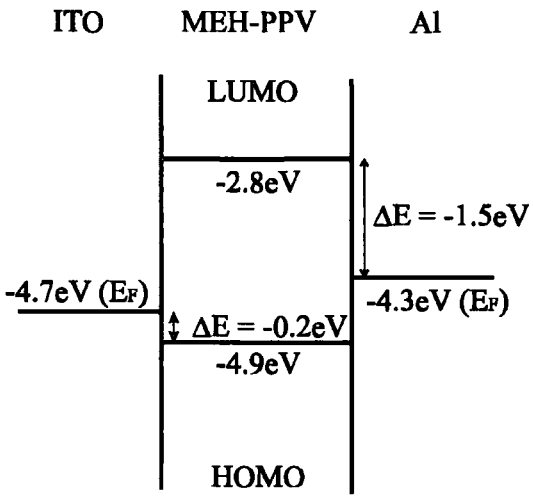

Figure 5.15 Potential energy diagram of an ITO/MEH-PPV/Al device. The HOMO and LUMO levels of MEH-PPV are obtained from reference [23].

Figure 5.16 shows plots of light output and external quantum efficiency against current density for the same device. The external quantum efficiency is 8×10^{-3} % at a current density of 13 mA cm^{-2}. This efficiency is comparable to that of single-layer PPV LEDs with an Al contact [7,29]. The relationship between the light output and current density can be described by a power law strongly dependent on the charge injection conditions (3.4 below 1×10^{-3} A cm^{-2} and 1.35 at higher current densities). The change of power at a certain current density has also been reported with several device structures by other workers [30].

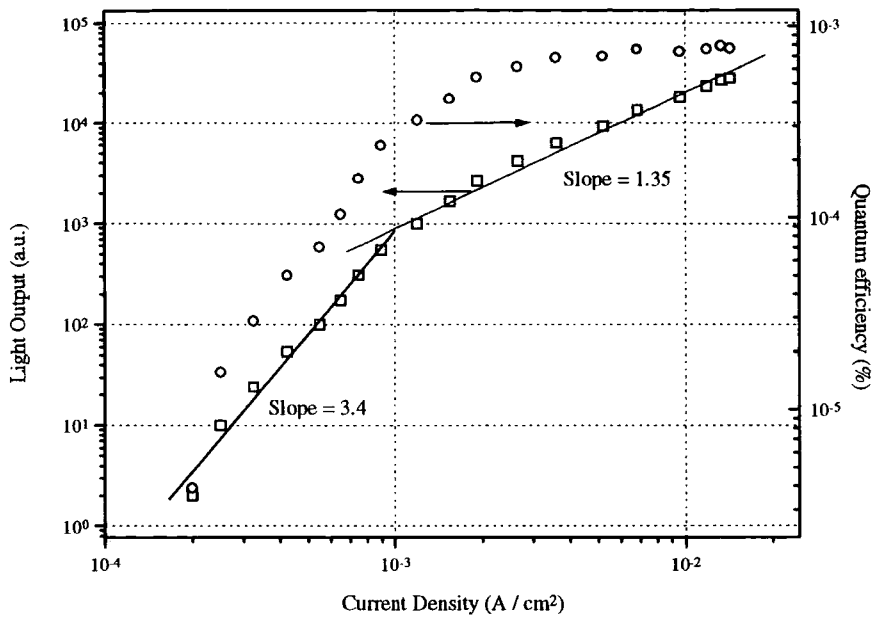

Figure 5.16 Light output and external quantum efficiency versus current density of the ITO/MEH-PPV(50 cycles)/Al device.

5.4.2 Ca Top Electrode

To investigate the effect of changing the barrier height for electron injection, the Al top electrode was replaced by Ca. To prevent the atmospheric oxidation of the Ca, Al (300 nm) was evaporated on top of the Ca (50 nm) without breaking the vacuum. In order to eliminate effects due to different film thicknesses, Al and Ca/Al devices were fabricated using the same MEH-PPV film. The current-voltage characteristics are compared in Figure 5.17.

Over the entire voltage range the currents for the Ca devices are lower than those for the Al devices. The lower current of the Ca devices was surprising because of the lower work function of Ca (2.9 eV) compared to Al (4.3 eV). Karg et al. [7] have reported ITO/PPV/Metal (Ca, Al) devices showing a lower current density in the Ca device. The lower currents in the Ca device might be explained by a high Schottky

barrier for majority carriers (holes) formed between PPV and the Ca electrode as shown in Figure 3.10.

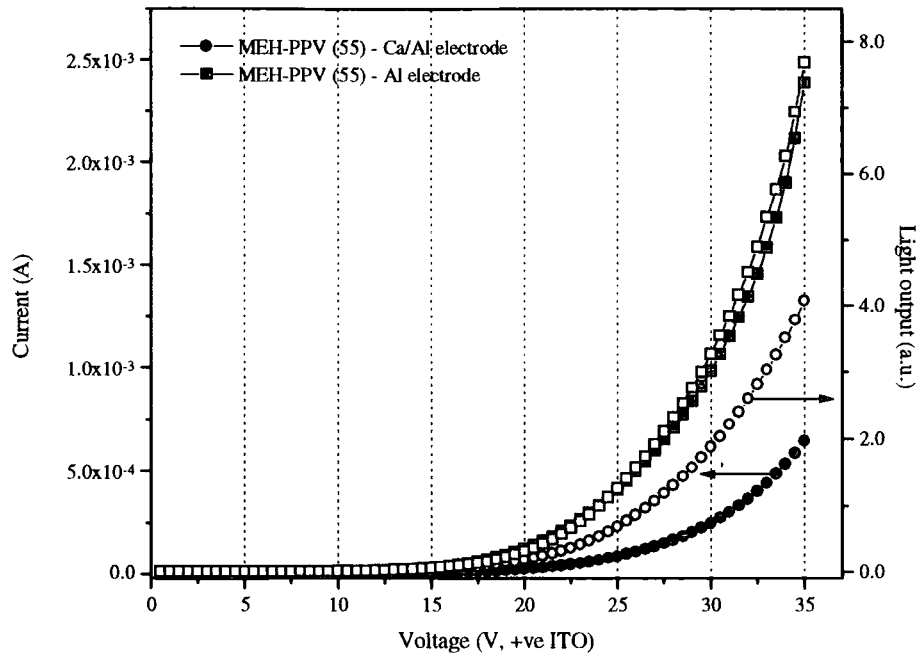

Figure 5.17 Comparison of the I-V and light output-V characteristics of the MEH-PPV(55 cycles) devices with Al and Ca/Al top electrodes. (open symbols: light output, full symbols: current)

However, our a.c. impedance spectroscopy results show that there is no depletion region within the MEH-PPV layer. The above explanation based on a Schottky barrier is therefore not appropriate for our devices. An interfacial oxide layer beneath the Ca electrode is likely to form during thermal deposition of the Ca at a vacuum level (10^{-6} mbar) leading to a more complicated interface structure.

By using Ultraviolet Photoemission Spectroscopy (UPS), Kiy et al. [31] reported that low work function metals such as Mg and Ca were oxidised in an ultra high vacuum (UHV) environment of 7×10^{-10} mbar. Furthermore, Birgerson et al. [32] showed that interactions between the Ca and polymer resulted in a 2 to 3 nm

thickness of interfacial oxide layer beneath the cathode electrode. An insulating layer such as CaO is found to improve the electron injection [33] and block the hole carriers resulting in more balanced carrier transport. The effect of an insulating layer will be further discussed in Chapter 6. The quantum efficiencies of our devices were 1.2×10^{-3} % for the Ca electrode device and 6×10^{-4} % for the structure with an Al electrode.

5.4.3 PL and EL Spectra

The electroluminescence (EL) and photoluminescence (PL) spectra for the MEH-PPV devices are shown in Figure 5.18. The EL spectrum is similar to the PL spectrum (λ_{EX}: 420 nm) indicating that the same excited state (singlet exciton) can be produced either by recombination of the injected electrons and holes or by photoexcitation. The peak of EL (590 nm) is slightly blue-shifted compared to the peak of PL (598 nm). There is a shoulder at around 630 nm in both the PL and EL spectra.

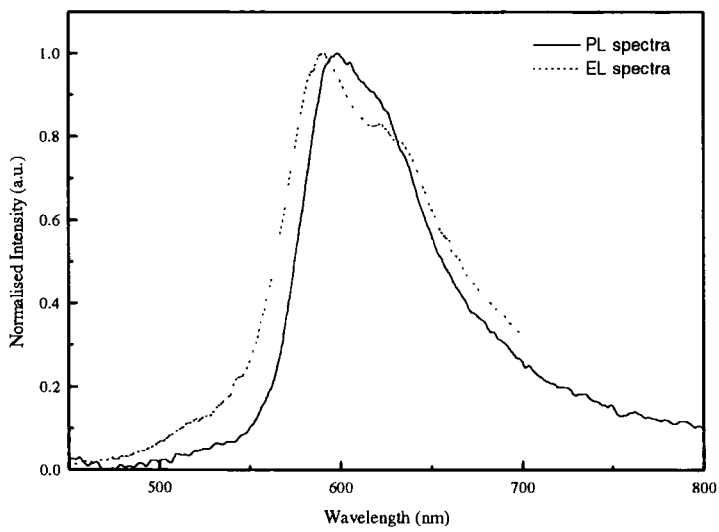

Figure 5.18 Normalised PL and EL spectra for ITO/MEH-PPV(50 cycles)/Al device.

The full width at half maximum (FWHM) of EL, 103 nm, is larger than that of PL, 82 nm. The emission zone is near the Al electrode because of low electron mobility and a higher electron injection barrier. At the polymer/Al interface, Al atoms can migrate into the polymer and react with the carbon in the vinylene groups resulting in a shorter conjugation length of the polymer [34]. This could be an explanation for the blue shift of the EL spectra. Joule heating during operation is a further effect. This could also induce deformation and reduce the effective conjugation length [35,36].

5.5 Summary

Y-type LB films of MEH-PPV were deposited at a surface pressure of 17 mN m^{-1} with a transfer ratio of 0.95 ± 0.03. The linear dependence of absorption intensity and thickness with the number of LB cycles confirmed the reproducibility of LB deposition.

A.c. impedance spectroscopy showed that no depletion region exists in devices composed of MEH-PPV LB films suggesting that the Schottky barrier model is not applicable. The increase in the hole barrier height derived from the F-N tunnelling model at low temperature range indicates that this model does not fully explain the measured I versus V characteristics either. However, the I-V curves could be modelled by SCL current theory with a trap distribution, over a wide temperature and thickness range.

The LB devices produced an orange light output under forward bias (+ve, ITO). The external quantum efficiency was in the range of 10^{-4} %. The similarity of PL and EL spectra suggested that the same excited state (singlet exciton) was

responsible for emission in both cases. A device with a Ca top electrode showed a lower current and a higher external quantum efficiency than that of the device with a Al top electrode.

References

1. A. Chowdhury, J. Chowdhury, P. Pal and A.J. Pal, *Solid State Communications*, **107**, 1998, 725.

2. T. Ostergard, J. Paloheimo, A.J. Pal and H. Stubb, *Synth. Met.*, **88**, 1997, 171.

3. K. Aramata, M. Kamachi, M. Takahashi and A. Yamagishi, *Langmuir*, **13**, 1997, 5161.

4. L.T.M. Saraga, *J. Chem. Phys.*, **52**, 1955, 181.

5. T.Q. Nguyen, V. Doan and B.J. Schwartz, *J. Chem. Phys.*, **110**, 1999, 4068.

6. C.L. Gettinger and A.J. Heeger, *J. Mol. Cryst. Liq. Cryst.*, **256**, 1994, 507.

7. S. Karg, M. Meier and W. Riess, *J. Appl. Phys.*, **82**, 1997, 1951.

8. S.H. Kim, K.H. Choi, H.M. Lee, D.H. Hwang, L.M. Do, H.Y. Chu and T.H. Zyung, *J. Appl. Phys.*, **87**, 2000, 882.

9. A.J. Campbell, D.D.C. Bradley and D.G. Lidzey, *J. Appl. Phys.*, **82**, 1997, 6326.

10. W. Bijnens, J. Manca, T.D. Wu, M. D'Olieslaeger, D. Vanderzande, J. Gelan, W. de Ceuninck, J. de Schepper and L.M. Stals, *Synth. Met.*, **83**, 1996, 261.

11. M.C. Petty, C. Pearson, A.P. Monkman, R. Casalini, S. Capaccioli and J. Nagel, *Colloid. Surface A*, **171**, 2000, 159.

12. S. Karg, W. Riess, B. Dyakonov and M. Schwoerer, *Synth. Met.*, **54**, 1993, 427.

13. J. Scherbel, P.H. Nguyen, G. Paasch, W. Brutting and M. Schwoerer, *J. Appl. Phys.*, **83**, 1998, 5045.

14. P.E. Burrows, Z. Shen, V. Bulovic, D.M. McCarty, S.R. Forrest, J.A. Cronin and M.E. Thompson, *J. Appl. Phys.*, **79**, 1996, 7991.

15. L. Bozano, S.A. Carter, J.C. Scott, G.G. Malliaras and P.J. Brock, *App. Phys. Lett.*, **74**, 1999, 1132.

16. A.J. Campbell, D.D.C. Bradley and D.G. Lidzey, *J. Appl. Phys.*, **82**, 1997, 6326.

17. P. Stallinga, H.L. Gomes, H. Rost, A.B. Holmes, M.G. Harrison, R.H. Friend, F. Biscarini, C. Taliani, G.W. Jones and D.M. Taylor, *Physica B*, **273-274**, 1999, 923.

18. I.H. Campbell, D.L. Smith and J.P. Ferraris, *Appl. Phys. Lett.*, **66**, 1995, 3030.

19. L. Bozano, S.A. Carter, J.C. Scott, G.G. Malliaras and P.J. Brock, *Appl. Phys. Lett.*, **74**, 1999, 1132.

20. N.E. Agbor, M.C. Petty, A.P. Monkman and M. Harris, *Synth. Met.*, **55-57**, 1993, 3789.

21. P. Gattinger, H. Rengel, D. Neher, M. Gurka, M. Buck, A.M.V. de Craats and J.M. Warman, *J. Phys. Chem. B*, **103**, 1999, 3179.

22. A.J. Heeger, I.D. Parker and Y. Yang, *Synth. Met.*, **11**, 1994, 23.

23. P.S. Davids, S.M. Kogan, I.D. Parker and D.L. Smith, *Appl. Phys. Lett.*, **69**, 1996, 2270.

24. J.S. Kim, M. Granstrom, R.H. Friend, N. Johansson, W.R. Salaneck, R. Daik, W.J. Feast and F. Cacialli, *J. Appl. Phys.*, **84**, 1998, 6859.

25. L. Chkoda, C. Heske, M. Sokolowski, E. Umbach, F. Steuber, J. Staudigel, M. Stossel and J. Simmerer, *Synth. Met.*, **111-112**, 2000, 315.

26. I.H. Campbell, P.S. Davids, D.L. Smith, N.N. Barashkov and J.P. Ferraris, *Appl. Phys. Lett.*, **72**, 1998, 1863.

27. S. Daz, A. Chowdhury, S. Roy and A.J. Pal, *Phys. Sstat. Sol.*, **178**, 2000, 811.

28. J.M. Lupton and I.D.W. Samuel, *J. Phys. D: Appl. Phys.*, **32**, 1999, 2973.

29. S. Dailey, M. Halim, E. Rebourt, L.E. Horsburgh, I.D.W. Samuel and A.P. Monkman, *J. Phys: Condens. Matter*, **10**, 1998, 5171.

30. S. Miyata and S. Nalwa, *Organic Electroluminescent Materials and Devices*, Gordon and Breach Publishers, Netherlands, 1997, 61.

31. M. Kiy, I. Gamboni, I. Biaggio and P. Gűnter, *Proc. SPIE Organic Light-Emitting Materials and Device*, **San Diego**, 2000, 290.

32. J. Birgerson, M. Fahlman, P. Broms and W.R. Salaneck, *Synth. Met.*, **80**, 1996, 125.

33. M. Meier, M. Colle, S. Karg, E. Buchwald, J. Gmeiner, W. Riess and M. Schwoerer, *Mol. Cryst. Liq. Cryst.*, **283**, 1996, 197.

34. T.W. Lee and O.O. Park, *Adv. Mat.*, **12**, 2000, 801.

35. S.D. Jung, D.H. Hwang, T.H. Zyung, W.H. Kim, K.G. Chittibabu and S.K. Tripathy, *Synth. Met.*, **98**, 1998, 107.

36. K. Yoshino, S. Nakajima, D.H. Park and R.I. Sugimoto, *Jpn. J. Appl. Phys.*, **27**, 1988, L716.

Chapter 6.

Improvements in MEH-PPV LB Film Device Performance

6.1 Introduction

Following the reports on organic LEDs with conjugated polymers such as poly (*p*-phenylenevinylene), many attempts have been made to improve the external quantum efficiency and the lifetime. In this chapter, we record attempts to increase the performance of LEDs based on MEH-PPV LB films by several means. The incorporation of insulating arachidic acid (AA) LB layers is described in Section 6.2. Section 6.3 discusses the use of an electron transport polymer poly(6-hexylpyridine-2,5-diyl) (PHPY) between the emissive layer and the Al top electrode. The effect of annealing the MEH-PPV LB films on the device lifetime is also detailed in Section 6.3.

6.2 Incorporation of Insulating LB Layers

6.2.1 Background

One approach to increase the efficiency and brightness of organic LEDs is to modify the electrodes. By inserting an insulating layer such as CaO [1], SiO_2 [2] or LiF [3] beneath the cathode electrode, the electron injection is found to be enhanced. The anode electrode, usually indium-tin-oxide (ITO), can be treated (e.g. with an oxygen plasma [4]) to reduce the turn-on voltage. ITO/polyaniline [5] and ITO/poly(3,4-ethylene dioxythiophene) bilayer anodes [6] have also been shown to produce improved device

performance. Here, we describe attempts to insert arachidic acid (AA) layers between the electrodes and the MEH-PPV.

6.2.2 Device Structures

Arachidic acid (AA) was purchased from Sigma (Sigma grade). The AA monolayer was deposited at a surface pressure of 30 mN m^{-1} onto ITO patterned glass and MEH-PPV LB films, with a transfer ratio of 0.85 (averaged for both the up and down strokes).

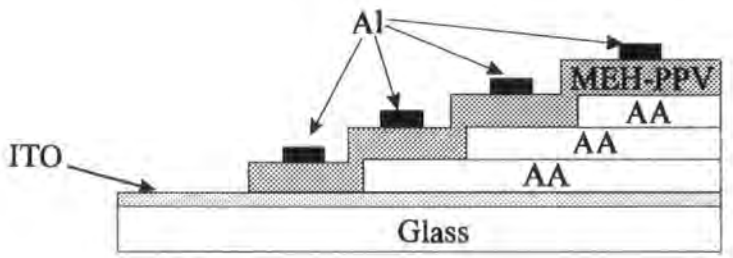

(a)

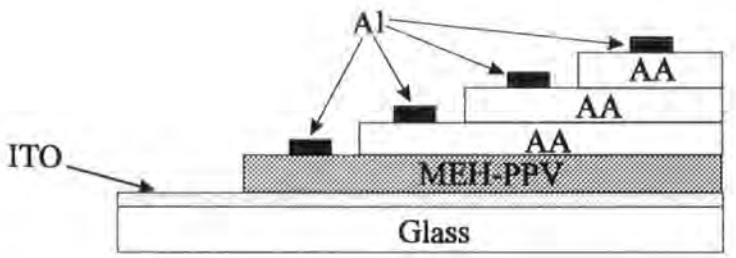

(b)

Figure 6.1 Schematic diagrams of light emitting device structures used in this work: (a) ITO/AA/MEH-PPV/Al device; (b) ITO/MEH-PPV/AA/Al device.

Various numbers of AA LB layers were deposited beneath (Figure 6.1(a)) and above (Figure 6.1(b)) the MEH-PPV LB film. Before evaporating the cathode electrode, all the samples were placed for 12 hours in a high vacuum of approximately 10^{-6} mbar to remove excess moisture.

6.2.3 Device Characteristics

ITO/AA/MEH-PPV/Al Devices

Figure 6.2(a) compares the current versus voltage behaviour for devices in which different numbers of AA layers were sandwiched between the ITO and the MEH-PPV layer (i.e. device structure as shown schematically in Figure 6.1(a)). In Figure 6.2(b), the light output against applied voltage is plotted on a log-linear scale.

For the reference ITO/MEH-PPV/Al device, the work function of the ITO is reasonably well matched to the HOMO level of the MEH-PPV (assuming that the offset between the ITO Fermi level and the HOMO level of MEH-PPV is approximately 0.2 eV, from Figure 5.15). Therefore, holes (majority carriers) are relatively easily transported across this interface and dominate the I-V characteristics. In contrast, the light output from the LED device will be determined by the minority carrier injection at the MEH-PPV/Al interface. Figure 6.2 reveals that the effect of introducing the insulating AA layers between the ITO and the MEH-PPV is mainly to decrease the current at high biases and to increase the turn-on voltage for electroluminescence. The insertion of AA LB films therefore acts as a hole blocking layer. Part of the applied voltage is dropped across this insulating layer at high forward bias so that a lower electric field is applied to the MEH-PPV layer. Therefore, a greater applied voltage is needed to maintain the electron injection from the Al electrode to the MEH-PPV layer.

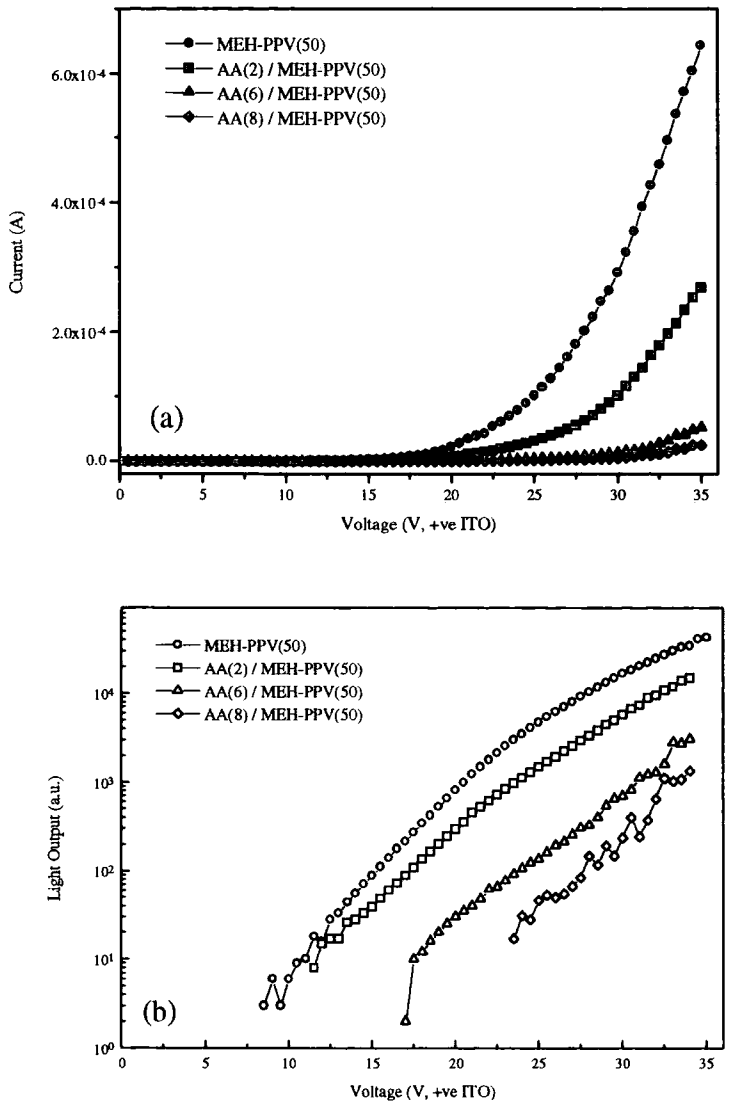

Figure 6.2 (a) I-V characteristics for ITO/AA(0, 2, 6, 8 cycles)/MEH-PPV(50 cycles)/Al devices containing different thicknesses of fatty acid. (b) The light output versus voltage curve on log-linear scale. The number of LB deposition cycles is shown for each device structure.

Figure 6.3 shows a plot of the light output versus current density for the devices whose I-V characteristics have been shown in Figure 6.2. All the data lie close to the same straight line indicating that no significant change in external quantum efficiency results from the incorporation of the AA film between the ITO cathode and the MEH-PPV layer. All the device quantum efficiencies were around 7×10^{-4} % at a current density of 10^{-3} A cm^{-2}. It should also be noted that the structures incorporating the AA layers between the

ITO and the MEH-PPV layer were electrically noisy in operation, giving a large scatter of data points.

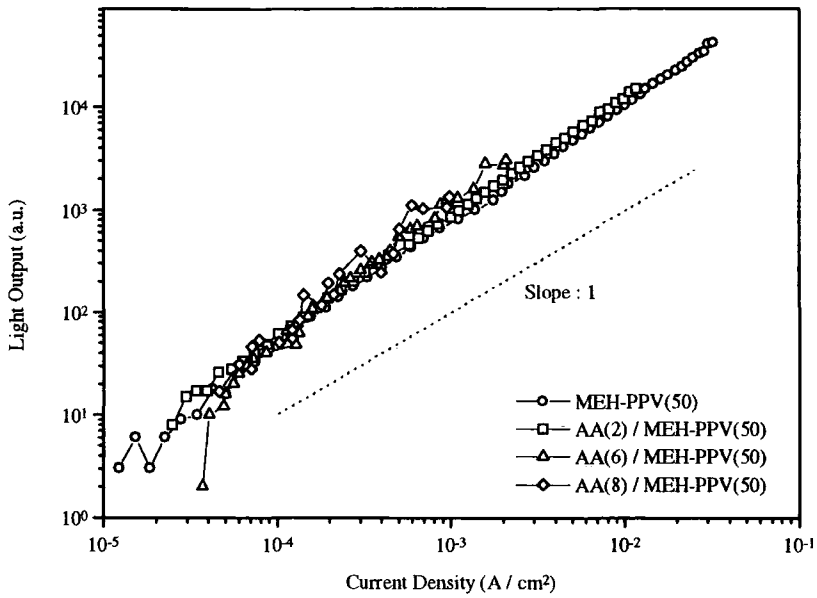

Figure 6.3 Log-log graph showing light output versus current density for ITO/AA(0, 2, 6, 8 cycles)/MEH-PPV(50 cycles)/Al devices.

ITO/MEH-PPV/AA/Al Devices

Figure 6.4(a) shows the current versus voltage for ITO/MEH-PPV/AA/Al structures with different numbers of fatty acid layers. A decrease in current with increasing AA thickness is evident at forward biases. This result is consistent with the data published by Kim et al. for ITO/spin-coated MEH-PPV/poly(methyl methacrylate) LB film/Al structures [7]. Here, insertion of the LB films resulted in a current decrease at all bias voltages. However, in our experiments the I-V characteristics were found to be very dependent on the AA film quality. In the case of a poor AA LB film (when no deposition was recorded during the downstrokes), the current increased with increasing AA film thickness. We have considered the possibility that this increase of current with the fatty acid film thickness may be the result of the removal of MEH-PPV during the AA LB

deposition. To investigate this possibility, we have monitored the optical absorption of an ITO/MEH-PPV structure as AA layers were progressively deposited on top. No evidence for the removal of the polymer was found.

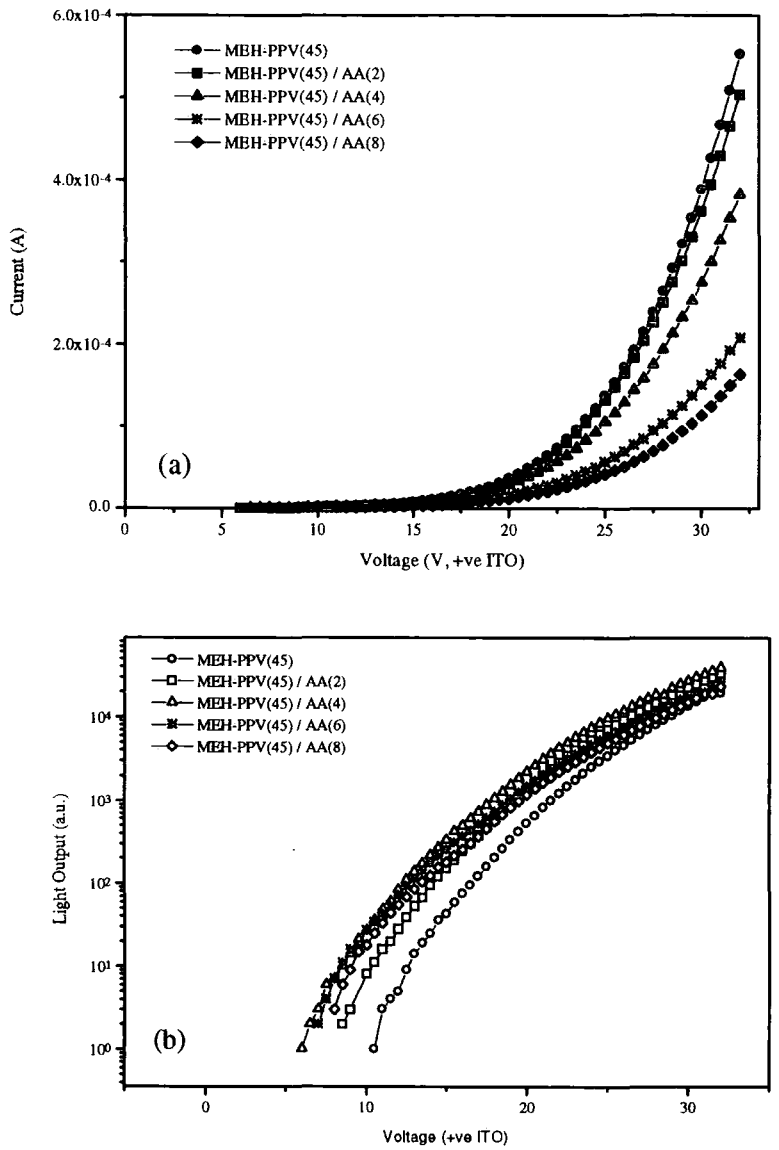

Figure 6.4 (a) I-V characteristics for ITO/MEH-PPV(40 cycles)/AA(0, 2, 4, 6, 8 cycles)/Al devices containing different thicknesses of fatty acid. (b) The light output versus voltage curve on log-linear scale.

The graph of light output versus voltage for the same devices is shown in Figure 6.4(b). For our devices, the turn-on voltage for EL decreases with increasing AA thickness up to 4 cycles of AA LB film and increases after this thickness. These turn-on voltages are

10.5 V for a pure MEH-PPV device, 6 V for the device containing 4 cycles of AA and 8 V for the device with 8 cycles of AA. The external quantum efficiency increases with increasing AA cycles as shown in Figure 6.5. The quantum efficiencies are 5.4×10^{-4} %, 8.9×10^{-4} %, 1.3×10^{-3}, 1.5×10^{-3} % and 1.7×10^{-3} % at a current density of 10 mA cm^{-2} for devices with AA(0), AA(2), AA(4) AA(6) and AA(8), respectively.

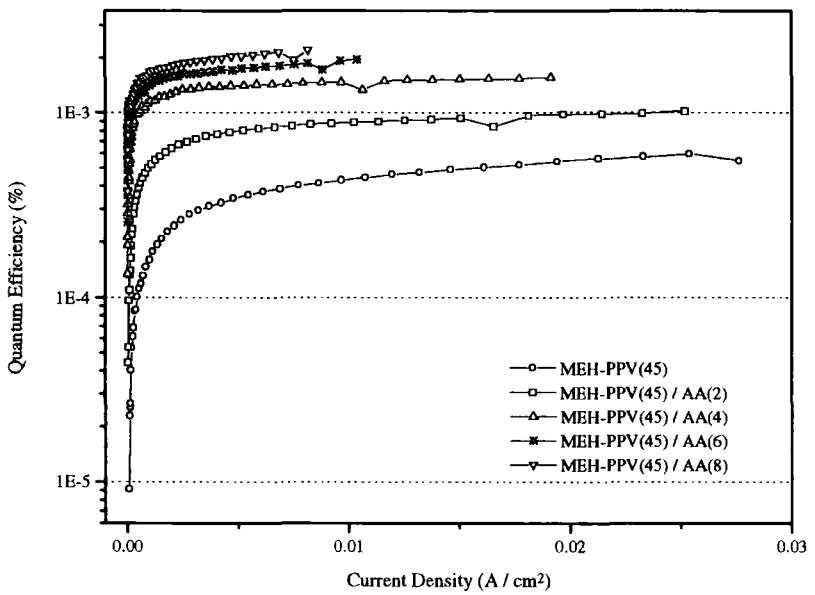

Figure 6.5 Log-log graph showing light output versus current density for ITO/MEH-PPV(40 cycles)/AA(0, 2, 4, 6, 8 cycles)/Al

The trends of quantum efficiency, emission intensity (normalised with that of the device with AA(0) at 10 mA cm^{-2} and 32 V) and turn-on voltage with different AA LB cycles are shown in Figure 6.6. The quantum efficiency increases rapidly and tends to saturation with the number of AA LB cycles. However, the intensity of emission decreases after 4 cycles. The device with AA(4) has the highest light output over the entire voltage range (Figure 6.4(b)) and the lowest turn-on voltage.

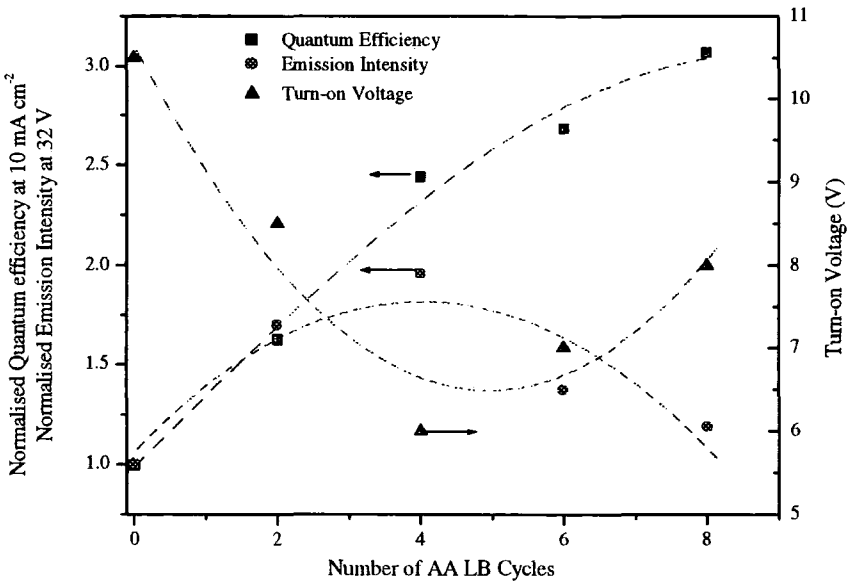

Figure 6.6 The trend of quantum efficiency, emission intensity and turn-on voltage for the device with different AA LB cycles.

6.2.4 Energy Band Model

The schematic energy band diagram in Figure 6.7(a) represents the situation in forward bias for an ITO/MEH-PPV/Al device. The electron current injected from the Al is limited by a barrier of about 1.5 eV at the polymer/Al interface. It is only at large applied biases, when electrons can overcome such a barrier, that the electron current becomes significant and EL can be observed. A significant difference for the devices incorporating the AA layers is that the Al Fermi level is no longer 'tied' to the energy band structure of the polymer (Figure 6.7(b)).

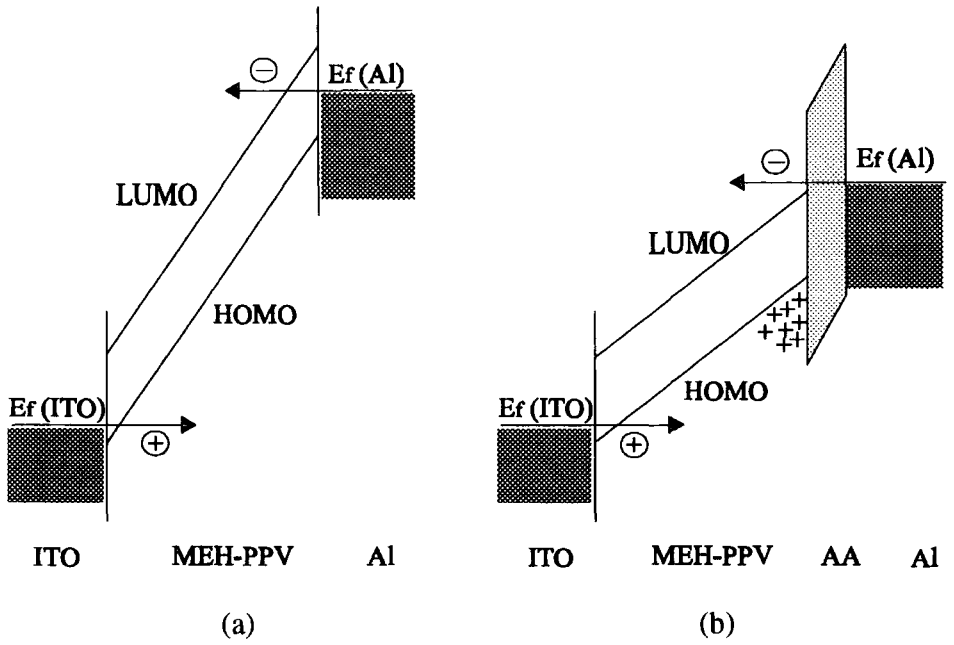

Figure 6.7 Potential energy diagrams for (a) ITO/MEH-PPV/Al structure and (b) ITO/MEH-PPV/AA/Al structure. In both cases a positive bias is applied to the ITO electrode.

MEH-PPV is a hole transporting material. Therefore, holes can drift to the MEH-PPV/AA interface and accumulate as a space charge, thereby increasing the internal built-in field in the AA layers and thus modifying the barrier of electron injection. As the applied voltage is increased, some of this is dropped across the AA layer and consequently, a lower electric field is associated with the MEH-PPV layer, as shown in Figure 6.7(b). The Al Fermi level can move with respect to the LUMO level in the MEH-PPV aligning filled electron states in the metal with vacant states in the polymer. As long as the fatty acid layer is 'transparent' to electrons, the electrons can tunnel through this layer and recombine with the holes.

The turn-on voltage for EL decreases up to 4 cycles. This is because the existing higher potential drop in the AA layer, due to more efficient confinement of holes with increasing the thickness, leads to better matching of the Al Fermi level with the polymer LUMO level. After 4 cycles this layer becomes an insulating layer. This

induces an increase in turn-on voltage for EL, in order to have an electron injection from Al.

The precise mechanism of conduction through the arachidic acid film is still unclear because the optimum film thickness for turn-on voltage (8 layers of AA LB film) used in this work is too thick (21 nm) to support simple quantum mechanical tunnelling. However, Petty et al. [10] revealed that relatively thick AA LB films could support large currents in metal/AA/inorganic semiconductor devices. From this point of view, the AA layer should preferably be called as a 'spacer' layer rather than an 'insulating' layer.

The dominant d.c. conduction processes in LB multilayer films of fatty acids are a matter of some debate; a number of different processes have been suggested [11]. For example, low electric field ($<10^5$ V m^{-1}) conduction has been interpreted in terms of the hopping of charge carriers by thermally assisted tunnelling between planar distributions of localised states; these are assumed to occur at the interface between successive monolayers. It is possible that fortuitous alignment of such levels in the AA with the energy bands of MEH-PPV could provide a path for the increased electron current.

In terms of external quantum efficiency, a relatively thick spacer layer is preferable because less holes flow to the Al electrode without recombination. Moreover, the presence of the fatty acid layer between the polymer and the top electrode will also separate the light emission zone from the metal. Some (or all) of the enhanced light output may result from the reduction in nonradiative quenching effects by the cathode electrode [9].

6.3 Incorporation of an Electron Transporting Layer

6.3.1 Background

Electron and hole transporting layers can be sandwiched between the cathode and the emitting layer, and between the anode and the emitting layer, respectively, to increase the charge carrier injection from each electrode and hence improve the charge balance [12,13]. Poly(2-methoxy,5-(2'ethylhexyloxy)-*p*-phenylenevinylene) (MEH-PPV) and poly(6-hexyl-2,4 pyridinediyl) (PHPY) LB films have been used as the emissive layer and electron transporting layer, respectively, in this section. The electron transporting layer was deposited, using the LB technique, on top of the MEH-PPV LB film to make a dual-layer device (ITO/MEH-PPV/PHPY/Al). An alternate-layer device comprising of 30 cycles of MEH-PPV alternated with PHPY is also described. Both the dual-layer and alternate-layer devices are compared with the MEH-PPV single layer reference device in terms of external quantum efficiency.

6.3.2 LB Deposition of PHPY

The LB dipping conditions for MEH-PPV were the same as those noted in the previous chapter. PHPY was synthesised in the Durham Physics Department and its structure is shown in Figure 6.8.

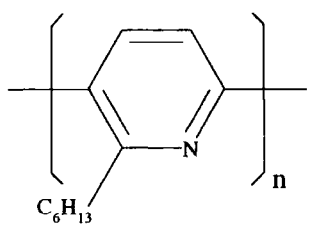

Figure 6.8 Molecular structure of poly (6-hexyl-2,5 pyridinediyl).

The molecular weight is of the order of 5,000. The PHPY layer was deposited using the conventional vertical LB technique. A dipping pressure of 30 mN m^{-1} was used. At this surface pressure, poor Y-type deposition was possible, with transfer ratios of 0.45 ± 0.03 for the downstrokes and 0.95 ± 0.03 for the upstrokes. Dual-layer systems were constructed by depositing PHPY on top of the MEH-PPV. For the alternate-layer structure, two LB layers (one LB cycle) of MEH-PPV were first deposited onto the ITO substrate; this was followed by two LB layers of PHPY. This deposition sequence was repeated using an alternate-layer LB trough. Figure 6.9 shows the structure of dual-layer and alternate-layer devices.

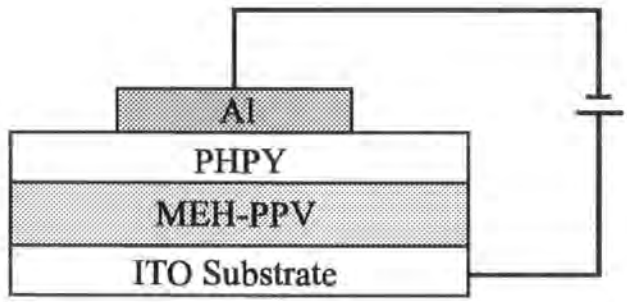

(a)

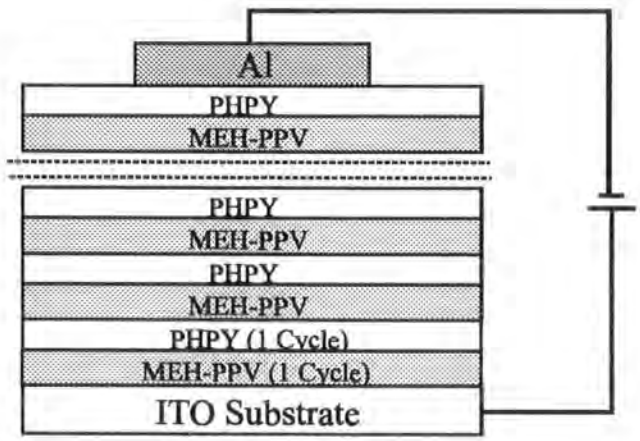

(b)

Figure 6.9 Schematic structures of (a) MEH-PPV / PHPY dual-layer device and (b) device comprising MEH-PPV (1 LB cycle) alternated with PHPY (1 LB cycle)

6.3.3 Dual-Layer Device characteristics

Figure 6.10 contrasts the forward bias current versus voltage and light output versus voltage characteristics for the single layer and the dual-layer LEDs. The latter device consisted of 10 cycles of PHPY LB films deposited on top of 30 cycles of MEH-PPV LB films; the total organic film thickness was 190 nm. The reference device is based on MEH-PPV LB films (50 cycles, 210 nm).

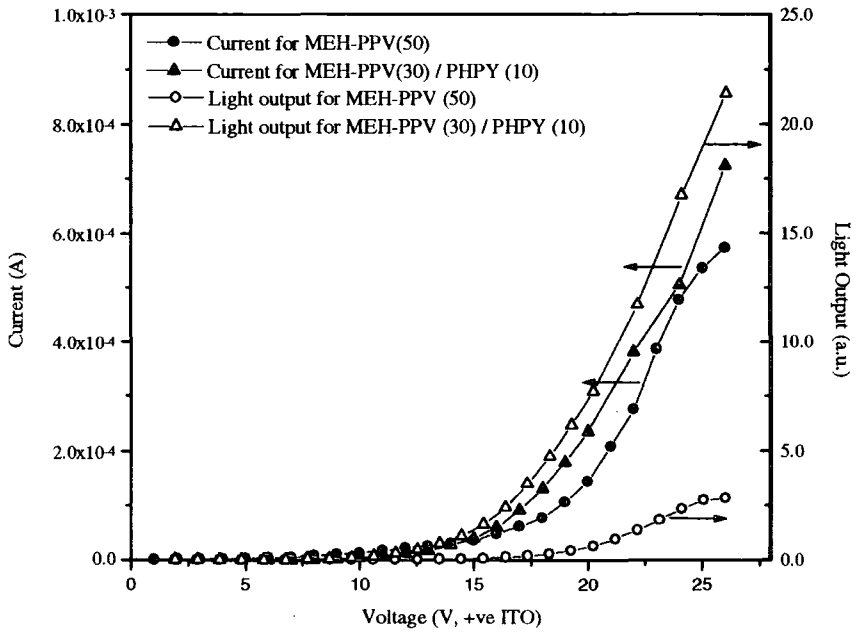

Figure 6.10 Comparison of the current versus voltage and light output versus voltage characteristics for a single layer and a dual-layer structure.

The forward currents measured for the two structures are similar. However, the light output for the dual-layer device is about one order of magnitude higher than for the single layer device, indicating a corresponding higher external quantum efficiency. The light output versus current density data for both devices are shown in Figure 6.11(a) and the external quantum efficiency is plotted versus current density in Figure 6.11(b). For high current density, the light output is approximately proportional to current density, resulting in a constant quantum efficiency. The

saturated external quantum efficiency is 7.5×10^{-3} % for the dual-layer structure and 5.7×10^{-4} % for the single layer structure.

The turn-on voltage of light output for the dual-layer device is 4 V, which is approximately one half that of single layer device. This suggests that electrons can be injected at a lower voltage due to the lower energy barrier for electrons between the cathode and the PHPY LB film. This is illustrated in the energy diagram, Figure 6.12, which shows the energy barrier for electron injection is 0.9 eV in the dual-layer device and 1.5 eV in the single layer device. For the purpose of this diagram, the energy bands for PHPY are assumed to be similar to those of poly(2,5-pyridinediyl) [14,15].

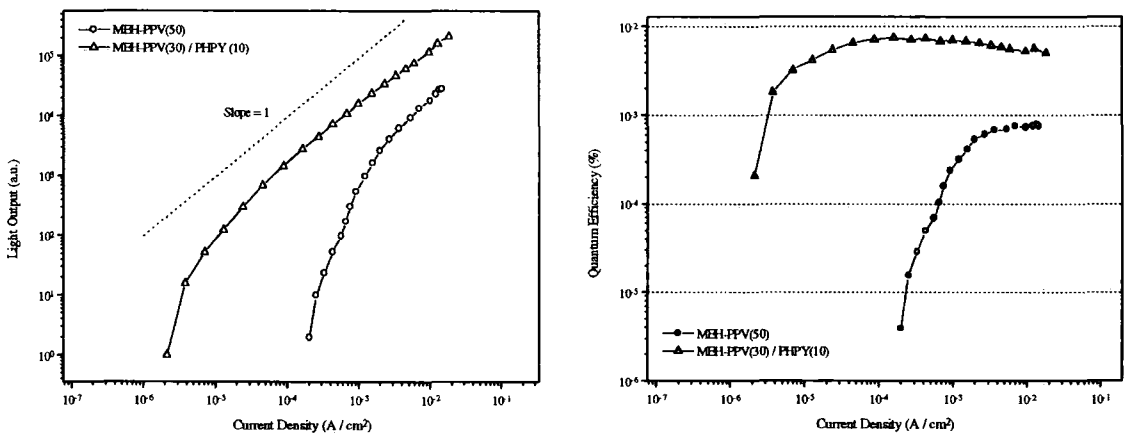

(a) (b)

Figure 6.11 (a) Light output and (b) external quantum efficiency versus current density characteristics for a MEH-PPV single layer device and a MEH-PPV/PHPY dual-layer device.

The higher external quantum efficiency for the dual-layer device can be explained by considering the charge transport characteristics and energy band structures of the two organic materials. Pyridine-based polymers are well known as electron transporting materials [14] whereas MEH-PPV is a good hole transporting material. The HOMO level for MEH-PPV is close to the ITO Fermi level and, in forward bias, holes are easily

transferred from the ITO to the MEH-PPV. Furthermore, more electrons can be injected from the Al into the PHPY layer in the dual-layer device than into the MEH-PPV in the single layer device due to the lower electron injection barrier, as shown in Figure 6.12.

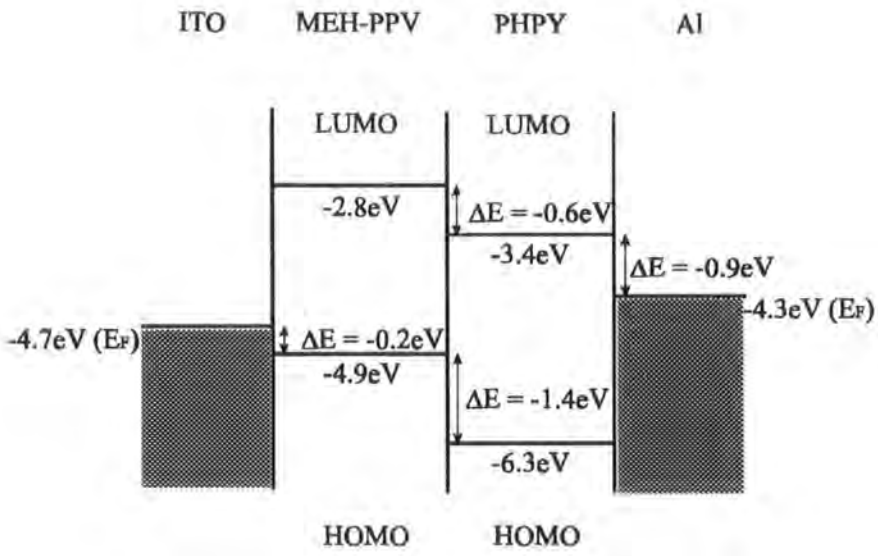

Figure 6.12 Potential energy diagram for the ITO/MEH-PPV/PHPY/Al structure.

At the MEH-PPV/PHPY interface there is a barrier of 0.6 eV for electrons and 1.4 eV for holes. Consequently, electrons injected from the Al electrode are transferred relatively easily from PHPY to MEH-PPV, while holes are blocked and accumulate in the MEH-PPV layer, i.e. at the interface between the two polymers. Hence, carrier recombination in the dual-layer device takes place in the MEH-PPV layer away from the Al electrode, avoiding nonradiative quenching effects of metal. In contrast, carrier recombination that takes place near the Al electrode in the reference device is likely to decay nonradiatively. Due to the more balanced injection for both charges, the dual-layer device has an improved device performance than the single layer device in terms of quantum efficiency, turn-on voltage for EL and light output.

Figure 6.13 contrasts the EL spectra of single and dual-layer devices when a positive bias is applied to ITO electrode. Orange-yellow light was clearly visible through the ITO glass. The EL spectrum of the dual-layer device is similar to that of the single layer MEH-PPV device, confirming that light emission originates from the MEH-PPV layer. This is consistent with the explanation based on the potential energy diagram.

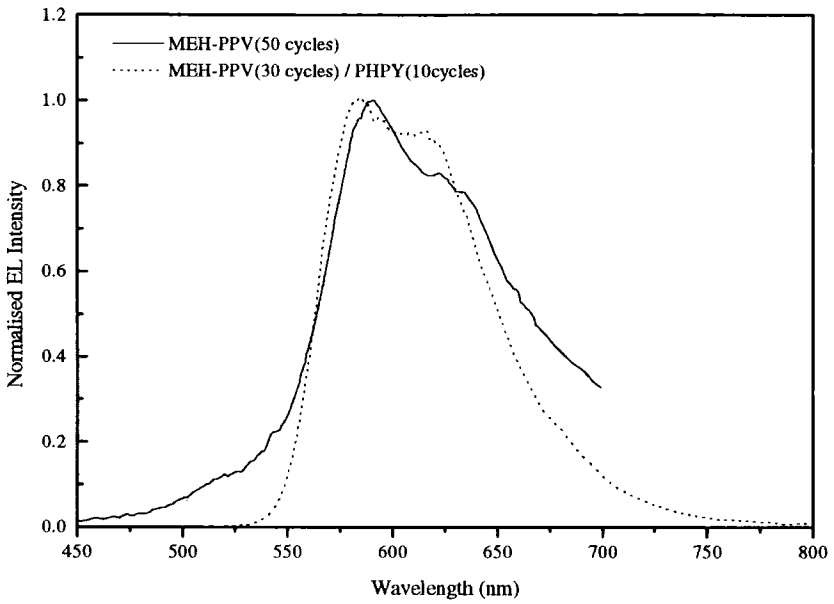

Figure 6.13 Normalised EL intensity for a MEH-PPV single layer device and MEH-PPV/PHPY dual-layer device.

6.3.4 Alternate-Layer Device

An alternate-layer system (ITO/30 cycles of MEH-PPV(1) and PHPY(1)/Al) was designed with the hope of more effective confinement of charge carriers. The I-V characteristics of alternate-layer device are compared with the single-layer MEH-PPV(50) device in Figure 6.14.

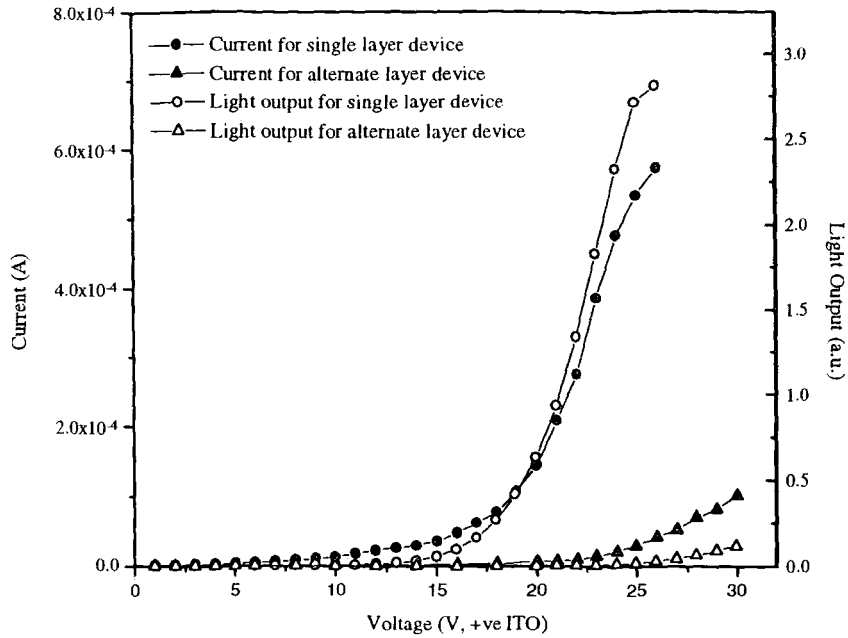

Figure 6.14 Comparison of the current versus voltage and light output versus voltage characteristics for a single layer (212 nm) and an alternate-layer (192 nm) structure.

The forward current for the alternate-layer system is one order magnitude lower than that of MEH-PPV single layer device even though the total film thickness is thinner than the single layer device. This lower current can be explained from the potential energy diagram (Figure 6.15) which is composed of 30 adjacent energy barriers. Energetically there is a quantum well in each MEH-PPV/PDPY interface. Thus each carrier (hole, electron) must surmount these barriers to migrate to the opposite electrode. Given the high energy barrier, these carriers are likely to be trapped in the MEH-PPV layer closest to the ITO electrode. The low current is ascribed to this slow carrier movement. The external quantum efficiency of the alternate-layer system is 1.0×10^{-4} %, even lower than the value of 6.0×10^{-4} % measured for the single layer system.

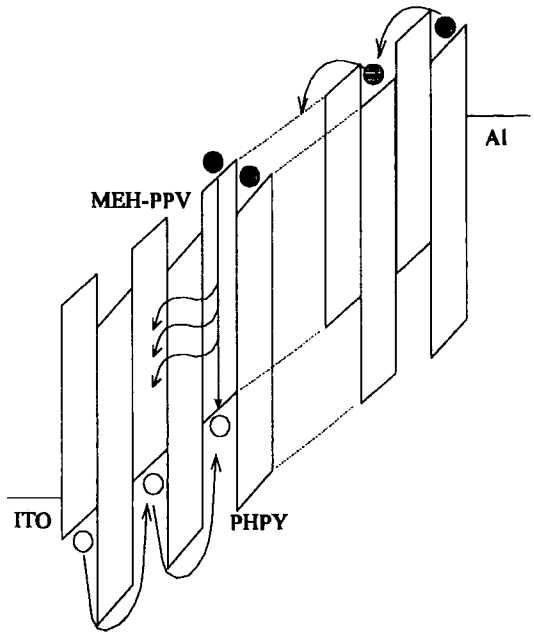

Figure 6.15 Energy diagram of alternate-layer device. ●: electrons, ○: holes

6.3.5 Optimisation of Film Thickness

In experiments using spin-coated dual-layer devices, it was found that the ratio of the thickness of the polymer layers could be used to optimise the LED efficiency [14,15]. The efficiencies of MEH-PPV/PHPY dual-layer devices incorporating different numbers of LB layers are shown in Table 3.

Device structure	Total thickness (nm)	External quantum efficiency (%)
ITO/MEH-PPV(50)/Al	212	6.0×10^{-4}
ITO/MEH-PPV(20)/PHPY(10)/Al	136	4.3×10^{-3}
ITO/MEH-PPV(30)/PHPY(10)/Al	190	7.5×10^{-3}
ITO/MEH-PPV(30)/PHPY(15)/Al	204	4.7×10^{-3}
ITO/MEH-PPV(50)/PHPY(25)/Al	263	8.0×10^{-4}
ITO/30 cycles of MEH-PPV(1) and PHPY(1)/Al	192	1.0×10^{-4}

Table 3. External quantum efficiencies of LEDs (single layer, dual-layer and alternate-layer structures). The figures in brackets refer to the number of LB deposition cycles.

The quantum efficiency of the MEH-PPV(50)/PHPY(25) device is one order of magnitude less than that of the MEH-PPV(30)/PHPY(10) structure. For thick films, the chance that holes and electrons are trapped in each material without recombination is high. On the other hand, for thin films it is possible for holes and electrons to drift to the opposite electrode without recombination. This suggests an optimum device total thickness and optimum thickness ratio should exist. In our work, ITO/MEH-PPV(30)/PHPY(10)/Al was the best structure in terms of external quantum efficiency.

The photograph of the EL emission from a MEH-PPV(30)/PHPY(10) device was taken with an exposure time of 5 minutes and is shown in Figure 6.16. Edge emission can be seen by total reflection within the ITO glass substrate. Gu et al. [16] showed that by redirecting the edge emitted light, the surface emission can be enhanced by 70 % to 90 %.

Figure 6.16 Photograph of EL emission from a dual-layer device.

6.4 Thermal Annealing Effects

6.4.1 Background

Following the initial work with organic LEDs using conjugated polymers, there have been significant improvements in device performance. High external quantum efficiencies of over 8 % [17] and colours covering the entire visible range are now commonplace. However there still remain problems with the polymer film and electrodes being vulnerable to oxidation and chemical degradation leading to short device lifetime.

The degradation of organic LEDs is often accompanied by the formation of black spots on the electrode(s). Possible reasons for these include: crystallisation of amorphous organic films [18]; the reaction between the organic material and the electrode [19]; the reaction of the top electrode with water and oxygen [20]; oxidation of organic layer by ITO [21] and poor contact between the organic layer and the electrode [22].

To improve the lifetime, elaborate encapsulation and packaging schemes are considered in order to exclude water and oxygen [23]. The use of hole transporting material with high T_g (glass transition temperature) [24], polymeric anodes instead of ITO [25] and doping the emissive layer [26] have also been used to prolong the lifetime.

The LB layers used in this work are exposed to aqueous solutions and possibly contain moisture which is detrimental to device lifetime. In this section, different post-deposition drying treatments are used prior to evaporation of the Al top electrode. The effect of drying the MEH-PPV LB film on the device performance, especially on the device lifetime, is studied.

6.4.2 Device Fabrication

MEH-PPV LB films (55 cycles) were deposited on four ITO-patterned substrates at the same time. Each substrate was treated by a different drying method. These were: drying at room temperature in a high vacuum (10^{-6} mbar) for 12 hours; annealing at 35 °C in high vacuum for 12 hours; and annealing at 60 °C in high vacuum for 12 hours. Finally, Al was evaporated onto the films to complete the LED devices. These devices were compared to those made from as-deposited films, without any drying treatment.

We have also undertaken further studies to improve the device operating lifetime: (I) by inserting a thin layer of LiF between the MEH-PPV LB layer and Al electrode to eliminate any chemical reaction between them and (II) by simple encapsulation of the entire device with adhesive tape to protect the Al electrode against direct contact with air and moisture. The LiF layer (≈ 2 nm) was thermally evaporated onto the 35 °C annealed MEH-PPV LB film and the Al electrode (150 nm) was then evaporated without breaking the vacuum. The encapsulation tape was 3M VHB acrylic adhesive tape, which covered the entire organic LED. If this procedure was undertaken carefully, no deleterious effects on the devices or their electro-optical characteristics were noted.

It should be noted that there was always a little variability in the electrical and optical characteristics of devices fabricated under seemingly identical conditions. This was due to the difficulty in reproducing the LB film thickness to better than 10 %. The experiments described in this section were therefore undertaken using a number of different devices. The trends in the characteristics, with different annealing conditions, were the same for all the structures investigated and therefore the results shown in this section can be considered as 'typical'.

6.4.3 Device Performance

The current versus voltage characteristics of the four devices, processed in different ways, are contrasted in Figure 6.17. Little effect on the current versus voltage curves is evident on drying the MEH-PPV layer in high vacuum prior to Al evaporation. However, annealing the MEH-PPV produces a marked increase in forward current for the same applied voltage.

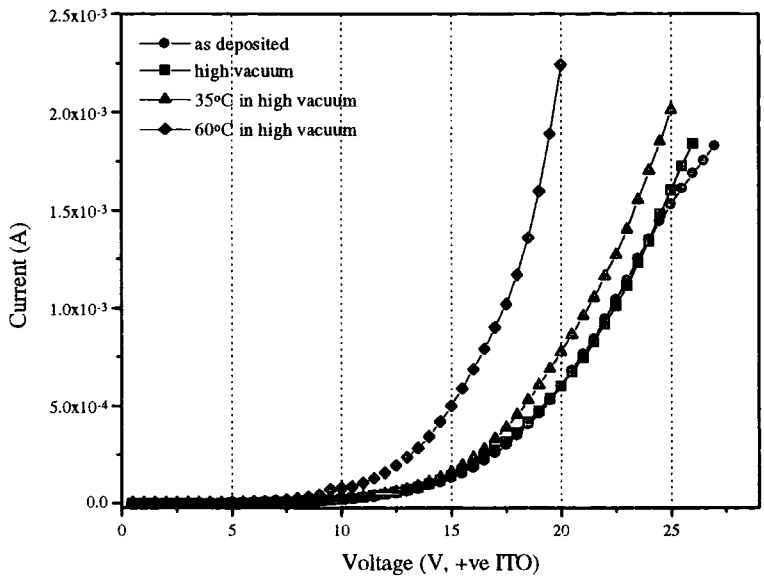

Figure 6.17 Current versus voltage characteristics for MEH-PPV subjected to various drying methods.

We suggest that this effect is simply related to a thickness decrease for the organic layer during the processing. Measurements with the surface profilometer revealed that annealing at 60 °C for 12 hours in high vacuum resulted in a thickness decrease of 80 nm (i.e. 38 % decrease in the initial thickness), while annealing at 35 °C for the same time produced a 26 nm thickness decrease (12 % decrease). No significant thickness change could be measured for the films dried at room temperature in high vacuum.

Light output was measurable for applied voltages greater than 2.5 V, independent of the film treatment. Figure 6.18 shows the quantum efficiency versus current density for the four devices whose current-voltage behaviour has already been given in Figure 6.16.

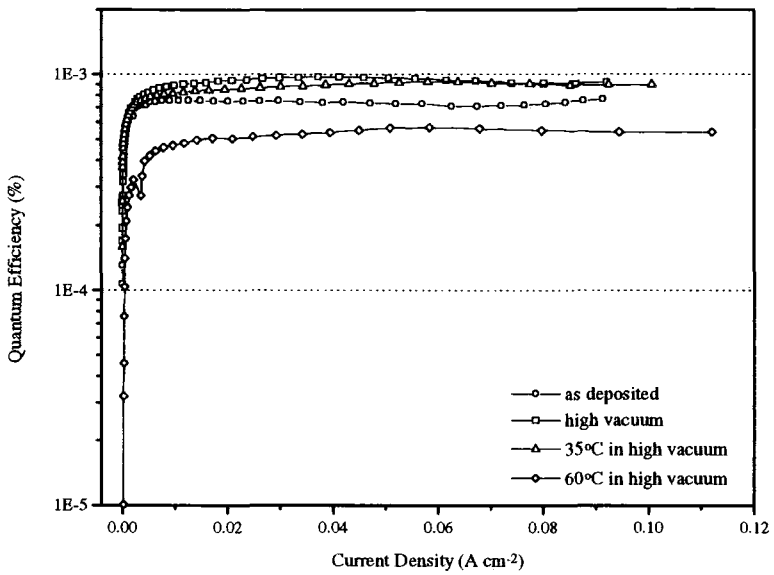

Figure 6.18 External quantum efficiency versus current density for the devices whose I-V characteristics are shown in Figure 6.17.

The quantum efficiencies measured at a current density of 40 mA cm^{-2} were 7.4×10^{-4} %, 1.0×10^{-3} %, 9.0×10^{-4} % and 5.3×10^{-4} % for the devices with the LB layers as-deposited, dried at room temperature in high vacuum, annealed at 35 °C in vacuum and annealed at 60 °C in vacuum, respectively. (It is important to note that the device efficiencies have not been optimised in this work, e.g. by the use of a higher work function cathode.) The device processed at room temperature in high vacuum for 12 hours has the highest quantum efficiency. The lower quantum efficiencies for the annealed devices may simply be related to nonradiative decay paths resulting from the enhanced packing of the polymer layers. For example, annealing might produce aggregates and interchain interactions, which may promote quenching effects as a result of the formation of excimers or ground state aggregates [27].

An alternative explanation is that if the organic layer is too thin, then nonradiative quenching effects near electrodes may reduce the light output. It has also been noted that the change of film structure from amorphous to polycrystalline decreases the ionisation potential of the organic film (related to a change in film density) [28]. A previous report shows that no significant degradation was observed in spin-coated MEH-PPV films that were subjected to heat treatment up to 120 °C for 21 hours [29]. In our case, the annealing temperature of 60 °C is much lower than the glass transition temperature of MEH-PPV, 210 °C [29]. No evidence for a crystalline structure in the 60 °C annealed MEH-PPV LB films was seen using low angle X-ray scattering.

6.4.4 Optical Characterisation

Although relatively large thickness changes were observed on thermal annealing, only relatively minor changes in the optical absorbance (for polymer layers deposited onto quartz) were evident, Figure 6.19. The data for the as-deposited film and for the film dried in high vacuum are virtually identical whereas annealing at elevated temperature slightly reduces the intensity of the absorption bands.

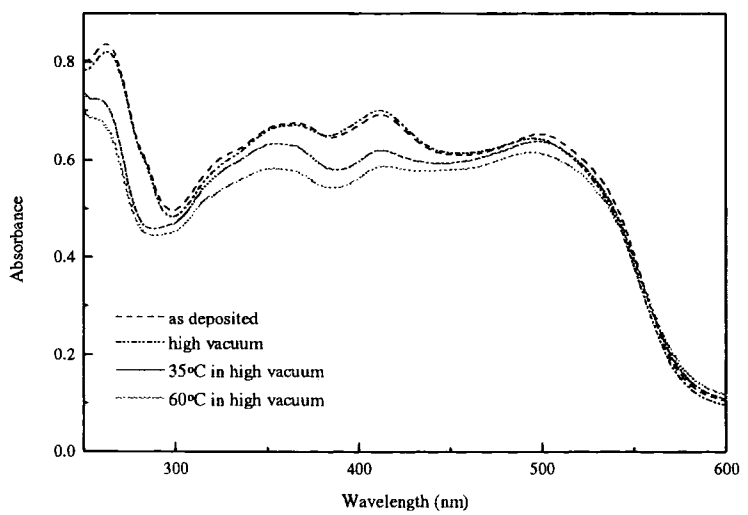

Figure 6.19 UV-Vis. absorption spectra of MEH-PPV LB films subjected to various drying methods.

The absorption edges of the four films occur at the same energy. It is notable that the absorption peaks (498 nm, 364 nm and 262 nm) are slightly blue shifted with increasing annealing temperature. This is probably the result of formation of H-aggregates of materials in LB film, as shown in Figure 6.20.

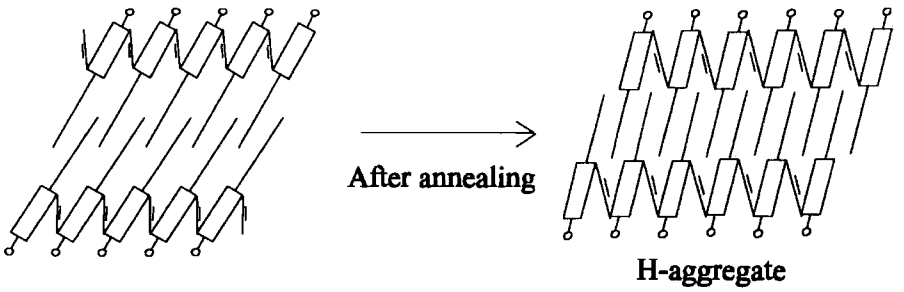

Figure 6.20 H-aggregation of molecules in LB film during thermal annealing.

Free movement of the side chains of MEH-PPV and torsion of the polymer backbone, which are commonly expected in the spun films and result in short conjugation lengths [30,31], are not likely to occur in the particular multilayered LB film structure during thermal treatment. Instead, the MEH-PPV LB films will probably become more closely packed with increasing temperature, leading to enhanced molecular order. Considering that the film thickness becomes thinner after annealing, the side chains of MEH-PPV might be strongly interleaved with those of interfacing layer as shown in Figure 6.20.

In the H-aggregated structure, more intra- and interchain excimers within the same layer could be formed by the phenyl groups which face each other along the polymer backbone. Due to the closer distance between layers, delocalised electrons along the polymer backbone can influence the electron cloud of the subsequent layer. This produces more excimer formation by interchain interaction.

The normalised PL spectra, excited at 420 nm, for the films subjected to different drying methods, are compared in Figure 6.21. The PL peak is slightly red shifted with

increasing temperature, which reflects more aggregates and excimer formation formed due to increased intra- and/or interchain interaction. Work by Nguyen et al. has shown that annealing spin-coated MEH-PPV films at 215 °C for several hours increases the degree of interchain interactions and facilitates charge transport [32].

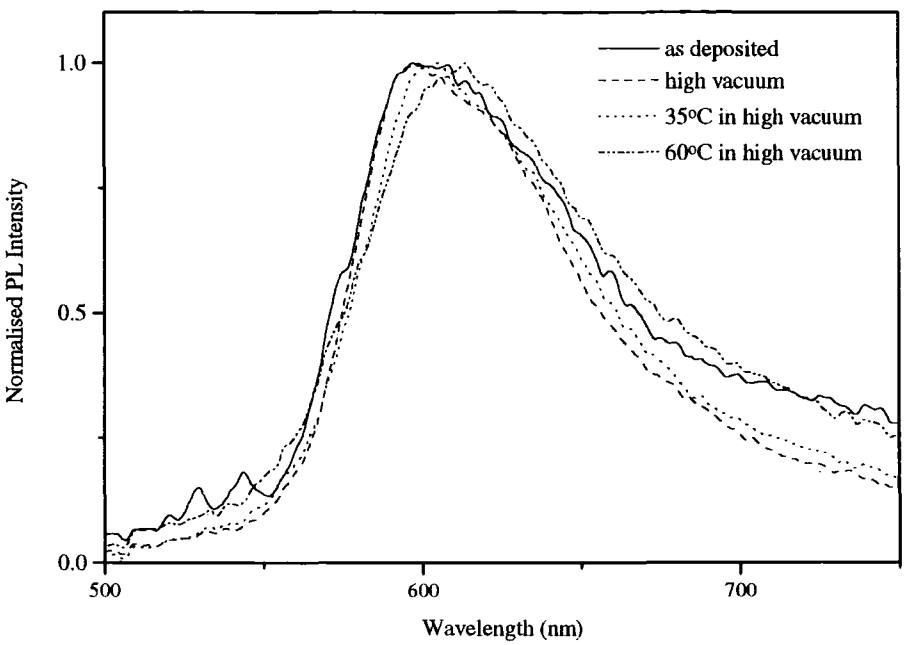

Figure 6.21 Normalised PL spectra of MEH-PPV LB films subjected to various drying methods. Excitation wavelength is 430 nm.

6.4.5 Operating Lifetime

The stability of the organic LEDs was studied by applying a constant current stress (current density: 15 mA cm^{-2}). Figure 6.22 shows the voltage variation with time for different devices. Device failure was accompanied by a rapid increase in the voltage across the structure. The approximate lifetimes were 1000 s, 2500 s, 3500 s and 5500 s for devices with the LB layers as-deposited, left at room temperature in high vacuum, annealed at 35 °C in high vacuum and annealed at 60 °C in high vacuum, respectively. It is clear that longer lifetimes can be achieved with higher annealing temperatures. A further

lifetime test was undertaken at a constant voltage, Figure 6.23. Although all the devices exhibited a similar light output at the beginning of the experiment, the EL decayed rapidly and was almost undetectable after two hours, except for the 60 °C annealed film device.

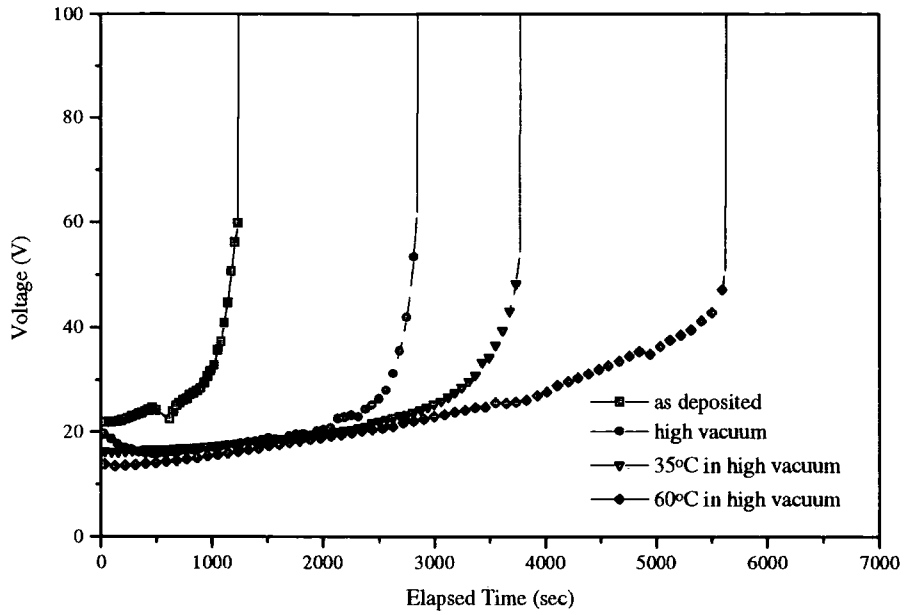

Figure 6.22 Lifetime experiments using a constant current (current density of 15 mA cm^{-2}). The abrupt voltage increase is related to irreversible device failure.

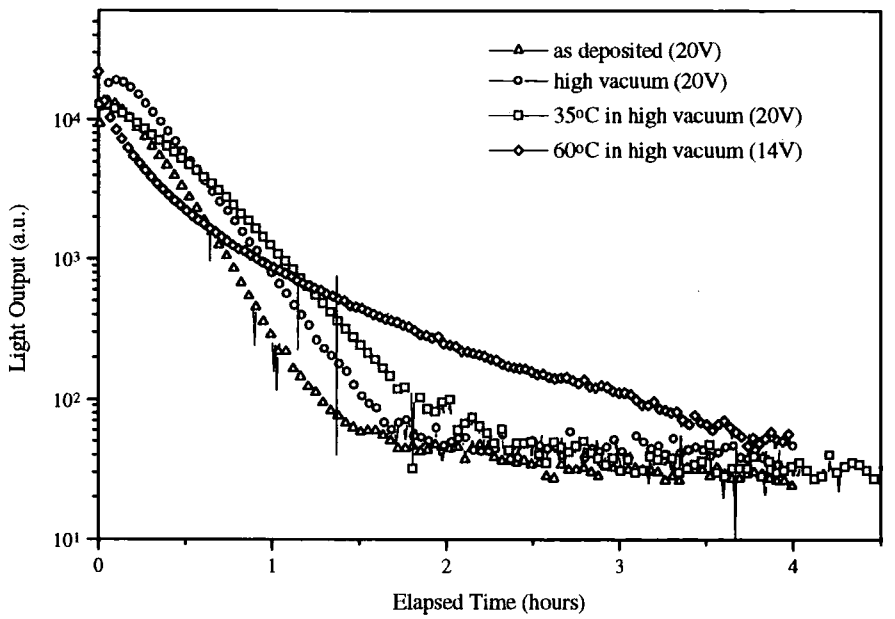

Figure 6.23 Lifetime experiments using a constant applied voltage.

What appears to make the difference to the lifetimes of our LED structures is the uniformity of the deposited organic film. The as-deposited LB layer is uneven, as confirmed by our surface profile measurement (Figure 6.24). This results in a very nonuniform electric field throughout the device. Thin regions can become shorted during operation, leading to high currents. This, in turn, leads to joule heating and finally to rupture of the aluminium. Annealing the LB film results in a relatively more uniform film thickness.

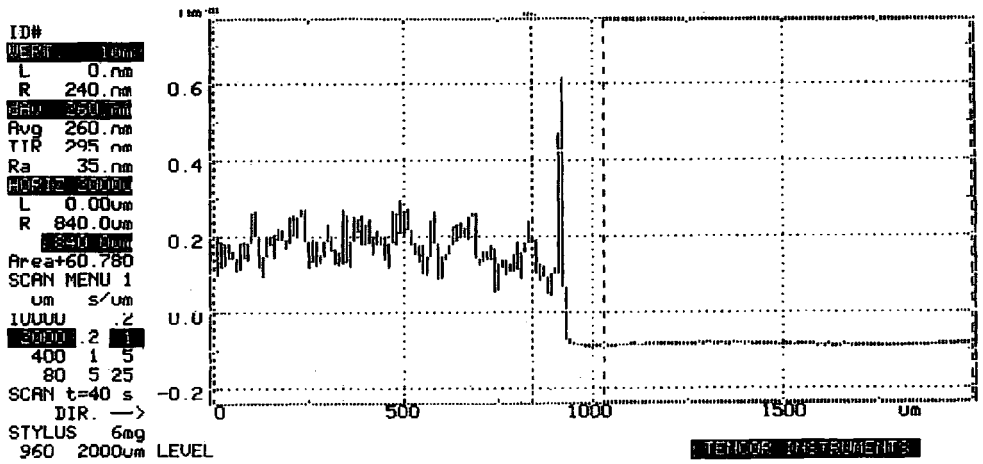

Figure 6.24 Surface profile of MEH-PPV LB film as-deposited.

A smoother surface was evidenced by the surface roughness (R_a parameter) measured by the surface profilometer: 44.5 nm, 35.4 nm, 33.2 nm and 33.8 nm for the LEDs with the LB layers as-deposited, dried at room temperature in high vacuum, annealed at 35 °C in high vacuum and annealed at 60 °C in high vacuum, respectively. Using atomic force microscopy, Lee and Park [33] showed that a smoother MEH-PPV surface was observed as the annealing temperature increases.

The optical micrographs shown in figure 6.25 provide images of the Al surface in different devices following the constant current stress of current density of 15 mA cm^{-2} for 25 min. It is evident that the metal electrodes of devices in which the LB films have been

annealed at elevated temperatures (Figures 6.25(c) and (d)) are more continuous than those in the untreated device (Figure 6.25(a)) and the structure processed at room temperature in high vacuum (Figure 6.25(b)).

In common with other reports, the device degradation was found to be associated with the degradation of the aluminium electrode [19]. Dark regions were observed on the electrode's surface using scanning electron microscopy (SEM). These increased in size over time until they eventually covered most of the active surface of the Al and the light output was no longer detectable. Figure 6.26 contrasts SEM images obtained for a fresh Al electrode (Figure 6.26(a)) and an Al electrode from a device annealed at 35 °C that had been subjected to a constant current stress until the EL output was no longer detectable (Figure 6.26(b)); an enlargement of one of the dark regions is shown in Figure 6.26(c).

EDX analysis was performed inside a dark region (Figure 6.27(a)), outside this region (Figure 6.27(b)) and on a fresh Al electrode (Figure 6.27(c)). The signals due to Si, In and Ca indicate that the X-ray beam can penetrate the organic layer to the glass substrate (the Au signal originates from the gold coating used to prepare the samples for the SEM work). For the measurements in a dark region, the higher Si peak intensity, relative to the Al, indicates that Al has been removed. The SEM picture in Figure 6.26 seems to confirm this hypothesis. Studies by Do et al. with organic LEDs based on evaporated molecular crystals reached similar conclusions [34]. These workers have suggested that a morphological change in the aluminium electrode is initiated by the presence of pin-holes in the metal cathode.

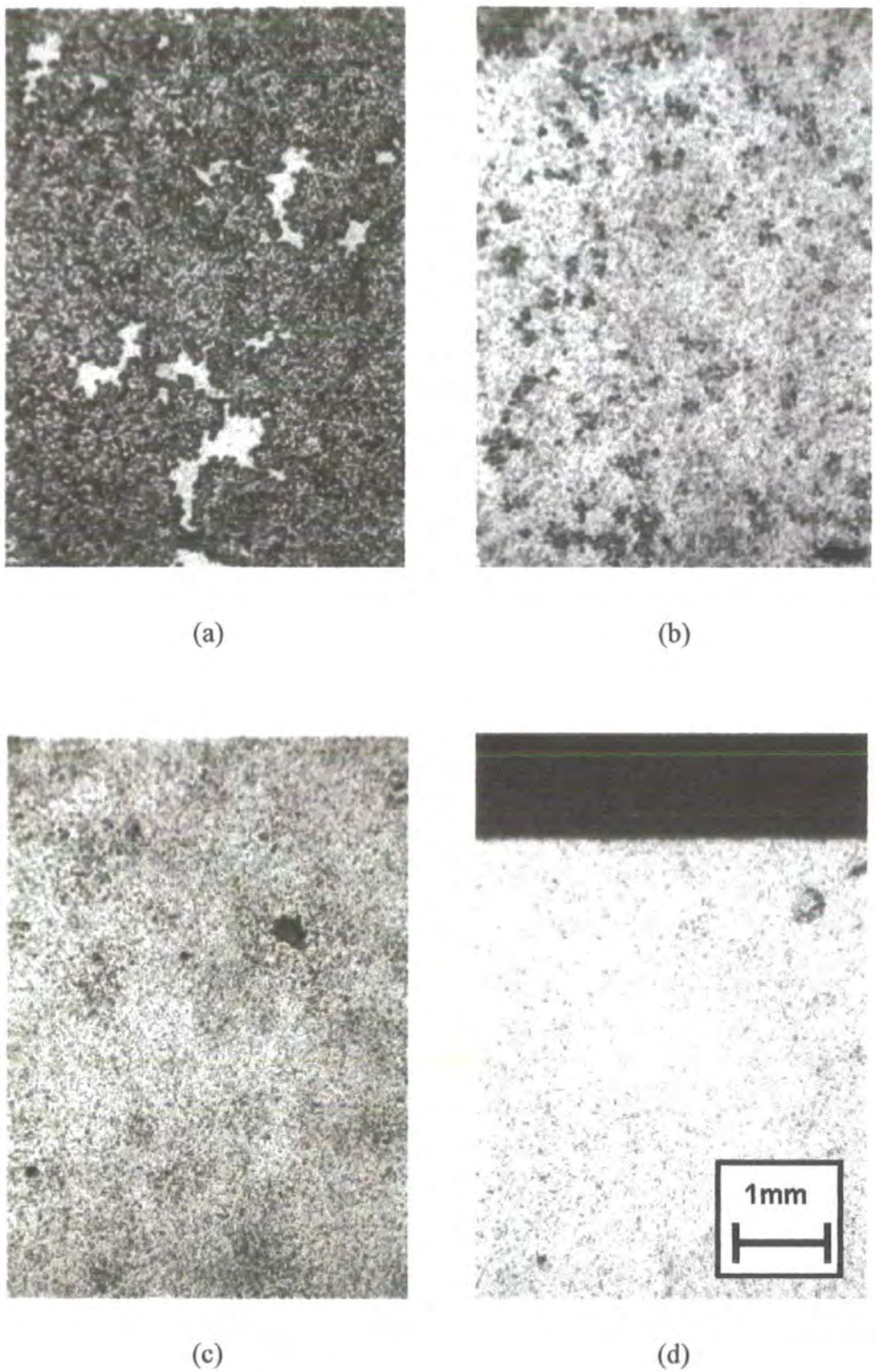

Figure 6.25 Optical micrographs (×20 magnification) of the surface of the Al electrode following a constant stress (current density = 15 mA cm^{-2}) applied for 25 minutes. Photographs correspond to devices processed in different ways before the deposition of the Al top electrode: (a) untreated; (b) dried for 12 h in high vacuum; (c) annealed for 12 h at 35 °C in high vacuum; and (d) annealed for 12 h at 60 °C in high vacuum.

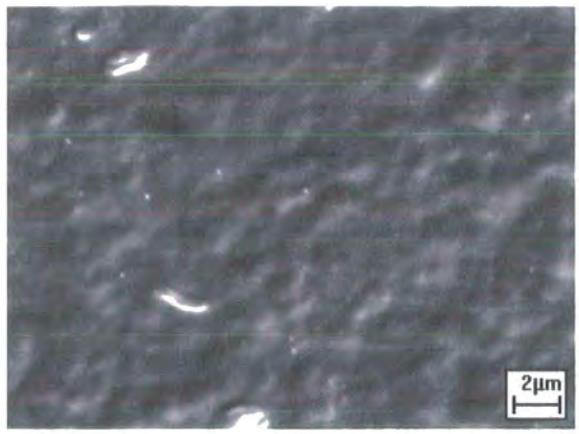

(a)

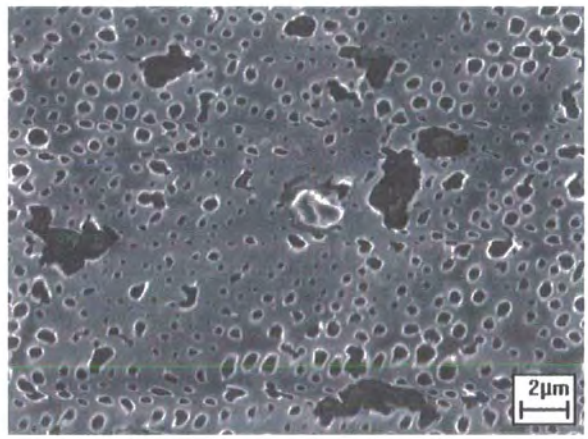

(b)

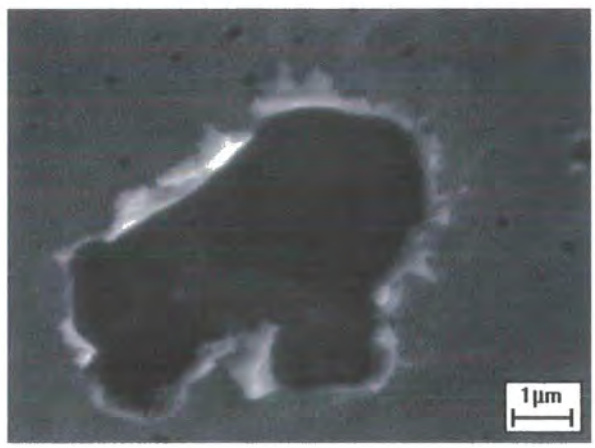

(c)

Figure 6.26 SEM images of (a) a freshly evaporated Al electrode and (b) an Al electrode from the device annealed at 35 °C that had been subjected to a constant current stress until the EL output was no longer detectable. (c) Image of Al electrode focusing on one of the dark regions in (b).

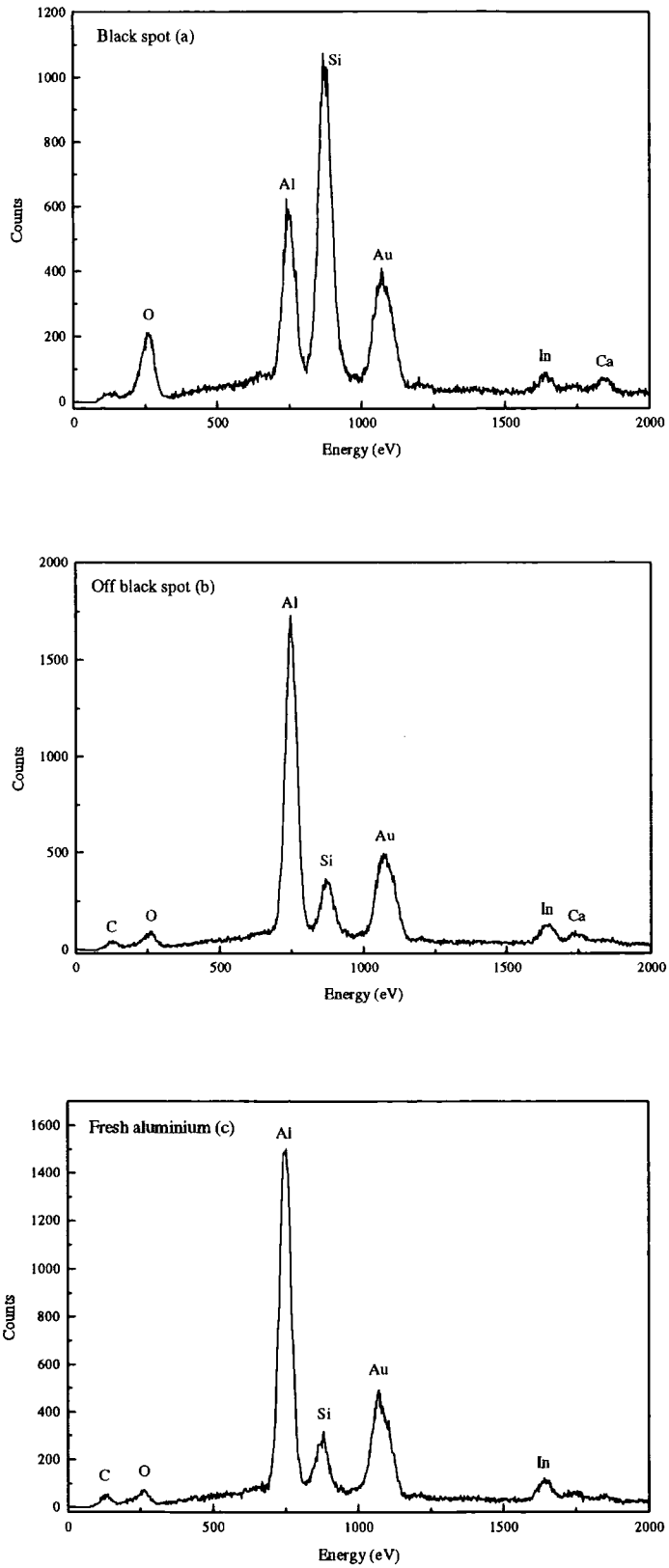

Figure 6.27 EDX spectra for Al electrode. (a) Dark region (b) off dark region and (c) freshly evaporated Al electrode.

6.4.6 Improvement of Operating Lifetime

The lifetime of the devices reported here is too short for commercial applications. Chemical reactions between the cathode top electrode and the organic material [35] and reactions between the cathode and the ambient atmosphere [36] are both detrimental to the lifetime of organic LEDs. Although our lifetime experiments were undertaken in a low vacuum (10^{-2} mbar), there was still sufficient air/moisture present to degrade the device. We have therefore undertaken a preliminary study of methods that might be used to improve the device lifetime. Figure 6.28 shows the light output decay for different modified organic LED configurations incorporating a LiF (≈ 2nm) layer between the polymer and aluminium electrode and the encapsulation tape.

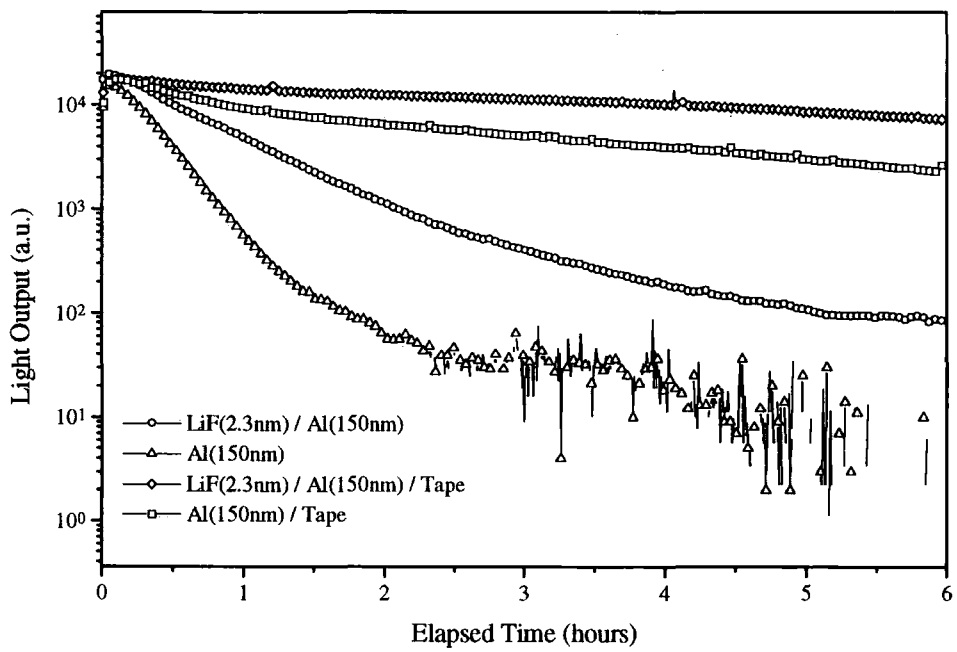

Figure 6.28 Lifetime experiments for ITO/MEH-PPV(55)/Al structures incorporating LiF and/or encapsulation tape. Constant voltage (20 V) was applied to the devices.

Incorporation of the LiF buffer layer provides a useful increase in the device operating lifetime. A more significant improvement (lifetime > 11 h) is obtained with the

encapsulation tape. In agreement with other work [37], our results illustrate that the protection of top electrode from the air and moisture is a crucial factor if long operating times are to be achieved.

6.5. Summary

The insertion of AA layers between a MEH-PPV film and an Al cathode was found to shift the I-V characteristics to higher voltages. However, the turn-on voltage for EL decreased with increasing AA thickness up to 8 layers (4 cycles), 4.5 V lower than that of the pure MEH-PPV device, and the external quantum efficiency increased by a factor of three in the case of MEH-PPV/AA (8 cycles) device compared to the device without AA layer.

By using the electron transfer material, PHPY, between the MEH-PPV and the Al electrode, more electrons could be injected from Al electrode at lower voltage. This increased the external quantum efficiency up to 7.5×10^{-3} %, more than one order of magnitude higher than the single layer device and decreased turn-on voltage.

Annealing the MEH-PPV LB film before Al evaporation resulted in a closely packed polymer film leading to more aggregates or higher intra- and/or interchain interaction between layers. This interaction shifted the PL spectrum to the red and could promote nonradiative decay channels leading to lower quantum efficiency. On annealing, the LB film surface became smoother, which prolonged the device lifetime.

The operating lifetime of MEH-PPV single-layer devices could be further increased by the use of a thin layer (< 2 nm) of lithium fluoride (LiF) at the polymer/Al interface and more effectively by encapsulation of the whole Al top electrode with an adhesive tape.

References

1. M. Meier, M. Cölle, S. Karg, E. Buchwald, J. Gmeiner, W. Riess and M. Schwoerer, *Mol. Cryst. Liq. Cryst.*, **283**, 1996, 197.

2. I.D. Parker and H.H. Kim, *Appl. Phys. Lett.*, **64**, 1994, 1774.

3. L.S. Hung, C.W. Tang and M.G. Mason, *Appl. Phys. Lett.*, **70**, 1997, 152.

4. J.S. Kim, M. Granström, R.H. Friend, N. Johansson, W.R. Salaneck, R. Daik, W.J. Feast and F. Cacialli, *J. Appl. Phys.*, **84**, 1998, 6859.

5. S. Karg, J.C. Scott, J.R. Salem and M. Angelopoulos, *Synth. Met.*, **80**, 1996, 111.

6. T.M. Brown, J.S. Kim, R.H. Friend, F. Cacialli, R. Daik and W.J. Feast, *Appl, Phys. Lett.*, **75**, 1999, 1679.

7. Y.E. Kim, H. Park and J.J. Kim, *Appl. Phys. Lett.*, **69**, 1996, 599.

8. W. Riess, H. Riel, P.F. Seidler and H. Vestweber, *Synth. Met.*, **99**, 1999, 213.

9. H. Becker, S.E. Burn and R.H. Friend, *Phys. Rev. B.*, **56**, 1997, 1893.

10. M.C. Petty, J. Batey and G.G. Roberts, *IEE Proc.*, **132**, 1985, 133.

11. M. Sugi, T. Fukui and S. Iizima, *Mol.Cryst. Liq. Cryst.*, **50**, 1979, 183.

12. C.W. Tang and S.A. Vanslyke, *Appl. Phys. Lett.*, **51**, 1987, 913.

13. J. Kido, *Phys. World*, **12**, 1999, 27.

14. S. Dailey, M. Halim, E. Rebourt, L.E. Horsburgh, I.D.W. Samuel and A.P. Monkman, *J. Phys: Condens. Matter*, **10**, 1998, 5171.

15. S. Dailey, M. Halim, I.D.W. Samuel and A.P. Monkman, *Proc. SPIE Organic Light-Emitting Materials and Devices*, **San Diego**, **3148**, 1997, 82.

16. G.Gu, D.Z. Garbuzov, P.E. Burrows, S. Venkatesh and S.R. Forrest, *Opt. Lett.*, **22**, 1997, 396.

17. M.A. Baldo, S. Lamansky, P.E. Thompson and S.R. Forrest, *Appl. Phys. Lett.*, **75**, 1999, 4.

18. E.M. Han, L.M. Do, N. Yamamoto and M. Fujihira, *Synth. Met.*, **273**, 1996, 202.

19. L.M. Do, M. Oyamada, A Koike, E.M. Han, N. Yamamoto and M. Fujihira, *Thin Sol. Fi.*, **273**, 1996, 209.

20. J.R. Sheats, H. Antoniadis, M. Hueschen, W. Leonard, J. Miller, R. Moon, D. Roitman and A. Stocking, *SCI.*, **273**, 1996, 884.

21. J.C. Scott, J.H. Kaufman, P.J. Brock, R. DiPietro, J. Salem and J.A. Goitia, *J. Appl. Phys.*, **79**, 1996, 2745.

22. J. McElvain, H. Antoniadis, M.R. Hueschen, J.N. Miller, D.M. Roitman, J.R. Sheats and R.L. Moon, *J. Appl. Phys.*, **80**, 1996, 6002.

23. P.E. Burrows, V. Bulovic, S.R. Forrest, L.S. Sapochak, D.M. McCarty and M.E. Thompson, *Appl. Phys. Lett.*, **65**, 1994, 2922.

24. S. Tokito, H. Tanaka, K. Noda, A. Okada and Y. Taga, *Appl. Phys. Lett.*, **70**, 1997, 1929.

25. S.A. Carter, M. Angelopoulos, S. Karg, P.J Brock and J.C. Scott, *Appl. Phys. Lett.*,**70**, 1997, 2067.

26. J. Shi and C.W. Tang, *Appl. Phys. Lett.*, **70**, 1997, 1665.

27. S.A. Jenekhe and J.A. Osaheni, *SCI.*, **265**, 1994, 765.

28. M.D. Joswick, I.H. Campbell, N.N. Barashkov and J.P. Ferraris, *J. Appl. Phys.*, **80**, 1996, 2883.

29. M. Atreya, S. Li, E.T. Kang, K.G. Neoh, Z.H. Ma, K.L. Tan and W. Huang, *Polymer Degradation and Stability*, **65**, 1999, 287.

30. S.D. Jung, D.H. Hwang, T.H. Zyung, W.H. Kim, K.G. Chittibabu and S.K. Tripathy, *Synth. Met.*, **98**, 1998, 107.

31. A. Bolognesi, C. Botta, G. Bajo, R. Österbacka, T. Östergard and H. Stubb, *Synth. Met.*, **98**, 1998, 123.

32. T.Q. Nguyen, R.C. Kwong, M.E. Thompson and B.J. Schwartz, *Appl. Phys. Lett.*, **76**, 2000, 2454.

33. T.W. Lee and O.O. Park, *Adv. Mater.*, **12**, 2000, 801.

34. L.M. Do, D.H. Hwang, H.Y. Chu, S.H. Kim, J.I. Lee, H. Park and T.Y. Zyung, *Synth. Met.*, **111-112**, 2000, 249.

35. M. Matsumura, K. Furukawa and Y. Jinde, *Thin Sol. Fi.*, **331**, 1998, 96.

36. H. Aziz, Z. Popovic, C.P. Tripp, N.X. Hu, A.M. Hor and G. Xu, *Appl. Phys. Lett.*, **72**, 1998, 2643.

37. P.E. Burrows, V. Bulovic, S.R. Forest, L.S. Sapochak, D.M. McCarty and M.E. Thompson, *Appl. Phys. Lett.*, **65**, 1994, 2922.

Chapter 7.

Devices based on MEH-PPV Spin-Coated Films

7.1 Introduction

In this chapter, all the LEDs described are based on MEH-PPV spun films. Many techniques have been used to improve the device efficiency and lifetime.

Initially, the optical properties of MEH-PPV spun film are compared to those of MEH-PPV LB films. The performance of devices made with both types of films are also contrasted in Section 7.2. Dual-layer devices were made by thermally evaporating a new electron transporting material, 2,5-bis[2-(4-*tert*-butylphenyl)-1,3,4-oxadiazol-5-yl]pyridine (PDPyDP). In Section 7.3, the properties of this compound are compared with those of 1,3-bis[2-(4-*tert*-butylphenyl)-1,3,4-oxadiazol-5-yl]benzene (OXD-7) which is widely used as an electron transporting material. Despite improved device performance, such as higher quantum efficiency and lower turn-on electric field for EL, the devices incorporating PDPyDP were not stable. Several strategies to improve the device stability are therefore described: doping (Section 7.4); inserting a buffer layer between the electrode and the organic film (Section 7.5); thermal annealing (Section 7.6); and changing the Al evaporation condition (Section 7.7).

7.2 Comparison of Spun and LB Films

In this section the properties of MEH-PPV spun films are compared to those of LB films. The device characteristics of devices made from both types of films are then discussed.

7.2.1 Spin-Coating of MEH-PPV

MEH-PPV was dissolved in a mixed solvent of 50 % chloroform and 50 % *p*-xylene to achieve adequate viscosity. The concentration was 6.6 mg ml^{-1}. The solution was dropped onto ITO patterned glass or quartz before spinning. At first, a low spin speed (800 ~ 1000 rpm) was used for 3 seconds to spread the solution evenly over the substrate. A higher spin speed (2600 ~ 2800 rpm) was then used for 30 seconds to reduce the film to the required thickness. The spin speed was chosen by calibrating film thickness against spin speed. Without any heat treatment, the spun films were placed in a high vacuum chamber to evaporate the Al top electrode.

7.2.2 Comparison of optical properties

The UV-Vis. absorption spectra of a MEH-PPV spun film (120 nm), an LB film (30 cycles, 140 nm) and a solution in chloroform (1×10^{-3} mole) are compared in Figure 7.1.

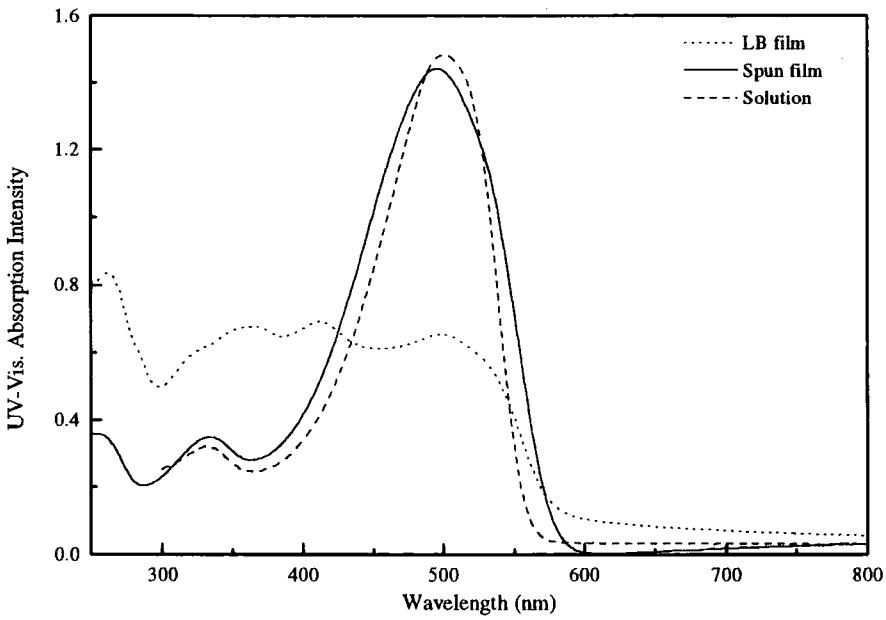

Figure 7.1 UV-Vis. absorption spectra of MEH-PPV LB film (140 nm), spun film (120 nm) and solution in chloroform (1×10^{-3} mole).

The shape of the absorption spectrum of the spun film is similar to that from a 1×10^{-3} mole MEH-PPV solution in chloroform where there is a broad π-π^* transition absorption peak at 500 nm and a small absorption band around 334 nm. Shi et al. [1] reported that the polymer chains are expected to coil more tightly in nonaromatic solvents such as THF and $CHCl_3$ resulting in disordered films.

In the case of the LB film, the absorption spectrum is broad and includes absorption bands at 412 nm and 364 nm. These can probably be ascribed to aggregate formation due to particular molecular ordering and specific alignment of molecules in the LB film. The peaks are blue-shifted with increasing annealing temperature, Figure 6.19, and the absorption intensity becomes significant with increasing number of LB cycles, Figure 5.4.

The normalised PL spectra of the solution and the two films, excited at 420 nm, are shown in Figure 7.2. The PL spectrum of the spun film is red-shifted and broader compared to that of the solution, while the absorption spectrum is similar to that of the solution after spin casting (Figure 7.1). The red-shift of PL, without a significant change in the absorption spectrum, originates from excimers formed by interchain interactions in the spun film. These interactions are predictably maximized in the solid state when the polymer chains are closely packed. Samuel et al. [2] revealed the formation of emissive interchain excimers in a cyano-substituted PPV in which the absorption and the PL spectra of this material had the same characteristics as those reported here.

The PL peak of the LB film is slightly red shifted (2 nm) compared to that of the spun film. The peak of the 0-0 transition and the excimer peak (0-1 transition) at around 590 nm and 620 nm, respectively, appear in the PL spectra of both films. The

PL of the LB film has an extended tail, which emits red light near the 0-2 band due to aggregate formation [3].

A fitting procedure, using three Gaussian curves, was applied to the PL spectra and the best fit parameters for the PL spectra are inset in each figure. The Gaussian curves, numbered 1, 2 and 3, represent the 0-0, 0-1 and 0-2 emission bands, respectively. Table 4 shows the relative intensity ratios of the 0-0 transition (I_o) to the excimer (I_E) emission and the wavelength of the PL peak of each spectrum. The curve fitting reveals that the LB film sample contains more excimers and aggregates compared to the spun film.

	LB film	Spun film	Solution
Ratio (I_o/I_E)	0.3	0.4	0.6
Peak wavelength (nm)	591	589	564

Table 4. Ratios of the excimer to the 0-0 transition emission for MEH-PPV in different forms.

The LB technique stacks molecules densely, layer by layer, so that π-conjugated polymers are deposited in order (π-stacking) resulting in strong interchain interactions between the polymer backbones (π-π overlap). These interactions enhance the excimer formation, which can increase nonradiative decay and hence reduce the PL efficiency [4].

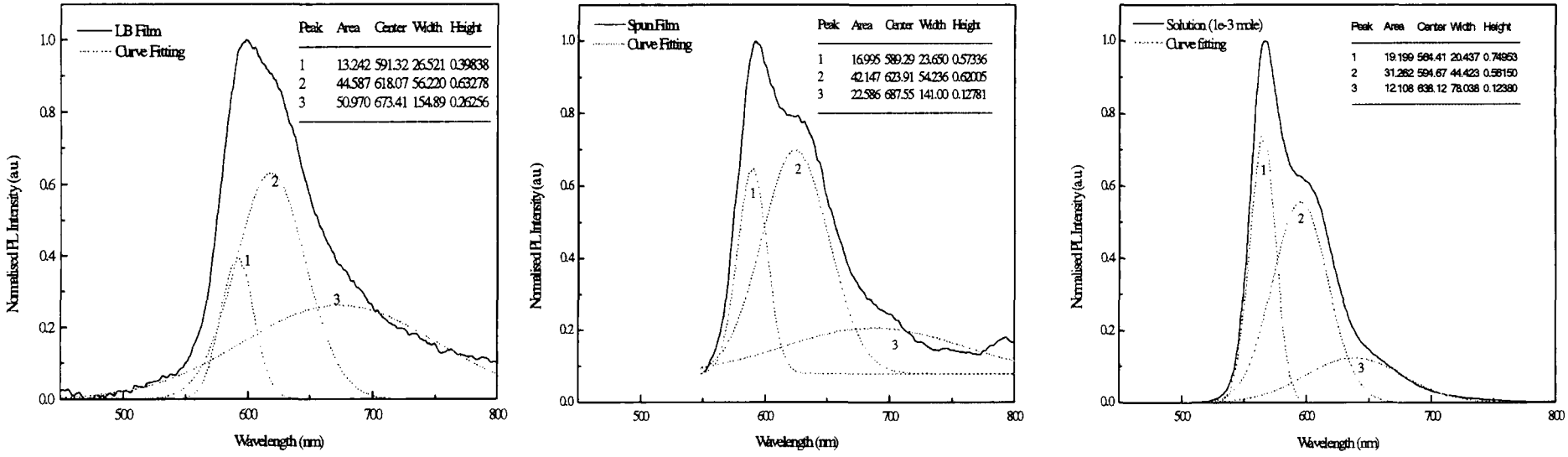

Figure 7.2 PL spectra of (a) MEH-PPV LB film (30 cycles, 140 nm), (b) spun film (120 nm) and (c) solution (1×10^{-3} mole) in chloroform. Three Gaussian curves are fitted to these curves and their parameters are inset. The number of the Gaussian curves represent: 1 for the 0-0 band; 2 for the excimer formation; and 3 for the aggregation band.

7.2.3 Comparison of Device Characteristics

Organic LEDs were made by both the LB technique and the spin coating method. The film thickness was 250 nm for the LB film and 120 nm in the case of the spun film. Current versus voltage characteristics of both devices are compared in Figure 7.3; plots of quantum efficiency against current density are inset.

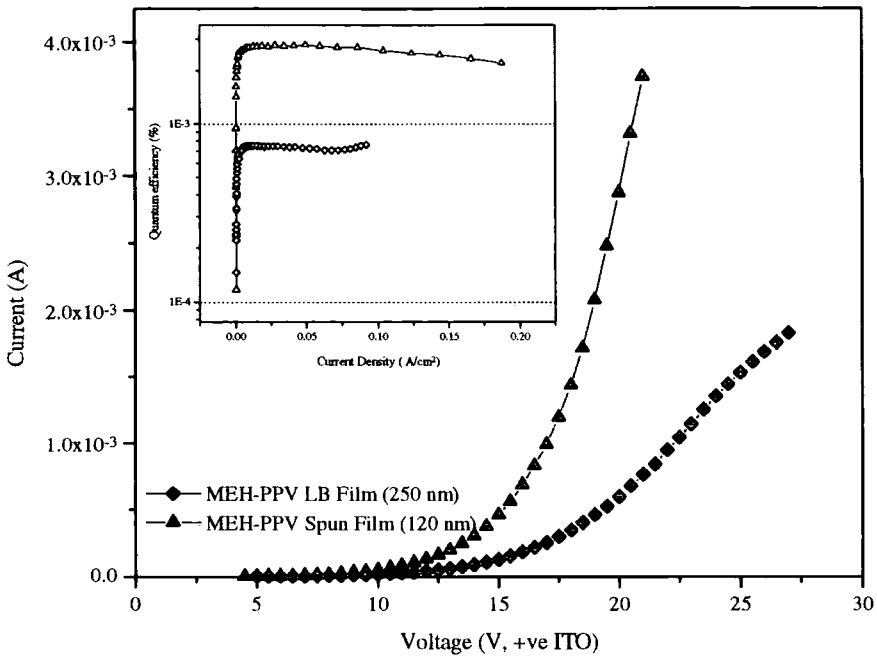

Figure 7.3 I-V characteristics of devices with MEH-PPV LB and spun films. The quantum efficiency against current density for both devices is inset.

For the two devices shown, the quantum efficiency of the structure made with the spun film, 2.8×10^{-3} %, is four times higher than that of the LB-based LED, 7.3×10^{-4} %. Measurements of a number of devices with different film thicknesses revealed that LEDs based on the spun films always possessed higher efficiencies than those fabricated with LB films. The quantum efficiencies of the latter devices were usually of the order 10^{-4} % compared to 10^{-3} % for the former devices. The lower quantum efficiency of the LB film device can be explained by increased excimer

formation, as discussed in the previous section. This results in nonradiative decays, reducing the device quantum efficiency.

Spun films retain a degree of aggregation in solution, in which the bulky side chains have a high degree of freedom for rotation, hindering the π-π stacking of the polymer backbone. This decreases the backbone planarity, lowering the conjugation length. The reduced conjugation length results in a decrease of the exciton mobility along the conjugated backbones. Consequently, more efficient confinement of excitons in the conjugated segments can be achieved, preventing the nonradiative decay [5]. It was reported that the degree of aggregation of MEH-PPV solution was affected by the solvent and the solution concentration [6]. Therefore, it is important to choose an appropriate solvent so as to minimise the polymer aggregation and improve the quantum efficiency.

The LB film consists of a closely packed ordered phase in which the polymer backbones cannot move freely. This elongates the conjugation length within the polymer backbones. As the conjugation length increases, the excitons have more chances of encountering quenching sites and consequently, recombining nonradiatively while moving along the polymer backbone. The LB films also contain moisture which causes some chemisorption and adsorption of water on the Al electrode. It has been shown previously that the work function of Al increases by chemisorption of water [7]. This phenomenon can increase the energy barrier for electron injection, leading to lower device quantum efficiency.

The EL spectra of the two devices are similar (Figure 7.4). The EL peak of the device with the LB film is slightly red-shifted compared to the device with the spun

film. This illustrates that the excitons in the LB device move along a longer conjugated polymer backbone losing some of their energy before radiative decay.

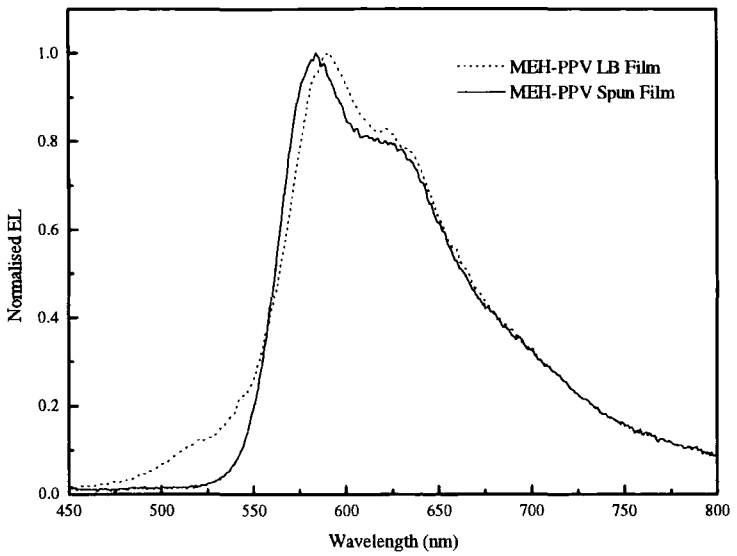

Figure 7.4 EL spectra of MEH-PPV LB and spun films.

7.2.4 Device Operating Lifetime

Electrical stress tests were carried out with the two devices described above. The luminance decay of both devices is compared in Figure 7.5. A constant voltage of 18 V was applied to both structures. The initial electric load (V × J) was: 0.38 W cm^{-2} for the LB film device; and 0.75 W cm^{-2} for the device based on the spun film. The light output from the device with the LB film decreased rapidly and no light output could be measured after 4 hours due to the device breakdown. The light output from the device with the spun film shows a different behaviour with time. This diminished rapidly over the first 5 minutes. Following this, the light output decreased monotonically with an increasing luminance decay rate.

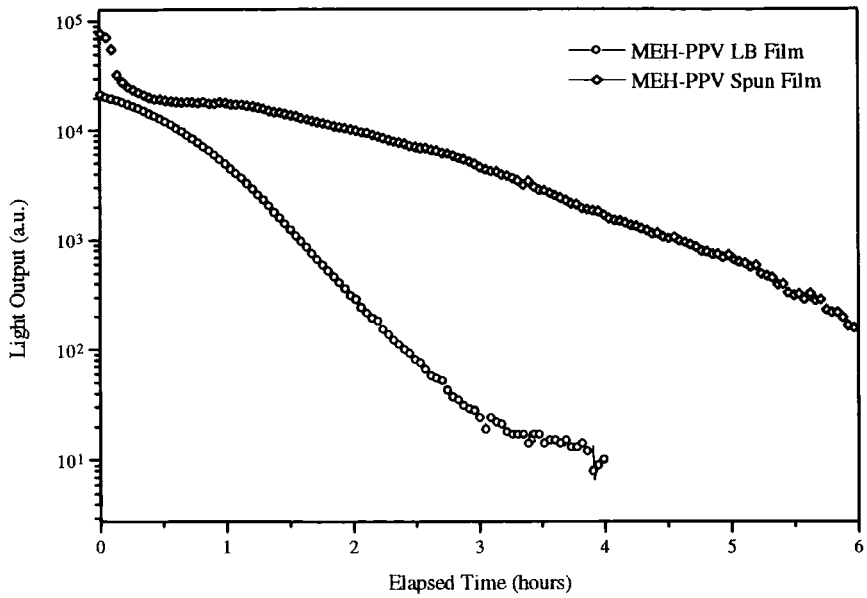

Figure 7.5 Luminance decay for LEDs with MEH-PPV spun and LB films. A constant voltage (18 V) was applied to the devices.

As discussed in the Section 6.4, the device lifetime is affected by the film roughness. Although the LB technique is an excellent method for controlling the precise film thickness, the polymer LB films possess a relatively uneven surface as mentioned previously in Section 5.2.3. Higher currents flow through the thinner regions, eventually leading to localised breakdown. The surface profile of a spun film, shown in Figure 7.6, can be compared with that of an LB film (figure 6.24). The surface of the spun film is very smooth with a roughness index, R_a, < 5 nm, which is superior to the R_a value of 44 nm for the LB film. It is therefore anticipated that a uniform electric field is distributed over the device area.

Scanning electron micrographs of both films, with magnifications of 1500, also show that the surface of spun film is very flat and uniform whereas the surface of LB film includes many features, Figure 7.7.

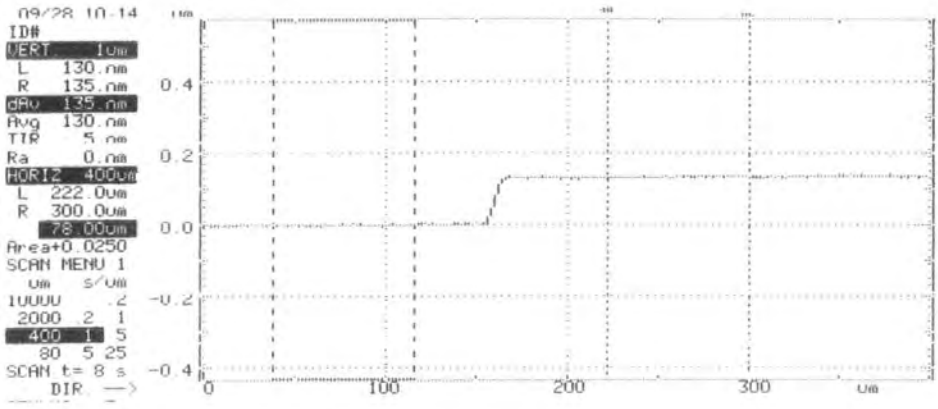

Figure 7.6 Surface profile of MEH-PPV spun film

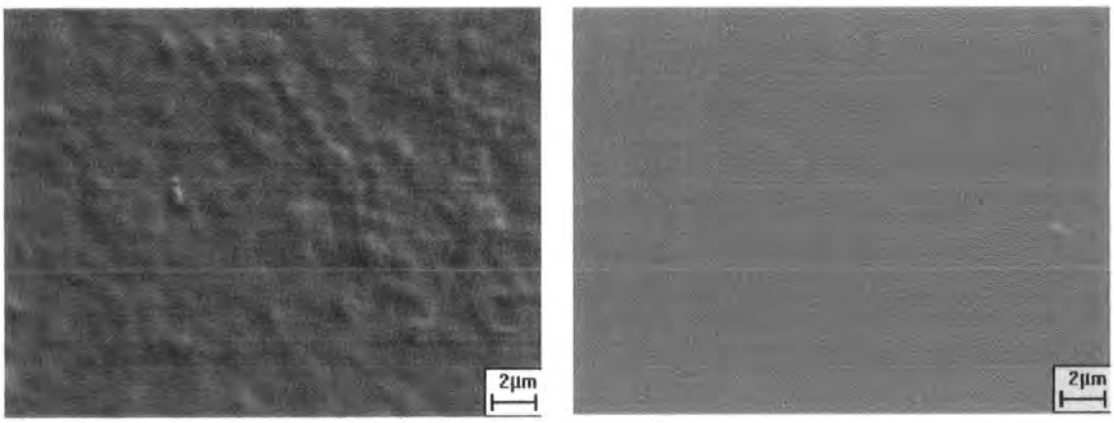

(a) (b)

Figure 7.7 SEM images of (a) an MEH-PPV LB film and (b) an MEH-PPV spun film. The magnification is 1500.

7.3 Dual-Layer Devices

7.3.1 Background

1,3,4-Oxadiazole (OXD) has been incorporated as an electron injecting and hole blocking material in organic LEDs. Its derivative, 1,3-bis[2-(4-*tert*-butylphenyl)-1,3,4-oxadiazol-5-yl]benzene (OXD-7) has been used as a popular electron transporting material and has resulted in a significant improvement in device

performance [8]. Pyridine is an electron deficient compound and has also formed the basis of an efficient electron transporting layer [9]. Higher electron-injection ability could reasonably be expected from a hybrid of pyridine and oxadiazole. C.S. Wang et al. has, therefore, synthesised a new bis-OXD system incorporating pyridine, 2,5-bis[2-(4-*tert*-butylphenyl)-1,3,4-oxadiazol-5-yl]pyridine (PDPyDP) [10].

For our initial experiments, devices with electron transporting layers, such as PDPyDP or OXD-7, were fabricated and compared with a single layer MEH-PPV device.

7.3.2 Device Structure

The chemical structures of all the organic compounds used in this section are shown in Figure 7.8. OXD-7 and PDPyDP were synthesised in Durham.

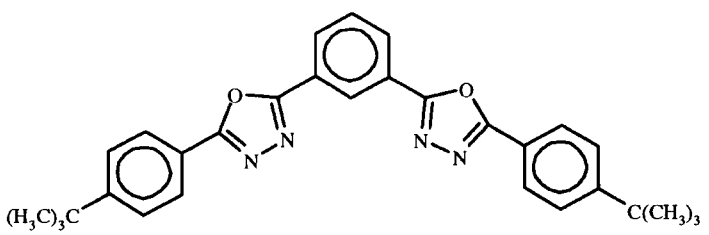

OXD-7

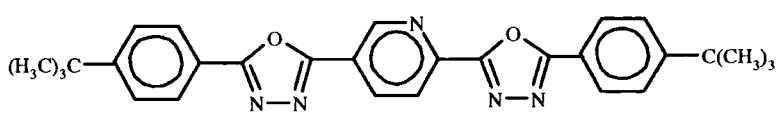

PDPyDP

Figure 7.8 Molecular structures of OXD-7 and PDPyDP.

The MEH-PPV solution was made using the method described in the previous section. A film of dry thickness ca. 120 nm was formed for the single layer devices while a film of ca. 80 nm thickness was spin-coated for the dual-layer device.

The second layer of electron-injecting material was thermally evaporated at a pressure of 10^{-6} mbar using an evaporation rate of 0.1 - 0.2 nm s^{-1}. Each compound was placed in a glass crucible and the temperature was monitored by an attached thermocouple. The sublimation temperature was 160 °C for both the PDPyDP and OXD-7 and the film thickness of both films was around 60 nm. The film thickness was monitored using a quartz crystal sensor.

7.3.3 Device Characteristics

Three devices, using spin-coated MEH-PPV as the emissive material, were fabricated: pure MEH-PPV (thickness 114 nm); MEH-PPV/OXD-7 (150 nm) and MEH-PPV/PDPyDP (143 nm). The current versus electric field characteristics of these devices are compared in Figure 7.9 and plots of their quantum efficiencies against current density are inset. The curves for the dual-layer device are shifted to lower electric field compared to that of MEH-PPV single layer device.

At a current density of 25 mA cm^{-2}, the quantum efficiency of each device is: 2×10^{-3} % for MEH-PPV, 2.2×10^{-2} % for MEH-PPV/OXD-7 and 9.3×10^{-2} % for MEH-PPV/PDPyDP. Dual-layer devices incorporating electron transporting layers can therefore improve the external quantum efficiency by up to two orders of magnitude compared to the single layer device. This improvement can be explained by an increase in electron injection owing to a lower energy barrier between LUMO level of the electron transporting layer and the Al Fermi level. The quantum efficiency of the MEH-PPV/PDPyDP device is nearly a factor of five higher than that of the device containing the OXD-7, illustrating the higher electron transporting ability of PDPyDP over OXD-7.

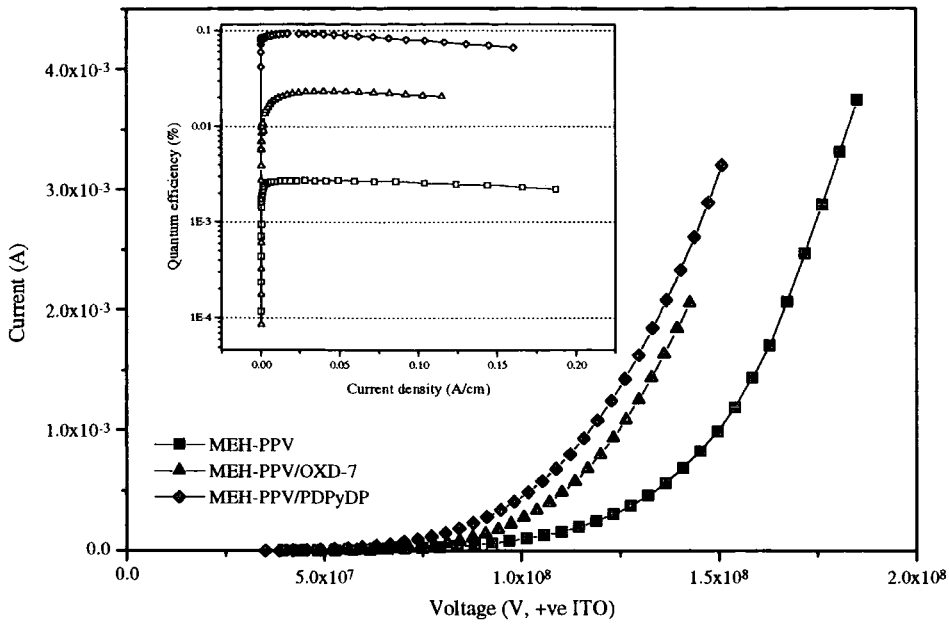

Figure 7.9 Currents versus electric field of the single and dual-layer LEDs. Plots of external quantum efficiencies against current density are inset.

This increased electron transporting ability could be the result of two possible effects. First, the electron deficient pyridine ring decreases the LUMO level of PDPyDP more than that of a benzene ring. Therefore, the energy barrier for electron injection is decreased. Secondly, higher electron mobility in PDPyDP is expected than in OXD-7. Wang et al. [10] showed that PDPyDP molecules are packed parallel to each other so that the overlap of molecular orbitals of PDPyDP molecules in the solid state is enhanced. In contrast, OXD-7 molecules have lower degree of intermolecular interactions in the solid state.

The light output versus electric field for the three devices is shown in Figure 7.10. The turn-on electric field of MEH-PPV/PDPyDP is lowest of all devices (MEH-PPV: 1.32×10^{8} V m^{-1}, MEH-PPV/OXD-7: 9.4×10^{7} V m^{-1} and MEH-PPV/PDPyDP: 6.2×10^{7} V m^{-1}). The device incorporating PDPyDP has a lower turn-on electric field than the device with OXD-7, supporting the hypothesis described above.

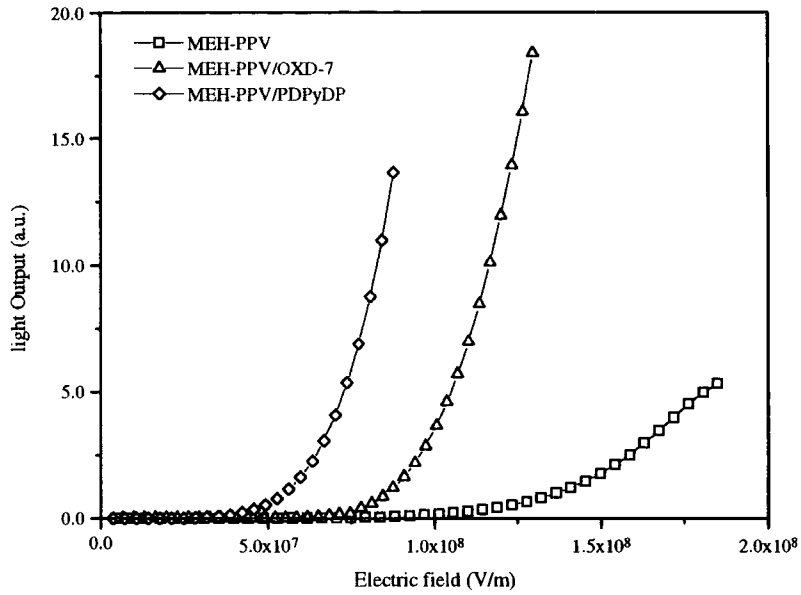

Figure 7.10 Light output versus electric field for the LEDs.

The normalised EL spectra of the dual-layer devices are identical to that of MEH-PPV single-layer device (Figure 7.11). This shows that, in dual-layer devices, electrons move into the MEH-PPV layer and recombine with holes to produce the light output.

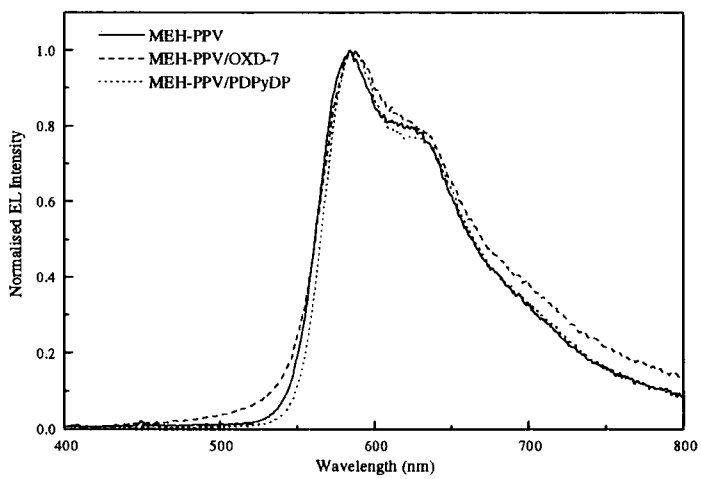

Figure 7.11 EL spectra of the devices.

7.3.4 Dark Area Formation in the EL Image

Despite the higher quantum efficiency, the devices incorporating a PDPyDP layer were not stable. The device current decreased rapidly after one day storage (with no applied bias) in a low vacuum (10^{-1} mbar) as shown in figure 7.12(a). A photograph of the EL emission taken through the ITO one day after evaporating the Al top electrode, is shown in figure 7.12(b). Dark areas, which produced EL emission when the device was freshly made, increased rapidly in area with storage time. However, the light output decreased at a similar rate to the current, resulting in no particular change in the external quantum efficiency. No light was emitted after 2 days of storage.

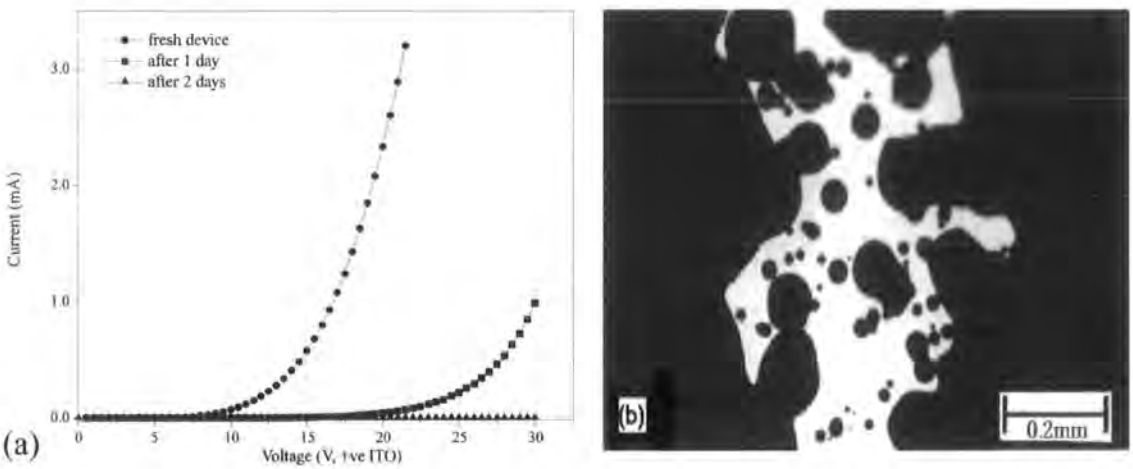

Figure 7.12 (a) Current versus voltage characteristics measured at various times for a MEH-PPV/PDPyDP device and (b) EL image (viewed through the ITO electrode) one day after Al evaporation.

Two possibilities may explain this device degradation: one is decomposition or chemical interaction between the PDPyDP layer and Al electrode, leading to a loss of the material properties as an electron transporting material; the other explanation is poor adhesion of the PDPyDP layer to the Al electrode resulting in detachment of the

Al electrode from the PDPyDP layer. The next sections will describe several ways to increase the stability of the dual-layer device.

7.4 Rubrene Doping of MEH-PPV

7.4.1 Background

By adding an appropriate dopant to an organic layer, the energy barrier at the organic/organic interface can be lowered, resulting in higher efficiencies and longer operating lifetimes. For example, it has been reported that the lifetime of Alq_3/TPD EL devices can be greatly improved by rubrene(Ru) doping of either the Alq_3 or the TPD layer [11,12].

7.4.2 Device Characteristics

Rubrene was purchased from the Aldrich Co. and its molecular structure is shown in Figure 7.13. A mixture of rubrene and MEH-PPV, with different ratios by weight, was dissolved in a mixed solvent consisting of 50 % chloroform and 50 % *p*-xylene and sonicated for several hours to disperse the rubrene in the host material. A rubrene-doped MEH-PPV (MEH-PPV(Ru)) layer was formed by spin-coating.

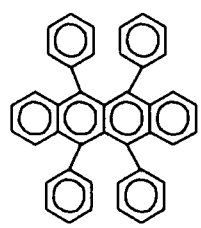

Figure 7.13 Molecular structure of rubrene.

Figure 7.14 shows the graph of current against electric field for devices with different doping percentages of rubrene. The current at a fixed field becomes smaller with increased doping of rubrene and reaches a minimum with the 30 % rubrene doped device. Above this doping level, the current increases and is slightly higher than that of the undoped device at the doping percentage of 50 %.

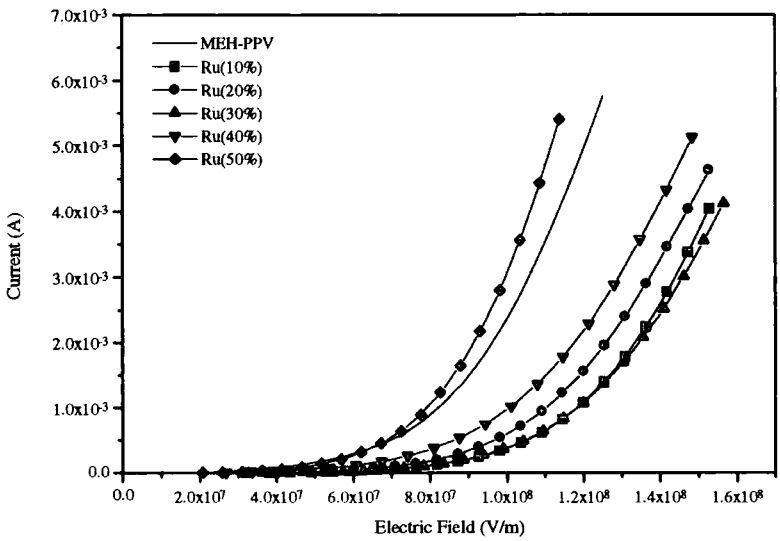

Figure 7.14 A comparison of the current-electric field characteristics and quantum efficiency for rubrene-doped and undoped MEH-PPV devices.

The lower device current (doping percentage < 30 %) may be explained by consideration of energy levels of the rubrene (LUMO : -3.2 eV, HOMO : -5.4 eV [13]), when compared to those of MEH-PPV (LUMO : -2.8 eV, HOMO : -4.9 eV [14]). Majority carriers, holes, can be injected into the HOMO level of the MEH-PPV and migrate to neighbouring molecules and consequently move towards the cathode. Meanwhile, rubrene molecules act as randomly distributed hole traps resulting in a decrease in the device current as shown in Figure 7.15. At high doping levels, the distance between rubrene sites becomes small and trapped holes can be transferred, via the rubrene, towards the cathode without release to the MEH-PPV. The higher

current seen at over 50 % doping is ascribed to hole transfer via both the materials. Other groups [13,15] have reported a decrease of current with increasing concentration of rubrene doping in both single-layer and dual-layer devices.

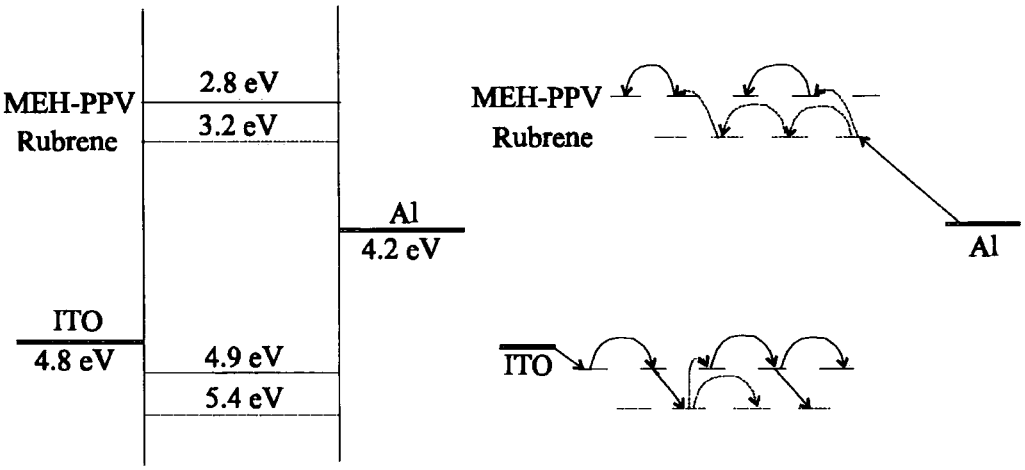

Figure 7.15 Schematic representation of (a) the energy levels of the materials and (b) hole and electron transporting process in a rubrene-doped MEH-PPV device.

The 20 % rubrene-doped device has the highest external quantum efficiency - 1.4×10^{-2} %, one order of magnitude higher than the undoped device (2.0×10^{-3} %) at a current density of 0.1 A cm^{-2} (Figure 7.16). Above 20 % doping, this value decreases with increasing doping level of rubrene. The high efficiency is due to reduced excimer formation with increasing doping as shown in the PL spectra excited at 420 nm (Figure 7.17). Dilution of the conjugated polymer by blending with an inert polymer has been reported to hamper the interchain transport or excimer formation [16]. The rubrene film has a PL peak at 580 nm. In the doped films, the emission originates from the MEH-PPV regardless of the doping level.

In a highly doped system, both charges can be trapped in rubrene and transferred towards the opposite electrode via adjacent rubrene molecules without energy transfer to emissive material, MEH-PPV. This results in poor emission.

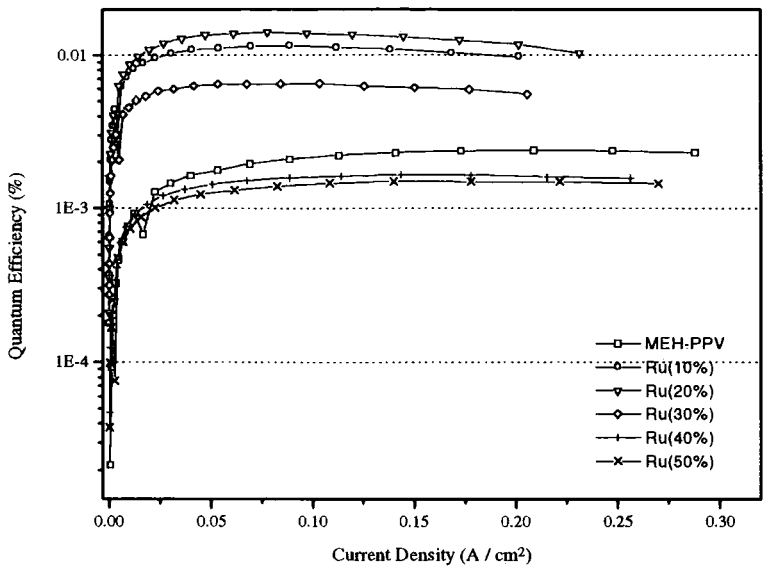

Figure 7.16 Plots of quantum efficiency versus current density for devices with various doping ratio of rubrene.

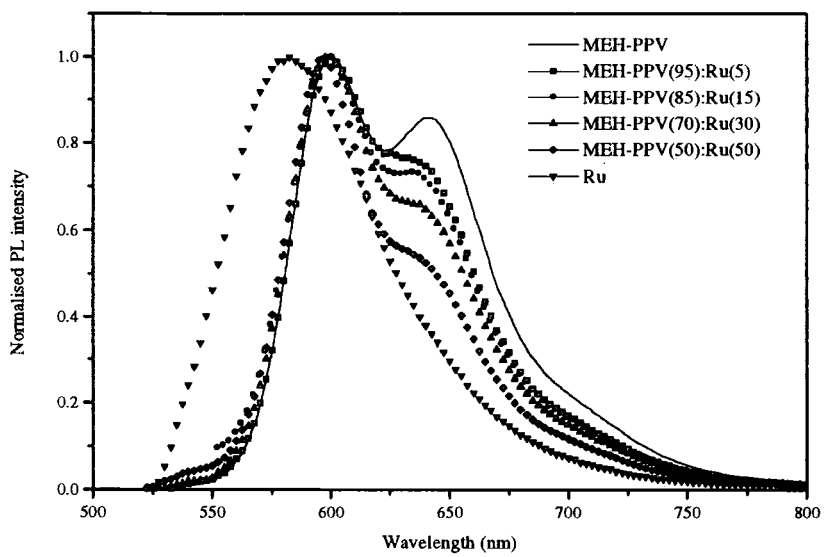

Figure 7.17 PL spectra of MEH-PPV(Ru) with various doping ratio of rubrene.

The electroluminescence spectra (Figure 7.18) of the doped devices show the same features as the PL spectra. The excimer band, near 630 nm, is reduced with increasing doping level and the EL emission originates from the MEH-PPV regardless of doping percentage. This is in contrast to other reports in which EL comes from

dopant which has much lower bandgap located inside the energy levels of the host material [11,17].

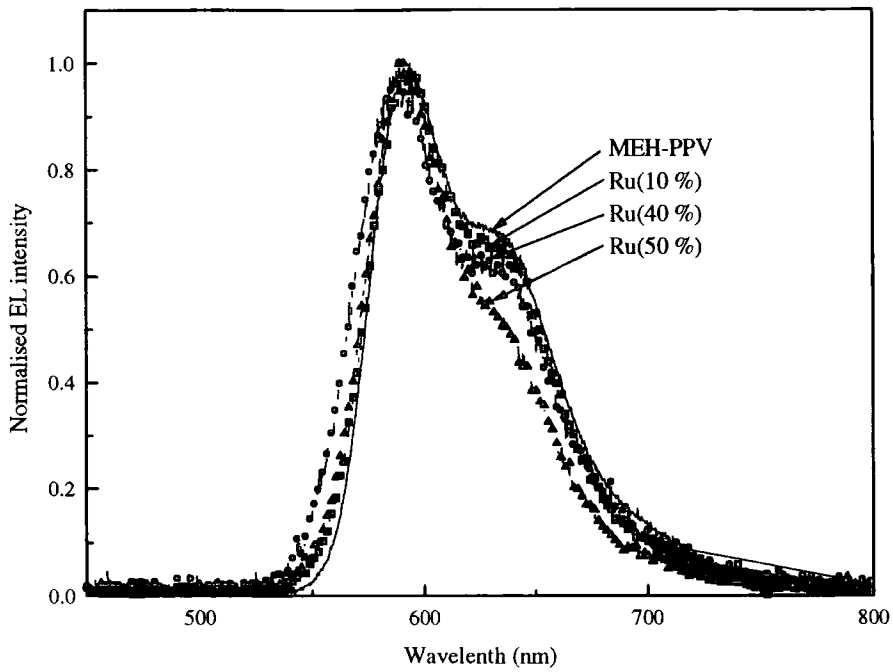

Figure 7.18 EL spectra of MEH-PPV devices with various doping ratio of rubrene.

7.4.3 Device Operating Lifetime

Lifetime or luminance measurements were undertaken with a constant current of 0.2 mA through both the rubrene-doped (20 %) and undoped MEH-PPV devices (N.B. Figure 7.19 contrasts with the constant voltage experiment shown in Figure 7.5). The initial electric loads were 0.14 W cm^{-2} and 0.16 W cm^{-2} for the undoped and rubrene-doped devices. The initial luminance of the rubrene-doped device is one order of magnitude higher than that of the undoped device. In the case of the doped device, the initial voltage of 15.5 V changed to 17 V after 10 hours to maintain the constant current. In contrast, the voltage across the undoped device increased from 13.7 V to

17 V over 6 hours and then increased rapidly up to 37 V, breaking down the device after 8 hours.

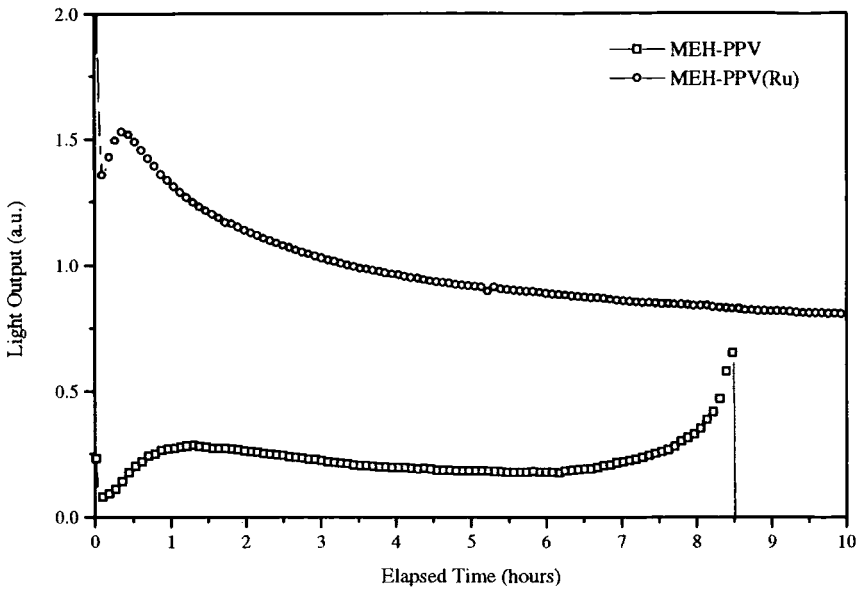

Figure 7.19 Luminance decay of both rubrene-doped and undoped MEH-PPV devices at a constant current of 0.2 mA.

In conclusion, by doping rubrene into MEH-PPV (20 % by weight), the lifetime increases and the external quantum efficiency increases by one order of magnitude.

7.5 Use of Interfacial Layers

7.5.1 Background

The two electrode interfaces in the LED structure are very important since the contacts between the metals and the organic layers can be generally poor. To improve this, a copper phthalocyanine (CuPc) layer was introduced between the anode and the MEH-PPV, and an additional electron transporting layer of Alq_3 between the PDPyDP layer and the Al top electrode. A CuPc layer has been deposited on ITO

with a good coverage and was observed to improve hole injection and to enhance device lifetime [12]. An Alq_3 layer has been reported to form metal-Alq_3 complexes at the cathode/organic interface [18], which could prevent poor adhesion of the organic layer to the cathode.

7.5.2 Device Structures

CuPc and Alq_3 were purchased from the Aldrich Co. Their chemical structures are shown in Figure 7.20. These materials were also thermally evaporated at a rate of 0.1 ~ 0.2 nm s^{-1}, at 290 °C for CuPc and 185 °C for the Alq_3.

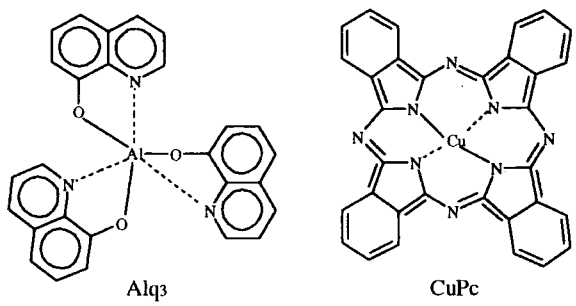

Figure 7.20 Molecular structures of Alq_3 and CuPc.

Three LED structures were fabricated in addition to the MEH-PPV(Ru)/PDPyDP device. The devices were: (I) MEH-PPV(Ru)/PDPyDP reference device; (II) CuPc/MEH-PPV(Ru)/PDPyDP; (III) MEH-PPV(Ru)/PDPyDP/Alq_3; and (IV) CuPc/MEH-PPV(Ru)/PDPyDP/Alq_3. The individual layer thicknesses were: MEH-PPV(Ru) ≈ 80 nm; PDPyDP ≈ 60-70 nm; CuPc ≈ 15 nm; Alq_3 ≈ 30 nm. This resulted in total organic layer thickness of: device (I) - 150 nm; device (II) - 163 nm, device (III) - 170 nm; and device (IV) - 200 nm. Device (IV) had a thicker Alq_3 layer

resulting in a total thickness of both electron transporting layers. The LED structure for device (IV) is shown schematically in Figure 7.21.

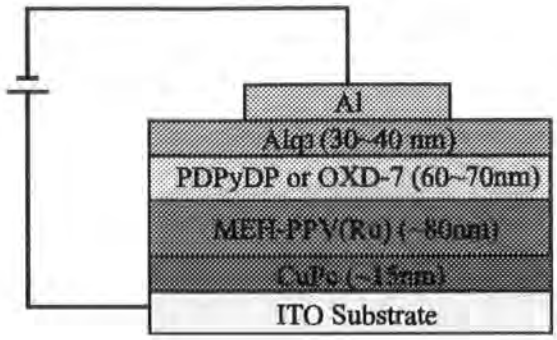

Figure 7.21 Structure of multilayer LED.

7.5.3 Device Performance

The electrical characteristics and quantum efficiency of the devices are shown in Figure 7.22. The electrical characteristics of the devices incorporating the CuPc buffer layer are shifted to lower electric fields as compared to the devices without it. This result may be explained in terms of a lower injection barrier for holes at the ITO/hole transporting layer interface – the ionisation potential for CuPc (4.7 eV, [19]) is reported to be better matched to the workfunction of ITO (4.7 eV) than the HOMO level of MEH-PPV (4.9 eV). A similar result was reported by Karg et al. [20] for a device incorporating a hole buffer layer, polyaniline (PaNi).

The electric field required to give light emission is 2.0×10^{7} V m^{-1} for the reference device, 1.2×10^{7} V m^{-1} for the device incorporating the CuPc, 3.5×10^{7} V m^{-1} for the device with the Alq_3 and 2.7×10^{7} V m^{-1} for the device including both buffer layers.

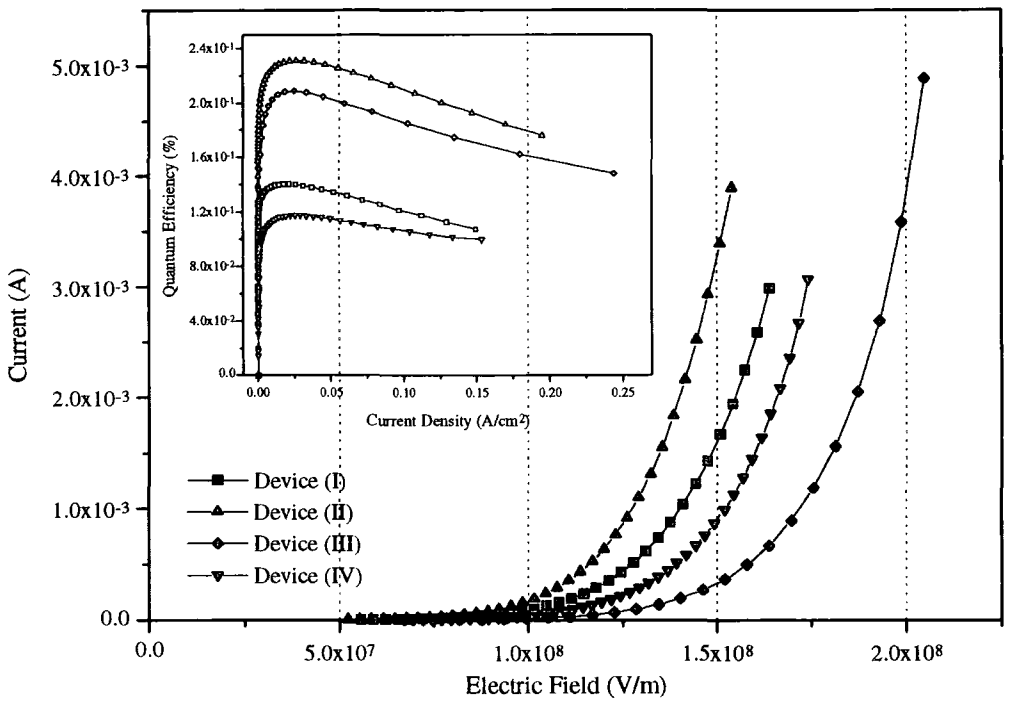

Figure 7.22 Current versus electric field characteristics for LEDs incorporating CuPc and Alq_3 layers.

The quantum efficiencies of these structures, measured at a current density of 10 mA cm^{-2}, are: device (I) - 0.14 %; device (II) - 0.26 %; device (III) - 0.21 %; and device (IV) – 0.11 %. Device (II), with a CuPc layer, has a lower turn-on threshold electric field and a twofold increase in external quantum efficiency as compared to the reference device. Vestweber et al. [21] have observed similar effects for LEDs containing a CuPc buffer layer. The external quantum efficiency of device (IV), incorporating the CuPc layer, has a lower value than that of device (III) without it. This could be attributed to the migration of less electrons to the emission zone, resulting in unbalanced charge carriers. More electrons are liable to be trapped during migration in thicker electron transporting layers.

Orange-yellow light was easily visible under ambient lighting conditions from all the devices studied. The EL spectra are shown in Figure 7.23. In each case, there is

a peak at 590 nm together with a shoulder at 630 nm, coincident with the output of the MEH-PPV single layer device. This suggests that in all device structures, recombination of excitons takes place radiatively in the MEH-PPV.

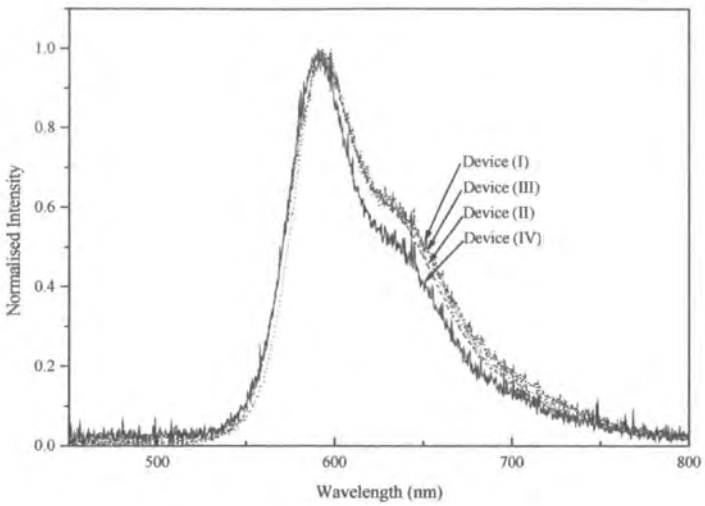

Figure 7.23 EL spectra of the LEDs.

To date, a maximum quantum efficiency of 0.7 % has been achieved with the MEH-PPV(Ru) (100 nm)/PDPyDP (60 nm) structure and a maximum brightness of 4040 cd m^{-2} at the current density of 0.3 A m^{-2}. The photograph of the EL emission from this structure is shown in Figure 7.24. Notably, a great deal of the emitted light was waveguided to the glass edge.

Figure 7.24 Photograph of EL emission for the MEH-PPV(Ru)/PDPyDP structure.

7.5.4 Dark Area Formation (Storage Lifetime)

The current in the CuPc-containing device (II) decreased over a period of one day in a similar fashion to the reference device (Figure 7.25(a)). This device also degraded rapidly after one day storage as shown in Figure 7.25 (b). In contrast, the characteristics of the device incorporating Alq_3 between the PDPyDP and the Al (device (III)) were more stable, as shown in Figure 7.25(c). The EL image of this device, shown in Figure 7.25(d) (again, measured after storage in a low vacuum and with no applied bias) reveals much fewer dark areas compared with the device without the Alq_3 layer. Figure 7.25(f) shows the EL image of the device containing both CuPc and Alq_3 (device (IV)). There are now comparatively few dark regions. In fact, the device current even increased after one day storage and then decreased slowly (Figure 7.25(e)). A number of devices with different thicknesses of the Alq_3 layer revealed that the dark area formation was reduced with increasing the thickness of the Alq_3 layer. The fewer dark areas of device (IV) compared to device (III) is attributed to the thicker Alq_3 layer. These results support the hypothesis that the dark regions in the EL image are associated with the interface between PDPyDP and the Al top electrode.

McElvain et al. [22] reported the diminution of dark region growth in dry nitrogen conditions. It was suggested that the penetration of oxygen and moisture through pin-holes in the top metal degraded the adhesion of the electrode to the adjacent organic layer. The reduction of dark areas by insertion of an Alq_3 layer can then be explained by superior adhesion of this compound to the Al electrode, e.g. via Alq_3-metal complex chemical bonding [18].

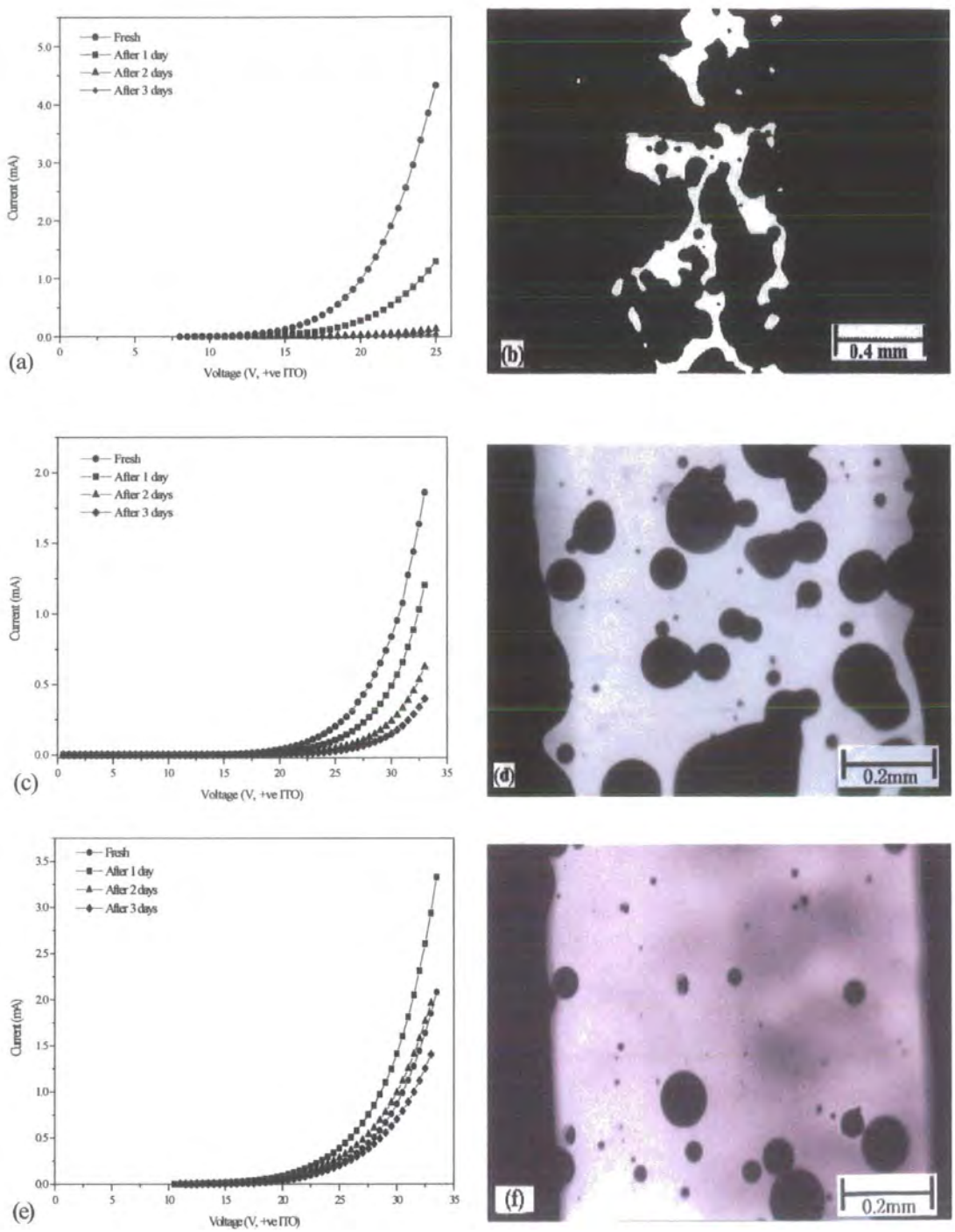

Figure 7.25 Current versus voltage characteristics of (a) CuPc/MEH-PPV(Ru)/PDPyDP, (c) MEH-PPV(Ru)/PDPyDP/Alq_3, and (e) CuPc/MEH-PPV(Ru)/PDPyDP/Alq_3 at various times. EL images of (b) CuPc/MEH-PPV(Ru)/PDPyDP, (d) MEH-PPV(Ru)/PDPyDP/Alq_3, and (f) CuPc/MEH-PPV(Ru)/PDPyDP/Alq_3 after one day storage (no voltage applied) in a low vacuum.

7.5.5 Operating Lifetime

A different degradation experiment was undertaken by measurement of the EL output over time under an electrical stress (i.e. in contrast to the storage experiments described above). A constant d.c. current of 0.2 mA, equivalent to a current density of 10 mA cm^{-2}, was passed through all the devices and the EL output monitored as a function of time. The results are shown in Figure 7.26. The resulting half-lives (initial voltage) were: device (I) - 1 h (19.2 V); device (II) - 11 h (18.3 V); device (III) - 4 h (23.4 V); and device (IV) - 35 h (26 V). The half lifetime for device IV was calculated by extrapolation within the stabilized region.

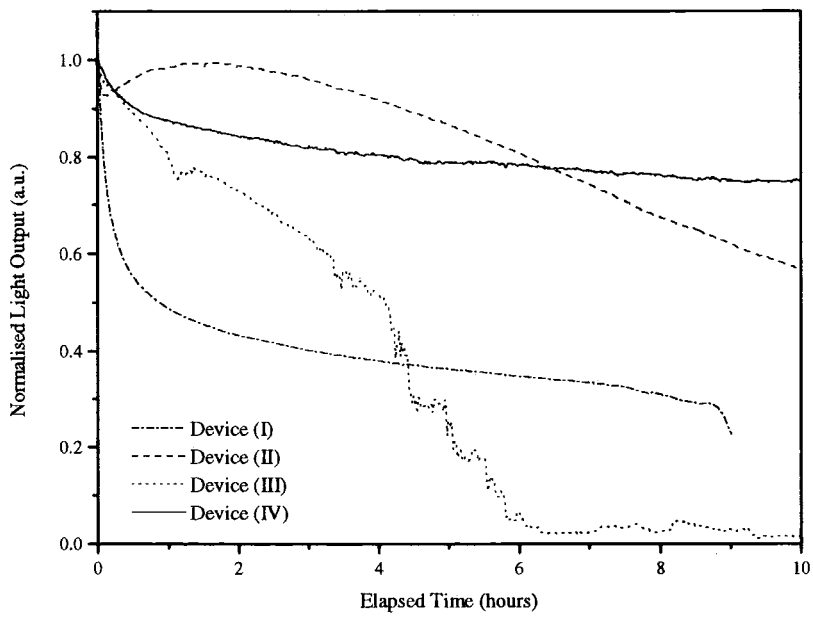

Figure 7.26 Luminance decay of LEDs with constant current of 0.2 mA.

The MEH-PPV(Ru)/PDPyDP/Alq_3 device had completely degraded after six hours. This device had a shorter lifetime than the reference device (9 hours) because of the higher initial voltage, which induced a higher initial electric field throughout the

device. When the Al electrode was viewed under an optical microscope, it was evident that the metal layer had 'erupted' in many places, presumably due to local heat dissipation. This type of degradation is different from that seen in the storage experiments, in which the Al electrode remained continuous but possibly became delaminated from the electron-transporting layer.

Figure 7.26 reveals that incorporation of a CuPc buffer layer can significantly improve the operating lifetime of the LEDs, considering the high initial voltage of 26 V applied in device (IV). Several authors have offered explanations for the increased lifetime by using a CuPc buffer layer. For example, Adachi et al. [23] showed a reciprocal relationship between the lifetime and the energy barrier to holes at the ITO interface. A large energy barrier to hole injection at the ITO/hole transporting layer interface results in joule heating. This in turn causes local aggregation of molecules and possibly crystallisation of the hole transporting material. From this point of view, a low energy barrier to hole injection is a prerequisite to prolong the device lifetime. Here, CuPc layer has a lower hole injection barrier by 0.2 eV compared to the MEH-PPV layer.

Scott et al. [24] have suggested that an indium-tin oxide (ITO) anode provides a source of oxygen. This can cause a reaction with the adjacent charge transporting material that is detrimental to the device performance. For example, a loss of conjugation length can occur by a chemical reaction of the oxygen with the vinyl carbon by the formation of C=O groups. Yan et al. [25] reported that the presence of these groups was inversely correlated to PL quantum yield and the device lifetime. It has been shown that it is advantageous to incorporate a very thin buffer layer of a material such as copper phthalocyanine (CuPc) [18] or polyaniline (PaNi) [26]

between the ITO and the hole transporting layer. As well as providing increased hole injection, the buffer layer also prevents oxygen from penetrating into the emissive material.

There is a further explanation. The surface morphology of ITO is notoriously uneven. Evaporation of the CuPc layer may produce a much smoother electrode surface. This would result in a more even electric field distribution in the LED and reduce the number of high field regions which could lead to localised breakdown.

7.6 Annealing Experiments

The device degradation is attributed to a poor contact between the PDPyDP layer and the Al top electrode. Lee et al. [27] demonstrated that post-deposition annealing improved the adhesion of the top Al electrode to the underlying organic film (MEH-PPV) by promoting the formation of particular chemical bonds. This enhanced interfacial adhesion increased the effective area for electron injection, leading to more balanced charge injection. Therefore, we have studied the effects of heat treatment on dual-layer LEDs using already degraded MEH-PPV(Ru)/PDPyDP devices.

7.6.1 Experimental Details

Dual-layer devices were fabricated by thermal evaporation of PDPyDP (≈ 50 nm) onto spun films of MEH-PPV(Ru) (≈ 80 nm). After measuring the I-V characteristics of fresh devices, the devices were stored in a low vacuum chamber (10^{-1} mbar). Some devices were kept in air to investigate the effect of oxygen/moisture in air on the dark area formation. Annealing was performed on the samples stored in a

low vacuum for three days after fabrication. Samples were attached to a heated plate in a low vacuum chamber. Different annealing temperatures of 140 °C, 160 °C, 175 °C and 195 °C were used for 30 minutes on each sample. The growth of the dark areas in the EL image was recorded using a camera mounted on an optical microscope (×10 magnification) in a dark room. The EL light projected through the ITO glass to the camera with an exposure time of two minutes.

Quartz/MEH-PPV(Ru)/PDPyDP structures were made for the UV-Vis. and PL spectra measurements, respectively, to see whether the device degradation originated from a chemical or physical change.

7.6.2 Comparison of Dark Area Growth for Devices Stored in Air or in Vacuum

The current decrease of a device stored in air is compared with that of a device stored in a low vacuum in Figure 7.27.

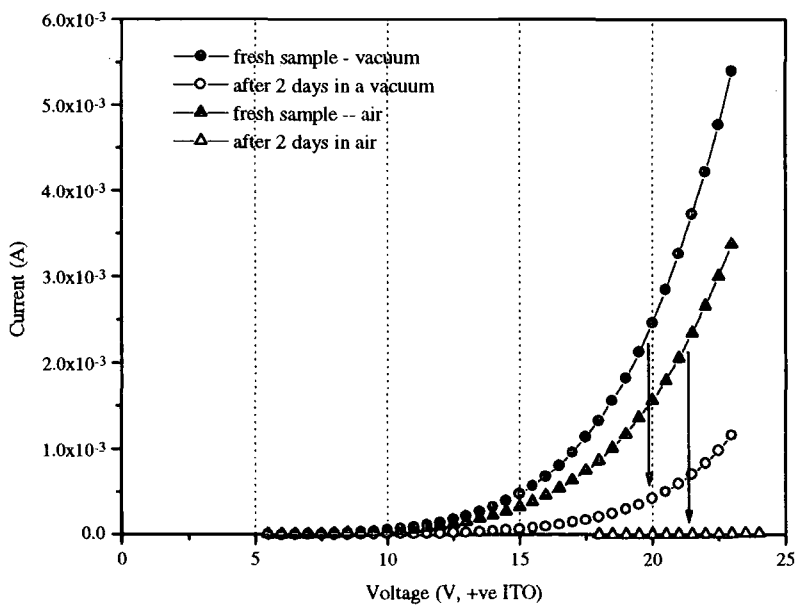

Figure 7.27 Comparison of I-V characteristics between devices kept in air and in vacuum.

The current in the device stored in air decreased from 3.4 mA to 11 μA at 25 V after 2 days storage. In contrast, the current of the device stored in vacuum decreased from 5.4 mA to 1.2 mA at 25 V after 2 days storage. This result suggests that air and/or moisture have an effect on the device stability by penetration through the Al electrode and stimulating the delamination of the Al electrode from the PDPyDP layer. The current drop was accompanied by an increase in the dark area formation in the EL image. Aziz et al. [28] reported that this kind of dark formation was independent of the electrical bias but was accelerated by increasing the humidity in the atmosphere.

7.6.3 Effect of Annealing on I-V Characteristics

The degraded samples (stored in a low vacuum for 3 days after Al evaporation) were annealed at different temperature for 30 minutes. The I-V characteristics are shown in Figure 7.28(a) and their light outputs against voltage are shown in Figure 7.28(b). The turn-on voltage for EL is 2 ~ 2.5 V in all devices. Both the current and light output versus voltage curves were shifted to higher voltages after storage (no applied bias). However, following suitable heat treatment, these characteristics approached those of a freshly fabricated device. In fact, annealing for 30 minutes at 195 °C almost fully restored the current versus voltage curve. There seems to be no particular device improvement below the sublimation temperature of the electron transporting layer (≈ 160 °C). The light output also increased to reach a maximum when annealed at 160 °C, but decreased if the annealing temperature was over 160 °C (Figure 7.28(b)).

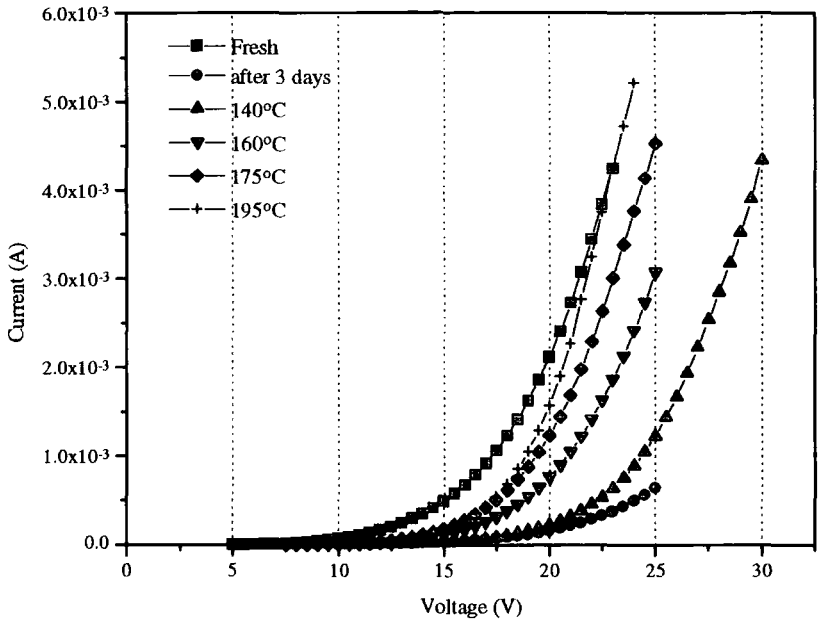

(a)

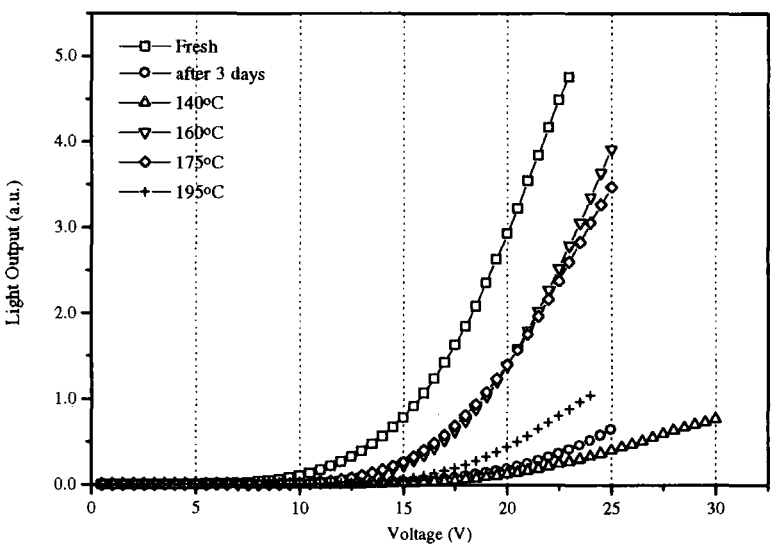

(b)

Figure 7.28 (a) I-V characteristics of devices subjected to annealing at various temperature and (b) light output versus voltage characteristics.

Figure 7.29 shows the quantum efficiency versus current density plots of the devices annealed at various temperatures. The quantum efficiencies of the devices, measured at a current density of 10 mA cm^{-2}, were: 2.4×10^{-1} % for the fresh device;

1.8×10^{-1} % for the device following storage for three days in vacuum; 8.0×10^{-2} % after annealing at 140 °C, 3.1×10^{-1} % after annealing at 160 °C, 2.2×10^{-1} % after annealing at 175 °C and 6.6×10^{-2} % after annealing at 195 °C. From an efficiency viewpoint, annealing at 160 °C appears to be the optimum process.

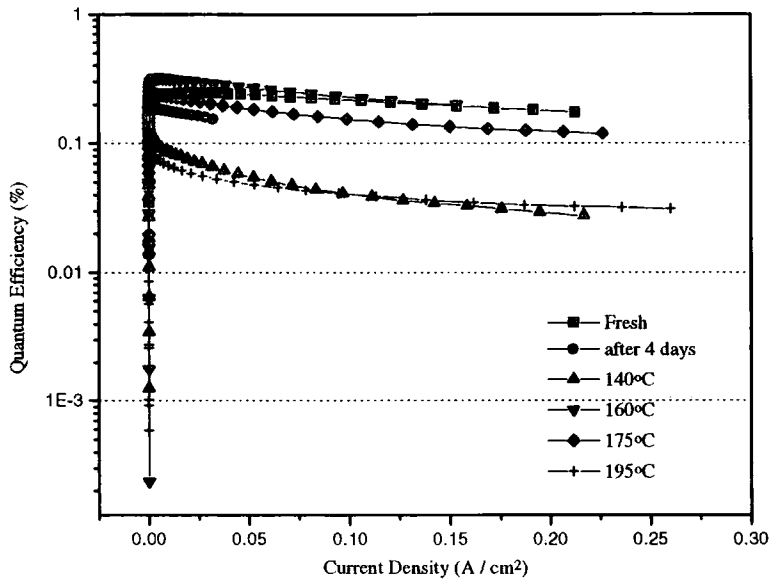

Figure 7.29 Quantum efficiency of the devices annealed at various temperatures.

7.6.4 Effect of Annealing on PL, UV-Vis. Absorption Spectra

The PL (excitation wavelength of 420 nm) and UV-Vis. absorption spectra are shown in Figure 7.30. A Quartz/MEH-PPV(Ru)/PDPyDP/Al structure was made for the PL experiment. A similar structure, but without the Al layer, was used for the UV-Vis. absorption measurements. The PL output originated from the MEH-PPV layer and possesses two peaks: a main band at 600 nm together with an excimer peak at 635 nm. The PL intensity did not decrease after 5 days storage in low vacuum, in contrast to the EL output, and retained its shape over time. The PL emission output originated from the entire sample area, and there was no evidence of dark areas in the

PL output. This observation suggests that the dark areas seen in the EL image are still active in the PL emission. Hence, the dark area growth is not attributed to degradation of the organic materials and a luminescence quenching process over time. After annealing at 160 °C for 30 minutes, the PL intensity decreased to 60-70 % of its original maximum value and broadened. The relative intensity of the excimer peak at 635 nm increased.

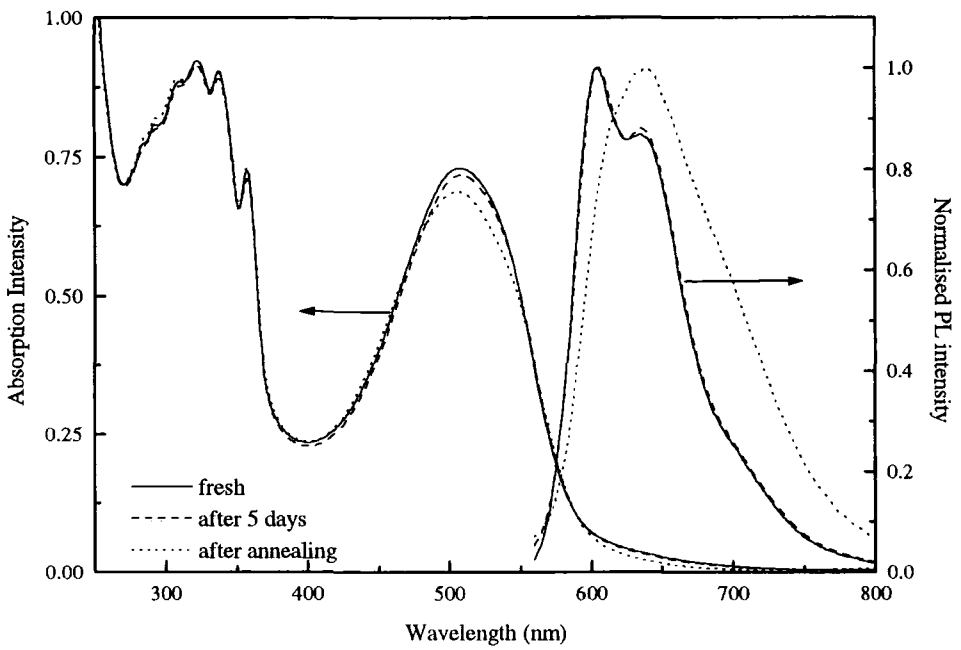

Figure 7.30 UV-Vis absorption spectra of quartz/MEH-PPV(Ru)/PDPyDP and normalised PL spectra of quartz/MEH-PPV(Ru)/PDPyDP/Al.

The increased excimer formation on annealing probably results from increased interchain interactions in the MEH-PPV(Ru) layer due to more chain packing in the case of stiff chain molecules such as π-conjugated polymers [29]. This excimer formation might be expected to lower the PL quantum efficiency and consequently to lead to lower EL external quantum efficiency. The higher quantum efficiency measured for the LED annealed at 160 °C is probably due to improved interfacial contact, which provides an increase in the electron injection from the Al electrode. As

a consequence, the improved contact compensates for the loss in the PL quantum efficiency.

There are no notable optical changes in the UV-Vis. absorption spectra with storage time and after the annealing treatment. The peak of 507 nm originates from the MEH-PPV while the bands at higher energy (300 ~ 350 nm) are from the PDPyDP. This suggests that the bandgap of MEH-PPV is unaffected by annealing at 160 °C for 30 minutes. All three curves are very similar to the fresh, vacuum-stored and annealed samples, again confirming that dark area growth in the EL image with storage time is not the result of any chemical decomposition of the organic layers.

7.6.5 Effect of Annealing on Dark areas in EL Image

The growth of the dark areas in the EL output was monitored with time by recording the EL image. Dark areas are evident in the EL images of all the devices, even the freshly prepared sample (Figure 7.31(a)). Upon storage in a low vacuum, these dark regions merge and islands of larger area are formed (Figure 7.31(b)). After 5 days storage in low vacuum, a large portion of active area was covered by dark areas (Figure 7.31(c)) resulting in a lower EL output. A careful study of the photographs, which were taken from identical areas of the same device, reveals that the increasing dark regions in the EL image are formed by the growth of existing dark 'spots' rather than by the nucleation of new spots. The dark regions observed in the EL image are created by initial defects, introduced during device fabrication. After annealing at 160 °C for 30 minutes, Figure 7.31(d) shows a substantial decrease in the area of the dark regions and an increase in the EL emission from the entire device

area. A close inspection of the EL image after annealing reveals nuclei, which possibly act as initial points of delamination.

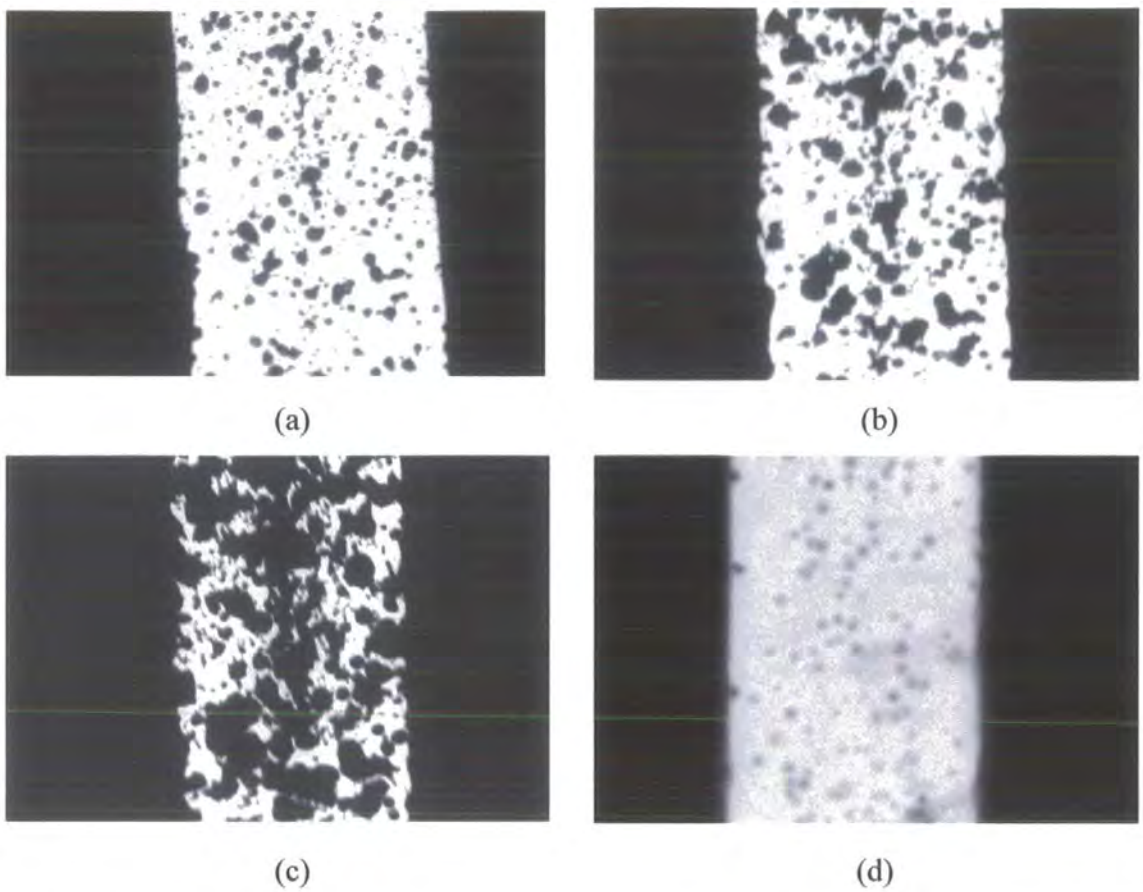

Figure 7.31 Dark area growth of the same device with time. (a) EL image of fresh device, (b) EL image of device stored in vacuum for 4 days, (c) EL image just before annealing treatment (after 5 days), and (d) EL image just after annealing. The device width is 1 mm.

In line with other workers [22], we suggest that the dark areas evident in the EL images correspond to regions in which there is poor physical and electrical contact between the PDPyDP layer and the Al cathode. Over time, further delamination of the metal top contact occurs, resulting in a decrease in the EL output from the LED. Annealing at a temperature approaching the sublimation temperature of PDPyDP, 160 ^{o}C, can accelerate inter-diffusion of the PDPyDP and the aluminium layer, e.g. via either formation of chemical bond, such as a C-Al bond [29] or improved molecular

atomic level interactions. The improved adhesion provides an increase in the conducting path for electron injection from the Al electrode leading to restored light output from the degraded device.

7.6.6 AFM Studies

Figure 7.32 shows surface morphologies of the Al surface observed by AFM at various states and with no voltage applied to the LED structure before the measurement: (a) immediately after Al evaporation; (b) after one day storage in air; and (c) after annealing with sample (b) at 160 °C for 30 minutes. The roughness of the Al surface can be evaluated by the surface parameters of the AFM images as listed in table 5.

	RMS (nm)	Average height (nm)	Maximum range (nm)
Just after Al evaporation	5.05	29.44	69.37
After one day storage	7.28	94.72	144.61
After annealing at 160 °C for 30 min.	5.94	66.64	99.89

Table 5. Surface parameters of AFM images of the Al surface at various states.

The morphology after one day storage shows sharp peaks arising over the whole Al surface, resulting in a twofold increase in the maximum range (maximum height – minimum height) compared with that of the fresh Al surface. The rough edge line of Figure 7.32(b) shows the possible existence of cavities between the Al surface and the adjacent layer. The peaks disappear and the Al surface becomes smoother after the annealing treatment. However, the surface is still not as smooth as that of the fresh surface.

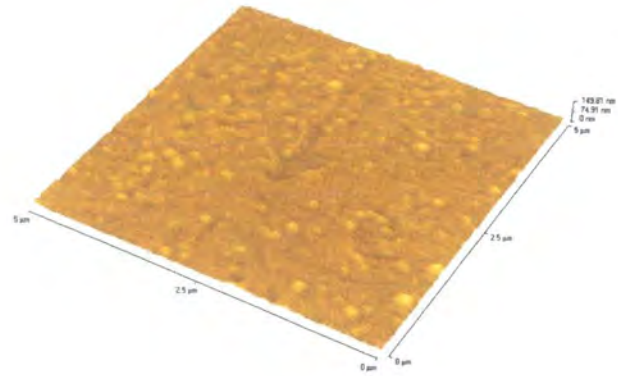

(a)

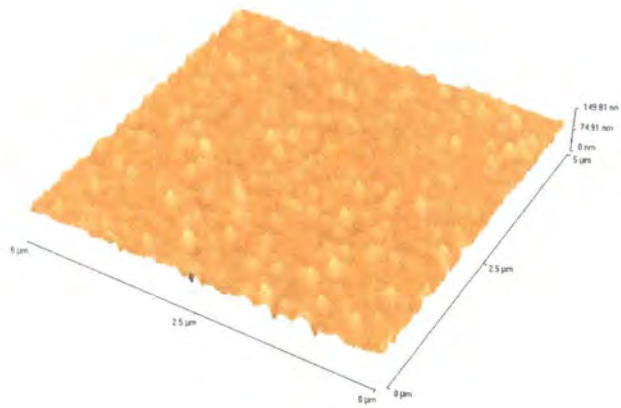

(b)

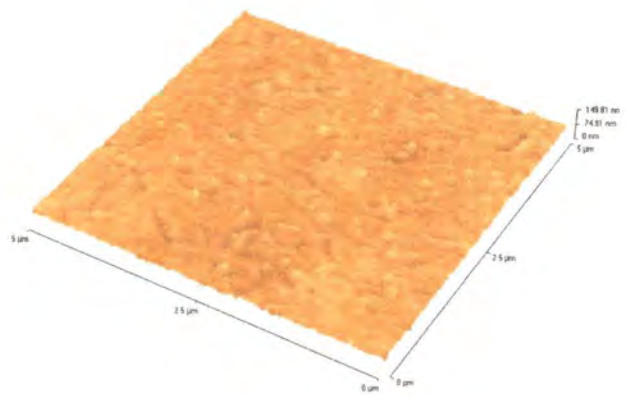

(c)

Figure 7.32 AFM images of the Al surface of (a) fresh device, (b) device stored for one day in air and (c) device after annealing treatment at 160 °C for 30 minutes.

7.6.7 Storage and Operating Lifetime Tests

Figure 7.33 shows the stability with time of a device annealed at 160 °C for 30 minutes. After the annealing treatment, the sample current and the light output did not decrease as rapidly as the fresh device with storage time. This suggests that annealing results in a reasonably strong bond between the PDPyDP and the Al electrode.

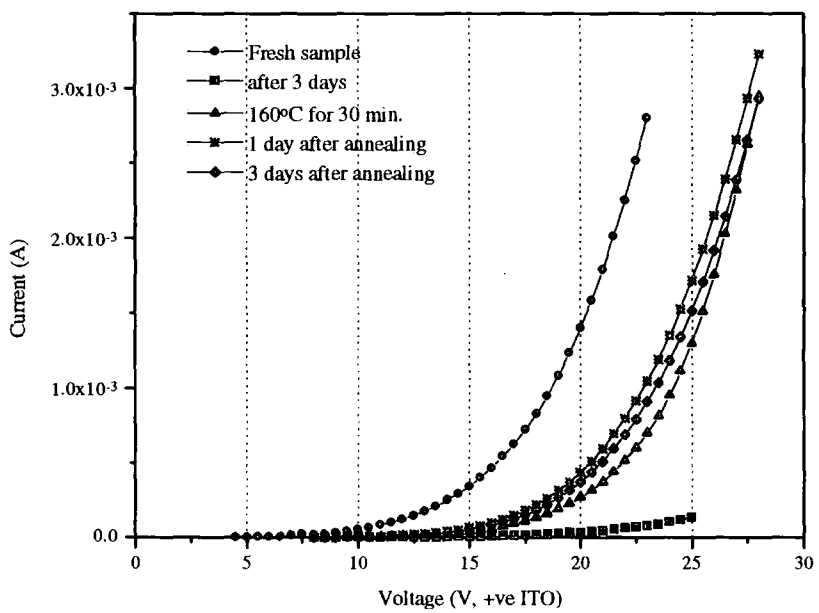

Figure 7.33 The change of I-V characteristics of MEH-PPV(Ru)/PDPyDP device with time after annealing at 160 °C for 30 minutes.

To study the device operating lifetime, a constant current of 0.2 mA, equivalent to a current density of 10 mA cm^{-2}, was passed through the LEDs that had been subjected to the annealing treatments at 160 °C and 175 °C. The EL output (measured in low vacuum) was monitored with time and compared with that of the fresh device in Figure 7.34. The light output of a fresh device decreased rapidly over one hour and the device was completely degraded (no detectable EL output) after 9 hours of constant current stress. In contrast, both of the annealed LEDs exhibited significantly increased lifetimes. In the case of the structure annealed at 175 °C, the

EL output first showed a slight increase during the first stages of the stress experiment and then stabilized.

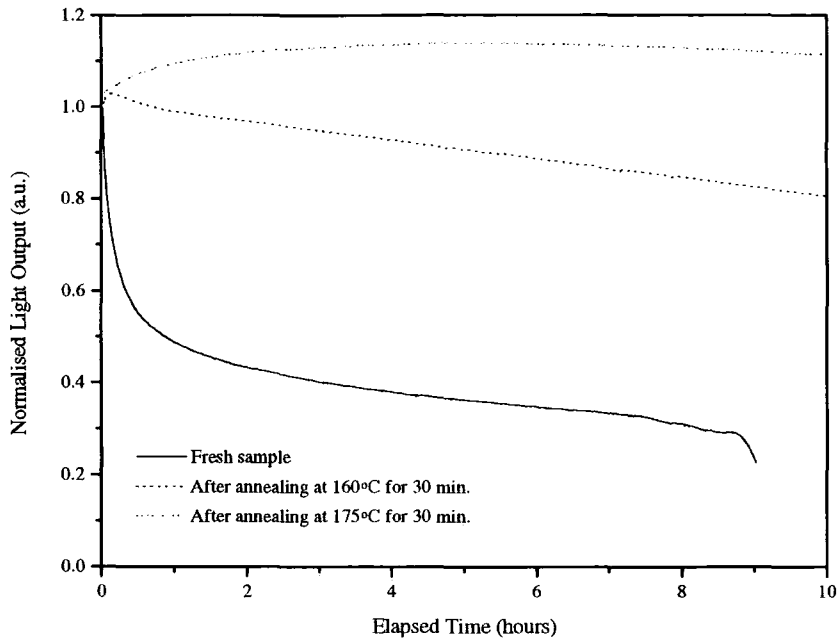

Figure 7.34 Luminance decay test with constant current (0.2 mA) after annealing.

Despite the longer lifetime, it should be noted that the device annealed at 175 °C possessed a lower external quantum efficiency than the structure treated at 160 °C. Esselink et al. [30] showed that as the annealing temperature increased, the diffusion length of Al atoms into the polymer layer increased and a stable interface with the conjugated polymer could be formed. At high annealing temperatures, Al atoms can diffuse further into the polymer and form chemical bonds deeply inside this layer. The emission zone for EL therefore is moved closer to the Al electrode, which can act as a quenching site for excitons, consequently lowering the quantum efficiency. Choice of the annealing temperature requires a compromise to be made between device lifetime and device efficiency. The decrease in the quantum efficiency at higher temperatures

(195 °C) may be related to some morphological change in the emissive layer, such as a transition from an amorphous to a polycrystalline structure.

7.7 Al Evaporation

The results in the previous section suggest that the bonds formed between the aluminium cathode and the evaporated electron transporting layer is important in determining both the storage and operating lifetime of our LEDs. We therefore have undertaken a series of experiments in which the rate of evaporation and thickness of the aluminium were varied. The Al evaporation rate of all the former devices is 1.6 nm s^{-1}.

Several devices were made with different conditions for the Al evaporation: (I) rate, 0.25 nm s^{-1} and thickness, 150 nm; (II) rate, 3.5 nm s^{-1} and thickness, 150 nm; (III) rate, 3.5 nm s^{-1} and thickness, 300 nm; and (IV) rate, 14 nm s^{-1} and thickness, 300 nm. The I-V characteristics of these devices were recorded with storage day. Figure 7.35 shows the current (a) and quantum efficiency (b) variation with storage day, which are normalised with the values of the fresh devices at 20 V.

There is a trend for the device using a slower Al evaporation rate to degrade more rapidly than devices produced with higher evaporation rates. The currents and the quantum efficiencies decreased with time and finally remained constant after devices were fully degraded as shown in Figure 7.35. The lifetimes are: 3 days for the device (I); 5 days for the device (II); 11 days for the device (III); and still active up to

13 days for the device (IV). Device (IV) with a thicker Al electrode is more stable than the device with a thinner one (III).

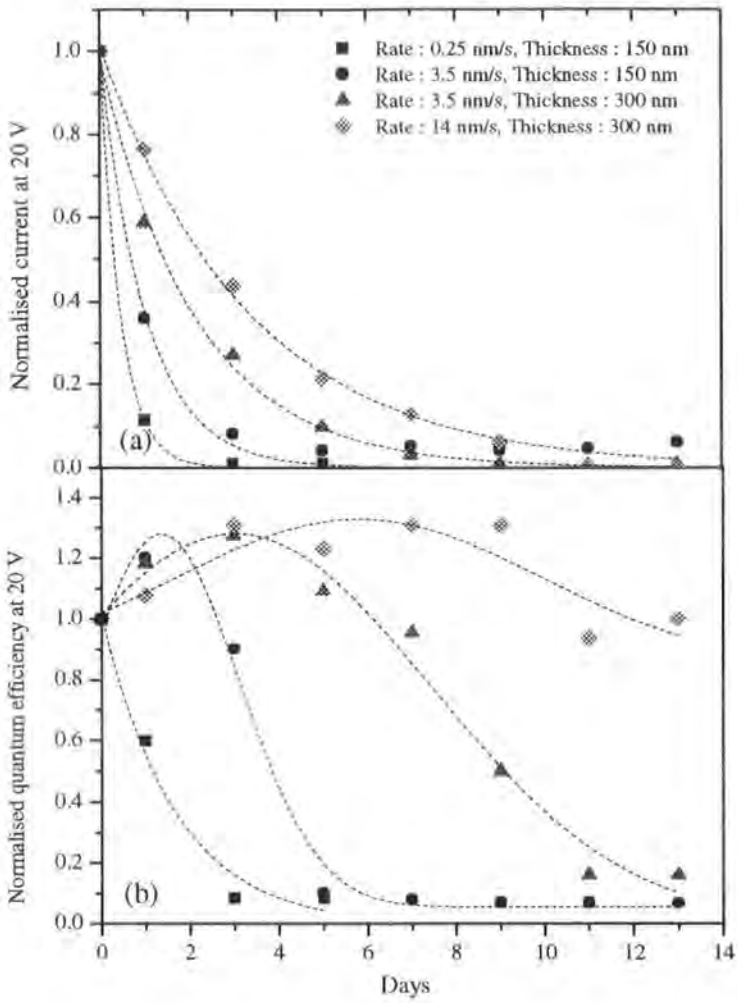

Figure 7.35 The current and quantum efficiency change with storage time. The values at 20 V are normalised with those of fresh device at the same voltage.

The rate at which aluminium is deposited onto a surface has been found to greatly influence the properties of the resulting film [31]. This can arise from a competition between attack by residual gases at the freshly coated aluminium surface and the deposition of another layer of aluminium. The most important species to consider are oxygen and water, which attack the Al surface during evaporation

causing a rougher surface. As the rate of evaporation is increased, the arrival of Al at the substrate outpaces the arrival of the background gases. The AFM images of the Al electrodes for the devices in which the Al was evaporated at 0.25 nm s^{-1} and 3.5 nm s^{-1} are shown in Figure 7.36(a) and (b), respectively. These were taken immediately after the Al evaporation.

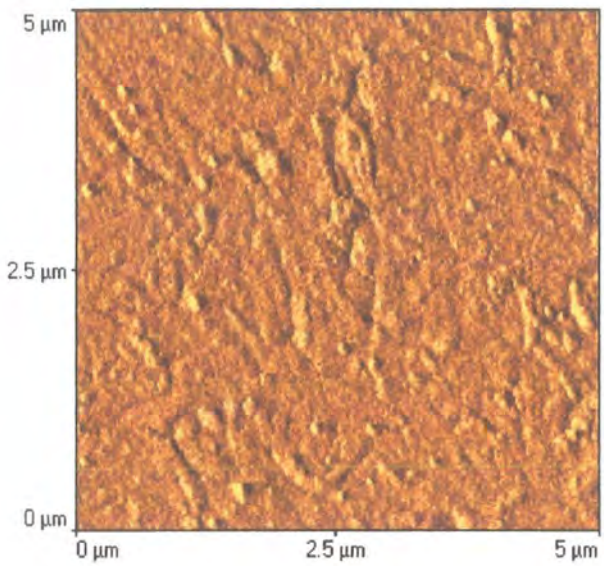

(a)

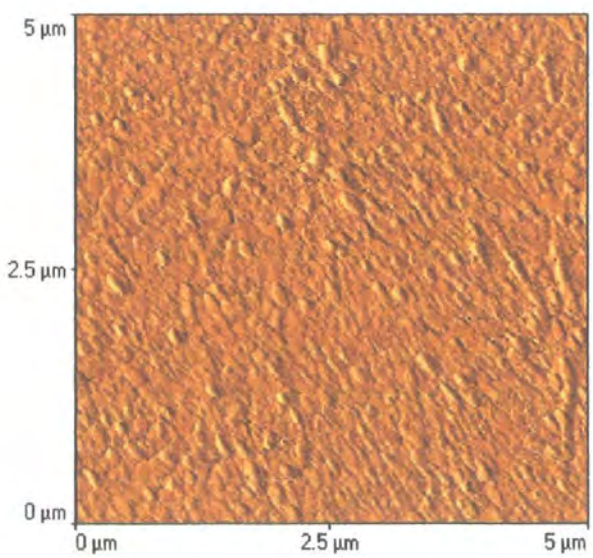

(b)

Figure 7.36 AFM image of the Al electrode evaporated at the rate of (a) 0.25 nm s^{-1} and (b) 3.5 nm s^{-1}.

The Al surface evaporated at the lower rate is very rough and has many deep valleys. On the other hand, the surface evaporated at the higher rate is a more uniform surface. An Al surface with sharp peaks and deep valleys is likely to have pin-holes, allowing the penetration of oxygen and moisture penetration and leading to a rapid device degradation [32]. Figure 7.37 shows the light output decay of fresh devices with different Al evaporation conditions at a constant current of 0.2 mA. The device with a thicker electrode evaporated at a higher rate has a longer operating lifetime. Although there were improvements over devices with thinner/slower evaporated Al electrodes, the effect on the operating lifetime was not as marked as that produced by annealing.

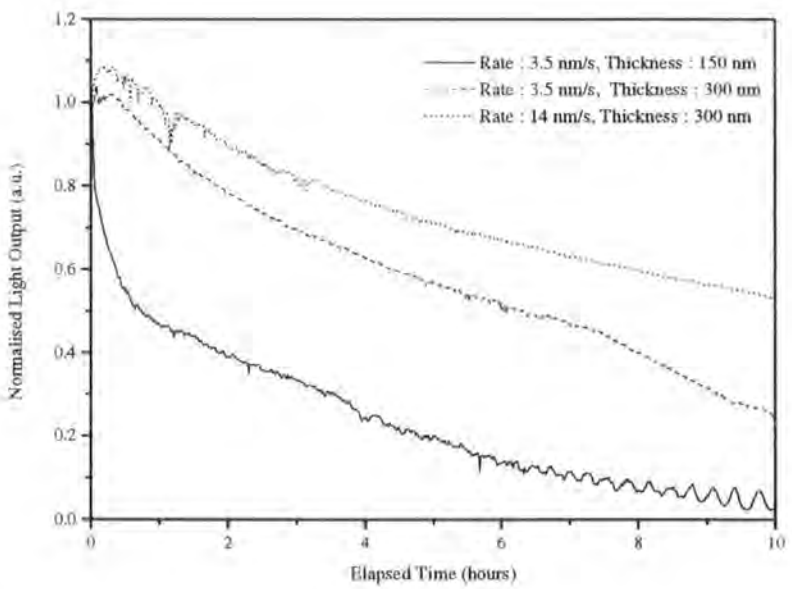

Figure 7.37 Light output decay for the devices with Al electrode evaporated under different conditions.

7.8 Summary

Spin-coated MEH-PPV films possess less excimer formation and a shorter conjugation length in comparison with the MEH-PPV LB films. Consequently, LEDs incorporating spun films have higher quantum efficiencies than devices with LB films.

2,5-bis[2-(4-*tert*-butylphenyl)-1,3,4-oxadiazol-5-yl]pyridine (PDPyDP) has been shown to be a useful material as an electron transporting layer in organic LED structures. The optimally performing dual-layer device, ITO/MEH-PPV(Ru) (100 nm)/PDPyDP (60 nm)/Al possessed a luminance of approximately 4×10^3 cd m^{-2} at an operating current density of 0.3 A cm^{-2} and an external quantum efficiency of 0.7 %. Despite a low electron injection barrier at the interface between the PDPyDP layer and the Al top electrode, dark regions appeared in the EL image over storage time, resulting in degradation of the device. This is ascribed to the delamination of Al electrode from the organic layer due to weak cohesion.

By inserting (I) a CuPc buffer layer between ITO and the emissive layer and and an Alq_3 layer between the Al electrode and the PDPyDP layer and (II) doping rubrene into the MEH-PPV layer, the storage and operating lifetime of the device was much improved but, still vulnerable to the heat generated during operation.

Annealing above the sublimation temperature of PDPyDP promoted the adhesion between this material and the Al electrode, owing to improved bonds resulting in either C-Al chemical bonds or molecular atomic level interactions. Annealing of the degraded devices restored sample currents and light output and in addition to give a notable increase in lifetime.

Using a relatively fast evaporation rate for aluminium produced a more uniform Al surface and a thicker Al electrode had less pin-holes on the surface. These effects prevented the penetration of moisture and/or oxygen, thereby reducing the delamination of the metal and improving the storage and operating lifetime of the devices.

References

1. Y. Shi, J. Liu and Y. Yang, *J. Appl. Phys.*, **87**, 2000, 4254.

2. I.D.W. Samuel, G. Rumbles, C.J. Collison, B. Crystall, S.C. Moratti and A.B. Holmes, *Synth. Met.*, **76**, 1996, 15.

3. N.Q. Nguyen, *J. Phys. Chem. B*, **104**, 2000, 237.

4. T. Miyashita, M. Matsuda, M.V.D. Auweraer and F.C.D. Schryver, *Macromolecules*, **27**, 1994, 513.

5. A. Bolognesi, C. Botta, G. Bajo, R. Osterbacka, T. Ostergard and H. Stubb, *Synth. Met.*, **98**, 1998, 123.

6. M. Zheng, F. Bai and D. Zhu, *J. Photoch. Photobio. A: Chemistry*, **116**, 1998, 143.

7. T. Fort and R.L. Wells, *Surf. Sci.*, **32**, 1972, 543.

8. Y. Hamada, C. Adachi, T. Tsutsui and S. Saito, *Jpn. J. Appl. Phys.*, **31**, 1992, 1812.

9. S. Dailey, M. Halim, E. Rebourt, L.E. Horsburgh, I.D.W. Samuel and A.P. Monkman, *J. Phys: Condens. Matter*, **10**, 1998, 5171.

10. C. Wang, G.Y. Jung, Y. Hua, M.R. Bryce, C. Pearson, M.C. Petty, A.S. Batsanov, A.E. Goeta and J.A.K. Howard, *Chem. Mater.*, **13**, 2001, 1167.

11. Z.L. Zhang, X.Y. Jiang, S.H. Xu, T. Nagatomo and O. Omoto, *J. Phys. D: Appl. Phys.*, **31**, 1998, 32.

12. Y. Sato, S. Ichinosawa and H. Kanai, *IEEE J. Sel. Top. Quantum Electron.*, **4**, 1998, 40.

13. M.S. Jang, S.Y.Song, H.K.Shim, T.H. Zyung S.D. Jung, and L.M. Do, *Synth. Met.*, **91**, 1997, 317.

14. I.D. Parker, *J. Appl. Phys.*, **75**, 1994, 1656.

15. M. Uchida, C. Adachi, T. Koyama and Y. Taniguchi, *J. Appl. Phy.*, **86**, 1999, 1680.

16. M. Granström and O. Inganäs, *Appl. Phys. Lett.*, **68**, 1996, 147.

17. T. Sano, Y. Hamada, and K. Shibata, *IEEE J. Sel. Top. Quantum Electron.*, **4**, 1998, 34.

18. A. Curioni and W. Andreoni, *J. Am. Chem. Soc.*, **121**, 1999, 8216.

19. S.A. VanSlyke, C.H. Chen and C.W. Tang, *Appl. Phys. Lett.*, **69**, 1996, 2160.

20 S. Karg, J.C. Scott, J.R. Salem and M. Angelopoulos, *Synth. Met.*, **80**, 1996, 111.

21. H. Vestweber and W. Riess, *Synth. Met.*, **91**, 1997, 181.

22 J. McElvain, H. Antoniadis, M.R. Hueschen, J.N. Miller, D.M. Roitman, J.R. Sheats and R.L. Moon, *J. Appl. Phys.*, **80**, 1996, 6002.

23. C. Adachi, K. Nagai and N. Tamoto, *Appl. Phys. Lett.*, **66**, 1995, 2679.

24. J.C. Scott, J.H. Kaufman, P.J. Brock, R. DiPietro, J. Salem and J.A. Goitia, *J. Appl. Phys.*, **79**, 1996, 2745.

25 M. Yan, L.J. Rothberg, F. Papadimitrakopoulos, M.E. Galvin and T.M. Miller, *Phys. Rev. Lett.*, **73**, 1994, 744.

26. J.C. Scott, S.A. Carter, S. Karg and M. Angelopoulos, *Synth. Met.*, **85**, 1997, 1197.

27. T.W. Lee and O.O. Park, *Adv. Mat.*, **12**, 2000, 801.

28. H. Aziz, Z.Popovic, S. Xie, A.M. Hor, N.X. Hu, and G. Xu, *Appl. Phys. Lett.*, **72**, 1998, 756.

29. M. Logdlund and J.L. Bredas, *J. Chem. Phys.*, **101**, 1994, 4357.

30. F.J. Esselink and G.Hadziioannou, *Synth. Met.*, **75**, 1995, 209.

31. C.W. Hollars and R.C. Dunn, *Rev. Sci. Instrum.*, **69**, 1998, 1747.

32. L.M. Do, *Synth. Met.*, **111-112**, 2000, 249.

Chapter 8.

Conclusions and Suggestions for Further Work

8.1 Conclusions

Organic light emitting devices have been fabricated based on poly(2-methoxy-5(2'-ethylhexyloxy)-*p*-phenylenevinylene), MEH-PPV. Thin films of MEH-PPV were deposited by either the Langmuir-Blodgett technique or spin-coating.

The pressure versus area curve of the MEH-PPV Langmuir film reveals the onset of collapse of the monolayer at 16 mN m^{-1}. No deposition was seen with a surface pressure within the 'condensed' region. However, Y-type LB films of MEH-PPV were deposited onto indium tin oxide (ITO) glass and quartz substrates at a surface pressure of 17 mN m^{-1} and pH of 5.2 – 5.6 with a transfer ratio of 0.95 ± 0.03. It is assumed that the stability of the condensed floating film is increased by the interleaving of short side chains between layers in the collapsed film.

Single-layer MEH-PPV LEDs were made by the LB technique. The current versus voltage and light output versus voltage curves exhibited rectifying behaviour. Orange-yellow light was visible to the naked eye in a darkened room under forward bias. The external quantum efficiency of these devices was about 8.0×10^{-4} % at a current density of 10^{-2} A cm^{-2}.

Several models were fitted to the I-V data to find the conduction mechanism within the MEH-PPV single-layer device. Cole-Cole plots from a.c. impedance spectroscopy measurements revealed no depletion regions associated with a Schottky barrier within the device. Furthermore, the thickness and temperature dependence of

the I-V characteristics were not in agreement with the predictions of Fowler-Nordheim tunnelling theory. Two different regions could be seen in log(I)-log(V) graph. The slope changed from 2 at low applied voltage (space charge limited current) to 5~6 at high applied voltage (trap charge limited current). This power law dependence of the I-V characteristics could be modelled by SCL current theory with a trap distribution over large temperature and thickness ranges.

Several strategies were used to increase the external quantum efficiency of LEDs based on MEH-PPV LB films. The insertion of arachidic acid (AA) layers between the MEH-PPV film and the aluminium cathode was found to decrease the turn-on voltage for electroluminescence (EL) and to increase the external quantum efficiency. In contrast, depositing the fatty acid layer between the polymer and the ITO anode resulted in poorer device performance.

LB layers of the electron-transporting material, poly(6-hexyl-2,5-pyridinediyl) (PHPY), were deposited on top of the MEH-PPV LB films to make a dual-layer device (ITO/MEH-PPV/PHPY/Al). Z-type transfer of the PHPY was observed at a dipping pressure of 30 mN m^{-1}. The EL spectrum of the dual-layer device was nearly the same as that of the MEH-PPV single-layer device, confirming that light emission originated from the MEH-PPV layer. The external quantum efficiency increased to 7.5×10^{-3} %, about ten times greater than that measured from the MEH-PPV single-layer device. The reason for the greater external quantum efficiency is that the injection of more electrons leads to a more balanced charge carrier recombination which takes place at the interface between the MEH-PPV and the PHPY layer. The PHPY layer also moves the recombination region away from the Al electrode, avoiding nonradiative quenching effects. The turn-on voltage for EL in the dual-layer

structure was 4 V lower than that of the single-layer device due to the lower energy barrier for electrons at the Al cathode.

Annealing the MEH-PPV LB films prior to evaporation of the Al electrode enhanced the packing of the polymer thin film. This was confirmed by a reduction in thickness. UV-Vis. absorption spectra, in which the absorption peaks were blue-shifted with increasing annealing temperature, suggested the aggregation of molecules in the LB films. The PL spectrum was red-shifted as the annealing temperature increased, suggesting that more aggregation and intra- and/or interchain interactions occur by enhanced packing of the polymer.

Devices in which the organic film was dried in a high vacuum at room temperature possessed the highest external quantum efficiency. The lower efficiency for devices composed of pre-annealed LB films was ascribed to aggregates or intra- and/or interchain interactions, which promote nonradiative decay channels. However, a longer operating lifetime could be obtained by annealing the LB film at an elevated temperature before metallisation. The degradation of devices was attributed to the rupture of the Al electrode surface. The main reason for the short lifetime was an uneven LB film surface which resulted in a nonuniform electric field.

The operating lifetime of the MEH-PPV single-layer device could be further increased by the use of a thin layer (< 2 nm) of lithium fluoride (LiF) between the polymer film and the Al electrode and by encapsulation of the whole device with an adhesive tape.

The optical properties of MEH-PPV spun films were compared with those of the LB films. A fitting procedure to the photoluminescence spectra using three Gaussian curves revealed that the LB film samples had more excimer formation and

aggregation. This was ascribed to the π-π overlap within the stack which enhances the interchain interaction. This excimer formation can increase nonradiative decay in solution and in the solid state. Consequently, the external quantum efficiency of devices fabricated using spun films was four times higher than that of devices with LB films.

Scanning electron microscopy and surface profile measurements of both types of film showed that the surface of the spun film was very uniform and even, whereas the surface of the LB film was rough. The uneven surface results in a very non-uniform electric field within the device which caused device breakdown. Longer lifetimes were exhibited in the devices with spun film than in the devices with LB films.

A new bis-OXD system incorporating an electron deficient compound of pyridine, 2,5-bis[2-(4-*tert*-butylphenyl)-1,3,4-oxadiazole-5-yl]pyridine (PDPyDP), was synthesized as an electron-transporting and hole-blocking material. Its properties as an electron-transporting layer within the LEDs was compared with the analogue, 1,3-bis[2-(4-*tert*-butylphenyl)-1,3,4-oxadiazole-5-yl]benzene (OXD-7), a compound widely used as an electron transport material. The external quantum efficiency of dual-layer devices with a PDPyDP layer on an MEH-PPV spun film was approximately a factor of five higher than that of devices using OXD-7. This could be explained by the lower LUMO level and higher electron mobility of the PDPyDP layer. However, the PDPyDP devices were not stable. The current and the EL intensity both decreased during storage in low vacuum (10^{-1} mbar) and dark, non-emissive regions were evident when the device was viewed through the ITO electrode

during operation. These dark regions in the EL image enlarged over a period of time resulting in degradation of the device.

A number of strategies were adopted to improve the storage and operating lifetime of the devices incorporating a PDPyDP layer. Devices with rubrene doped MEH-PPV exhibited external quantum efficiencies that were greater by one order of magnitude and showed improved operating lifetime compared with the undoped device. The best luminance for the dual-layer devices utilising rubrene-doped MEH-PPV and PDPyDP was 4×10^3 cd m^{-2} at a current density of 0.3 A cm^{-2}. A maximum external quantum efficiency of 0.7 % was observed for this dual-layer system. The real value could be over 1 % (i.e. measured with an integrating sphere instead of a photodiode) considering that about 50 % of the emitted light from the device is waveguided to the glass substrate edge [1].

Despite the high brightness, dark regions were still evident in the EL image of the rubrene-doped device. The growth of these regions was ascribed to the delamination of the Al cathode from the PDPyDP layer. This was caused by the poor interfacial contact of the PDPyDP layer with the Al cathode, which was accelerated by moisture/air penetration through pin-holes in the Al electrode surface. Insertion of a copper phthalocyanine (CuPc) layer between the ITO and the emissive layer and a tris (8-hydroxyquinoline) aluminium (Alq_3) layer between the electron transporting layer and the Al top electrode significantly improved the storage and operating lifetime of the devices.

The sample currents and light output of the degraded devices could be restored by annealing above the sublimation temperature of the PDPyDP, 160 °C, for 30 minutes. The currents and light output were still lower than those of fresh devices

due to a possible morphology change in the organic films. However, the quantum efficiencies of devices annealed at 160 °C were comparable with those of fresh ones.

Dark areas in the EL image were eliminated and the EL originated from the entire device area after annealing. These results show that the adhesion of the PDPyDP layer to the Al electrode was improved either by the formation of stronger chemical bonds between Al atoms and PDPyDP molecules such as the Al-C bond or by molecular atomic-level interactions. After the annealing treatment, the device was relatively stable. For example, the EL output of the device annealed at 175 °C showed no sign of decrease up to 10 hours during a constant current stress of 0.2 mA. This is in contrast to the fresh device which had completely degraded after 9 hours.

The smoothness of the Al electrode surface is an important factor for the device stability and lifetime. Devices with a thicker electrode evaporated at a higher rate had a better performance in terms of storage and operating lifetime.

8.2 Suggestions for Further Work

Once photons are generated within the device, not all can escape to the external world. There are several reasons for this, illustrated in Figure 8.1 [2].

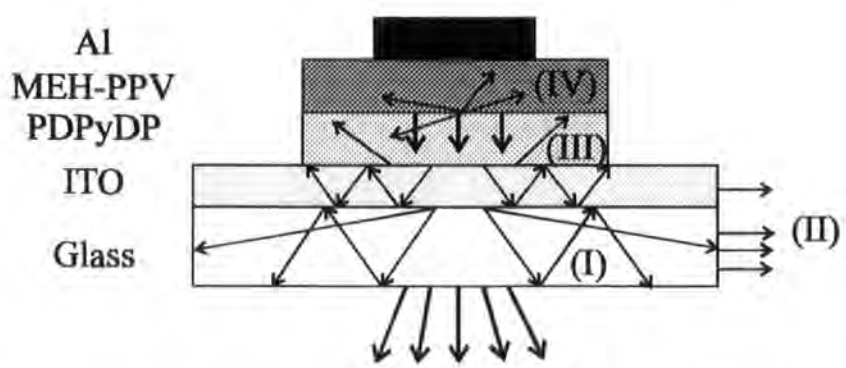

Figure 8.1 A diagram showing the reflection of rays within organic LEDs.

The processes shown in the figure are:

(I) Reflection from the interface between the glass and the air.

(II) Edge emission, which is waveguided to the edge of the medium owing to total reflection within the glass and ITO layer. The absorption of the ITO layer is negligible since the ITO thickness of 45 nm is very thin compared with the glass thickness of 0.7 mm.

(III) Reflection from the ITO surface. This is related to the critical angle, θ_c.

(IV) Self-absorption by trapping centres within the material, etc.

Such processes could be reduced or even eliminated by modifying the device structure, leading to higher external quantum efficiencies. Several schemes for this are suggested below.

8.2.1 Prevention of Reflection at the Glass-Air Interface

To minimize the reflectivity losses, the reflectivity coefficient R should be considered. This is given by Fresnel's equation for a medium of refractive index n_2 and external medium with refractive index n_3

$$R = \frac{(n_2 - n_3)^2}{(n_2 + n_3)^2} \tag{8.1}$$

When an additional dielectric medium with refractive index n_1 is placed on top, the reflectivity coefficient R becomes

$$R = \frac{(n_1 n_3 - n_2^2)^2}{(n_1 n_3 + n_2^2)^2} \tag{8.2}$$

Modified ITO glass can be exploited to decrease R. A SiN layer (400 nm, n ≈ 1.85 [3]) was deposited on the glass by chemical vapour deposition and the ITO layer (45 nm) was subsequently deposited on the SiN layer. Using a refractive index of 1.5 at a wavelength of 590 nm [3] for the glass and 1 for the air, the reflectivity coefficient of the modified ITO glass is 0.15, which is lower than that of normal ITO glass, 0.36.

A dual-layer MEH-PPV (85 nm)/PDPyDP (70 nm) and a single-layer MEH-PPV spun film were deposited on the modified ITO glass. Their I-V characteristics and external quantum efficiencies are compared with devices fabricated on the normal ITO glass in Figure 8.2 and the results are summarized in Table 6.

The external quantum efficiency increased by 37 % for the single layer MEH-PPV device and by 31 % for the dual-layer device. The preliminary data support the idea of minimizing the reflectivity between the glass and the air by inserting a dielectric medium which has a higher refractive index than the glass. In theory, modified ITO glass with a dielectric medium with refractive index of 2.1 has the lowest reflectivity coefficient, leading to more light output from the glass surface. Therefore, a search for the best medium and its thickness dependence on the light output should be explored.

Device	MEH-PPV (at 0.2 A cm^{-2})	MEH-PPV/PDPyDP (at 0.1 A cm^{-2})
Normal ITO glass	2.7×10^{-3} (%)	2.6×10^{-1} (%)
Modified ITO glass	3.7×10^{-3} (%)	3.4×10^{-1} (%)
Increase	37 %	31 %

Table 6. Comparison of the external quantum efficiency between devices with and without a SiN layer.

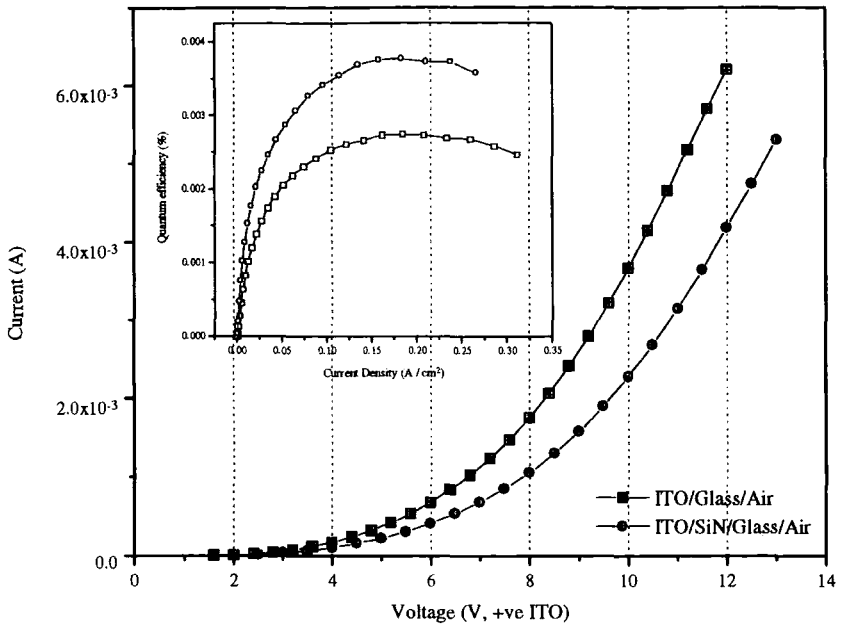

(a)

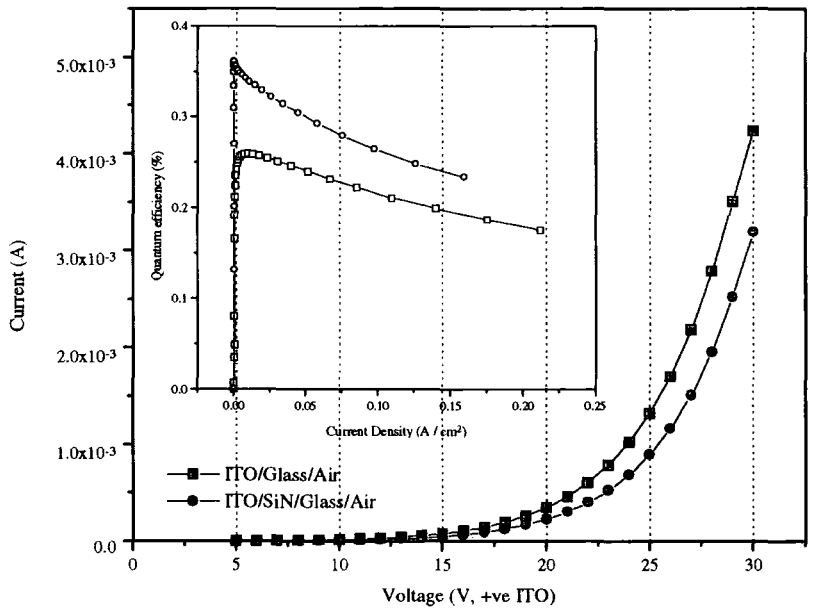

(b)

Figure 8.2 Comparison of I-V characteristics and the external quantum efficiencies for devices based on normal ITO glass and modified ITO glass. (a) single-layer MEH-PPV structure, (b) dual-layer MEH-PPV/PDPyDP structure. (closed symbols: current, open symbols: light output)

8.2.2 Elimination of Total Reflection within the Glass

(Scheme 1)

Devices based on flat ITO glass are not good in terms of radiant flux and intensity. Bulovic et al. [4] showed that a large portion of the total light was emitted from the glass edge by total internal reflection. It is possible that, by redirecting the edge-emitted light, the substrate surface emission can be greatly enhanced [1]. To decrease the total internal reflection, the geometrical design of glass with a lens type at one side are required, as shown in Figure 8.3. The geometrically modified ITO substrate can be made by sputtering ITO on the flat side of glass. This lens type glass can direct the light forward and reduce total internal reflection.

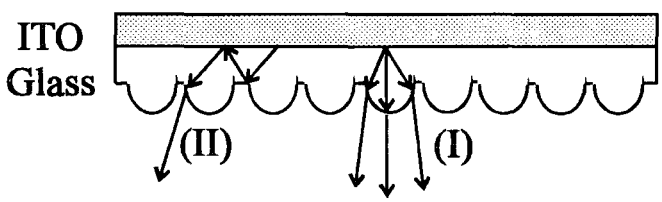

Figure 8.3 A geometrically modified ITO glass. (I) light directed forward by the lens type glass, (II) prevention of total reflection by the eclipsed shape.

(Scheme 2)

The glass is the source of total internal reflection as noted above. So, why not try to make the organic LEDs without glass? Edge emission would then be eliminated. An aluminium layer can be evaporated onto a polished silicon wafer and then the electron-transporting and emissive layer can be deposited. Finally organic LEDs without glass can be realised by sputtering an ITO layer on top, as depicted in Figure 8.4. The sputtering conditions must be adjusted so that the ITO layer has a low refractive index, a high critical angle and a low reflectivity coefficient at the interface with the air.

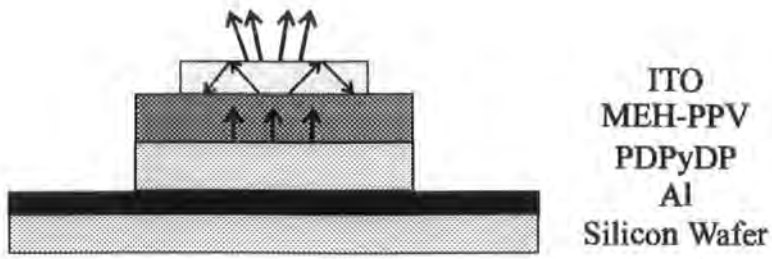

Figure 8.4 Modified device structure without the glass.

8.2.3 Increase of The Critical Angle, θ_c

When a ray of light passing from a dense to a less dense medium, e.g. glass to air, meets the surface, a portion of the light does not emerge, but is internally reflected. At a certain angle, called the critical angle, the light no longer emerges into the air above the surface. In the case of a medium with refractive index n which interfaces with air, the critical angle of θ_c is given by

$$\theta_c = \sin^{-1}(1/n) \qquad (8.3)$$

Thus, a higher critical angle is required for more light to emerge from the surface to the outside world. Greenham et al. [5] showed that external quantum efficiency was a factor of $2n^2$ smaller than internal quantum efficiencies. A medium with a smaller refractive index can have a higher critical angle. Given that the ITO layer interfaces with air, the refractive index of the ITO glass should be well matched with that of the air. The refractive index could be changed by altering the sputtering process conditions such as oxygen amount, processing temperature and pressure, etc, to give a higher critical angle.

References

1. G. Gu, D.Z. Garbuzov, P.E. Burrows, S.Venkatesh and S.R. Forrest, *Opt. Lett.*, **22**, 1997, 396.

2. D. Wood, *Optoelectronic Semiconductor Devices*, Prentice Hall, **London**, 1994, 85.

3. R.C. Weast, and M.J. Astle, *CRC Handbook of Chemsitry and Physics*, CRC Press, **Florida**, 1978

4. V. Bulovic, V.B. Khalfin, G. Gu and P.E. Burrows, *Phys. Rev. B*, **58**, 1998, 3730.

5. N.C. Greenham, R.H. Friend and D.D.C. Bradley, *Adv. Mater.*, **6**, 1994, 491.

Publications

1. **G.Y. Jung**, C. Pearson, M. Kilitziraki, L.E. Horsburgh, A.P. Monkman, I.D.S. Samuel and M.C. Petty, "Dual-layer Light Emitting Devices based on Polymeric Langmuir-Blodgett Films", *J. Mater. Chem.*, **1**, 2000, 163.

2. **G.Y. Jung**, C. Pearson, L.E. Horsburgh, I.D.W. Samuel, A.P. Monkman and M.C. Petty, "The Effect of Insulating Spacer Layers on the Electrical Properties of Polymeric Langmuir-Blodgett Film Light Emitting Devices", *J. Phys. D.: Appl. Phys.*, **33**, 2000, 1029.

3. **G.Y. Jung**, C.S. Wang, C. Pearson, M.R. Bryce, I.D.W. Samuel and M.C. Petty, "Electroluminescent Devices Incorporating a New Oxadiazole Derivative", *Proc. SPIE Organic Light-Emitting Materials and Device*, **San Diego**, 2000, 307.

4. C.S. Wang, **G.Y. Jung**, Y. Hua, C. Pearson, M.R. Bryce, M.C. Petty, A.S. Basanov, A.E. Goeta and J.A.K. Howard, "An Efficient Pyridine and Oxadiazole Containing Hole-Blocking Material for Organic Light Emitting Diodes: Synthesis, Crystal Structure and Device Performance", *Chem. Mater.*, **13**, 2001, 1167.

5. **G.Y. Jung**, A. Yates, I.D.W. Samuel and M.C. Petty, "Lifetime Studies of Light Emitting Diode Structures Incorporating Polymeric Langmuir-Blodgett Films", *Mater. Sci. & Eng. C*, in press.

6. **G.Y. Jung**, C. Pearson and M.C. Petty, "The Use of LB Insulating Layers to improve the Efficiency of Light Emitting Diodes based on Evaporated Molecular Films", Contributed to *Studies in Interface Science*, edited by D. Mobius and R. Miller, Elsevier.

7. **G.Y. Jung**, C.S. Wang, P. Cea, C. Pearson, M.R. Bryce and M.C. Petty, "The Effects of Processing Conditions on the Efficiency and Lifetime of Organic Light Emitting Devices Incorporating a New Oxadiazole Derivative", submitted to *J. Appl. Phys.*, 2001.